AAAS

Science

4 SEPTEMBER 2025

RULES OF THUMB

The importance of a hand that holds in the evolution of rodents **p. 1049**

Microbial innovation: Changing the future, one cell at a time

At the State Key Laboratory of Microbial Technology (SKLMT), microbial science and technology drive solutions for a changing world.

Every year, 1.27 million deaths are attributed to harmful microbes that have evolved to evade treatment. This antimicrobial resistance (AMR) goes beyond antibiotics to include antivirals, antifungals, and antiparasitics. Left unchecked, the World Bank estimates AMR could cost the global economy trillions of dollars annually by 2030, while the World Health Organization ranks AMR as a top 10 global public health threat.

"Deaths from infections far exceed other diseases, even surpassing cancer," says Youming Zhang, director of China's State Key Laboratory of Microbial Technology (SKLMT). Founded 30 years ago, SKLMT is one of the first national key laboratories in China focused on microbiology. Their scientists are not only tackling microbial resistance but addressing other global challenges as well, such as clean energy and plastic waste.

Resistance and recombineering

Even early in Zhang's career, working as a microbial engineer in Germany, he imagined a future in which it would be possible to treat untreatable infections by editing microbial genomes. Zhang's vision led him to an approach that enables precise, large-scale modifications to microbial, as well as eukaryotic, genomes: Red/ET recombineering.

Red/ET is an abbreviation for particular recombinases—enzymes that facilitate DNA exchange—derived from bacteriophages, viruses that infect bacteria. When asked about the difference between Red/ET recombineering and CRISPR/Cas, Zhang says, "If you imagine CRISPR technology like a pair of scissors that could efficiently cut the DNA, then Red/ET recombineering technology is like glue, providing crucial genetic materials … to fundamentally alter the DNA." In the case of AMR, Red/ET recombineering could allow researchers to create phage mutants and new therapeutics that target and kill antibiotic-resistant bacteria.

Rolf Müller is a professor of pharmaceutical biotechnology at Helmholtz Institute for Pharmaceutical Research Saarland and a longtime collaborator with Zhang at SKLMT. A key milestone, according to Müller, is SKLMT's recent expansion of recombineering applications to a broader range of microbial hosts, noting the potential of such advances to enable breakthroughs in the fight against resistant pathogens, such as *Escherichia coli*. "This is scientifically impressive," Müller adds.

Microbiology for a better tomorrow

SKLMT is advancing solutions to major environmental challenges—on land and at sea—with innovations in microbial science. To help turn plant waste into useful products like fuel and chemicals, SKLMT scientists developed a microbe that produces enzymes to break down tough plant fibers, along with a special yeast that can turn different types of plant-derived sugars into energy. Their work supports cleaner and more efficient processes in industries such as bioenergy, food/feed production, and paper making. On the marine front, SKLMT researchers pioneered a technique that makes it easier to grow ocean-dwelling microbes in the lab. This work led to the creation of a large collection of enzymes that can break down marine plastic. Among their key findings is a salt-tolerant enzyme that can fully degrade polyethylene terephthalate (PET)—a major contributor to plastic pollution—within three days, says Zhang, offering a potential solution for more efficient plastic recycling.

While pushing the envelope at the microbial research frontier, SKLMT now concentrates on the professional growth of young scientists. "Our goal is to empower more young teams to lead core research directions and create biotech enterprises that impact billions of lives," says Shengying Li, executive deputy director of SKLMT.

Looking ahead, SKLMT is poised to lead the next wave of biotechnological innovation. With a clear vision to drive sustainable development and strengthen global scientific leadership, the laboratory is committed to empowering young researchers, pioneering breakthrough technologies, and transforming industries from agriculture to healthcare. As Zhang puts it, SKLMT will continue to "fuel the green, healthy, and equitable future of humanity," turning cutting-edge science into real-world solutions.

PHOTO: STATE KEY LABORATORY OF MICROBIAL TECHNOLOGY PHOTO BY YU HOU

A 200 square-mile stretch of China's Optics Valley has been recreated as a virtual city—complete with simulated households, businesses, and institutions—using a Large Social Simulator that models how populations interact with public resources to improve urban planning and emergency response.

Civilization in the making: From AGI agent to AGI society

PKU-Wuhan Institute for Artificial Intelligence leads provocative AI experiments in social development.

In the popular game *Civilization*, players must guide a tribe through the ages—starting with stone tools and simple huts, ending with spaceflight and diplomacy. The excitement lies in the development of human societies from primitive communities to full-fledged civilizations. Now imagine playing *Civilization* not with pixels, but with autonomous artificial general intelligence (AGI) minds.

In 2024, the Beijing Institute for General Artificial Intelligence (BIGAI) unveiled Tong Tong, an AGI child and a groundbreaking experiment in autonomous development. By 2025, she had "grown" from a curious 3-year-old to a more self-assured 6-year-old, capable of negotiating for better outcomes and showing signs of evolving judgment. Like a human child, Tong Tong doesn't just learn—she's growing up.

BIGAI's director, Song-Chun Zhu—also chief scientist at the PKU-Wuhan Institute for Artificial Intelligence (PKU-Wuhan), an emerging research hub bridging Peking University's strengths in social sciences with the frontier of AGI—is aiming to model not just intelligent agents but entire societies. What begins with individual minds like Tong Tong, Zhu believes, may one day scale into full societies of AGIs—forming communities, cities, and ultimately, artificial civilizations modeled on the real world.

A giant leap in concept

Zhu and his team have attempted to create AGI agents with human-like cognition using a "CUV framework," a guiding principle for building autonomous agents with purpose and goals. Under this concept, C is the AGI's thinking system, U is its ability to perceive and act, and V its internal motivations. Together, they form a "CUV space" that defines how individual AGI agents learn, reason, and act. This is fundamentally different from large language model (LLM)-based AI, which primarily mimics human behavior rather than performing autonomous, goal-directed actions.

"But humans are not just intelligent individuals," says Zhu. "We are social agents bound by invisible contracts, like atoms held together by chemical bonds." So, shaping AGI agents shouldn't be done in a vacuum. "To understand civilization and build socially aware AGI, we must simulate society itself, not just the minds within it," says Zhu.

To model this social evolution, Zhu and his team have proposed a three-stage simulation for AGI social development:

1. Community: Modeling small-scale social units and relationships.
2. City: Scaling up to urban environments where diverse agents interact through transportation, economics, and services.
3. Civilization: Simulating macro-level societal systems involving institutions, values, and long-term collective behavior.

In this social simulation framework, agents are organized hierarchically across multiple layers, including individual agents (e.g., citizens), organizational agents (e.g., companies, schools), and societal-level agents (e.g., governments). Each level of agent is modeled with its own CUV framework, allowing for distinct cognitive processes, perception-action pathways, and motivational systems specific to that level. Through interactions among these layers, social structures continuously evolve, such as the formation of families, institutions, and enterprises, reflecting the

PHOTO: PROVIDED BY PKU-WUHAN INSTITUTE FOR ARTIFICIAL INTELLIGENCE

dynamic processes of societal development.

A city in simulation

In October 2024, Zhu's vision took a major step forward with the launch of the "Large Social Simulator 1.0,"a large-scale simulated urban environment.

Led by PKU-Wuhan and supported by cross-disciplinary collaborators from Peking University, Tsinghua University, BIGAI, and the Optics Valley of China, the project draws on de-identified real-world data from an approximately 200 square-mile community of 1.18 million people: China's Optics Valley. This initiative aims at advancing socially intelligent AGI by exploring how autonomous agents navigate complex societal challenges—such as cooperation, inequality, value alignment, crisis response, economic systems, and urban planning—by modeling the emergence and evolution of social behavior in a realistic, large-scale environment.

This mockup shows images from Longlasting Civilization, a newly opened VR experience hall where visitors journey back to the Stone Age alongside the AGI agent TongTong.

"We chose China's Optics Valley because it strikes an ideal balance of scale, complexity, and readiness," said Zhu. As a national high-tech zone with advanced infrastructure, the Optics Valley provides a rich environment to test how AGI agents can simulate and eventually support complex societal decision-making. The area serves as a microcosm of modern Chinese urban life, encompassing universities, tech companies, hospitals, schools, transit systems, and a highly supportive local government. "It's not just a simulation," Zhu emphasized. "It's a partnership between cross-disciplinary research and real-world urban development."

Transforming social science

Compared to the natural sciences, social science disciplines such as sociology, economics, psychology, and political science have been slower to develop and adopt experimental tools, though experiments are increasingly integrated into these fields' research.

Viewed through the lens of AGI, social sciences play a pivotal dual role: they provide guidance to AGI societies, and those societies in turn offer a powerful platform to test social science theories and methodology. Zhu believes AGI is offering social sciences an opportunity to restructure and align with a more vigorous scientific approach. For example, the simulation of China's Optics Valley offers exactly such an opportunity to shift the paradigm in social sciences, allowing social scientists to better control and even repeat their experiments. In a way, the Large Social Simulator represents a groundbreaking fusion of AGI research and social sciences, a catalyst for reimaging the social sciences, according to Zhu.

More broadly, this signals that the next frontier of AI research may be in the humanities and social sciences. Many of today's grand challenges, such as social development, civilizational evolution, and AI alignment, remain unresolved within current technical paradigms. By integrating AGI with large-scale social modeling, social simulators offer a promising foundation to systematically explore, test, and prototype solutions to these critical human-centric problems.

Peng Lu, the president of the Asian Social Simulation Association (ASSA), a key social science collaborator, echoes Zhu's assessment. He says, "The large-scale social simulator addresses the challenge of conducting repeatable experiments in society, enabling improvements in the quality of public policy and enhancing the overall well-being of the society."

Global vision for social simulation

Currently, the Large Social Simulator is at the community and city level, with the scope limited to one urban setting in China. Following Zhu's three-stage vision of AGI simulation, PKU-Wuhan, along with collaborating partners, aims to eventually scale up the simulation to the civilization level. "We hope this simulation will uncover patterns so that, at the global, international level—among nations and civilizations—we can study how different civilizations compete, cooperate, and interact," says Zhu.

PKU-Wuhan also aims to open the Large Social Simulator to global researchers to deepen collaborations across the AGI and social sciences disciplines. This is crucial, because while the technology of AGI advances, we humans collectively will have to answer a key question: How will the increasingly powerful AGI coexist with us?

As Zhu puts it, "We are not just simulating society—we are rehearsing the future." With the social simulator and AGI research, Zhu and his teams hope to chart a course toward a world in which human values and AGI coevolve. The ambition is bold: to help humanity navigate an age of accelerating change with foresight, cooperation, and wisdom.

In October 2024, Zhu and Lu's teams brought that vision to life with Longlasting Civilization, a VR experience hall where visitors can step through the ages of humanity alongside AGI companions. The project, which blends immersive history with cutting-edge AI, has since earned global recognition, winning the UNESCO 2025 Award for World Heritage Education Innovation.

PHOTO: PROVIDED BY PKU-WUHAN INSTITUTE FOR ARTIFICIAL INTELLIGENCE

Chen Institute & Science Prize for AI Accelerated Research

The Chen Institute and *Science* Prize for AI Accelerated Research aims to identify and promote innovative applications of artificial intelligence that accelerate the pace of scientific research. Young scientists from around the world are invited to submit a 1,000-word essay describing their AI-driven projects.

An independent panel of judges will award a Grand Prize of $30,000, with the winner's essay published in Science and an accompanying five-year subscription to the magazine. Additionally, up to two runners-up will receive $10,000 each, with their essays published in Science online and the same five-year subscription benefit.

The 2025 winners will join the Chen Scholars community, and they will present their work alongside Nobel Laureates and other leaders in academia, industry and research at AIAS 2025, a two-day meeting October 28-29, organized by the Chen Institute in partnership with UC Berkeley College of Computing, Data Science, and Society.

Apply today!

CONTENTS

4 SEPTEMBER 2025 | VOLUME 389 | ISSUE 6764

964

Fire retardant is a possible source of toxic chromium in LA air samples.

PHOTO: MARIO TAMA/GETTY IMAGES

EDITORIAL

NEWS

FEATURES

COMMENTARY

POLICY FORUM

PERSPECTIVES

BOOKS ET AL.

Your bridge to successful innovation.

NEB's Customized Solutions Team is here to help, and serves as a bridge to the support and resources you need to ensure your success.

Creating the right partnership is essential when pioneering a new life science product. Every aspect of development – technical expertise, reagent optimization, manufacturing scale, turnaround time, reagent quality, and comprehensive logistical support – is vital for achieving your objectives. And in the regulated markets landscape, these challenges magnify, demanding an even more specialized approach.

Your Bridge to Successful Innovation

- Leverage NEB's 50 years of experience in enzymology and reagent manufacturing
- As an extension of your team, we prioritize a deep understanding of your objectives, work with you on an optimal solution, and help to anticipate your future needs
- Benefit from our ISO 9001- and 13485-certified processes and commitment to quality, as well as our GMP-grade* production facility, and specialized lyophilization facility for the highest quality production standards
- Access unparalleled support from our dedicated account managers, program managers, technical scientists and production teams
- We work closely with you on inventory management and global distribution through our network of NEB-owned subsidiaries, to ensure successful commercialization

NEB's Customized Solutions Team will help you access novel products, meet quality specifications, speed time to market, and streamline your supply chain, allowing you to focus more on what matters most — innovation.

Ready to start the discussion? Learn more at
www.neb.com/customizedsolutions.

** "GMP-grade" is a branding term NEB uses to describe products manufactured or finished at NEB's Rowley facility. The Rowley facility was designed to manufacture products under more rigorous infrastructure and process controls to achieve more stringent product specifications and customer requirements. Products manufactured at NEB's Rowley facility are manufactured in compliance with ISO 9001 and ISO 13485 quality management system standards. However, at this time, NEB does not manufacture or sell products known as Active Pharmaceutical Ingredients (APIs), nor does NEB manufacture its products in compliance with all of the Current Good Manufacturing Practice regulations.*

NEW ENGLAND Biolabs®

ON THE COVER

This red squirrel's hands display tiny nail-bearing thumbs, alongside large claw-bearing digits. A survey of hand morphologies and feeding behaviors reveals that the combination of thumbnails and dexterous food-handling is prevalent among living rodents. This likely dates back to their earliest ancestors, linking the evolution of the hand and thumb with that of the teeth and jaw. See page 1049. Photo: sduben/iStock

ON THE PODCAST

Finding HIV's last bastion in the body, and playing the violin like a cricket

PHOTO: SIMA TIANMIN/VCG/GETTY IMAGES

Science **serves as a forum for discussion of important issues related to the advancement of science by publishing material on which a consensus has been reached as well as including the presentation of minority or conflicting points of view. Accordingly, all articles published in *Science*—including editorials, news, commentary, and book reviews—are signed and reflect the individual views of the authors and not official points of view adopted by AAAS or the institutions with which the authors are affiliated.** *Science* (ISSN 0036-8075) is published weekly on Thursday, except last week in December, by the American Association for the Advancement of Science, 1200 New York Avenue, NW, Washington, DC 20005. Periodicals mail postage (publication No. 484460) paid at Washington, DC, and additional mailing offices. The title *Science* is a registered trademark of the AAAS. Domestic individual membership, including subscription (12 months): $165 ($74 allocated to subscription). Domestic institutional subscription (51 issues): $2865; Foreign postage extra: Air assist delivery: $135. First class, airmail, student, and emeritus rates on request. Canadian rates with GST available upon request, GST #125488122. Publications Mail Agreement Number 1069624. **Printed in the U.S.A. Change of address:** Allow 4 weeks, giving old and new addresses and 8-digit account number. **Postmaster:** Send change of address to AAAS, P.O. Box 96178, Washington, DC 20090–6178. **Single-copy sales:** $15 each plus shipping and handling available from backissues.science.org; bulk rate on request. **Authorization to reproduce** material for internal or personal use under circumstances not falling within the fair use provisions of the Copyright Act can be obtained through the Copyright Clearance Center (CCC), www.copyright.com. The identification code for *Science* is 0036-8075. *Science* is indexed in the *Reader's Guide to Periodical Literature* and in several specialized indexes.

Science AAAS

EDITOR-IN-CHIEF **Holden Thorp**, hthorp@aaas.org

EXECUTIVE EDITOR Valda Vinson

EDITORS, RESEARCH Sacha Vignieri, Jake S. Yeston **EDITOR, COMMENTARY** Lisa D. Chong

DEPUTY EXECUTIVE EDITOR Lauren Kmec

DEPUTY EDITORS Stella M. Hurtley (UK), Phillip D. Szuromi **SENIOR EDITORS** Caroline Ash (UK), Michael A. Funk, Angela Hessler, Di Jiang, Priscilla N. Kelly, Marc S. Lavine (Canada), Sarah Lempriere (UK), Mattia Maroso, Yevgeniya Nusinovich, Ian S. Osborne (UK), L. Bryan Ray, H. Jesse Smith, Keith T. Smith (UK), Jelena Stajic, Peter Stern (UK), Yury V. Suleymanov, Valerie B. Thompson, Brad Wible **ASSOCIATE EDITORS** Jack Huang, Sumin Jin, Bianca Lopez, Sarah Ross (UK), Madeleine Seale (UK), Corinne Simonti, Ekeoma Uzogara **SENIOR LETTERS EDITOR** Jennifer Sills **NEWSLETTER EDITOR** Christie Wilcox **RESEARCH & DATA ANALYST** Jessica L. Slater **LEAD CONTENT PRODUCTION EDITORS** Chris Filiatreau, Harry Jach Sr. **CONTENT PRODUCTION EDITOR** Amelia Beyna **CONTENT PRODUCTION EDITORS** Anne Abraham, Robert French, Julia Haber-Katris, Nida Masiulis, Abigail Shashikanth, Suzanne M. White **SENIOR PROGRAM ASSOCIATE** Maryrose Madrid **EDITORIAL MANAGER** Joi S. Granger **EDITORIAL ASSOCIATES** Aneera Dobbins, Lisa Johnson, Jerry Richardson, Anita Wynn **SENIOR EDITORIAL COORDINATORS** Alexander Kief, Ronmel Navas, Isabel Schnaidt, Alice Whaley (UK), Brian White **EDITORIAL COORDINATORS** Samuel Bates, Clair Goodhead (UK), Kat Kirkman, Daniel Young **ADMINISTRATIVE COORDINATOR** Karalee P. Rogers **ASI DIRECTOR, OPERATIONS** Janet Clements (UK) **ASI OFFICE MANAGER** Carly Hayward (UK) **ASI SR. OFFICE ADMINISTRATORS** Simon Brignell (UK), Jessica Waldock (UK) **COMMUNICATIONS DIRECTOR** Meagan Phelan **DEPUTY DIRECTOR** Matthew Wright **SENIOR WRITERS** Walter Beckwith, Joseph Cariz, Abigail Eisenstadt **WRITER** Mahathi Ramaswamy **SENIOR COMMUNICATIONS ASSOCIATES** Zachary Graber, Sarah Woods **COMMUNICATIONS ASSOCIATES** Kiara Brooks, Haley Riley, Mackenzie Williams

NEWS EDITOR Tim Appenzeller

NEWS MANAGING EDITOR John Travis **INTERNATIONAL EDITOR** David Malakoff **DEPUTY NEWS EDITORS** Rachel Bernstein, Martin Enserink, David Grimm, Eric Hand, Michael Price, Kelly Servick, Matt Warren (Europe) **SENIOR CORRESPONDENTS** Daniel Clery (UK), Jon Cohen, Jeffrey Mervis **ASSOCIATE EDITORS** Michael Greshko, Katie Langin **NEWS REPORTERS** Jeffrey Brainard, Adrian Cho, Phie Jacobs, Jocelyn Kaiser, Rodrigo Pérez Ortega (Mexico City), Robert F. Service, Erik Stokstad, Paul Voosen, Meredith Wadman **CONSULTING EDITOR** Elizabeth Culotta **CONTRIBUTING CORRESPONDENTS** Vaishnavi Chandrashekhar, Dan Charles, Warren Cornwall, Andrew Curry (Berlin), Ann Gibbons, Kai Kupferschmidt (Berlin), Andrew Lawler, Mitch Leslie, Virginia Morell, Dennis Normile (Tokyo), Catherine Offord, Cathleen O'Grady, Elisabeth Pain (Careers), Charles Piller, Zack Savitsky, Richard Stone (Senior Asia Correspondent), Gretchen Vogel (Berlin), Lizzie Wade (Mexico City) **INTERNS** Nazeefa Ahmed, Annika Inampudi **COPY EDITORS** Julia Cole (Senior Copy Editor), Hannah Knighton, Cyra Master (Copy Chief) **ADMINISTRATIVE SUPPORT** Meagan Weiland

CREATIVE DIRECTOR Beth Rakouskas

DESIGN MANAGING EDITOR Chrystal Smith **GRAPHICS MANAGING EDITOR** Chris Bickel **PHOTOGRAPHY MANAGING EDITOR** Emily Petersen **MULTIMEDIA MANAGING PRODUCER** Kevin McLean **DIGITAL DIRECTOR** Kara Estelle-Powers **DESIGN EDITOR** Marcy Atarod **DESIGNER** Noelle Jessup **SENIOR SCIENTIFIC ILLUSTRATOR** Noelle Burgess **SCIENTIFIC ILLUSTRATORS** Austin Fisher, Kellie Holoski, Ashley Mastin **SENIOR GRAPHICS EDITOR** Monica Hersher **GRAPHICS EDITOR** Veronica Penney **SENIOR PHOTO EDITOR** Charles Borst **PHOTO EDITOR** Elizabeth Billman **SENIOR PODCAST PRODUCER** Sarah Crespi **SENIOR VIDEO PRODUCER** Meagan Cantwell **SOCIAL MEDIA STRATEGIST** Jessica Hubbard **SOCIAL MEDIA PRODUCER** Sabrina Jenkins **WEB DESIGNER** Jennie Pajerowski

CHIEF EXECUTIVE OFFICER AND EXECUTIVE PUBLISHER

Sudip Parikh

PUBLISHER, SCIENCE FAMILY OF JOURNALS Bill Moran

DIRECTOR, BUSINESS OPERATIONS & ANALYSIS Eric Knott **MANAGER, BUSINESS OPERATIONS** Jessica Tierney **SENIOR MANAGER, BUSINESS ANALYSIS** Cory Lipman **BUSINESS ANALYSTS** Kurt Ennis, Maggie Clark, Isacco Fusi **BUSINESS OPERATIONS ADMINISTRATOR** Taylor Fisher **DIGITAL SPECIALIST** Marissa Zuckerman **SENIOR PRODUCTION MANAGER** Jason Hillman **SENIOR MANAGER, PUBLISHING AND CONTENT SYSTEMS** Marcus Spiegler **CONTENT OPERATIONS MANAGER** Rebecca Doshi **PUBLISHING PLATFORM MANAGER** Jessica Loayza **PUBLISHING SYSTEMS SPECIALIST, PROJECT COORDINATOR** Jacob Hedrick **SENIOR PRODUCTION SPECIALIST** Kristin Wowk **PRODUCTION SPECIALISTS** Kelsey Cartelli, Audrey Diggs **SPECIAL PROJECTS ASSOCIATE** Shantel Agnew

MARKETING DIRECTOR Sharice Collins **ASSOCIATE DIRECTOR, MARKETING** Justin Sawyers **GLOBAL MARKETING MANAGER** Allison Pritchard **ASSOCIATE DIRECTOR, MARKETING SYSTEMS & STRATEGY** Aimee Aponte **SENIOR MARKETING MANAGER** Shawana Arnold **MARKETING MANAGER** Ashley Evans **MARKETING ASSOCIATES** Hugues Beaulieu, Ashley Hylton, Lorena Chirinos Rodriguez, Jenna Voris **MARKETING ASSISTANT** Courtney Ford **SENIOR DESIGNER** Kim Huynh

DIRECTOR AND SENIOR EDITOR, CUSTOM PUBLISHING Erika Gebel Berg **ADVERTISING PRODUCTION OPERATIONS MANAGER** Deborah Tompkins **DESIGNER, CUSTOM PUBLISHING** Jeremy Huntsinger **SENIOR TRAFFIC ASSOCIATE** Christine Hall

DIRECTOR, PRODUCT MANAGEMENT Kris Bishop **PRODUCT DEVELOPMENT MANAGER** Scott Chernoff **ASSOCIATE DIRECTOR, PUBLISHING INTELLIGENCE** Rasmus Andersen **SR. PRODUCT ASSOCIATE** Robert Koepke **PRODUCT ASSOCIATES** Caroline Breul, Anne Mason

ASSOCIATE DIRECTOR, INSTITUTIONAL LICENSING MARKETING Kess Knight **ASSOCIATE DIRECTOR, INSTITUTIONAL LICENSING SALES** Ryan Rexroth **INSTITUTIONAL LICENSING MANAGER** Nazim Mohammedi, Claudia Paulsen-Young **SENIOR MANAGER, INSTITUTIONAL LICENSING OPERATIONS** Judy Lillibridge **MANAGER, RENEWAL & RETENTION** Lana Guz **SYSTEMS & OPERATIONS ANALYST** Ben Teincuff **FULFILLMENT ANALYST** Aminta Reyes

ASSOCIATE DIRECTOR, INTERNATIONAL Roger Goncalves **ASSOCIATE DIRECTOR, US ADVERTISING** Stephanie O'Connor **US MID WEST, MID ATLANTIC AND SOUTH EAST SALES MANAGER** Chris Hoag **DIRECTOR, OUTREACH AND STRATEGIC PARTNERSHIPS, ASIA** Shoupeng Liu **SALES REP, ROW** Sarah Lelarge **SALES ADMIN ASSISTANT, ROW** Victoria Glasbey **DIRECTOR OF GLOBAL COLLABORATION AND ACADEMIC PUBLISHING RELATIONS, ASIA** Xiaoying Chu **ASSOCIATE DIRECTOR, INTERNATIONAL COLLABORATION** Grace Yao **SALES MANAGER** Danny Zhao **MARKETING MANAGER** Kilo Lan **ASCA CORPORATION, JAPAN** Rie Rambelli (Tokyo), Miyuki Tani (Osaka)

DIRECTOR, COPYRIGHT, LICENSING AND SPECIAL PROJECTS Emilie David **RIGHTS AND PERMISSIONS ASSOCIATE** Elizabeth Sandler **LICENSING ASSOCIATE** Virginia Warren **RIGHTS AND LICENSING COORDINATOR** Dana James **CONTRACT SUPPORT SPECIALIST** Michael Wheeler

EDITORIAL
science_editors@aaas.org

NEWS
science_news@aaas.org

INFORMATION FOR AUTHORS
science.org/authors/
science-information-authors

REPRINTS AND PERMISSIONS
science.org/help/
reprints-and-permissions

MULTIMEDIA CONTACTS
SciencePodcast@aaas.org
ScienceVideo@aaas.org

MEDIA CONTACTS
scipak@aaas.org

PRODUCT ADVERTISING & CUSTOM PUBLISHING
advertising.science.org
science_advertising@aaas.org

CLASSIFIED ADVERTISING
advertising.science.org/
science-careers
advertise@sciencecareers.org

JOB POSTING CUSTOMER SERVICE
employers.sciencecareers.org
support@sciencecareers.org

MEMBERSHIP AND INDIVIDUAL SUBSCRIPTIONS
science.org/subscriptions

MEMBER BENEFITS
aaas.org/membership/
benefits

INSTITUTIONAL SALES AND SITE LICENSES
science.org/librarian

Improve the stewardship of federal research funds

Jennifer Lodge and **Richard Stanton**

Federal spending for scientific research in the United States is at a pivotal point of change. The funding system is now under close scrutiny by the Trump administration and Congress for the return it provides to taxpayers. Support from different federal agencies has already been diminished, and more change is coming. It is up to the research community to provide constructive solutions that improve accountability for federal money while preserving a partnership with the government that can continue to catalyze economic growth, place the US at the forefront of scientific knowledge, and improve lives.

Federal funding supports not only direct costs such as salaries and supplies for research projects, but also indirect costs that pay for facilities and administrative services necessary to conduct research in a safe, ethical, and secure manner. Under the current system, each research institution negotiates its own indirect cost rate with the government, which is a percentage of the direct costs, based on a list of allowable items. For many universities and medical schools, the indirect reimbursement rate generally ranges from 50 to 70%, and because portions of the indirect rate are capped and some expenses cannot be included, the institutions themselves also contribute funds to support research.

It is up to the research community to... improve accountability for federal money...

Policy-makers are now focused on indirect costs and the difficulty in assessing their value, which is a reasonable exercise and can benefit the research community if approached with care. They are focused on the negotiation process, variability of rates across institutions, clarity on how the funds are spent, and whether there are incentives for efficiency. The Trump administration has proposed an across-the-board 15% cap on reimbursements for indirect costs, which would be devastating and shortsighted. The research community can and should offer a workable alternative.

One such solution is a more transparent means of identifying the costs of carrying out research. In July, a coalition of major academic, medical, and research associations called the Joint Associations Group on Indirect Costs (JAG) proposed an alternative to the 15% cap called the Financial Accountability in Research (FAIR) model. It is a framework that aims for better accuracy by tying reimbursement more precisely to the actual costs of the work performed. JAG has solicited feedback on FAIR from the scientific community through webinars and townhalls, and the model is being presented to some members of Congress and Trump administration officials.

Multiple members of JAG, which includes small, large, public, and private universities as well as hospitals and independent research institutes, have tested the FAIR model with their own funding data to assess what implementation would look like in different scenarios. Although some details need to be worked out, FAIR offers a means to categorize specific types of research in a way that dollars can be tracked to their original intent of supporting the costs of a specific project. Certainly, the new system will take time and additional effort to adopt at every institution, which is why JAG is recommending a 2-year implementation timeframe to create systems that support FAIR.

Although feedback for FAIR has been broadly supportive, some university leaders and researchers have raised concerns about the workload and difficulty of implementing the new system, with critics saying that it is at least as complex as the system it would replace. Another common concern is whether FAIR will save the government money or require it to spend more to fully reimburse the costs of doing research, making it hard to win the support of the administration and Congress. Conversely, others wonder whether institutions themselves will end up covering more of these costs. FAIR is a framework that enables rational discussion with policy-makers about what should be allowable. The greater transparency that FAIR offers should provide a solid basis for these discussions, and by better demonstrating the accountability of research dollars entrusted to institutions, FAIR would reflect a deep commitment to stewardship, accountability, and public trust.

Congress may address indirect costs as it sets spending levels for the 2026 fiscal year—which begins on 1 October. And President Trump has ordered the White House Office of Management and Budget to revise the current system to eliminate waste and abuse of federal dollars. A 15% flat rate would devastate research missions at most institutions. But if scientists want to retain government and public confidence in their quest for knowledge and progress, then the scientific community must promptly come together and craft workable solutions. There is little time to waste. □

Jennifer Lodge* is the vice president for Research and Innovation at Duke University, Durham, NC, USA, and is a member of JAG. jennifer.lodge@duke.edu
Richard Stanton* is the vice chancellor for Medical Finance and Administration at Washington University in St. Louis, St. Louis, MO, USA. richard.stanton@wustl.edu
*The opinions expressed are those of the authors and not of JAG.

10.1126/science.aeb8307

INFECTIOUS DISEASES

Burkina Faso halts plan to fight malaria with transgenic mosquitoes

Misinformation campaign may have eroded trust and led to a "brutal, humiliating" raid on a research center **KAI KUPFERSCHMIDT**

Target Malaria entomologists hold up a mosquito trap in Bana, Burkina Faso, in 2018.

On 11 August, the international nonprofit Target Malaria celebrated a milestone: In the village of Souroukoudingan, Burkina Faso, its researchers released about 16,000 male mosquitoes genetically modified to produce almost exclusively male offspring. The release, the first of its kind in Africa, was part of a project supported by the Gates Founation that aims to rid the world of malaria using a so-called gene drive, a controversial technique to help desirable genes spread through a population fast.

But a week later, that dream suffered a major setback. On 18 August, judicial police showed up at the Research Institute in Health Sciences (IRSS) in Bobo-Dioulasso, a key partner in Target Malaria, to stage what scientists described as a "brutal, humiliating" raid. According to minutes of a 26 August meeting between researchers and the country's science minister, IRSS scientists were "treated like criminals, with their offices and laboratories sealed and marked as crime scenes." The minutes noted that "everyone was searched, including their vehicles, on the grounds that researchers might be carrying mosquitoes in their pockets."

Four days later, the government suspended all of Target Malaria's activities in Burkina Faso indefinitely. IRSS scientists killed the mosquitoes still living in their insectary, and the government sent a team to spray insecticides in Souroukoudingan to kill the mosquitoes released there.

Researchers are still trying to understand exactly why, after 13 years of work in Burkina Faso, Target Malaria has itself become a target. "We're just patiently waiting to find out what's going on, trying to find out rationales and explanations," says Austin Burt, an evolutionary geneticist at Imperial College London (ICL) and global principal investigator for the project. "I just kind of hope that we can have some sort of discussion and find out if there's a way that somehow things can continue."

The move is "a real blow" to hopes for gene drives, says Fredros Okumu, a vector biologist at the University of Glasgow and the Ifakara Health Institute in Tanzania. "Target Malaria has made a huge investment in Burkina Faso" by training scientists and engaging with communities, he says. And although lab research can continue, finding sites for field tests has now become a lot harder, says Mark Benedict, a mosquito geneticist who until recently worked for Target Malaria. "Burkina Faso and Target Malaria were the most fully developed partnership, so it's chilling." The collapse of the project there may discourage other possible host countries.

But opponents of Target Malaria are pleased. "This project has no future in Burkina Faso or in Africa," says Ali Tapsoba, a spokesperson for the Coalition for Monitoring Biotechnological Activities in Burkina Faso. "This will constitute a precedent for all other African countries."

TARGET MALARIA WAS founded in 2012 with the aim of developing genetically modified mosquitoes to help fight malaria, which kills more than half a million people every year, most of them African children under age 5. Coordinated by ICL with partner institutions in Burkina Faso, Mali, and Uganda, it has focused on gene drives, which can lead certain gene variants to be passed on preferentially to the next generation. When applied to a variant that disrupts egg production in female mosquitoes, for example, a gene drive could quickly suppress the population of malaria-transmitting mosquitoes or even eradicate them. But critics fear the uncontrolled spread of certain genes could have unpredictable effects. "It's a new, little-known, and very powerful technology that causes profound and unprecedented changes in nature," Tapsoba says.

As a precaution, Target Malaria has pursued a stepwise approach. In July 2019, researchers released several thousand male mosquitoes in the village of Bana that had been genetically modified to be sterile, to see how they would do. (The study showed the genetically modified males died earlier than nonmodified ones.)

The 11 August release in Souroukoudingan was the next step. The male mosquitoes were modified to carry a gene encoding for an enzyme that shreds the X chromosome in

PHOTO: TARGET MALARIA

germ cells during sperm production, leading to almost exclusively male offspring. No gene drive was at work; males only passed on the gene to half of their offspring, and the gene was likely to disappear over time. The plan was to do up to five releases 6 weeks apart. (The team is still developing a gene drive for the sex-skewing gene.) Several independent assessments, including a review by Burkina Faso's biosafety regulatory authority and a separate environmental study, concluded the risks of the release were "negligible," Burt says.

From the start, Target Malaria has tried to engage local communities. "We've put a lot of effort into explaining what we're doing, developing glossaries in the local languages and things like that," Burt says. "It was very important for us that we get community buy-in."

"Target Malaria seemed to me to be progressing in a very cautious, methodical, keep-everybody-on-board sort of way," says Luke Alphey, a mosquito geneticist who co-founded Oxitec, a company developing genetically modified mosquitoes, and is now at the University of York. "So it's a bit of a surprise it happened to them."

But opposition to the project has grown, fueled in part by false accusations spread through social media, such as that Target Malaria was weaponizing mosquitoes to sterilize people. The claims are part of a wider pattern of disinformation campaigns in the region often linked to Russian networks, says Mark Duerksen, a security expert at the Africa Center for Strategic Studies, which is funded by the U.S. Department of Defense. "We've seen this kind of public health disinformation really take off in the last 12, 18 months," he says.

The campaigns aim to sow "distrust of the West as having nefarious plots in Africa," Duerksen says—and they play into the "sovereignist narrative" of Burkina Faso's government, led by Ibrahim Traoré, a young military officer who took power in 2022 after two coups. Traoré has emphasized national autonomy and has revoked the licenses of many foreign nongovernmental organizations.

TARGET MALARIA SEEMED to enjoy government support as recently as March 2024, when research minister Adjima Thiombiano, an ecologist, visited IRSS. He was "pleased" with the project, Abdoulaye Diabaté, Target Malaria's principal investigator in Burkina Faso, wrote in a blog post. (Target Malaria said Diabaté did not have time to talk to *Science*.)

But at the 26 August meeting between Thiombiano and IRSS's parent agency, the National Center for Scientific and Technological Research, Thiombiano argued the research should have been done in greenhouses, and said only one of three experts he consulted was in favor of the project. According to the minutes, Thiombiano also cited a lack of public support and said the government had decided to end work on genetically modified mosquitoes and instead focus on "finding endogenous solutions to the malaria problem."

Benedict says that without Burkina Faso's participation, testing gene drive mosquitoes elsewhere in Africa will be more difficult. Because insects don't respect borders, a decision to release them would likely need an agreement between many countries, he notes. "I do think this makes the possibility of reaching a regional agreement to release gene drive mosquitoes more doubtful in the near term," Benedict says.

But Burt remains optimistic. "It's a new technology," he says. "We never thought this would be easy." □

IN FOCUS

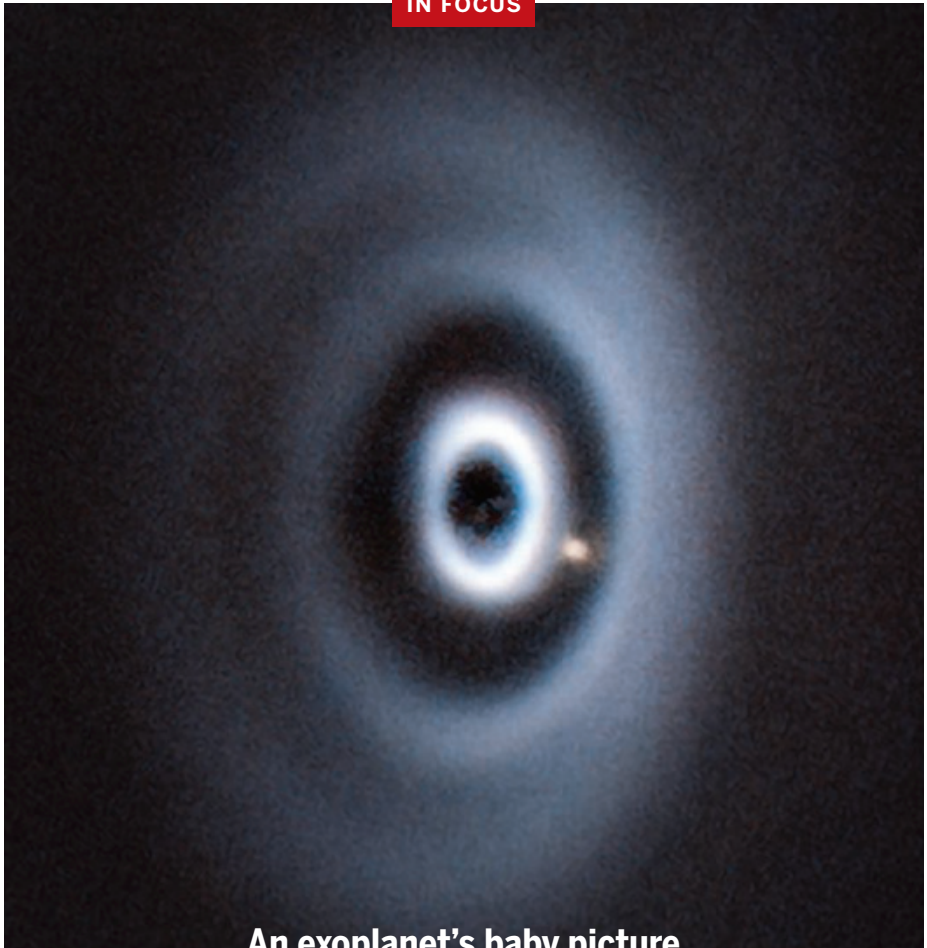

IMAGE: ESO/R. F. VAN CAPELLEVEEN *ET AL.*

An exoplanet's baby picture

Astronomers have long been able to see the disks of gas and dust around young stars from which planets form, and more recently the dark rings thought to be carved out by newborn planets scooping up matter. Now, the sharpest eyed telescopes on the ground and in space can capture fledgling planets themselves, such as this image of exoplanet WISPIT 2b, snapped by the European Southern Observatory's Very Large Telescope in Chile. Weighing five times the mass of Jupiter, it orbits a young, Sun-like star (blacked out). Other rings in the disk may be signs of additional nascent planets, suggesting the image shows a planetary system like our own in the making. —Daniel Clery

ASTRONOMY

Was a blob of dark matter spotted in the Milky Way?

If confirmed, vast cloud could test predictions about the Galaxy's hidden architecture

DANIEL CLERY

It has a mass millions of times that of the Sun and spans hundreds of light-years. It's so close by in the Galaxy it would loom larger in the sky than the Sun or Moon—if you could see it. But this immense cloud—identified by astronomers in a preprint posted online in July—is made of utterly invisible dark matter.

Dark matter, thought to outweigh normal matter in the universe by more than five to one, reveals itself only through its gravity. Its actual nature is mysterious. But simulations of how the universe has evolved suggest the Milky Way not only is enveloped in a diffuse dark matter "halo" 1 trillion times more massive than the Sun, but also contains countless smaller clumps called subhalos that roam among the stars. The dark matter cloud, if confirmed, would mark the first detection of a subhalo within the Milky Way. If astronomers can find more, their size and distribution could help constrain the nature of dark matter.

"It's an exciting start of a new era," says Niayesh Afshordi, an astrophysicist at the Perimeter Institute. He's not sure the evidence for the cloud is strong enough for a firm claim of discovery, but the technique the team used—tracking the slowdown of celestial clocks called pulsars—holds great promise, he says. "This is the beginning of a new type of astronomy." He hopes the new object represents the "tip of the iceberg."

The prevailing cosmological theory holds that dark matter is a heavy, slow-moving particle, prone to clumping, that shapes galaxy formation by drawing ordinary matter to it. The clumping would help explain why astronomers see many small dwarf galaxies surrounding larger ones. The theory also suggests large galaxies should be populated with abundant dark matter subhalos, ranging in mass from billions of Suns to no more than the mass of Earth. If instead the dark particle is light and fast-moving, dark matter would be less clumpy, and small subhalos would be rare.

Better maps of the Milky Way have encouraged astronomers to begin to hunt for signs that subhalos are shaping it. One promising tactic has been to examine streams of stars, stretched out by the Milky Way's gravity, that surround the Galaxy's disk. Some of these streams have breaks in them—as if something unseen has crashed through. But astronomers haven't yet been able to conclusively pin a break on a dark matter subhalo. "The Milky Way is kind of a messy place," says Mike Boylan-Kolchin, an astrophysicist at the University of Texas at Austin. "There are lots of other objects … that could pass through these streams."

Instead, Sukanya Chakrabarti, an astrophysicist at the University of Alabama in Huntsville, and her colleagues looked for clues in pulsars, the superdense remnants of exploded stars. Pulsars spin fast, sending out metronomic pulses of radio waves that sweep across Earth like the beam of a lighthouse, sometimes hundreds of times per second.

Her team focused on pulsars that are paired with other pulsars or stars. As the pulsar orbits its partner, moving toward and away from Earth, the radio pulses throb in frequency. The throbbing enables researchers to measure the orbital

IMAGE: MAX PLANCK INSTITUTE FOR ASTROPHYSICS

A simulation shows how large clumps of dark matter (white) surround the Milky Way (yellow). The Galaxy is also thought to contain smaller clumps or subhalos.

period with extreme precision and track any changes. Using archives of pulsar data going back more than a decade, Chakrabarti's team measured how the orbital period of 27 pulsar pairs gradually decayed. Known effects, such as the emission of gravitational waves by the whirling masses, would be expected to gradually shrink their orbits. But any extra orbital decay would imply that the gravity of a large nearby mass is tugging on the pulsars.

Of the 27 pulsar binaries, a handful in the same area of sky showed similar levels of anomalous decay. The team's modeling suggests something weighing about 10 million solar masses is dragging on all of them. An unusual concentration of normal matter—stars or gas—could be responsible. But the researchers found nothing when they combed the star catalog of Europe's Gaia satellite—the most exhaustive current list—and a similar map of molecular gas clouds. A giant black hole could also explain the extra decay—but it would have to outweigh the supermassive black hole at the galactic center yet remain undetected. "We've gone through every possible data set," Chakrabarti says. "We don't know, but we tend to think that it's more likely to be a subhalo."

Others remain skeptical. "It's going to take a lot more for people to definitively see this as a detection," Boylan-Kolchin says. If it does hold up, even this first subhalo could offer insight about dark matter. The team's modeling suggests the mass in the dark matter cloud is unevenly distributed, which would point to an unusual kind of dark matter, Boylan-Kolchin says. "That's the exciting prospect, I'd say."

Chakrabarti says their measurements will get better as they find more cosmic clocks and monitor them for longer. Thankfully, the team can piggyback on global efforts that are using pulsars to hunt for a background "hum" of gravitational waves from merging supermassive black holes, says Vincent Lee, an astrophysicist at the University of California, Berkeley. "Using the same set of observations to study dark matter—another missing piece in our understanding of the cosmos—means we really get a remarkable return on investment," he says. □

THEY SAID IT

The ship is going down and we are powerless.

A respondent in a survey posted on bioRxiv on 27 August that asked U.S. researchers who are training young scientists about the impact of grant terminations.

TRUMP TRACKER

HOUSE REJECTS TRUMP'S NIH CUT Like a U.S. Senate panel in July, a House of Representatives spending subcommittee has rejected a proposal from President Donald Trump's administration to slash the budget of the National Institutes of Health (NIH) by 40%. A bill released this week would give the agency a base budget of about $47 billion in 2026, essentially the same as this year. The Advanced Research Projects Agency for Health, however, an independent agency within NIH that funds risky, cutting-edge research, would see a 37% cut, and the bill would ban NIH funding for "gain-of-function" pathogen experiments and fetal tissue research. The bill would also slash spending at the Centers for Disease Control and Prevention (CDC) by 19%. If approved by the House Committee on Appropriations and the full House, the bill's spending levels would need to be reconciled with the Senate's version, which boosts NIH's budget by $400 million. —Jocelyn Kaiser

CDC DIRECTOR FIRED CDC, still reeling from a deadly shooting at its Atlanta campus, was thrown into further chaos on 27 August by the ousting of its director, Susan Monarez, and related resignations of multiple top agency officials. Monarez, on the job for only a few weeks, was reportedly fired by Department of Health and Human Services Secretary Robert F. Kennedy Jr. following a clash over his demands to change federal vaccine policies. After her lawyers challenged Kennedy's authority to do so, the White House formally announced that Monarez was out. Four other prominent CDC officials resigned on the same day. The exodus sparked consternation within the agency and stoked fears about the future of U.S. public health. CDC employees are "very discouraged," says Anna Yousaf, a physician and researcher at CDC's National Center for Immunization and Respiratory Diseases, who emphasized she is speaking in her personal capacity. "People are feeling that this is the beginning of the end for evidence-based vaccine recommendations from CDC." —Phie Jacobs

In January, wildfires ravaged sections of Los Angeles, burning 20,000 hectares and torching more than 16,000 structures.

PHOTO: REUTERS/DAVID SWANSON

WILDFIRE SCIENCE

Carcinogenic metal detected in air after LA fires

The unusually tiny particles of hexavalent chromium could pose a health hazard despite low levels, researchers say

WARREN CORNWALL

When fires tore through several Los Angeles neighborhoods in early January, they left behind more than charred homes and skeletons of cars. The infernos, which killed 30, also created an airborne plume of an unusual toxic metal that lingered months after the flames had died, according to new research.

Hexavalent chromium, a known carcinogen linked to lung cancer, was detected in air samples in late March at levels more than 200 times greater than in typical LA air. Most of the particles were so small they could slip between lung cells and into a person's bloodstream. "I've never seen anything like this in the atmosphere before," says Michael Kleeman, an environmental engineer at the University of California (UC), Davis who led the research.

The region's air quality agency, the South Coast Air Quality Management District (AQMD), cautioned against drawing conclusions about health risks, noting that the study's sampling was limited and the agency's own data did not show a chromium spike. "This limited-four sample survey in the context of the comprehensive data collected by South Coast AQMD does not suggest there is an immediate health risk," it said in a statement.

The new work is part of an ambitious project involving multiple universities to document contaminants in air, soil, homes, and the bodies of people in the wake of the fires. Earlier findings have shown elevated lead in ash and both lead and mercury in firefighters. The scientists released the new research as a preprint, without peer review, to quickly alert policymakers and the public.

Chromium is commonly found in rocks and plants and is used to preserve steel, wood, and other materials. Usually, it's in a form known as chromium III, which has low toxicity and is a nutrient. But when oxidized to create chromium VI—known as hexavalent chromium—it becomes far more toxic. It was made infamous in the 2000 movie *Erin Brockovich*, which told the story of the real-life legal case involving people whose water was tainted by the metal.

The levels in samples taken by the UC Davis crew in fire-damaged areas fall well below the workplace exposure limit of 200 nanograms per cubic meter of air, set by the National Institute for Occupational Safety and Health. They ranged from 8.1 nanograms to 21.6 nanograms per cubic meter in Altadena and Pacific Palisades, the neighborhoods hit hardest by the fires. But that's above the 0.1-nanogram level the U.S. Environmental Protection Agency (EPA) considers a cause for concern in indoor air.

Those safety thresholds also don't take into account the size of the

particles. Air quality concerns often focus on particles smaller than 2.5 microns because they can lodge deep in the lungs. But nanoparticles smaller than one-tenth of a micron can more easily pass throughout the body, says Michael Jerrett, an environmental health scientist at UC Los Angeles who took part in the study. "There's really no existing research that I'm aware of that deals with chromium VI in the nanoparticle size," he says.

Nearly all of the chromium particles in the new study were smaller than 0.056 microns, notes Scott Fendorf, a Stanford University soil biogeochemist not involved in the LA research. "That makes a very different toxic profile, and we need to awaken to that," he says.

In the new preprint, the researchers used air pollution models to show that in the worst case, the chromium might have exceeded the EPA screening cutoff at distances of 10 kilometers or more from its origin, an area encompassing as many as half a million residents.

Fendorf's research has found elevated levels of the same metal in ash from wildfires that burn in places with rocks and soil containing high levels of chromium III, which heat can transform into the more toxic version. But the tiny size of the particles found in LA suggest they are coming from particles suspended in a vapor or liquid, he says.

The researchers aren't sure where the problematic chromium originated. Peter Green, a UC Davis environmental chemist involved in the research, pointed to flame retardant dropped on the fire from airplanes as one possible source. These liquid retardants often contain chromium to prevent corrosion of carrying tanks. But home electronics, solar panels, or vehicles could also have emitted chromium as they burned.

A top priority now, scientists say, is to see whether chromium levels remain high in the damaged neighborhoods, and whether they are turning up in people's bodies and homes. Now that major cleanup efforts have ended, chromium levels are likely to fall as soil isn't being disturbed, Kleeman says. He hopes to do another round of air sampling to check. Other scientists in the consortium are watching for the metal in blood tests of residents and monitoring for it in people's homes.

Repeated monitoring is crucial, Jerrett says. A short-term blip in airborne chromium would be unlikely to raise cancer risk, he says. But, "If these elevated levels persist, they could present serious health risks for residents and workers in the burn areas."

The South Coast AQMD says its data so far are reassuring. Its monitoring turned up slightly elevated levels of total chromium in some samples between February and July. But those efforts did not distinguish between the different types of the metal. A station in central LA, located more than 10 kilometers southeast of the nearest burned area, did not show higher than normal levels of hexavalent chromium even during the fires, the agency stated. □

WEATHER FORECASTING

India tests new tools to predict local monsoon floods

"Hyperlocal" forecasts help Mumbai prepare for dangerous downpours

VAISHNAVI CHANDRASHEKHAR, in Mumbai, India

Every monsoon season, from June to September, this coastal city of 18 million braces for chaos. With heavy rains and weather alerts that sometimes arrive too late, Mumbai can be caught off-guard by downpours that strand commuters, force last-minute school closures, and sometimes cause flooding that endangers lives.

During a nearly weeklong spell of heavy rain last month, however, the chaos eased a bit. With the aid of an experimental model that leverages artificial intelligence (AI) to produce neighborhood-level weather forecasts, combined with radar-based "nowcasts," the city avoided the worst. Officials announced school closures the evening before the worst day and deployed water pumps to neighborhoods flagged for the heaviest rain. Mumbai still experienced flooding—1 month's rain fell in just 4 or 5 days, overwhelming its stormwater system in many areas. But fewer people were stranded and cleanup was faster. "A forecast that gives us area-wise predictions, that's as good as it gets," says Abhijit Bangar, a senior city official.

The forecasting project—a collaboration between the Indian Institute of Technology (IIT) Bombay, which developed the model; the regional meteorological department; and a city agency—reflects a growing push in India toward hyperlocal forecasting and nowcasting. Such finer grained forecasting has become common in the United States and some other nations, but it is still emerging in South Asia. In India, for example, rainfall predictions historically focused on larger scale seasonal trends that affect monsoon-dependent agriculture.

But meteorologists began to look more closely at disaster prevention after 1999, when a supercyclone caused almost 10,000 deaths in eastern India. The disaster led to better warning systems that have slashed death tolls. "The value of saving lives and reducing misery was established," says Krishna Achutarao, a senior climate scientist at IIT Delhi.

The flooding threat has only increased since then: Heavy rainfall days have become both more frequent and intense in Mumbai, with the average volume of rain on such days rising from 131 millimeters between 2014 and '18 to 182 millimeters between 2019 and '25. "Disaster management is demanding better local predictions," says climate scientist Raghu Murtugudde of the University of Maryland.

Even 5 years ago, however, "No one would talk about trying to forecast an urban flood," Achutarao says. That changed in 2017 when rains battered Chennai, one of India's biggest cities, prompting the Indian government to fund the development of a flood forecasting model that influenced the one now used here.

These models face a challenging task. In tropical monsoon climates, local weather systems often spring up and move quickly, making them hard to predict. Standard global weather models also struggle to forecast these systems because of their relatively low spatial resolution, about 25 square kilometers. And local topography can cause wide spatial variability in flooding. "These [smaller scale] processes are still not fully understood," says IIT Bombay climate and water scientist Subimal Ghosh, who worked on the Chennai model before helping adapt it for Mumbai.

To develop the Mumbai forecasts, Ghosh, Murtugudde, and Puja Tripathy, then a doctoral student, used past output from a U.S. Global Forecast System model to develop an AI-powered model trained on a few years of data from 36 Mumbai weather stations. Initially, they found the model did a better job of forecasting local precipitation, but it had to be fine-tuned to better predict

Residents of Mumbai, India, navigate flooded streets after heavy monsoon rains in August.

extreme events. In tests during 2024's monsoon, it was able to provide 3 days' warning of every heavy rainfall event except one.

This year, the team fed those advance warnings to Mumbai officials along with area-specific precipitation estimates. They also tried out a new model for nowcasts of rainfall over the next 90 minutes, based on regional radar data. And residents were able to check an experimental website that provided real-time information on flooding, drawing on water sensors placed around the city as well as firsthand reports sent in by more than 100 people. (Ghosh's personal experience helped inspire the crowdsourcing: On a heavy rain day in 2019, when Mumbai schools closed early, a WhatsApp group of parents helped him track his 3-year-old's school bus as it navigated waterlogged streets.)

For municipal officials, the timely, high-resolution forecasts provided the confidence they needed to close schools ahead of time—but also to reopen them the next day despite some public pressure to keep them shut. "They looked at all the forecasts. They followed the science," Ghosh says. Researchers plan to further fine-tune the model in future monsoons.

Bangar now hopes to include the forecasts in an early warning system that is part of a proposed city flood mitigation plan. In the meantime, other hyperlocal forecasting efforts are emerging across India. Last year, the rainy southern state of Kerala launched a community-based flood forecast system in two river basins. And in May, the national government launched the Bharat Forecasting System, a weather prediction model developed by the Indian Institute of Tropical Meteorology (IITM) that is supposed to forecast weather at a scale of 6.5 kilometers, down from the 12 kilometers of a previous version.

The Bharat system can't yet produce truly hyperlocal forecasts, says IITM scientist Medha Deshpande, but she and other researchers hope to improve it by drawing on regional data from India's rapidly expanding radar and weather monitoring network. Hyperlocal forecasts, the researchers note, require hyperlocal data. □

ANIMAL EXPERIMENTATION

Vote by Dutch lawmakers threatens major primate research center

The Netherlands aims to be a "world leader" in animal-free research

MARTIN ENSERINK, in Rijswijk, Netherlands

The future of one of Europe's largest nonhuman primate research centers is hanging in the balance. On 3 July, just before its summer recess, the Dutch House of Representatives voted to end monkey studies at the Biomedical Primate Research Centre (BPRC), located in this suburb of The Hague, by 2030. The amendment would not necessarily shutter BPRC, which holds about 950 monkeys of three species. But it stipulates that a growing share of its €12.5 million annual subsidy—reaching 100% by 2030—would go to animal-free research or the development of alternatives.

The narrow 76-74 victory for animal rights activists surprised many of the primate center's supporters and has spurred an intense lobbying campaign on its behalf. An open letter by representatives of seven Dutch and European biomedical groups warns that the move is "far-reaching, ill-considered, and harmful to public health."

The proposal seems unlikely to clear the smaller Dutch Senate, where it will be discussed on 9 September. But some Dutch scientists say the House vote shows that shifting political winds can rapidly erode lawmakers' support for animal experimentation. The push to end monkey studies at BPRC—contained in an amendment to a broader budget bill—came from the Party for the Animals, which only has three seats in the House. But it was backed by the radical-right Party for Freedom, which won 37 seats in a 2024 election victory and is expected to make gains in the Senate in 2027 as well.

Critics of primate research applaud the move and say it's a chance for the Netherlands to set an example. U.S. agencies such as the National Institutes of Health and the Food and Drug Administration have recently led the way in the transition away from animal experimentation, notes Jarrod Bailey, director of medical research at the Physicians Committee for Responsible Medicine, which promotes alternatives to animal research. "There's an

PHOTO: INDRANIL ADITYA/NURPHOTO VIA GETTY IMAGES

opportunity here that I would like to see the Netherlands take, on behalf of Europe, and show how progressive science can be," he says.

BPRC, one of only a handful of such centers in Europe, has its own monkey breeding colony. It works mostly with academic researchers, from the Netherlands and abroad, who come to the center to study infectious diseases such as HIV, malaria, tuberculosis, and neurodegenerative conditions such as Alzheimer's and Parkinson's disease.

Like most primate research centers, it has faced criticism. But instead of remaining silent, a common strategy, BPRC has for years practiced transparency as a way to win hearts and minds. It frequently hosts tours of the facility, and during the COVID-19 pandemic, a reporter and photographer for a daily newspaper visited multiple times to document the lives and deaths of Chips and Dip, two rhesus macaques used in a vaccine study. Photos and videos showed researchers and animal caretakers handling the animals lovingly. "We have nothing to hide," says veterinarian scientist and BPRC Director Merel Langelaar, who last month showed *Science* around spacious enclosures where the monkeys, living in groups, were running around and playing with swings and toys.

But some Dutch politicians have long had BPRC in their crosshairs. In 2016, the House adopted a motion resolving that primate research would eventually be phased out, without setting a deadline. Following a 2019 agreement with the Dutch government, BPRC has reduced the number of animals enrolled in studies to 150 per year. An expert panel that studied the center's future at lawmakers' request issued a report in March that explored four possible scenarios, ranging from expanding the number of studies at BPRC to ending them. To the critics' disappointment, the panel did not express a preference.

Dutch scientists, too, are divided over animal research. The Netherlands has expressed the ambition to become a "world leader" in the transition to animal-free research, and a consortium of universities, institutes, and companies recently won a 10-year, €124.5 million grant for a new center for animal-free biomedical translation, named Ombion, that was launched on 7 July. Participants in Ombion will double the amount to almost a quarter-billion euros.

The center's initial focus will be on amyotrophic lateral sclerosis, cystic fibrosis, osteoarthritis and rheumatic diseases, and chronic lung diseases. "It will be an example for the world as a central infrastructure for alternatives" for animal experimentation, says Merel Ritskes-Hoitinga, a veterinary scientist at Utrecht University who's involved in Ombion. Advances in nonanimal technologies—such as organoids, organs on a chip, and artificial intelligence—mean that a 5-year deadline for ending primate research is reasonable, Ritskes-Hoitinga says: "And without a deadline, nothing will happen."

Many supporters of primate research say they, too, would like to ultimately phase out such work, and BPRC already spends 17% of its budget on developing alternatives. But researchers championing the transition to animal-free studies have "massively overpromised," says neuroscientist Stefan Treue, who leads the German Primate Center. For much of the work done at BPRC, including its vaccine and brain studies, "there is simply no replacement—not in the foreseeable future," he says.

BPRC's supporters also warn that abandoning primate research in the Netherlands would only shift it to China and other countries where ethical rules may be looser—and make Europe more medically vulnerable. It would "seriously jeopardise national and indeed European pandemic preparedness," Jonathan Ewbank, director general of the European Research Infrastructure on Highly Pathogenic Agents, wrote in a letter.

Langelaar agrees. Theoretically, BPRC could sustain primate research by using money from sources other than the government. But maintaining a breeding colony is simply impossible without government support, she says. "And once you end this, there will be no way back." □

> **"Once you end this, there will be no way back."**
>
> **Merel Langelaar**
> Biomedical Primate Research Centre

IN FOCUS

Ant queen produces sons of two species

Sex is strange in many social insects—but the Iberian harvester ant (*Messor ibericus*) takes the weirdness to the next level. *M. ibericus* queens must mate with males of another species, *M. structor*, to produce worker ants. Such obligatory flings happen in a few other ant species, but *M. ibericus* also uses *M. structor* sperm to somehow clone the distantly related males (right), researchers report this week in *Nature*. By keeping these sexual captives, *M. ibericus* ants can live in environments that lack *M. structor* colonies. The Iberian queens also lay unfertilized eggs that become *M. ibericus* males (left); their sperm is needed to fertilize eggs that become new Iberian queens. "Just when you think you've seen it all, social insects reveal another surprise," says Michael Goodman, an evolutionary biologist at the Georgia Institute of Technology.
—Erik Stokstad

PHOTO: YANNICK JUVÉ AND JONATHAN ROMIGUIER

Last Gift participant Jim Dunn (right) and his wife, Susan Dickerson, at their home in August 2024.

DIVIDENDS FROM DEATH

Rapid autopsies on people infected with HIV may help researchers find a cure

JON COHEN, in San Diego

In May 2003, Jim Dunn, then 55, had been severely ill for 7 months and could barely stand up. His doctors thought he had Parkinson's disease, and as part of the workup they did a lumbar puncture to analyze his cerebrospinal fluid. Dunn and his wife, Susan Dickerson, were sitting together on a medical exam table when they learned the results. "The doctor came in, looked at Jim, looked at his record, literally threw the record on the counter," Dickerson says. "And he said, 'You don't have Parkinson's, you have full-blown AIDS,' and walked out."

Sitting in their living room here in August 2024, the couple recalled how shocked they were by the callous doctor—and the diagnosis. "I didn't fit the profile," Dunn said.

A father of three who moved to California from a small town in Illinois shortly before he first became ill, Dunn had taken early retirement from tractormaker John Deere. He had tested negative for HIV when he married Dickerson (who had two kids of her own) in 1995 and later when he took out a life insurance policy. He said he must have become infected through heterosexual sex; he had no history of injecting drugs. "My drug of choice has always been, well, I am full-blooded Irish," he joked.

Antiretroviral drugs promptly brought Dunn's decimated immune system back to health. Joining HIV support groups helped Dunn and Dickerson—who tested negative—understand that he could live a full life with HIV. But in 2005, unrelated to his HIV infection, Dunn developed squamous cell cancer on the top of his head, and the tumor wrapped around his jaw. That was followed by melanoma, esophageal cancer, and then brain cancer. He had repeated surgeries and volunteered for one clinical trial after another to test experimental cancer drugs. Although his jawline was disfigured and part of his skull removed and replaced with skin flaps, he kept defying the odds. "He's a man with nine lives," Dickerson said.

In 2019, Dunn joined a trial that aims to help find a cure for HIV. But he knew it would not cure his own infection. The study would take place after he died.

Dunn became a participant in the Last Gift Study, a pioneering project at the University of California San Diego (UCSD) that aims to study the bodies of HIV-infected people immediately after their deaths through a "rapid autopsy." By promptly sampling tissues, Last Gift hopes to trace where in the body the virus hides and how it moves—clues to how it might be vanquished in living people.

"It's a fantastic, very innovative project," says Carlos del Rio, an HIV researcher at Emory University. "But it also is a project that shows how people living with HIV are willing to go the extra mile to contribute to science even after they're dead."

NORMALLY, AUTOPSIES are performed a day or two after death. Cells, starved of oxygen and nutrients, have largely

PHOTOS: (LEFT TO RIGHT) J. COHEN/*SCIENCE*; SARA GIANELLA WEIBEL

The rapid autopsy team at the University of California San Diego obtains more than 1000 samples from each Last Gift Study donor.

disintegrated by then. Blood has clotted into jelly. Bacteria and viruses in the gut have moved to other tissues. Proteins have broken down into peptides and then amino acids. DNA and its cousin RNA—which is even more fragile—have started to fall apart. That makes it hard for researchers to learn the state of a patient's disease at the time of death.

Rapid autopsies, used in cancer research for nearly 40 years, are started within hours. Cells are still alive and can be extracted and grown in lab cultures or transferred to lab animals for further study of disease processes and treatments. RNA, which reveals which genes are turned on, can be rescued. Entire organs, including the brain, are still intact. Most important, HIV can be quantified and sequenced, in both its RNA and DNA forms, precisely where it resides in the body.

Although drugs can powerfully suppress the virus, "HIV hides in the tissues, and one of the reasons why we cannot really cure people is because we don't know where it hides," says Sara Gianella Weibel, a physician-scientist at UCSD who helps run Last Gift. She has its logo—a puzzle piece with an AIDS ribbon—tattooed on her arm.

This latent infection means the virus will surge back if drug treatment is interrupted. It also causes inflammation that, over decades, leads to increased rates of cancer, heart disease, and neurocognitive dysfunction. "The reason I became an HIV doctor was that I saw that modern miracle of antiretroviral therapy," says Davey Smith, founder of Last Gift. "It'd be really nice to just get rid of the whole thing altogether."

For Dunn, the 16th person to volunteer for Last Gift, that choice was easy. He was grateful for trials that had prolonged his own life. "I just want to pay back," Dunn said. "If people hadn't stepped up prior to me, HIV would be a death sentence."

When Dunn met with *Science* last year, he knew his payback time was nearing. A month earlier, doctors had told him they no longer had any medicines to slow his cancer, and he had begun hospice care.

AN AIDS PATIENT Smith first saw 30 years ago as a medical intern planted the seed of Last Gift. HIV destroys the CD4 T cells that fight microbial invaders, and in 1996 the patient "had so few CD4 cells that you could name each one," Smith quips. The man had developed cryptococcal meningitis, a fungal infection that can cause brain damage, coma, and death. But then he joined a clinical trial of a new antiretroviral cocktail that fully suppressed the virus. "All of a sudden, he just does better and goes home and lives," Smith says.

Twenty years later, the man became Smith's patient again, when he was hospitalized with terminal pancreatic cancer. "He constantly complained that he couldn't be in research anymore," Smith says. "People were like, 'Oh, if you're dying, you can't.'"

Smith wasn't so sure.

When drugs fully suppress HIV, patients' levels of the virus drop so low it's undetectable on standard blood tests. But even then, lots of virus can often be found in biopsies of lymph nodes and the colon, two places that harbor large populations of CD4 T cells. In those cells, a so-called provirus—produced by an enzyme that converts HIV's RNA into DNA—becomes integrated into the chromosomes. Ensconced in human DNA, proviruses escape immune detection and elimination for years, unless they start to produce progeny virus. Latently infected CD4 T cells can also clone themselves, quietly expanding HIV's reservoirs.

These reservoirs stand in the way of a cure. One strategy is to eliminate them by "kick and kill," which prods the provirus to make new viral particles, destroying the infected cells and draining the reservoirs. A second approach, "block and lock," targets the suite of proteins and other factors that the provirus needs to make new virus, essentially making latency permanent.

So far, there's little evidence that either strategy works. What's more, researchers don't have a good idea of where all the reservoirs are. They can't take biopsies from most tissues in living patients, after all.

The cancer patient made Smith realize there might be a way to find and characterize every reservoir. "I was like, man, if we had somebody like this guy who we could do research on all the way up until the end, and we could get the body fast enough to get the viruses, we could learn a lot," Smith says. "That started the idea."

When Smith and Gianella Weibel first sought funding for the project from the U.S. National Institutes of Health (NIH), reviewers questioned the ethics of enrolling vulnerable people in a study that did not offer them any direct benefit. In cancer research, rapid autopsies are often done at the end of clinical trials that might prolong patients' lives. That was not the plan with Last Gift. But participants would still receive something important, the duo said: the knowledge they might help others. "They get altruistic benefit," Smith says.

Last Gift's elaborate consent procedure stresses that the research won't cure the patient's illnesses or extend life, and investigators do not enroll people who are incapable of making an informed decision. An HIV community advisory board that Dunn sat on scrutinized and approved the protocol. The study has one cohort of participants who are within 6 months of death, and another, called "on deck," made up of people like Dunn, whose diseases are progressing more slowly.

Still, Jules Levin, who runs the National AIDS Treatment Advocacy Project, says he has "serious problems" with the project's ethics. He questions whether people facing death are in a proper state of mind to give their consent. He also questions the scientific goal. "I'm not convinced that there's enough progress that this is going to lead to any cure benefits," Levin says.

On top of ethical questions, rapid autopsies require a large team of trained people willing to rush to the morgue at any time and then work long hours to complete the job.

Despite these concerns, NIH has awarded the team more than $15 million over an 8-year period. To date, Last Gift has enrolled 62 participants and conducted 42 rapid autopsies. "The concept is fantastic," says Stanford University pathologist Jody Hooper, a leading specialist in rapid autopsy who consulted with the Last Gift team early on. "It's such an opportunity to do good from terrible situations," Hooper says. "I almost think of us as wrestling benefit away from death."

Now, similar projects are emerging elsewhere. Last Gift has inspired a rapid autopsy program for HIV in Canada and a nascent effort in Brazil. And it led Richard Strange, an 84-year-old man living with HIV in Washington, D.C., to push for a program at the National Cancer Institute (NCI). Strange, first diagnosed with HIV in 1993 and a self-described "clinical trial junkie"—he has been in 18 studies—reached out to Frank Maldarelli, an infectious disease researcher at NCI who has conducted 23 autopsies of HIV-infected people over the past 2 decades. Maldarelli hopes to soon receive a green light to start regularly doing rapid autopsies.

Strange, living in a retirement community and in excellent health, always carries a piece of paper with him with instructions to take his body to Malderelli within 6 hours of his death. Knowing he would be part of a rapid autopsy study would be "immensely satisfying," Strange says.

Davey Smith launched the Last Gift Study after a longtime HIV patient complained that he couldn't participate in studies because he had terminal cancer.

PHOTO: J. COHEN/*SCIENCE*

IN CANCER RESEARCH, rapid autopsies have delivered on their promise, illuminating "the dynamics of cancer evolution, early stages of carcinogenesis, and therapeutic resistance," Hooper and co-authors wrote in a December 2019 review. (They prefer the term "research autopsies" because it better describes the goal.) The procedures allow researchers to take samples of human tumor cells and transplant them into mice to create models of human disease, as Hooper and colleagues did to study rhabdomyosarcoma—a rare type of soft tissue cancer. Rapid autopsies can also guide treatments with existing drugs.

The strategy is catching on for other diseases, too. The 50 or so teams Hooper collaborates with are studying an increasingly broad range of questions, including development,

aging, heart disease, and the effects of chimeric antigen receptor T cells—engineered immune cells—against tumors. Today, there are 25 rapid autopsy programs, up from 15 a year ago, says Hooper, who is tracking the field's rise.

One NIH-funded project does "expedited" autopsies (within 24 hours of death) of people with Long Covid to trace SARS-CoV-2 in their bodies. The virus is known to linger in Long Covid patients, but "what hasn't been done yet is to establish that the viral persistence is truly related to the patient's symptoms," says James Stone, a pathologist at Massachusetts General Hospital who heads the effort. "It would be a stretch if you said, 'Well, you could only detect virus in the calf muscle, and yet, for some reason, they have brain fog.'" The team has done 250 autopsies so far.

But scientific insights from rapid autopsies accrue slowly. So far Last Gift has yielded a dozen papers on scientific findings. Some of them confirm what researchers had suspected: The largest HIV reservoirs, for example, typically are in the gut and lymph nodes. But Last Gift has revealed unique insights, too, which the scientists contend could guide cure efforts. "We are opening doors right now that allow us and our collaborators to envision new ways to look at the virus and ways to fight against it," UCSD molecular virologist Antoine Chaillon says.

One discovery came from participants who stopped taking antiretroviral drugs several weeks before they died. As expected, HIV levels rebounded quickly. Viral samples taken while they were still alive allowed the researchers to find the source reservoirs after death, and track how the viruses had found new homes after the drugs were stopped. "One of the big things we've learned is the blood repopulates these reservoirs very quickly," Smith says. "What if you were to stop that highway and really block the replenishment of the reservoirs?"

The autopsies also showed that reservoir size and location vary greatly between individuals, reflecting factors including their lifestyle (diet, smoking, opioid use), treatments, genes, and other diseases. One participant who developed cancer of the pancreas had extremely high HIV DNA levels in that organ, perhaps because infected T cells had traveled there to fight the tumor. At a recent HIV conference, Last Gift researchers described distinct HIV reservoirs in the jejunum, lymph nodes, the male genital tract, and the spinal cord. "In almost every patient, there is something special, and most of the time, you connect it back to their story," Gianella Weibel says. "Probably the real cure will have to be personalized, because every reservoir distribution looks different."

Any cure must eliminate or cripple a specific subset of proviruses: the fewer than 10% that produce viable progeny. Examining the brain's microglial cells, a common target of infection, the UCSD team and its many collaborators found they could distinguish those infected with defective proviruses from ones that have intact ones; the latter have switched on several genes that drive immune responses. In theory, a drug might only target microglial cells that have these genetic markers.

In an even more ambitious attempt to characterize reservoirs all over the body, the Last Gift researchers teamed up with Nadia Roan, an immunologist and virologist at UC San Francisco who specializes in quantifying specific proteins that cells produce in response to an HIV infection. Essentially, these proteins are sensors that detect viral components and turn on innate immune responses.

In a study published in January, Roan, Smith, Gianella Weibel, and colleagues analyzed single cells in 41 tissues from seven Last Gift donors. "Every immune cell in every different place has a different viral sensor, and basically that tells us that each reservoir is different," Smith says. "So, if we're going to be scooping out reservoirs in all these different tissues, we're going to have to know exactly what those viral sensors are and how the innate immune sensing works in each of those tissues. It's going to be a hard job."

Still awaiting approval is a study that would give Last Gift participants a potential HIV cure that shows promise in animals but is considered too risky for otherwise healthy people. Before they die, patients would receive so-called therapeutic interfering particles—genetically neutered, harmless versions of HIV designed to win the competition for cellular resources and replace the dangerous version. A rapid autopsy would assess the result.

Smith hopes more experimental therapies will follow. "That's what's going to really speed our push for a cure," he says.

JAMES CHRISTOPHER DUNN died with his wife by his side on 30 December 2024 at 7:25 a.m. Dickerson phoned Gianella Weibel 10 minutes later with the news. Two men in an unmarked van soon arrived to pick up Dunn. They draped his body in an American flag to honor his service in the U.S. Navy Reserve and then transported his corpse to the university morgue, a half-hour away.

A team of nine gathered there. They first read an acknowledgement, a tradition at Last Gift autopsies. "From our first breath to our last, each of us tells a unique story with our lives," it begins. "Today, we honor our donor, Last Gift 16, for this opportunity to further research into HIV and so many other unanswered questions about the human condition. Might we take a moment of silence now to honor their gift and express our gratitude for all the discoveries this altruistic act will yield?"

> "Probably the real cure will have to be personalized."
>
> **Sara Gianella Weibel**
> University of California San Diego

They put on *Blackbird* by the Beatles, one of Dunn's favorite songs.

Then they got to work. A "diener" skilled in cutting procedures stood at the center and carefully removed organs and tissues. Four "cutters" sliced what he gave them into small pieces. Four "tubers" put the biopsies in test tubes that each had color-coded caps and barcodes. At one station, technicians plunged tissue samples into liquid nitrogen within seconds of removal to flash-freeze them, preserving their molecular integrity. Gianella Weibel served as the team captain, moving from station to station to verify each sample was correctly processed and documented.

Some samples were immediately sent out to collaborating groups. "We want to maximize the gift that we're given," Smith says. A freezer in the basement of a UCSD lab still holds tissue from Dunn's body in 13 boxes, each of which contains 81 tubes that may yield rich information—whether they're analyzed tomorrow or decades from now.

"He'll therefore live forever," Dickerson says. "I am very happy Jim chose to do this." □

COMMENTARY

POLICY FORUM

AGRICULTURE

Can the global drone revolution make agriculture more sustainable?

Rapid growth in drone use is upending expectations but also inducing trade-offs

Ben Belton[1,2], Leo Baldiga[3], Scott Justice[4], Bart Minten[5], Sudha Narayanan[6], Thomas Reardon[2,7]

Use of drones has increased considerably over the past decade, reshaping activities as diverse as warfare, entertainment, delivery services, and disease control. One of the most consequential uses of drones—in agriculture—has taken off globally within only the past 5 years. This is upending expectations and may help to reconcile a fundamental sustainability dilemma—how to produce more food by using fewer inputs—but is also inducing trade-offs. This rapid change has been largely unnoticed by researchers outside of the specialized technical worlds of aeronautical engineering and precision agriculture. Little academic attention has been paid to the use of agricultural drones beyond the laboratory or trial plot. Evidence of the extent and effects of drones' real-world use is partial and fragmentary. We explored evidence and hypotheses about global agricultural drone diffusion and its implications for sustainability and set out an agenda for future policy and science.

Drones perform a growing array of tasks on farms, including sowing seeds; spreading fertilizers and feeds; spraying herbicides, pesticides, and fungicides; counting livestock; monitoring and mapping fields; and assessing crop health and yields. Crop

PHOTO: SIMA TIANMIN/VCG/GETTY IMAGES

A worker uses a drone to spray pesticide in a paddy field in Ji'an, Jiangxi Province, China, June 2020.

spraying is the most common agricultural drone use worldwide, followed by spreading fertilizers and broadcasting rice seed and cover crops. This multifunctionality makes drones powerful tools, with applications in virtually all types of farming. Crucially, drones may also improve crop yields and enhance sustainability compared with conventional practices.

The rapid rise of drones is helping equalize global inequalities in access to agricultural technology, putting in the hands of farmers in the Global South equipment as sophisticated as that previously only available to large farmers in the Global North. For example, smallholder rice farmers in Asia can now access, for as little as $10 per hectare from an outsource service provider, technology with capabilities comparable with the most state-of-the-art computer-assisted $400,000 ground rig on a 1000-ha soybean farm in the American Midwest. This pattern of technological leapfrogging is reminiscent of the shift from cash to mobile payments in many Global South countries.

INNOVATION AND GLOBAL DIFFUSION

Remote-controlled aircraft have been used in agriculture since the 1980s in some countries. But only in the past decade has a confluence of innovations linked to the design and manufacturing of multirotor drones made these machines easier to operate, more versatile, and increasingly useful to farmers, leading to a sudden global boom. The earliest multirotor drones used in agriculture were very small and could perform few tasks, but improvements in drone design have given rise to larger models capable of carrying heavier loads. Recent models are designed to carry loads of up to 100 kg—more than the weight of a typical sack of fertilizer. This capability has made drones suitable for a wide variety of agricultural tasks and for use on farms of all sizes.

Drone batteries have become smaller, lighter, longer lasting, and much faster charging, reducing downtime between flights to the brief period required to refill inputs and swap over a battery. Use of drones on farms was initially limited to "crop scouting" with cameras, and later to crop spraying by using motorized pumps. Recently, these functions have expanded. Advances in the design of drone attachments such as rotary atomizers (for spraying liquid crop protectants) and granule spreaders (for broadcasting seeds, fertilizer, and feed) make it possible to adjust droplet sizes and flow rates, substantially increasing the efficiency and evenness of input application. These attachments have been modularized, making it easy for a single drone to perform multiple tasks.

Early farm drones required a lot of skill to fly. Since then, miniaturization of improved sensors and software upgrades have greatly simplified flight planning and navigation and increased flying accuracy and automation, making drones easy to pilot.

The first farm drones were expensive for small farmers. Although this is still true for drone ownership, prices have fallen dramatically because of rapid technological advances and competition (*1*). Moreover, service provision by small businesses, farmer groups, and cooperatives—all of which hire out drones with pilots—has made it easy for farmers to access drones at rates similar to or lower than those paid to agricultural laborers (*2*).

All of these improvements have contributed to rapid global drone diffusion, the geography of which has been surprising. The agricultural mechanization revolution—using tractors and combine harvesters to speed up planting and harvesting and save labor—began in the Global North in the 1890s and took more than a century to reach parts of Asia. By contrast, the agricultural drone revolution began in China less than a decade ago and has spread rapidly from there to both the Global North and Global South. Two Chinese companies, DJI and XAG, produce the vast majority of drones used in agriculture worldwide.

To give a sense of the scale and extent of recent diffusion, the figure depicts reported numbers of agricultural drones operational in 10 countries in 2024. These countries span East, Southeast, South, and West Asia and North and South America. They are major agricultural economies that together account for 62% of the world's farms, 46% of its rural population, and 39% of its cropland (*3*). The figure also depicts the intensity of agricultural drone diffusion (drones per area of cropland) in relation to a measure of relative economic development for each country (purchasing power parity gross domestic product per capita). Agricultural drones are present in many other countries and regions, but we were unable to obtain estimates of numbers in those locations.

These data suggest four broad patterns of agricultural drone diffusion by country. We outline these below, in order of the intensity of that diffusion. To explain differences in diffusion across space, we characterized countries with respect to their relative abundance of land and labor, income level, prior adoption of agricultural mechanization before drones, and drone-related policy environment. We hypothesize that these factors condition the distinctive diffusion pathways seen in each group.

Japan and South Korea

Drone diffusion intensity is greater in these countries than anywhere else. This reflects land scarcity (small farms) to which early drone models were well adapted; labor scarcity and elderly farming populations, creating high demand for labor-saving technology; high income levels, making drones relatively affordable; high prior adoption of sophisticated small-scale agricultural machinery such as rice transplanters; and technology-positive regulatory and policy environments, including government subsidies for drone purchases.

China, Thailand, Turkey, and Vietnam

Drone diffusion has proceeded extremely rapidly in these countries but is yet to reach the intensity of Japan and South Korea. Countries in this group are also land scarce, with many small farms; face rural labor scarcity owing to urbanization and industrialization; are upper-middle income; and have already undergone widespread prior adoption of small-scale agricultural machinery, but with intermediate levels of technological sophistication. Policy approaches to agricultural drones in these countries have ranged from vigorous promotion through large-scale subsidies (China) to proactive modification of prior regulatory frameworks (Thailand). Turkey is somewhat less permissive in this regard; drone pilots must seek permission from police before flying because of security concerns.

Argentina, Brazil, and the United States

Agricultural drone diffusion began more recently in these countries and is proceeding rapidly but at a lower intensity than in Asian first-movers. These countries are land abundant (dominated by large farms), requiring large models of drone that have only recently been introduced. Countries in this group are also labor scarce, upper-middle or high income, and have high prior levels of adoption of sophisticated medium- to large-scale agricultural machinery, particularly on large grain farms. Many farms in these countries already own or use the services of expensive self-propelled or tractor-mounted spraying rigs or crop-dusting aircraft. As a result, drones were initially confined mainly to servicing areas where conventional machines have difficulty operating (such as hilly or boggy terrain, or close to pylons), but the range of uses is diversifying rapidly to include a wide variety of specialty crops. These countries have only very recently begun to update regulatory frameworks to accommodate and encourage agricultural drone use. Agricultural drone use in the United States is more highly regulated than in other countries in the group, and recent legislation has banned the import of some DJI drones, potentially slowing future diffusion there.

India

The total number of agricultural drones in India is quite large, but the intensity of diffusion is low. India is land scarce (dominated by small farms), labor abundant in some areas but scarce in others, a lower-middle-income country, and has moderate prior levels of basic small- to medium-scale agricultural mechanization. Government policy here is a two-edged sword that actively promotes drones in agriculture by providing hardware and training to rural women's groups but bans drone imports because of security concerns and with the aim of fostering an infant industry. Moreover, agricultural drone pilots must seek permission before flying. Combined with an abundant low-wage rural workforce and the semi-subsistence orientation of cereal production in many parts of the country, these factors mean the intensity of drone diffusion to date has been low.

Similarly, farm drone use has yet to emerge in most of sub-Saharan Africa in part because of farm labor not yet becoming scarce, as reflected in the limited diffusion of even basic conventional farm mechanization (*4*). Legal restrictions may prevent agricultural drone services emerging at all in some North African countries such as Egypt, where they are very tightly regulated because of security concerns. Restrictions in some countries involved in conflicts, including Myanmar, have ended the emergence of nascent agricultural drone sectors. Strict regulatory environments have slowed the takeoff of agricultural drones in labor-scarce, high-income locations, including Canada and the European Union, as well as in some middle-income countries such as South Africa and the Philippines.

Intensity of drone diffusion

Drone diffusion (drones per unit of cropland) and number of operational agricultural drones in 2024 are shown for 10 countries, in relation to purchasing power parity gross domestic product (GDP) per capita (*3*). The numbers under each country are the number of agricultural drones operational in 2024. See supplementary materials for details on data.

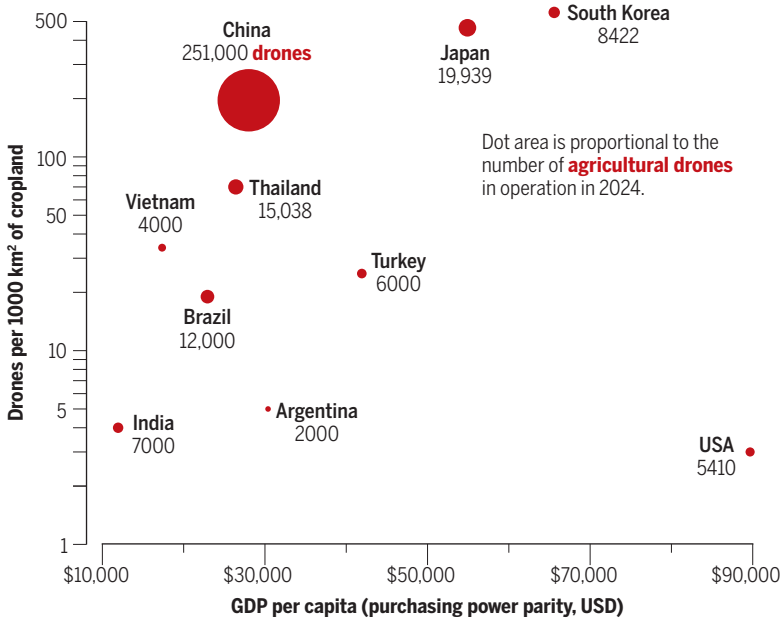

IMPLICATIONS FOR SUSTAINABILITY

Drones may affect agricultural sustainability through three main channels: productivity and resource use efficiency, rural livelihoods, and human health. These variables may reinforce one another, bringing about benefits to society and the environment. But there can be trade-offs that bring new negative externalities, especially in the context of the Global South.

Productivity and resource use efficiency

In theory, drones can be used to implement sustainability-enhancing "precision agriculture," by using sensors to capture spec-

GRAPHIC: M. HERSHER/*SCIENCE*

tral information from plants, analyzing it to provide crop health assessments, and using that analysis to support highly targeted variable-rate application of fertilizers or pesticides (*5*). In practice, such techniques have yet to be widely adopted (*2*), in part because different types of drones are currently required for multispectral sensing and input application. Nevertheless, drones may already contribute to environmental sustainability in several ways.

Drone attachments—rotary spreaders and atomizers—distribute seeds and fertilizer more evenly and disperse pesticides more effectively than broadcasting by hand or with "backpack sprayers" (a common practice on small farms in the Global South). Emerging evidence suggests that drones may reduce seed, fertilizer, and pesticide use by 20% or more compared with manual techniques [for example, (*6*)]. The even placement of seeds and fertilizer and improved penetration and deposition of fine spray droplets inside the crop canopy achieved with drones may increase utilization of these inputs by plants, reducing environmental losses and enhancing resource use efficiency (*7*).

Drones may raise crop yields by eliminating plant damage and soil compaction caused by heavy tractors (*8*). Using battery-powered drones to distribute inputs may reduce energy consumption compared with using conventional heavy machinery (*9*). Drones can also make it easier to implement conservation agriculture practices that reduce soil CO_2 emissions, such as relay sowing and seeding cover crops, because seed can be sown over mature crops in the field from the air. Drones might also allow smaller field sizes to be managed efficiently, reducing farm consolidation and enhancing landscape-level biodiversity (*10*).

Although data-intensive drone operations and analytics that would enable precision agriculture and variable-rate input applications (such as spot-spraying and targeted fertilizer spreading) are not yet widely used by farmers (*2*), these functions will likely become more deeply integrated into everyday practice over time as artificial intelligence and data-processing capabilities advance and as new generations of drone are developed that incorporate both sensing and input application functions. These functions have great potential to drive further improvements in input use efficiency and crop yields, but with the trade-off that the computationally demanding operations required to power them would sharply increase drones' energy demands.

A further promising area in which drones may reduce crop losses and bolster food security is through integration into early-warning systems for disaster risk reduction. For example, remotely sensed satellite data on soil moisture and vegetation cover can be used to predict possible locations for emergent locust infestations, and drones can be directed to these areas to detect locust concentrations and spray to prevent swarms developing (*11*).

Rural livelihoods

Drones may raise farm incomes and affect rural employment through several channels, contributing to the sustainability of rural livelihoods. Drones save labor by dramatically reducing the amount of time needed to apply crop inputs [for example, (*12*)]. This may free rural households to work off-farm, increasing and stabilizing incomes and managing risks, or to use labor for diversifying on-farm into high-value crops such as vegetables. By reducing the quantity of inputs and labor applied to each hectare of land, drones can save farmers money [for example, (*2*, *7*, *13*)].

In combination with conventional agricultural mechanization, agricultural drones eliminate most of the remaining physically demanding work associated with farming. In doing so, drones may help aging farmers to persist, as seen in South Korea, where the average farmer's age is over 60 years and drones already service 30% of farmland (*8*). Conversely, by minimizing the drudgery associated with farming, drones may increase agriculture's appeal to younger farmers, reducing the likelihood that they abandon it. Drone outsource service provision is itself an attractive occupation for rural youth. For example, nearly half of China's agricultural drone pilots are aged 30 or below (*14*). The drone revolution thus increases demand for skilled labor in rural areas.

However, the labor-saving nature of drones can induce a trade-off. In the Global North, agricultural drones are unlikely to displace much labor because displacement already occurred during earlier waves of conventional farm mechanization. But in the Global South, drones will displace some of the poorest agricultural laborers currently hired to spray, fertilize, or weed crops. However, farmers are most strongly incentivized to adopt drones in places where agricultural labor is scarce and rural wages are high, so relatively little displacement is likely to occur in low-income, labor-surplus countries. Moreover, the gender implications of drone adoption are poorly understood. For example, it is not clear whose labor is released or displaced, whether women can access opportunities to provide drone services, or whether drone services affect women's agency over farm management decisions.

Human health

A major benefit of spraying crops remotely by use of drones is that it substantially reduces the risk of farm workers' direct exposure to toxic chemicals, compared with applying them with handheld sprayers. The informal nature of farm work in the Global South means that safety precautions are often not followed when spraying by hand, so occupational health benefits there will be particularly large. However, drones typically fly two or more meters off the ground. This may increase the risk of spray drift to neighboring farms or bystanders, relative to ground-based spraying (*15*), particularly where regulations are absent or weakly enforced or where small farms produce a mixture of crops that could easily be damaged by stray herbicides.

IMPLICATIONS FOR SCIENCE AND POLICY

Like all important new technologies, drones arouse uncertainty and create new dilemmas. Several issues at the nexus of science and policy should be prioritized to help enhance the potential benefits and address the dilemmas.

Facilitating inclusive agricultural drone diffusion

Drone diffusion is occurring rapidly in countries with favorable conditions, but inequalities are emerging in these countries between the most productive agricultural zones and more peripheral areas. A new "digital divide" is also emerging at the global scale as drones diffuse more rapidly in some areas than others. Countries where favorable economic conditions for drone takeoff exist but diffusion is hindered by restrictive policies (for example, South Africa and the Philippines) can draw from the experience of high-diffusion countries to adjust the policy mix in ways that accelerate diffusion safely and responsibly. Drawing on these experiences can also help avoid wasteful investments in ineffective promotional programs.

The basket of policy tools that could accelerate diffusion includes subsidies and finance for drone purchases and the establishment of training, accreditation, licensing, and insurance schemes for drone operators. Depending on intent, these efforts can be designed to cater to individuals, small businesses, farmer groups, or franchises. Restrictive policies such as requiring drone pilots to seek permission before flying can be avoided by introducing standards that ensure pilots are proficient. Remote identification systems can allow drones to be tracked in real time and excluded from entry into sensitive areas by geofencing. Categorizing agricultural drones as farm machinery so that they do not fall under the purview of aviation regulations can greatly simplify their governance.

Reducing input use and raising farm yields

Current use of agricultural drones may already be inducing sustainability gains through lower input use and higher crop yields. But these gains have yet to be studied systematically, and few if any standard operating procedures specifically designed to maximize beneficial outcomes exist. Research in this area could lead to changes in labeling for agrochemicals that reflect higher efficacies when applied by drone, mandating lower levels of use as compared with that for conventional applications. Unlocking the power of drones to implement more sophisticated forms of precision agriculture may require public and private investments in digital infrastructure. For example, 5G networks enable reliable high-volume data transfer and real-time kinematic positioning networks to allow for more accurate spatial positioning of drones. Promoting precision agriculture will also require deeper integration of drone sensing, analytical, and input application functions, with training and extension needed to enable farmers, particularly smallholders, to adopt. Investments in public goods such as regional early-warning systems for locust monitoring and control can minimize crop losses and raise agricultural productivity.

Avoiding rural labor displacement

Policies to address potential displacement of farm workers by drones could include training for reskilling (including as drone operators or pilots' assistants). Cash buyouts and financial support for crop sprayers to acquire drones could reduce loss of income and accelerate the transition.

Minimizing risks to human and environmental health

The shift in many Global South countries from applying inputs by hand to applying them by drone presents a critical opportunity to formalize and professionalize crop spraying. This change would promote greater standardization and safety in an otherwise poorly regulated sector. Doing so would help to mitigate direct risks to human health for sprayers and risks to environmental health posed by excessive agrochemical use and spray drift. Regulatory frameworks can be designed to ensure that drone service providers must undergo training on safe agrochemical use. Such regulations should be designed in ways that do not exclude smaller players, who may need time and support to receive accreditation.

Maintaining technological sovereignty

The global drone market is highly concentrated. As drones become ubiquitous on farms worldwide, there is a possibility that future world events could disrupt supply or make drones vulnerable to cyberattacks (*10*). Public and private investments in research and development can support new drone technologies that induce competition and counter market concentration, but success is not guaranteed. Countries prioritizing national security concerns run the risk of denying farmers access to the most advanced and cost-effective drone technologies.

Ensuring equitable data use

Concentration in the global drone market raises questions about data sovereignty. These concerns will deepen as more data-intensive uses of agricultural drones grow. Who owns and has access to these data, where they are stored, and how they are used have implications for farmers' privacy, the ability to generate public goods, and—possibly—national security. Widespread information-intensive uses of drones would generate vast amounts of crop-specific geospatial data. If aggregated for processing with predictive models, these data could provide public goods, including seasonal yield predictions, accurate crop production estimates, or early warnings of pest infestations. Information collected by drones may also be used for verification of crop damage to support insurance payouts or compensation.

Conversely, if data are treated as the exclusive intellectual property of drone companies, they may become commodified, such as by selling user information for advertising. Such developments might give rise to business models in which drone companies have more to gain by monetizing farmer data than by providing high-quality services. Policy-makers may wish to consider legislation and public-private partnerships that ensure that drone data are retained on servers in the countries where they are generated and facilitate their use for development of public goods, without undermining farmer privacy.

The drone revolution is upending historical patterns of agricultural technology diffusion. In just 5 years, millions of farmers across Asia and beyond, many of them smallholders, have gained access to a powerful new technology with a broad and rapidly growing array of practical uses. There are strong indications that drones can raise the efficiency and productivity of farming, improve worker safety, and enhance rural livelihoods, but these impacts have yet to be evaluated rigorously. Applied interdisciplinary research and corresponding policy responses are urgently needed to steer the global drone revolution in ways that make agriculture more sustainable. □

REFERENCES AND NOTES

1. X. T. Zheng, *Yicai News* 12 June 2024 [in Mandarin]; https://www.yicai.com/news/102390075.html.
2. X. Quan, Z. Wang, T. Daum, X. He, R. Doluschitz, *agricultural engineering.eu*, **79**, 180 (2024).
3. International Food Policy Research Institute (IFPRI), Global agricultural drone distribution. Harvard Dataverse (2025); https://doi.org/10.7910/DVN/BWUQXJ.
4. X. Diao, H. Takeshima, X. Zhang, Eds., *An Evolving Paradigm of Agricultural Mechanization Development: How Much Can Africa Learn from Asia?* (IFPRI, 2020); https://doi.org/10.2499/9780896293809.
5. G. Sylvester, *E-Agriculture in Action: Drones in Agriculture* [Food and Agriculture Organization of the United Nations (FAO), International Telecommunication Organization, 2018].
6. L. Wang *et al*., *Agriculture* **12**, 397 (2022).
7. S. Meesaragandla, M. P. Jagtap, N. Khatri, H. Madan, A. A. Vadduri, *Results Eng.* **21**, 101870 (2024).
8. E. Ozkan, "Drones for spraying pesticides" (Ohio State University Agronomic Extension, 2023); https://agcrops.osu.edu/newsletter/corn-newsletter/2023-05/drones-spraying-pesticides.
9. Y. Seo, S. Umeda, N. Yoshikawa, *Int. J. Agric. Sustain.* **21**, 2247803 (2023).
10. H. H. Zeddies, G. Busch, M. Qaim, *Sci. Rep.* **14**, 15607 (2024).
11. G. A. Matthews, *Agronomy* **11**, 1052 (2021).
12. X. Quan, Q. Guo, J. Ma, R. Doluschitz, *Precis. Agric.* **24**, 1965 (2023).
13. FAO, ICRISAT, "Digital agriculture in action: Selected case studies from India," FAO Investment Centre, Country Investment Highlights no. 17 (FAO, 2022); https://doi.org/10.4060/cc0017en.
14. Z. Huang, H. Chen, 2024. "Regulatory framework for drone operations for agriculture in China: Challenges and opportunities," presentation for FAO webinar, "Drones for agriculture: Opportunities and challenges for the establishment of regulatory frameworks," 20 March 2024; https://www.youtube.com/watch?v=LP6w45taHI8&t=1s.
15. Organisation for Economic Co-operation and Development (OECD), "Report on the state of the knowledge: Literature review on unmanned aerial spray systems in agriculture," OECD Series on Pesticides, no. 105 (OECD Publishing, 2021).

ACKNOWLEDGMENTS

This paper is an output of the CGIAR Policy Innovations Program. The authors thank S. Rashid (IFPRI South Asia Region office) for support for the exploratory research efforts that facilitated development of this paper. L.B. acknowledges support by the National Science Foundation under award 2244164.

SUPPLEMENTARY MATERIALS

science.org/doi/10.1126/science.ady1791

10.1126/science.ady1791

[1]International Food Policy Research Institute (IFPRI), Dhaka, Bangladesh. [2]Department of Agricultural, Food and Resource Economics, Michigan State University, East Lansing, MI, USA. [3]Department of Geography, Environment, and Spatial Sciences, Michigan State University, East Lansing, MI, USA. [4]Independent Consultant, Yangon, Myanmar. [5]IFPRI, Vientiane, Laos. [6]IFPRI, New Delhi, India. [7]IFPRI, Washington, DC, USA. Email: ben.belton@cgiar.org

CHEMISTRY

Tandem sustainability

Modular solar chemistry may help replace fossil fuels in essential chemical production

Emiliano Cortés

Ethylene is the world's most produced organic chemical, underpinning industries worth trillions (*1*). This hydrocarbon compound is a key building block for manufacturing fuels, plastics, fertilizers, and pharmaceuticals. Ethylene is primarily derived from fossil fuels through steam cracking, a high-temperature process that removes hydrogen atoms from molecules or breaks down large molecules into smaller ones. This requires an energy-intensive cryogenic distillation to separate ethylene from a complex gas mixture, which consumes substantial energy and resources (*2*). Thus, a more selective and energy-efficient route to ethylene production is desired. On page 1037 of this issue, Jin *et al.* (*3*) report that light can unlock a fundamentally different mode of catalytic control for ethylene production, yielding >99% selectivity. This could offer an attractive way to obtain renewable ethylene that is often three to nine times more expensive to generate than fossil-derived ethylene through existing methods (*4*).

There are two main routes to achieving more sustainable ethylene: lowering the energy demand in synthesis and purification processes (ideally at room temperature and ambient pressure) and replacing fossil feedstocks with other carbon sources. One strategy toward the latter is to use carbon dioxide (CO_2) as a feedstock instead of hydrocarbons such as ethane and naphtha. Because transforming CO_2 or other simple molecules into more complex hydrocarbons generally requires hydrogenation, it is worth recalling that this reaction has for over a century relied on high-temperature catalysis for its simplicity: Apply heat and the reaction proceeds. Yet, this approach comes with steep trade-offs. At high temperatures (800° to 950°C), multiple reaction pathways are activated, making selective hydrogenation difficult to control. Each hydrogen molecule (H_2) usually split into two radicals that react indiscriminately. This leads to unwanted side reactions and the formation of carbon-based by-products, which clog and deactivate catalysts. As a result, valuable intermediates such as ethylene may undergo unwanted transformations or degrade completely, reducing overall selectivity (*5*). These challenges are even more acute when CO_2 is used as the feedstock, where direct C–C coupling and hydrogenation to ethylene remain unresolved and are currently pursued mostly through electrocatalytic approaches with limited selectivity.

Light can offer a mild and energy-efficient way to drive CO_2 hydrogenation with greater selectivity compared to using heat or electricity. This idea has fueled decades of research into photocatalysis that aims to replicate natural photosynthesis in which sunlight drives a reaction between water and CO_2 to produce energy-rich compounds. Early research in this direction focused on modifying titanium dioxide, which is one of the most studied photocatalysts, to absorb sunlight by introducing defects or decorating with gold nanoparticles (*6*). Although these strategies allowed titanium dioxide to capture more visible light, they often rely on plasmonic excitation (light-driven electron oscillations in metal nanoparticles) that ultimately produce heat (plasmonic heating). This excess heat can reduce selectivity by promoting undesired side reactions, as occurs in thermal catalysis. Another aspect of mimicking photosynthesis is using water as the hydrogen source. This involves splitting a water molecule into protons (H^+) and oxygen, which is a thermodynamically and kinetically demanding reaction. This adds complexity and reduces efficiency of CO_2 hydrogenation using water.

> **...photocatalysis could provide a sustainable alternative to thermal catalysis...**

Jin *et al.* took a fundamentally different approach. Rather than modifying titanium dioxide to absorb sunlight, the authors leveraged its intrinsic ability to absorb ultraviolet light to drive splitting of a hydrogen molecule into a proton and a hydride (H^-), instead of two radicals (which are produced in thermal catalysis). These charged species reacted selectively with CO_2, generating pure ethylene at room temperature. The wavelength and intensity of ultraviolet light could be precisely tuned by using light-emitting diodes to optimize the hydrogen-splitting process. This allowed the use of hydrogen directly as a feedstock, eliminating the need for simultaneous water splitting to create protons. Thus, the strategy of Jin *et al.* decouples hydrogen production from CO_2 hydrogenation. It also separates light harvesting from catalysis, allowing each step to be independently optimized (*7*). Unlike traditional methods that mimic photosynthesis, this "modular chemistry" avoids the burden of conducting concurrent operations of light harvesting and water splitting. The decoupling approach enables efficient ethylene production under ambient conditions without heating.

A photophysical mechanism plays an important role in fine-tuning the reactivity of hydrogen. Gold nanoparticles were coated with a thin layer of titanium dioxide. Under ultraviolet light at 365-nm wavelength, electrons were excited from titanium dioxide, then injected into gold nanoparticles. Simultaneously, holes (opposite analog to electrons) were trapped at the titanium dioxide–gold interface. This created a continuous charge-separated state with a negative charge on the gold nanoparticle and a positive charge at the metal-oxide interface. The nanoscale dipoles that were formed from this state resembled frustrated Lewis pairs (combinations of a Lewis acid and a Lewis base), which can split a hydrogen molecule into a proton and a hydride ion. Thus, the light-driven dipoles acted as "molecular scissors" for precise hydrogen activation under ambient conditions instead of splitting a hydrogen molecule into two neutral radicals, as in traditional thermal catalysis. These charged species are also much more selective in reactivity than the radicals, enabling highly selective hydrogenation of CO_2 to ethylene. Jin *et al.* achieved high rates of ethane and ethylene formation, outperforming previous photocatalytic systems by two orders of magnitude. Although

these numbers trail those of electro- and thermocatalytic methods in absolute rates, the approach of Jin *et al.* delivers an unmatched selectivity with near 100% purity of both ethane and ethylene. This sets a new benchmark in overcoming the trade-off between catalytic conversion and reaction control.

To circumvent the low energy efficiency of ultraviolet light–emitting diodes, Jin *et al.* expanded the photocatalysis strategy to materials that absorb visible light such as bismuth vanadate (*8*). This also required surface modification of the substrate material with gold nanoparticles to generate interfacial electric dipoles. In contrast to using ultraviolet light, electrons in both the substrate and the plasmonic component (gold) became activated under visible light, which induced heating and decreased selectivity below 85%. Although using visible light undermined performance, the approach of Jin *et al.* is not fundamentally limited by the type of light source. This also raises an important question about the most effective way of using sunlight to drive chemical reactions.

The modular chemistry of Jin *et al.* has potential for large-scale sustainable ethylene production. Solar cells could be integrated to harvest light and supply power to a water electrolyzer for the clean hydrogen feedstock and light-emitting diodes for photocatalysis. Green hydrogen is now approaching $1/kg in large-scale projects, and the cost of solar electricity to power light-emitting diodes is projected to substantially drop from $0.094/kWh (kilowatt-hour) in 2015 to $0.016/kWh by 2050 (*9*). The system of Jin *et al.* could also be combined with carbon capture technology for the feedstock CO_2 supply, which will further enhance sustainability of the approach. This may circumvent the fossil economy entirely.

Achieving sustainable ethylene production requires more than just a catalyst. It requires new approaches to reactor design. Light presents challenges that heat does not. It has limited penetration, poor directionality, and low energy density. Further studies are needed to deliver light efficiently to every catalytic site and confirm photocatalyst stability over many cycles. Compared to thermal systems that have been refined over a century, photocatalysis is still in its early stage of development. Similar to how solar cells eventually displaced fossil electricity, photocatalysis could provide a sustainable alternative to thermal catalysis for producing essential chemicals like ethylene. □

REFERENCES AND NOTES

1. *The New Plastics Economy: Rethinking the Future of Plastics* (World Economic Forum, 2016).
2. Y. Demirel, *Chem. Eng. Process. Tech.* **1**, 1005 (2013).
3. P. Jin *et al.*, *Science* **389**, 1037 (2025).
4. D. A. Toribio-Ramirez, R. J. Detz, A. Faaij, B. van der Zwaan, *Sustain. Energy Technol. Assess.* **77**, 104306 (2025).
5. J. Jia *et al.*, *Chem. Soc. Rev.* **46**, 4631 (2017).
6. H. A. Atwater, A. Polman, *Nat. Mater.* **9**, 205 (2010).
7. K. Zhu *et al.*, *Nat. Rev. Clean Technol.* 10.1038/s44359-025-00089-3 (2025).
8. M. Rahaman *et al.*, *Nat. Energy* **8**, 629 (2023).
9. E. Schroeder, P. Christopher, *ACS Energy Lett.* **7**, 880 (2022).

ACKNOWLEDGMENTS

The author acknowledges support from Deutsche Forschungsgemeinschaft under Germany's Excellence Strategy (EXC 2089/1–390776260), the Bavarian Program Solar Technologies Go Hybrid, and the Center for NanoScience.

10.1126/science.aea6759

Nanoinstitute Munich, Faculty of Physics, Ludwig-Maximilians-Universität München, Munich, Germany. Email: emiliano.cortes@lmu.de

QUANTUM TECHNOLOGY

Catching tiny signals

Quantum sensing can help detect diseases early and solve unanswered biomedical phenomena

Theodore Goodson III

Detecting tiny biological signals and biomarkers is crucial for early diagnosis of diseases and developing new therapies to improve human health (*1*). Quantum sensing monitors the changes in the behavior of matter at atomic and subatomic levels to achieve precise measurements of physical quantities. In contrast to traditional characterization methods that provide a signal that is averaged over a large group of molecules, quantum sensing can extract information at the single-atom (photon) level, which is particularly useful for biomedical applications. These approaches can interrogate properties across biological levels from a single molecule to an entire organism. Quantum sensing enhances traditional microscopy, spectroscopy, and bioimaging techniques by reducing the noise and enhancing the signal while maintaining high temporal and spatial resolutions. Thus, integrating quantum sensing techniques could enable the detection of weak biological signals that cannot be measured by conventional technologies without the need for invasive procedures.

Quantum sensing leverages the concept of quantum information science that transmits information by using the principles of quantum mechanics. It is based on three fundamental quantum properties: coherence, entanglement, and interference. Coherence allows a material or a system to maintain its dynamic properties, which is essential for high measurement precision. Entanglement enables two or more objects to experience a high degree of correlation even at a distance, which can be leveraged in measurements. Interference involves the wavelike properties of matter that result in constructive or destructive interaction of waves to amplify (or reduce) signals. Quantum sensing uses these concepts to develop enhanced detection measurements.

One promising quantum sensing technology is a portable atomic magnetometer (or an optically pumped magnetometer) that can identify functional defects in cardiac, brain, retinal, and muscle functions by measuring subtle changes in the magnetic field (*2*). The early versions of portable atomic magnetometers were limited by their bulky size and expensive cost. In addition, cryogenic temperatures were required to enhance sensitivity. This limitation was especially problematic for clinical monitoring of prenatal and postnatal pediatric patients because very high sensitivity was desired with minimal background noise. The next generation of portable atomic magnetometers, which are commercially available, are wearable and display a several-fold improvement in signal quality and spatial resolution without requiring cryogenic temperatures (*3*). These improvements allow measurements to be taken near the source tissue with ease of use, increasing their potential for wide deployment. Portable atomic magnetometers have been used on pediatric patients to detect rare genetic neurological conditions, such as epilepsy, and for preoperative surgical planning (*4*). They have also been used to detect the weak signals of fetal arrhythmias in early gestation in utero. (*5*, *6*). Portable atomic magnetometers could serve as a magnetic analog of the electrocardiogram (*7*, *8*) to substantially improve the clinical care and decision process of prenatal patients with high arrhythmias or familial arrhythmia risk, including rare genetic diseases.

Although existing quantum sensing technologies have demonstrated unmatched performance compared with classical sensors, they are often constrained by limited sensitivity, resolution, thermal damage to the sample, and the patient's reaction to high-intensity light. Emerging quantum sensing approaches could overcome these barriers by using nonclassical light sources such as entangled photons (two or

more photons with the same quantum state) and squeezed light (a form of light with reduced quantum uncertainty). Such techniques can image biological samples at low light intensity compared with conventional microscopes, which could avoid the issues of photodamage or photobleaching of cells.

Coupling spectroscopy methods such as Raman, Brillouin, and two-photon excited fluorescence methods with nonclassical light sources has been shown to improve the contrast of chemical, mechanical, and fluorescence signals of biological samples at very low levels of incident light (*8*–*11*). For example, Brillouin quantum imaging detects inelastic scattering of light to determine acoustic phonons (sound wave) in a molecule or a material (*11*). It uses very low optical power and excitation wavelengths at which light can pass through water with minimal absorption. This allows mechanical properties of biological samples to be probed in water to reduce detrimental effects from light and heat. In addition, entangled photons have demonstrated the imaging of cancer cells with low light intensity over an extended scanning time and area with negligible photodamage (*9*–*11*). Entangled photons have also enhanced conventional optical coherence tomography, providing increased resolution and reduced light dispersion (*12*). However, quantum light sources are still at an initial stage of development and have several challenges. For example, the process of generating entangled photons should be developed to improve efficiency and reduce acquisition time. Additionally, precise spectroscopic signatures of different atoms from nonclassical light sources must be determined to achieve accurate measurements.

Although there is a great landscape of prototypical quantum sensing devices for biomedical and clinical applications, they remain underexplored in these use cases. Developing practical biomedical quantum sensing technologies requires further engineering, testing, optimization, and validation at the laboratory and clinical levels. A standard calibration method should be developed to compare results from different lab tests without bias. Collaboration between experts in the field of biomedicine and quantum physics is needed to design and develop customized technology solutions for unanswered biomedical and clinical problems. Regulatory approvals for safe clinical use of quantum sensing are also important for large-scale deployment. □

REFERENCES AND NOTES

1. N. Aslam *et al.*, *Nat. Rev. Phys.* **5**, 157 (2023).
2. E. Boto *et al.*, *Nature* **555**, 657 (2018).
3. K. Safar *et al.*, *Sci. Rep.* **14**, 6513 (2024).
4. J. Atallah *et al.*, *Diagnostics* **12**, 1164 (2022).
5. O. Feys *et al.*, *Radiology* **304**, 429 (2022).
6. M. Xie *et al.*, *Proc. Natl. Acad. Sci. U.S.A.* **119**, e2114186119 (2022).
7. J. Smits *et al.*, *Sci. Adv.* **5**, eaaw7895 (2019).
8. C. A. Casacio *et al.*, *Nature* **594**, 201 (2021).
9. O. Varnavski, T. Goodson III, *J. Am. Chem. Soc.* **142**, 12966 (2020).
10. O. Varnavski *et al.*, *J. Phys. Chem. Lett.* **13**, 2772 (2022).
11. T. Li, F. Li, X. Liu, V. V. Yakovlev, G. S. Agarwal, *Optica* **9**, 959 (2022).
12. M. B. Nasr *et al.*, *Opt. Commun.* **282**, 1154 (2009).

ACKNOWLEDGMENTS

T.G. acknowledges support by the US Air Force Office of Scientific Research in the biophysics program through grant FA9550-20-1-0380; the Department of Energy, Biological and Environmental Research, through grant DE-SC0025872; and the National Science Foundation through grant 2004076.

10.1126/science.adj0029

Department of Chemistry, University of Michigan, Ann Arbor, MI, USA.
Email: tgoodson@umich.edu

NEUROSCIENCE

Do inhibitory interneurons encode information or just keep the rhythm?

Inhibitory interneurons may help encode the brain's internal representation of space

Michael T. Craig and **Ana González-Rueda**

One of the key ambitions for systems neuroscience is to understand how the activity of different neurons gives rise to the array of cognitive functions and behaviors seen throughout the animal kingdom. The essential building blocks of any neural circuit are glutamatergic excitatory and γ-aminobutyric acid–producing (GABA-ergic) inhibitory neurons, which interact to support cognitive processes such as sensation, perception, decision-making, memory, and spatial navigation. Excitatory neurons are typically seen as the cells encoding information within the brain, and inhibitory neurons as modulating information flow or providing the temporal coordination underlying brain rhythms. However, on page 994 of this issue, Valero *et al.* (*1*) report findings that challenge this model by suggesting that interneurons do indeed contribute to encoding of spatial information in the hippocampus.

The hippocampus has long been a central focus of neuroscience research. The 1957 study of patient H. M., who lost the ability to form new memories after bilateral hippocampal removal to treat epilepsy (*2*), cemented its role in memory. The subsequent discovery that excitatory, glutamatergic pyramidal cells in the hippocampus can act as place cells—neurons that fire only when animals are in certain places in their environment (*3*)—launched a field of research into the role of the hippocampus in spatial navigation. In humans, hippocampal neurons can also encode abstract concepts such as individual people, famously including "Jennifer Aniston" cells (*4*), neurons that responded to different images of this actor. These "concept cells" (*5*) can encode myriad abstract constructs, and it is likely that a single neuron will contribute to encoding different concepts in different contexts. This has led to debate about whether the hippocampus acts as a flexible processor of information by creating generalized cognitive maps for specific tasks (*6*) or whether spatial and memory systems coexist in separate circuits.

GABA-ergic inhibitory interneurons in the mammalian hippocampus are organized in families, with around 20 subtypes comprising ~15% of all neurons (*7*). Initially understudied, inhibitory interneurons are now seen as essential for brain circuit function, driving the brain rhythms that coordinate activity between different structures and controlling various aspects of excitatory neuron firing to route information through the brain. These interneurons are often parsed by expression of peptides that broadly relate to their function. For example, parvalbumin-expressing neurons typically inhibit pyramidal cell bodies (*7*), whereas somatostatin-expressing neurons usually target apical dendrites.

Valero *et al.* recorded from the hippocampus of mice navigating a spatial task and identified excitatory neurons or different classes of inhibitory interneuron, including those expressing parvalbumin or somatostatin, using "opto-tagging." This method involves inducing the expression of channelrhodopsin, a light-activatable ion channel, in a specific genetically defined neuronal cell type, which can then be identified by its electrophysiological response to light. The authors' key innovation was in training a supervised machine-learning classifier to distinguish the action potential waveform of different neuronal subtypes using the opto-tagged neurons as a "ground truth." They applied this classifier to

Inhibitory neurons regulate circuit function

Excitatory pyramidal cells (PC) in the cornu ammonis 1 (CA1) region of the mouse hippocampus are active in specific spatial locations (place fields). PCs receive inhibitory input from parvalbumin-positive and somatostatin-positive interneurons (PV and SST). PV cells target the cell body of the PC, reducing overall output (firing rate) of the cell. Experimental stimulation of PV cells reduces the selectivity of the PC place field. SST cells target the dendritic tufts of the PC, modulating the input it receives. Stimulation of SST cells disrupts the structure of the place field.

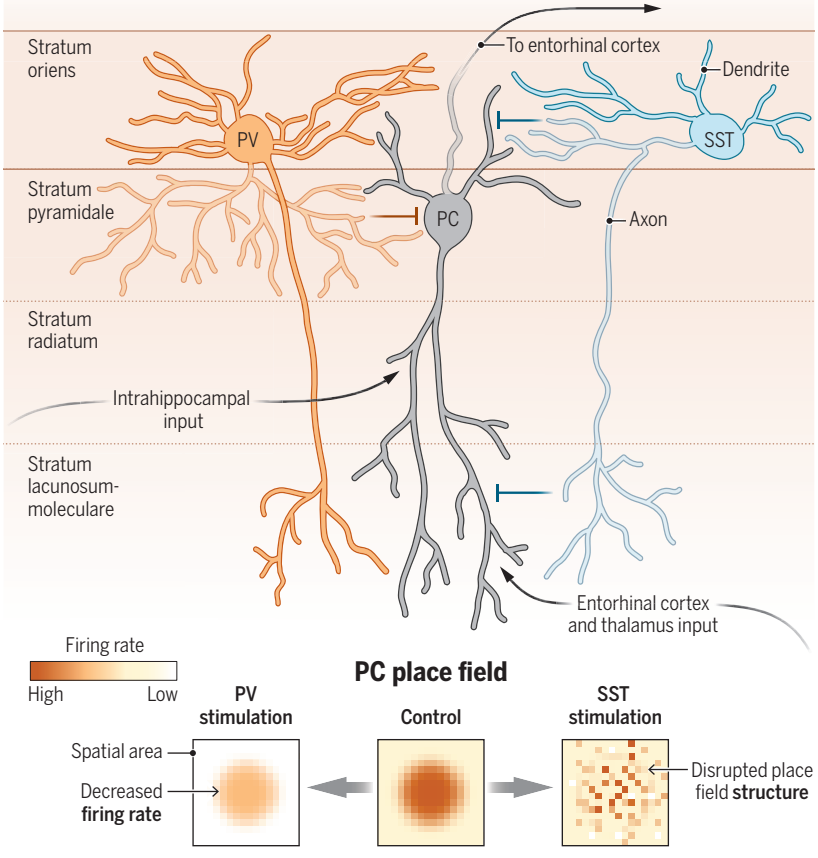

predict the identity of other recorded, non–opto-tagged, neurons. Previously, in vivo action potential waveforms could be used to distinguish only broad classes of interneurons, and opto-tagging typically identified just one genetically defined cell type per mouse. By combining opto-tagging with a classifier, Valero *et al.* achieve a step-change in resolution, enabling identification of multiple interneuron families simultaneously in a single mouse, thereby allowing their respective behaviors during spatial navigation to be observed.

The key conclusion of Valero *et al.* was that different classes of inhibitory interneurons appeared to support or encode different aspects of spatial information within the hippocampus. For example, the authors found that optogenetic stimulation of parvalbumin-expressing interneurons reduced the firing of pyramidal place cells within the cornu ammonis 1 (CA1) subfield of the hippocampus, which decreased the apparent selectivity of place coding. By contrast, stimulating somatostatin-expressing interneurons disrupted pyramidal place fields, reducing the consistency of place representations. These features might be expected based on the synaptic connectivity of these interneurons with different pyramidal cell compartments, enabling them to modulate either the inputs or the output of the pyramidal cell. For example, parvalbumin-expressing interneurons target pyramidal cell bodies or the axon-initial segment (*7*), so optogenetically activating them would be expected to suppress the firing of the place cells, as observed by Valero *et al.* The somatostatin-expressing family of neurons include bistratified and OL-M cells, which target different dendritic compartments of pyramidal cells (*7*). In CA1, intrahippocampal information arrives in stratum radiatum, whereas long-range inputs from the entorhinal cortex (relaying processed sensory information) or midline thalamus (providing goal-directed information from prefrontal cortex) arrive in stratum lacunosum-moleculare (*8*). Bistratified cells could inhibit the former, whereas OL-M cells could inhibit the latter, altering place cell contextual coherence (see the figure).

An important caveat is that the neuronal subtypes within somatostatin and parvalbumin families can differ in their action potential waveforms and participation in brain rhythms associated with different behavioral states (*7*, *9*, *10*). This is a potential confound when treating these families as a single cell type. Notably, the axons of parvalbumin neurons have a broad reach across the pyramidal layer of CA1 (where pyramidal cell bodies are located), allowing them to modulate the activity of many pyramidal cells to exert a global influence on hippocampal function. By contrast, somatostatin axons reach a smaller range of pyramidal cell apical dendrites, positioning them to modulate the inputs to individual pyramidal cells. Activating somatostatin cells as Valero *et al.* did could thus be expected to disrupt the specificity of ongoing inputs to individual place cells, leading to the more widespread firing pattern that was observed. An open question is whether this disruption merely degrades coding, or whether it provides a mechanism for reorganizing place cell identity in new environments, perhaps even enabling shifts from place-specific coding to the more abstract representations seen in concept cells.

The development of the cell type classifier by Valero *et al.* is perhaps the most valuable finding of the study. This classifier can be applied to existing datasets recorded across a broad range of behavioral tasks and species to analyze the contribution of inhibitory interneurons to information coding throughout the brain. The study also raises a philosophical question: Inhibitory interneurons are reciprocally connected with pyramidal cells, so does the observation of spatial information in interneurons imply that they are essential for encoding this information, or are they simply reflecting the activity of excitatory place cells? If the hippocampus does indeed provide a generalized conceptual map, what predictions could be made from the findings of Valero *et al.*? One would predict that activation of parvalbumin interneurons would make a Jennifer Aniston cell less likely to fire in response to an image of her, whereas activation of somatostatin interneurons may make these cells fire in response to the image of any blonde woman. Applying Valero *et al.*'s classifier to existing datasets might help answer the question of whether interneurons just route information through the brain and keep rhythm, or whether they also encode information. □

REFERENCES AND NOTES

1. M. Valero *et al.*, *Science* **389**, eadv5638 (2025).
2. W. B. Scoville, B. Milner, *J. Neurol. Neurosurg. Psychiatry* **20**, 11 (1957).
3. J. O'Keefe, J. Dostrovsky, *Brain Res.* **34**, 171 (1971).
4. R. Q. Quiroga, L. Reddy, G. Kreiman, C. Koch, I. Fried, *Nature* **435**, 1102 (2005).
5. R. Q. Quiroga, *Nat. Rev. Neurosci.* **13**, 587 (2012).
6. T. E. J. Behrens *et al.*, *Neuron* **100**, 490 (2018).
7. K. A. Pelkey *et al.*, *Physiol. Rev.* **97**, 1619 (2017).
8. M. T. Craig, J. Witton, *Science* **377**, 262 (2022).
9. M. T. Craig, C. J. McBain, *J. Neurosci.* **35**, 3616 (2015).
10. R. Chittajallu *et al.*, *Nat. Neurosci.* **16**, 1598 (2013).

10.1126/science.aea6738

School of Psychology & Neuroscience, College of Medical, Veterinary and Life Sciences, University of Glasgow, Glasgow, Scotland. Email: mick.craig@glasgow.ac.uk; ana.gonzalez-rueda@glasgow.ac.uk

GRAPHIC: N. BURGESS/*SCIENCE*

CARDIOVASCULAR HEALTH

Poking holes in the heart's rhythm

Neutrophils destabilize cardiac muscle membranes to promote arrhythmia

Edward B. Thorp

The mammalian innate immune system has evolved over millions of years as a first line of defense against pathogens and tissue injury. But what emerges when immunity encounters the syndromes of advanced age, wherein the selective evolutionary pressure is relatively short? In the case of human heart disease, the confrontation can lead to unintended and grave consequences. On page 1043 of this issue, Kumowski *et al.* (*1*) report that in mice, misdirected cross-talk between neutrophils and cardiac tissue predisposes the heart to arrhythmia and cardiac death and can inflict damage beyond the heart. Antimicrobial peptides normally released by neutrophils to fight infection damage the cell membrane of cardiomyocytes, causing ion leaks that disrupt the heart's electrical activity. These peptides may offer a new target for limiting tissue injury and death from ischemic heart disease.

Ischemic heart disease remains a major cause of morbidity and mortality. After a heart attack, or myocardial infarction, reduced oxygen and nutrient availability dysregulate how cardiomyocytes handle ions, which leads to intracellular sodium (Na^+) and calcium (Ca^{2+}) overload, membrane depolarization, acidosis, and electrical instability. Collectively, this altered ion flux sets the stage for irregular cardiac rhythms, including ventricular tachycardia, and, in many cases, sudden death. Direct treatment of the cardiac parenchyma—the functional heart tissue consisting of cardiomyocytes and specialized conducting muscle cells that initiate and propagate electrical impulses—remains a challenge because therapy has been limited to drugs with side effects or invasive procedures that ablate the problematic tissue causing the arrythmia (*2*). However, circulating immune cells, which contribute to disease progression, are more therapeutically accessible.

Most arrhythmias occur within the first 2 days after myocardial infarction (*3*). This coincides with the characteristic cellular inflammatory response to acute tissue injury. Early responders include neutrophils, which can disrupt muscle cell conduction of electrical impulses (*4*). Indeed, neutrophils are often implicated in unintended tissue damage in clinical settings and thus represent a potential target to ameliorate injury when blood flow is restored to the heart (reperfusion), although such a strategy remains mostly unrealized to date.

By surveying distinct immune cell populations in the ischemic myocardium of mice, Kumowski *et al.* found that a peptide called resistin-like molecule γ (RELMγ) was differentially expressed in neutrophils. This was localized to ischemic areas where tachycardia arises. The authors demonstrated that targeted deletion of the gene encoding RELMγ in neutrophils reduced acute ventricular tachycardia in mice. They also found that RELMγ causes electrical instability in the form of delayed electrical afterdepolarizations, which leads to cardiomyocyte death. Such consequences can result in ectopic cardiac beats that generate arrhythmogenic substrates—structural, cellular, or molecular abnormalities that create a favorable environment for arrhythmias—commonly found in the ischemic myocardium (*5*). Notably, resistin (RETN), the human homolog of RELMγ, was similarly expressed in infarcted myocardium of patients, and the concentration of RETN in blood after myocardial infarction also correlated with unfavorable patient outcomes (*6*). Treatment of cultured cardiomyocytes with neutrophil lysates and recombinant RELMγ were sufficient to trigger electrical instability. Given that RELMs are found in neutrophil granules that are secreted after exposure of neutrophils to bacterial-like ligands (*7*), it is possible that RELMs released by neutrophils are important effectors of arrythmia.

RELM peptides form pores in bacterial membranes (*8*). However, their interaction with cardiomyocytes was unknown. Kumowski *et al.* observed that densely packed RELMγ peptides congregated at the cardiomyocyte membrane surface, proximal to externalized membrane phosphatidylserine (a hallmark of cell death) and membrane repair proteins. RELMs are characterized by a positively charged β-sheet structure. This enables electrostatic interactions with negatively charged membrane lipids (*9*) in an acidic environment (*10*). Stressed cardiomyocytes flip negatively charged phosphatidylserine from the inner to outer phospholipid layer of the plasma membrane (*11*), and the myocardial pH can quickly become acidic as a result of anaerobic metabolism (*12*). The low pH likely affects the protonation of amino acids that facilitate the binding of RELM molecules to negatively charged membranes (*13*). In addition, RELM bears a hydrophobic α helix that harpoons the target membrane to disrupt lipid bilayers (*9*).

Misdirected injury response by neutrophils could be relevant to other scenarios...

Membrane perforations allow extracellular cations to enter the cell, leading to electrical instability, cell depolarization, and the formation of arrhythmogenic substrates (*5*). Kumowski *et al.* tracked extracellular dye entry into cells near RELMγ binding sites, which then spread throughout the cell. They observed the same for intracellular calcium sensors, which suggests that the influx of calcium through membrane breaches contributes to cell depolarization.

The detrimental roles of neutrophils after clinical reperfusion and in the heart are widely documented. Yet neutrophils also have wound-healing properties. As such, the en masse blockade of this cell type is problematic, and targeting neutrophil effectors, such as reactive oxygen species and myeloperoxidase, have yet to benefit clinical reperfusion. Thus, new targets are needed to rescue nonregenerative, but salvageable, cardiomyocytes. Kumowski *et al.* also reported a similar neutrophil attack mechanism on neuronal cells after experimental stroke in a mouse model. Misdirected injury response by neutrophils could be relevant to other scenarios, where different mechanisms selectively regulate the deployment of RELMs in various contexts. □

REFERENCES AND NOTES

1. N. Kumowski *et al.*, *Science* **389**, 1043 (2025).
2. J. Bhar-Amato, W. Davies, S. Agarwal, *Arrhythm. Electrophysiol. Rev.* **6**, 134 (2017).
3. R. H. Mehta *et al.*, *Am. J. Cardiol.* **109**, 805 (2012).
4. J. Grune *et al.*, *Nat. Cardiovasc. Res.* **1**, 649 (2022).
5. V. Ducceschi *et al.*, *Clin. Cardiol.* **19**, 325 (1996).
6. H. B. Erer *et al.*, *Kardiol. Pol.* **72**, 181 (2014).
7. E. A. Boström *et al.*, *Biochim. Biophys. Acta Mol. Cell Res.* **1793**, 1894 (2009).
8. D. C. Propheter *et al.*, *Proc. Natl. Acad. Sci. U.S.A.* **114**, 11027 (2017).
9. Y. Shai, *Biochim. Biophys. Acta Biomembr.* **1462**, 55 (1999).
10. H. Lambers *et al.*, *Int. J. Cosmet. Sci.* **28**, 359 (2006).
11. E. A. Dumont *et al.*, *Circulation* **102**, 1564 (2000).
12. H. Hirche *et al.*, *J. Mol. Cell. Cardiol.* **12**, 579 (1980).
13. E. Malik *et al.*, *Pharmaceuticals* **9**, 67 (2016).

ACKNOWLEDGMENTS

E.B.T. acknowledges support by the National Institutes of Health (grants R35HL177401 and R01HL175893) and the American Heart Association (grant AHA24SFRNPCN1289611).

10.1126/science.aea6159

Department of Pathology, Feinberg School of Medicine, Northwestern University, Chicago, IL, USA. Email: ebthorp@northwestern.edu

BOOKS ET AL.

SOCIOLOGY

Valuing women's work

Achieving gender equality is possible if we admit to past mistakes and tackle the mental load **Leah Ruppanner**

Will women ever stand on equal economic footing with men, and what would it take to equalize domestic labor—housework, childcare, and mental load—in the home? These questions have been discussed for decades, and yet each year, the gender gap remains. So what do we do? Two new books, Cordelia Fine's *Patriarchy Inc.* and Allison Daminger's *What's on Her Mind*, provide clear steps forward.

Fine's *Patriarchy Inc.* maps the historical context of how we are trained to think of gender as either biologically driven or socialized into us from birth. She starts the book with a simple yet provocative assertion: Gender is culturally inherited. Gendered expressions, she argues, can change, adapt, and shift over time, but we learn them from birth, and they are passed generationally through culture. She then traces the ways in which gender became institutionalized into capitalism—underscoring how a "different but equal" logic allows patriarchy to continue.

If women are just "different" from men, then we can justify a range of decisions women make as individual preference. These might include their tendency to cluster in low-paid caregiving jobs or to exit high-paid corporate jobs despite having the requisite education and qualifications. Fine underscores that this "different but equal" logic allows corporations to make tokenistic attempts to "include women" by keeping them separate, disempowered, and "different" from men. And it lends credence to the idea that industries dominated by men, such as finance and technology, are more valuable than others and "too important to fail." Ultimately, she argues that we cannot fully dismantle gender inequality until we identify the pervasiveness of "different but equal" ideologies in how we work, how we govern, and how we think about men and women.

It is exactly this notion of how gender is embedded in our minds that Daminger's *What's on Her Mind* tackles, helping readers understand how couples negotiate the mental load of family life. Remembering, organizing, and planning family life—tasks disproportionately borne by women—Daminger argues, are key, understudied behaviors that keep gender inequality intact. Her case studies echo Fine's argument that ideas about gender are so ingrained that they often reinforce gender inequality.

Patriarchy Inc.: What We Get Wrong About Gender Equality—and Why Men Still Win at Work
Cordelia Fine
Norton, 2025. 352 pp.

What's on Her Mind: The Mental Workload of Family Life
Allison Daminger
Princeton University Press, 2025. 248 pp.

Many of Daminger's interviewees describe their unequal division of the mental load as rational—the work simply fell to the partner with the best innate skills. And yet time and again, somehow mothers, more than fathers, always ended up with more high-effort but low-reward mental load tasks. As her participants argue, mothers are just inherently better and more skilled at the remembering of children's lives.

Daminger identifies the fallacy in this thinking by pointing to the ways traditional gender norms lock mothers into these mental loads in perpetuity. LGBTQIA+ parents are not immune to these dynamics, she reveals, but are able to thwart traditional gender norms and reallocate the mental load drudgery with less resistance and relationship conflict. Here, we can see that mental loads are reflections of the institutionalized patriarchal thinking that Fine identifies in *Patriarchy Inc.*

So where do we go from here? Each author provides concrete suggestions for next steps. Fine asks readers to dismantle our "different but equal" ideology in favor of a "different is valuable" approach. Daminger points us to the importance of centering the mental load in our discussions and not dismissing it as a "woman's issue," carefully articulating why having women bogged down in worries about lost socks and dirty dishes is a problem for everyone. In this way, Fine and Daminger emphasize the inherent worth of the work women do and ask that it be valued accordingly.

Their books also point to an outdated framework that is still being applied in contemporary contexts. Often, we still expect women to be the homemakers and men to be the breadwinners, despite the fact that these roles no longer reflect our lived realities. Women today are more likely to engage in paid employment and yet still carry most of the family's mental load. Men want to be more engaged in the emotional work of the home, connecting to children and partners in ways distinct from previous generations, but are boxed in by expectations that they will be their family's primary providers. After reading these two books, I was left with a clear sense that these expectations leave us all with less. But, as Fine asserts, the mistakes of our past are only a problem if we fail to remedy them. □

10.1126/science.adz8956

The reviewer is at the Future of Work Lab and the Gender Equity Initiative, University of Melbourne, Melbourne, Australia. Email: leah.ruppanner@unimelb.edu.au

ANTHROPOLOGY

The end of human exceptionalism

Anthropocentric worldviews harm us all, argues a primatologist **Barbara J. King**

The Arrogant Ape: The Myth of Human Exceptionalism and Why It Matters
Christine Webb
Avery, 2025.
336 pp.

One day in the superheated Namib desert, primatologist Christine Webb followed the lead of the chacma baboons she was observing and took a shaded rest break. Webb's human colleague and two dozen monkeys fell asleep, but like Webb, one baboon—a juvenile female—remained awake. "We blink at each other in the shadowy light," Webb writes in her new book, *The Arrogant Ape*, "knowing it's just us two left behind in the waking world." The monkey casually manipulated some pebbles and, just as Webb did, occasionally looked up at the sky. On the surface, nothing remarkable happened during this encounter. But it was transformative for Webb—and for good reason: "Never had I been so convinced of the minded life of a baboon—one as full, nuanced, and idiosyncratic as my own."

Most of us grow up immersed in a worldview that centers humans as more than and better than other animals. Rather than being an explicit teaching, this perspective surrounds us so thoroughly that it requires effort to even become aware of it. (Fans of Daniel Quinn's *Ishmael*, a 1992 novel that I taught for years to anthropology undergraduates, may recognize similar themes here.)

Webb pulls no punches in offering her take on the arrogance of this assumed human supremacy. On page 1, she notes "the most prominent theme in the history of Western thought: human beings are the most clever, moral, and capable species on earth." In response, she offers a catalog of fascinating examples of animal behavior, often drawing from her own research experiences with monkeys and apes in field and captive settings. Chimpanzees, she notes, for example, not only cooperate during hunts and in food-sharing but also may console other chimpanzees after a conflict, all in culturally variable ways that reveal their social, cognitive, and emotional complexity.

Webb's astute assessment of animal research emerges from experience working at the New York State Psychiatric Institute, where singly caged monkeys "desperate for some form of social contact" were held in a primate cognition lab. Evidence shows without question that stress damages the brain. Yet animal testing, which prioritizes human interests, stresses animals and, she believes, "jeopardizes the relevance of the science."

A great strength of the book comes from Webb's message that human exceptionalism dangerously amplifies our present ecological crisis. Effective responses to climate change, species extinction, and global pandemics will not come primarily from technological fixes, she argues. We must find healthier ways of coexisting with, and protecting the well-being of, other animals—and plants as well.

In a swipe at Elon Musk and Jeff Bezos that I judge to be well deserved, Webb defines Earth-exit strategies as a novel expression of human exceptionalism. Ours is an "entangled existence" with all the other creatures with whom we have coevolved, she maintains. Attempting to escape rather than repair that tangle is, in her estimation, a serious mistake.

Not all of Webb's statements convince, however. It is misleading, for example, to assert that *Homo sapiens* are the "only real animal" city dwellers come to know; many an urban resident observes or relates with squirrels, turtles, hawks, butterflies, coyotes, or other land, water, or air animals. And deeper questions emerge from her discussion of Indigenous practices toward animals.

Humanity must recognize and value animals' complex lives and resist frameworks that place human needs above those of other creatures, argues Webb.

PHOTO: LAURA STORM/ALAMY

Webb rightly recognizes Indigenous beliefs as very often escaping human exceptionalism because Native groups, many of whom view other beings as kin, live more sustainably than do many Westerners. However, for Webb, even to entertain questions about an aspect of Indigenous relationality with animals is wrong if one is not Indigenous. Decolonizing work does not permit this, she asserts, and in any case, Indigenous observations on nature are "inherently place-specific."

Yupik whalers, for instance, view a hunted bowhead whale's behavior as a process of thoughtful decision-making about whether she should or should not give herself in death to the whalers. If the hunters' interpretation is that, yes, the whale is ready to die for them, they kill her. Indigenous scholars do not speak from a single perspective on the topic of violence to animals. Does the important and necessary decolonial project by contrast require absolute silence regarding it? If so, might that silence only protect the very invisibility that powers human exceptionalism—wherever it occurs?

Overall, though, Webb's urgent message is successful. It sets readers a task, a challenging but not impossible one: "Overcoming human exceptionalism is less about learning something new than about unlearning and shedding a dominant, culturally ingrained perspective." Humans did not always act from an anthropocentric perspective, and not all humans do now. There is hope to be had, if we let the unlearning begin. □

10.1126/science.ady5473

The reviewer is a research fellow at PAN Works, Wilbraham, MA, USA, and professor emerita of anthropology at William & Mary, Williamsburg, VA, USA. Email: bjking@wm.edu

Vultures are threatened by the continued veterinary use of diclofenac and related drugs.

PHOTO: J.C. EAMES

Vulture conservation requires NSAID regulation

The toxic nonsteroidal anti-inflammatory drug (NSAID) diclofenac caused the collapse of vulture populations in South Asia in the 1990s (*1*, *2*). In 2006, India, Nepal, and Pakistan banned veterinary use of diclofenac (*1*, *2*), and later Bangladesh, Iran, Cambodia, and Oman enacted bans as well (*3*). The first bans were introduced just 2 years after the devastating effects of the drug were recognized, but progress in the 20 years since then has been limited. With the exception of Nepal (*4*), continued illegal sales of diclofenac and delays in banning other veterinary NSAIDs have hindered conservation success (*5*, *6*). In 2024, the Conference of the Parties to the Convention of Migratory Species (CMS) called for more effective testing and regulation of veterinary NSAIDs in vulture range states (*7*). Vulture populations depend on the Parties and other governments coordinating efforts to achieve the CMS goals, ban NSAIDs, and enforce veterinary restrictions.

In Spain, where 90% of European vulture populations live, diclofenac was licensed for veterinary use in 2013 (*8*), 7 years after the drug was first banned in Asia. Spanish NSAID regulations have been ineffective (*8*, *9*). In Spain, diclofenac and toxic NSAIDs ketoprofen and flunixin have been detected in the carcasses of domesticated ungulates provided at vulture feeding stations (*8*), and ketoprofen and flunixin have been found in the blood plasma of vultures and associated with the deaths of wild vultures (*9*).

No vulture range state has a rapid, evidence-based process for withdrawing legal approval from veterinary NSAIDs shown to be toxic to vultures, and no range state requires any evidence of safety to vultures before approving a new veterinary NSAID (*10*). Just two NSAIDs (meloxicam and tolfenamic acid) have been found to be safe for vultures, and in neither case did the pharmaceutical industry fund the testing (*10*). Although several NSAIDs other than diclofenac—including flunixin, ketoprofen, nimesulide, and aceclofenac—are toxic to vultures, these drugs are still widely available in parts of South Asia and Europe (*7*, *9*). Although Bangladesh banned ketoprofen in 2021 and India banned ketoprofen and aceclofenac in 2023 and nimesulide in 2024 (*10*), the bans were introduced more than a decade after toxicity of these drugs to vultures was established (*10*).

Governments and the pharmaceutical industry should share responsibility for the environmental and public health effects of NSAIDs. Parties to the CMS Convention include the range states India, Pakistan, Bangladesh, Spain, and Italy. These governments, and others that host vulture populations, should demonstrate their commitment to the conservation of these species and the important ecosystem services they provide (*11*, *12*) by taking action before the next CMS Conference of the Parties in March 2026.

Antoni Margalida[1,2] and Rhys E. Green[3,4]

[1]Institute for Game and Wildlife Research, Consejo Superior de Investigaciones Científicas (CSIC)–Universidad de Castilla–La Mancha (UCLM)–Junta de Comunidades de Castilla–La Mancha (JCCM), Ciudad Real, Spain. [2]Pyrenean Institute of Ecology, CSIC, Jaca, Spain. [3]Conservation Science Group, Department of Zoology, University of Cambridge, Cambridge, UK. [4]RSPB Centre for Conservation Science, Royal Society for the Protection of Birds (RSPB), Sandy, UK. Email: a.margalida@csic.es

REFERENCES AND NOTES

1. J. L. Oaks *et al.*, *Nature* **427**, 630 (2004).
2. R. E. Green *et al.*, *J. Appl. Ecol.* **41**, 793 (2004).
3. SAVE; https://save-vultures.org.
4. T. H. Galligan *et al.*, *Bird Conserv. Int.* **30**, 87 (2020).
5. V. Prakash *et al.*, *Bird Conserv. Int.* **34**, e1, 1 (2024).
6. T. H. Galligan *et al.*, *Bird Conserv. Int.* **31**, 337 (2021).
7. Convention on Migratory Species, "CMS Resolution 11.15 (Rev.COP13)" (2020); https://www.cms.int/sites/default/files/document/cms_cop13_res.11.15_rev.cop13_e.pdf.
8. A. Margalida *et al.*, *Science* **372**, 694 (2021).
9. M. Herrero-Villar *et al.*, *Sci. Total Environ.* **782**, 146890 (2021).
10. S. Cook *et al.*, *Ecol. Solut. Evid.* **5**, e12357 (2024).
11. A. Santangeli *et al.*, *iScience* **27**, 109925 (2024).
12. E. Frank, A. Sudharshan, *Am. Econ. Rev.* **114**, 3007 (2024).

10.1126/science.ady8601

Assess and protect jumbo flying squid

Nearly 1 million tonnes (*1*) of jumbo flying squid (*Dosidicus gigas*) are caught in the southeast Pacific annually. A transnational stock, the jumbo flying squid is harvested by thousands of artisanal vessels in Ecuadorian, Peruvian, and Chilean waters and hundreds of industrial Chinese vessels in the high seas (*2*). However, the jumbo flying squid stock has never been assessed across its entire distribution in the southeast Pacific. Although it is the most harvested invertebrate species in terms of tonnes landed (*1*), crucial population data remain unknown. In recent years, the yield has dropped substantially, suggesting that the stock could be in decline (*3*). To ensure sustainable practices, the international community should work together to monitor, assess, and manage the jumbo flying squid stock.

The South Pacific Regional Fisheries Management Organisation (SPRFMO) regulates harvests in the high seas, including the jumbo flying squid. The SPRFMO has taken some management actions, such as placing caps on the number of fishing vessels and implementing common protocols for data collected by observers on vessels operating in the high seas (*4*). However, a lack of international cooperation has hindered efforts to build a regional database and ensure that SPRFMO commission members share biological samples, mechanisms that are necessary for conducting regional stock assessments.

The SPRFMO mandates periodic performance reviews conducted by independent experts to assess the effectiveness of the management measures adopted by the organization (*5*). In 2024, the second SPRFMO performance review highlighted existing gaps in jumbo flying squid regional stock assessment and in data sharing among nations currently participating in the fishery (*6*). Closing such gaps through collaboration could prevent a collapse like that of the jumbo flying squid fishery in the Gulf of California (*7*) and could decrease the likelihood of large, unpredictable fluctuations in total catch like those of the Argentine shortfin squid (*Illex argentinus*) stock in the southwest Atlantic (*2*). Because El Niño's large-scale cycles create intense ecosystem and population variability (*8*), the jumbo flying squid stock should be assessed through ecosystem-based models.

The jumbo flying squid stock supports the livelihoods of thousands and provides food security to millions globally (*2*, *9*). The SPRFMO has successfully recovered species before; in 2013, the organization implemented policies that restored the large jack mackerel stock (*10*). To make similar progress with the jumbo flying squid, the SPRFMO will need to coordinate with Ecuador, Peru, Chile, and China. With strengthened international scientific collaboration, SPRFMO can protect the stock before it needs a recovery plan.

Rubén H. Roa-Ureta[1], Gang-Li[2], Xinjun Chen[3], Christian M. Ibáñez[4], Karen Belmar-Salinas[5], James N. Ianelli[6], Renato Gozzer-Wuest[7], Enrique Alonso-Población[8], Alexander I. Arkhipkin[9], Tania Mendo[10], Esteban Elías[11], Manuel Peralta[11], Teddy A. Escarabay[12], Rodrigo Wiff[13,14]

[1]Portugalete, Bizkaia, Spain. [2]College of Marine Living Resource Sciences and Management, Shanghai Ocean University, Shanghai, China. [3]Key Laboratory of Sustainable Exploitation of Oceanic Fisheries Resources, Ministry of Education, Shanghai, China. [4]One Health Institute, Facultad de Ciencias de la Vida, Universidad Andres Bello, Santiago, Chile. [5]Departamento de Evaluación de Pesquería, División de Pesquería, Instituto de Fomento Pesquero, Valparaíso, Chile. [6]Resource Ecology and Fisheries Management Division, Alaska Fisheries Science Center, National Oceanic and Atmospheric Administration, Seattle, WA, USA. [7]Innovations for Ocean Action Foundation, Lima, Peru. [8]Innovations for Ocean Action Foundation, Galicia, Spain. [9]Fisheries New Zealand, Ministry of Primary Industries, Wellington, New Zealand. [10]School of Geography and Sustainable Development, University of St. Andrews, St. Andrews, Scotland, UK. [11]Instituto Público de Investigación de Acuicultura y Pesca, Guayaquil, Ecuador. [12]Sustainable Fisheries Partnership, Honolulu, HI, USA. [13]Center of Applied Ecology and Sustainability, Pontificia Universidad Católica de Chile, Santiago, Chile. [14]Instituto Milenio en Socio-Ecología Costera, Santiago, Chile. Email: rodrigo.wiff@gmail.com

REFERENCES AND NOTES

1. FAO Fisheries Division, Statistics and Information Branch, FishStatJ: Universal software for fishery statistical time series (2024); https://www.fao.org/fishery/en/statistics/software/fishstatj.

The jumbo flying squid population could be in decline, but crucial data remain unknown.

PHOTO: BRIAN SKERRY/MINDEN PICTURES

2. A. I. Arkhipkin, C. M. Nigmatullin, D. C. Parkyn, A. Winter, J. Csirke, *Rev. Fish Biol. Fish.* **33**, 453 (2023).
3. I. S. Payá C., "Update of the Stochastic Production model in Continuous Time (SPiCT) applied to *Dosidicus gigas* in the FAO area 87" (Technical Report SC13 - SQ 06, SPRFMO, 2025); https://www.sprfmo.int/assets/Meetings/02-SC/13th-SC-2025/Squid/SC13-SQ06-Update-of-the-SPiCT-applied-to-Dosidicus-gigasin-FAO-area-87.pdf.
4. SPRFMO, "Conservation and management measure on the management of the jumbo flying squid fishery" (Technical Report CMM 18-2025, SPRFMO, 2025); https://www.sprfmo.int/assets/Fisheries/Conservation-and-Management-Measures/2025-CMMs/CMM-18-2025-Squid.pdf.
5. SPRFMO, "Convention on the conservation and management of high seas fishery resources in the South Pacific Ocean" (SPRFMO, 2022); https://www.sprfmo.int/assets/Basic-Documents/Convention-and-Final-Act/SPRFMO-Convention-2023-update-12May2023.pdf.
6. K. Robertson, K. Mundnich, S. Crothers, J. Mitchell, "Second SPRFMO performance review: Panel report and recommendations" (Technical Report, SPRFMO, 2024); https://www.sprfmo.int/assets/Meetings/01-COMM/13th-Commission-2025/Reports/SPRFMO-Second-Performance-Review-1.-Main-Report.pdf.
7. T. H. Frawley *et al.*, *ICES J. Mar. Sci.* **76**, 2413 (2019).
8. A. Arkhipkin, J. Argüelles, Z. Shcherbich, C. Yamashiro, *Can. J. Fish. Aquat. Sci.* **72**, 400 (2015).
9. Food and Agriculture Organization of the United Nations (FAO), "The state of world fisheries and aquaculture 2024 – Blue transformation in action" (FAO, 2024); https://doi.org/10.4060/cd0683en.
10. M. Perraudeau, *Mar. Policy* **163**, 106145 (2024).

10.1126/science.ady3495

Tariffs imperil US–Canada precision agriculture

Precision agriculture encompasses a data-driven suite of sensors, artificial intelligence (AI) analytics, and GPS-guided machinery that reduces fertilizer and pesticide inputs, increases yields, and boosts climate resilience (*1*). These tools deliver substantial environmental benefits by cutting agricultural runoff, economic gains through improved efficiency, and health advantages by reducing chemical exposure. In North America, farmers' access to and ability to afford precision agriculture technology depend on the free movement of its components across the

US–Canada border (*2*). The recent tariffs and retaliatory tariffs have disrupted the flow of goods and raised prices, threatening the expansion of precision agriculture in the US and Canada.

As of 4 June, the Trump administration reinstated a 50% tariff on imported steel (up from 25%) and simultaneously imposed substantial tariffs on printed circuit boards and related technical parts (*3*)—measures known to elevate costs throughout electronics and automation supply chains, including sensors and probe components (*4*). When 25% steel duties were imposed in 2018, the sticker price of new combines and replacement parts—vital components of precision agriculture—jumped by about 6%, and Saskatchewan dealers reported that growers were canceling plans for upgrades (*5*). Variable-rate fertilization systems, which rely on key hardware elements such as steel and printed circuit board components, enable North American farms to reduce nitrogen use by about 15% (*6*, *7*). Rising input costs now place those efficiency gains at risk.

Revenue shocks compound the squeeze. China's 8 March announcement of a 100% tariff on Canadian canola oil and meal—CAD920 million in 2024 exports—slashes the margins farmers rely on to finance next-generation tools (*8*). Every lost dollar or delayed component slows the diffusion of climate-smart technology.

To facilitate access to these tools, policy-makers should exempt precision agriculture hardware, software, and research inputs from any current or future tariff schedules, and future trade deals should include comprehensive exemptions for climate-smart agricultural inputs and technologies. These exemptions for agricultural technology would pay for themselves many times over through avoided fertilizer, water, and greenhouse gas costs (*9*). The US and Canadian governments should establish a bilateral US–Canada innovation fund that protects shared research and open-data protocols from political cycles. Policy-makers should also convert existing safety-net programs into "innovation dividends" that automatically rebate a portion of farmers' purchases of sensors and broadband and autonomous equipment during trade shocks. Keeping ideas, components, and data flowing freely is the surest path to resilient food systems—especially as drought, wildfire smoke, and soaring input prices challenge growers.

Asim Biswas

School of Environmental Sciences, University of Guelph, Guelph, ON, Canada.
Email: biswas@uoguelph.ca

REFERENCES AND NOTES

1. R. Gebbers, V. I. Adamchuk, *Science* **327**, 828 (2010).
2. E. Watson, "From fertilizer to machinery, how might tariffs impact the agtech sector?" *AgFunderNews*, 13 February 2025.
3. Z. Halpern-Shavim, E. Balkos, "U.S.–Canada tariffs: Timeline of key dates and documents," *Blakes*, 1 August 2025.
4. K. Mahajan, "Tariff impact analysis on volumetric soil moisture sensor market" *Market.us Scoop*, 15 April 2025.
5. Capital Steel Industries, "How steel tariffs are affecting farmers" (2025); https://csisteelbuildings.com/resources/local-insights/how-steel-tariffs-are-affecting-farmers?utm_source=chatgpt.com.https://www.blakes.com/insights/us-canada-tariffs-timeline-of-key-dates-and-documents/.
6. R. Grisso, M. Alley, W. Thomason, D. Holshouser, G. T. Roberson, "Precision farming tools: Variable-rate application" (Publication 442-505, Virginia Cooperative Extension, 2011).
7. B. Gu *et al.*, *Nature* **613**, 77 (2023).
8. K. Heppner, "China slaps steep tariffs on Canadian canola oil, meal, peas, pork, and seafood," *Realagriculture*, 7 March 2025.
9. D. J. Mulla, *Biosyst. Eng.* **114**, 358 (2013).

10.1126/science.ady6644

REVIEW SUMMARY

MICROBIOME

Dissecting microbial communities with single-cell transcriptome analysis

Andrew W. Pountain* and Itai Yanai*

Full article and list of author affiliations: https://doi.org/10.1126/science.adp6252

BACKGROUND: Microbes rarely exist as isolated cells but instead form dynamic, interactive communities that play critical roles in human development, metabolism, and immunity. Although investigations of these microbiomes have largely focused on these interactions at the level of species or higher microbial taxa, even cells of a single species can differ substantially in their gene content, physiology, and environment. This intraspecies heterogeneity may lead to functional diversification, whereby cellular subpopulations play different functional roles and influence survival in the face of external threats such as antibiotic stress. Single-cell transcriptomics has transformed our understanding of cellular diversity in mammalian systems, yet microbes are far smaller than mammalian cells and are protected by cell walls. Moreover, bacterial mRNAs are rapidly degraded. Hence, there has been a lack of methods to study global transcriptional diversity in microbial communities, limiting our understanding of these populations at the cellular level.

ADVANCES: Over the past 5 years the emergence of a diverse toolkit for single-cell gene expression now allows profiling in both bacteria and unicellular fungi. State-of-the-art methods that leverage advances in mammalian single-cell RNA sequencing can now analyze millions of microbial cells across multiple species. We describe these methods in terms of their general principles, including droplet-based and combinatorial barcode indexing, as well as the specific modifications required for the profiling of prokaryotes. We also review some of the outstanding challenges of these technologies, particularly the low number of transcripts captured per individual bacterium. In support of single-cell analysis, adaptations of fluorescence in situ hybridization are also able to provide high-resolution maps of gene expression within native microbial communities.

These methods have already yielded insights into the behavior of single-species cultures of microbes in vitro, illuminating drivers of transcriptional heterogeneity, variation in responses to antibiotic treatment, and mobile genetic element activity. Recently, similar methods have also been applied to more challenging communities, such as those colonizing the mammalian gut. These developments have enabled deeper exploration of functional diversification within microbial species, and in turn how host-derived environmental cues shape microbial states.

OUTLOOK: Single-cell transcriptomics are poised to redefine how we understand microbiome function and dynamics. Beyond studying the divisions of labor that support community-level behavior in simple biofilms, these technologies now allow us to explore these interactions across natural, multispecies ecosystems. Phenotypic heterogeneity in stress responses, long studied in pathogens, may be equally critical to how commensal populations withstand and recover from antibiotics or inflammatory disruption. Single-cell resolution also offers valuable insights into mobile genetic elements that shape microbial function but are not strictly bound to specific microbial species, making their distribution and activity extremely hard to resolve at a bulk metagenomic level.

Numerous outstanding challenges remain, particularly the need for experimental pipelines for harvesting, disaggregation, and unbiased sampling across many species, as well as bioinformatic challenges for mapping gene expression variation in undefined communities. There is also a need for further technological development that couples single-cell transcriptomics to other analysis modalities, such as genome sequencing. Nevertheless, single-cell transcriptomics already serves as an essential tool for understanding the population dynamics of these crucial communities. □

*Corresponding author. Email: andrew.w.pountain@uth.tmc.edu (A.W.P.); itai.yanai@nyulangone.org (I.Y.) Cite this article as A. W. Pountain, I. Yanai, Science 389, eadp6252 (2025). DOI: 10.1126/science.adp6252

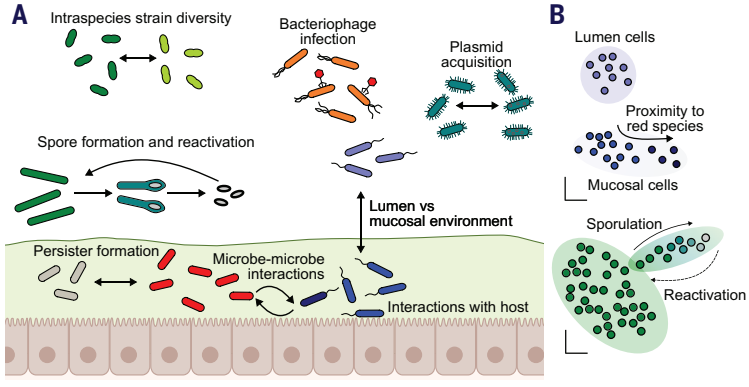

Microbiomes at the cellular level. (**A**) Microbiomes are interactive, multispecies communities, but bulk analysis obscures functional diversification among cells of the same species, arising from environmental and genetic heterogeneity. (**B**) The schematic dimensional reduction plots indicate how subpopulations are identified according to their gene expression profiles. Single-cell transcriptomics can help to reveal functional aspects of this heterogeneity and dissect microbial ecosystems at cellular resolution.

RESEARCH

IN *SCIENCE* JOURNALS

Edited by **Michael Funk**

LAYERED MATERIALS

Role of entropy in 2D and layered materials

As the number of elements in a material increases, the possibility of greater entropic contributions to ordering or disordering also increases. Wyatt *et al*. synthesized 40 MAX materials (where M is a transition metal, A is a group 13 or 14 element, and X is either C or N) using 2 to 9 M elements. They were able to quantify the impact of entropy versus enthalpy on the resulting structure and properties. Enthalpy-driven short-range order persisted until configurational entropy became sufficiently large to randomize metal configurations. Compositional disorder in the precursor phases directly influenced the surface terminations (–O, –OH, and –F) and electronic properties when converted to MXenes. —Marc S. Lavine

Science p. 1054, 10.1126/science.adv4415

Scanning electron microscopy image of a multilayer MXene

IMAGE: DEVYNN LEATHERMAN-MAY, BRIAN C. WYATT, AND BABAK ANASORI, PURDUE UNIVERSITY

APOPTOSIS

What anti-apoptotic proteins do in vivo

Anti-apoptotic proteins such as MCL-1 (myeloid cell leukemia-1) are potential targets for cancer therapeutics, but the full range of functions of these proteins has not been explored in vivo. MCL-1 has effects on metabolism not related to its effects on apoptosis. To evaluate and distinguish these functions, Brinkmann *et al*. replaced MCL-1 genes in mice with genes encoding other BCL-2 family members that are also anti-apoptotic but may not share MCL-1's other functions. MCL-1 was necessary for early embryogenesis, but this function was compensated for by the other anti-apoptotic proteins. However, later in development and after birth, the metabolic actions of MCL-1 were required and were only partially replaced by some other family members. These results may aid in the development of MCL-1 inhibitors as anticancer agents. —L. Bryan Ray

Science p. 1003, 10.1126/science.adw1836

ASTROPHYSICS

Reducing noise at LIGO with machine learning

Gravitational wave detectors have revolutionized astrophysics by detecting black holes and neutron stars. Most signals are captured in the 30- to 2000-Hz range, and the lower 10- to 30-Hz band remains largely unexplored because of persistent low-frequency control noise that limits sensitivity. Enhancing this sensitivity could increase cosmological reach. Using nonlinear optimal control through reinforcement learning with a frequency-domain reward, Buchli *et al*. developed a method that effectively reduces control noise in the low-frequency band. This method was successfully implemented at the Laser Interferometer Gravitational-Wave Observatory (LIGO) in Livingston and the Caltech 40 Meter Prototype, achieving control noise levels on LIGO's most demanding feedback control loop below the quantum noise, thus removing a critical obstacle to increased detector sensitivity. —Yury Suleymanov

Science p. 1012, 10.1126/science.adw1291

NEPHROLOGY

Hormonal influences on the kidneys

Although both men and women can develop chronic kidney disease, women of reproductive age appear to be relatively protected. By studying mice and human kidney tissue and urine samples, Conte *et al*. determined that renal progenitor cells are responsive to female sex hormones, showing increased proliferation and

differentiation into kidney podocytes in response to estrogen and progesterone at physiologically relevant concentrations. The same phenomenon played a key role in pregnancy-induced expansion of the podocyte population to accommodate the increased workload on the kidneys. Conversely, a failure of this adaptation contributed to preeclampsia and increased the risk of long-term kidney impairment in both mothers and offspring in mouse models, consistent with epidemiological data from humans. —Yevgeniya Nusinovich

Science p. 1016, 10.1126/science.adp4629

SEISMOLOGY

Muddy signs of silent fault slip

Earthquakes can trigger silent slip and mud volcanoes, but rarely have the processes been observed together or at long distances. Bayramov *et al*. documented the flare-up of more than 50 mud volcanoes in the West Caspian Kura basin and substantial aseismic slip across seven faults immediately after the 2023 Turkey-Syria earthquakes over 1000 kilometers away. Their findings suggest that seismic waves increased pore pressure in the basin, leading to regional inflation, mud volcano eruption, and reduced effective stress on faults. Faults in fluid-rich basins may thus be susceptible to far-reaching triggering by large earthquakes. —Angela Hessler

Science p. 996, 10.1126/science.adv8438

NANOMATERIALS

Nanodiamonds from activated adamantane

Adamantane can adopt the same tetrahedral carbon skeleton as diamond. Fu *et al*. found that electron-beam irradiation of adamantane crystallites in a transmission electron microscope at low temperatures (296 to 100 K) and under vacuum conditions led to the activation of carbon-hydrogen bonds. These conditions enabled the formation of carbon-carbon bonds to create a diamond lattice. —Phil Szuromi

Science p. 1024, 10.1126/science.adw2025

NEUROSCIENCE

$G\alpha_q$ propels the opioid paradox

Although opioids block nociceptive signaling, their prolonged use paradoxically increases pain sensitivity and promotes analgesic tolerance. These adverse effects involve the activation of *N*-methyl-D-aspartate-type glutamate receptors (NMDARs) and the metabotropic glutamate receptor mGluR5 in sensory neuron terminals in the spinal cord. Jin *et al*. found that treating rodents with morphine increased the coupling of mGluR5 to the G protein $G\alpha_q$, and that $G\alpha_q$ was required for morphine-induced increases in NMDAR activity at sensory neuron synapses in the spinal cord. Inhibition or knockdown of $G\alpha_q$ reduced morphine-induced hyperalgesia and analgesic tolerance. —Annalisa VanHook

Sci. Signal. (2025) 10.1126/scisignal.adu8839

CANCER

Panning for KRAS

KRAS is a frequently mutated oncogene, particularly in pancreatic ductal adenocarcinoma; however, most inhibitors are currently allele specific, so they only target a portion of KRAS-mutant cancers. McAndrews *et al*. sought to overcome this limitation by developing a pan-KRAS inhibitor (panKRASi), BI-2493. The authors showed the efficacy of their inhibitor across many KRAS mutant mouse models and described changes to tumor cells and the tumor immune microenvironment under treatment. These data provide preclinical support for a panKRASi that will be evaluated in a planned phase 1 clinical trial. —Dorothy Hallberg

Sci. Transl. Med. (2025) 10.1126/scitranslmed.adt5511

IN OTHER JOURNALS

Edited by **Corinne Simonti** and **Jesse Smith**

NEUROSCIENCE

Food for thought

Food ingestion in mammals usually starts with biting, followed by chewing and then swallowing. These behaviors are executed by muscles of the jaw and tongue, which are controlled by motor nuclei in the pons, medulla, and cervical spinal cord. However, the circuits for chewing are largely elusive. Sungeelee *et al.* identified Sup5^{Phox2b}, a group of glutamatergic neurons in the supratrigeminal area of the mouse hindbrain marked by the transcription factor *Phox2b*, the activity of which tracks jaw movements associated with lapping, biting, and chewing in the alert animal. Optogenetic perturbation of these excitatory reticular interneurons, whether by stimulation or inhibition, prevented volitional lapping and chewing. These findings provide new insights into the neural circuits underlying complex orofacial motor behaviors. —Peter Stern

Proc. Natl. Acad. Sci. U.S.A. (2025) 10.1073/pnas.2411174122

QUANTUM OPTICS

Routing for single photons

Quantum communication networks require the ability to route single photons into a particular channel. Berroir *et al*. demonstrated a low-power, all-optical method for directing guided single photons into two different channels through either reflection or transmission propagation modes. Their router consisted of silica nanofiber with an array of cesium atoms optically trapped in the evanescent field of the fiber surface. By optically pumping the atoms into an excited state, they were able to switch between two different modes of operation: electromagnetic-induced transmission and atomic Bragg reflection. Single photons entering the router could be directed on demand into either the reflection channel or the transmission channel. The demonstration provides a useful tool for the further development of quantum communication technologies. —Ian S. Osborne

Optica (2025) 10.1364/OPTICA.569736

ADDICTION

Craving astrocytes

Understanding the mechanisms mediating craving during abstinence could help in the identification of therapies for substance use disorders. Testen *et al.* showed that in rats, abstinence from cocaine administration in addicted animals resulted in pruning of astrocytes through microglia phagocytosis. This was found to occur in the nucleus accumbens, one of the main brain areas associated with the development of substance use disorders. Reducing microglia phagocytosis decreased cocaine-seeking behavior during abstinence, suggesting that this pruning process contributes to cocaine craving. —Mattia Maroso

Cell Rep. (2025) 10.1016/j.celrep.2025.116137

STEM EDUCATION

The physics of inclusive teaching

Within efforts to diversify education, there is a push to implement inclusive teaching practices. To understand the extent to which undergraduate-level physics instructors implement

GENETIC RESCUE

Saving the Florida panther

In 1995, eight panthers (*Puma concolor coryi*) from Texas were brought to Florida to genetically rescue the population there, which numbered fewer than 30 individuals at the time. To determine how this translocation affected the population, Aguilar-Gómez *et al.* sequenced 29 genomes from modern Florida panthers and compared them with previously published samples from North and South America. They found that the introduction of the Texas individuals increased heterozygosity across the genome and reduced homozygous deleterious variants, but also did not seem to be overrepresented in the genome. This suggests that this introduction has had overall positive effects on the Florida panther population without causing excessive loss of local ancestry.
—Corinne Simonti

Proc. Natl. Acad. Sci. U.S.A. (2025)
10.1073/pnas.2410945122

A genetic rescue attempt of the critically endangered Florida panther appears to be having a positive effect.

PHOTO: JOEL SARTORE/PHOTO ARK VIA MINDEN PICTURES

these practices, Rabby and Henderson conducted semi-structured interviews with 11 male introductory physics instructors focused on their use of and beliefs about them. Results show that instructors in the study: 1) do not make use of the full range of inclusive teaching practices, 2) do not implement them as much as they think they do, and 3) are not interested in using additional ones. These results suggest that significant work is needed to help introductory physics instructors understand, value, and implement the full range of inclusive teaching practices.
—Melissa McCartney

Phys. Rev. Phys. Educ. Res. (2025)
10.1103/96y2-cyf2

PREGNANCY

Alcohol affects family planning

Women who heavily consume alcohol or smoke cannabis daily usually do not desire to become pregnant soon. However, alcohol or drug use are both known to impair judgment and may increase unwanted pregnancies. To test whether these groups face similar pregnancy risks, Raifman *et al.* followed 2015 nonpregnant women ages 15 to 34 for more than a year. Among women who strongly desired to avoid pregnancy, heavy alcohol use, but not cannabis or other drug use, was associated with increased pregnancies. The study did not identify why alcohol was more likely to compromise reproductive autonomy than cannabis or other drugs. However, these results have policy implications because alcohol causes relatively more fetal harm than cannabis. —Ekeoma Uzogara

Addiction (2025)
10.1111/add.70135

ELECTROCATALYSTS

Disorder improves electrode performance

Solid oxide electrolysis cells (SOECs) offer promise in mitigating global warming by converting carbon dioxide into carbon monoxide. However, the poor catalytic efficiency of the anodic oxygen evolution reaction (OER) significantly limits device performance. Yu *et al.* investigated the double perovskite oxide $PrBaCo_2O_{5+\delta}$, a common SOEC anode, with varying degrees of cation ordering. Through comprehensive experimental characterization and theoretical calculations, the authors demonstrated that increasing A-site disorder, as achieved by increasing Pr content, enhanced oxygen exchange rates. As a result, SOECs incorporating the newly developed disordered $Pr_{1.5}Ba_{0.5}Co_2O_{5+\delta}$ exhibited reduced resistance and excellent OER performance.
—Jack Huang

J. Am. Chem. Soc. (2025)
10.1021/jacs.5c09331

RESEARCH ARTICLE SUMMARY

CANCER

Divergent FOXA1 mutations drive prostate tumorigenesis and therapy-resistant cellular plasticity

Sanjana Eyunni *et al.*

Full article and list of author affiliations:
https://doi.org/10.1126/science.adv2367

INTRODUCTION: Prostate cancer (PCa) is a transcription factor–driven malignancy in which androgen receptor (AR) signaling plays a central role in promoting cancer cell proliferation. Androgen deprivation therapy (ADT), which inhibits AR signaling, remains the cornerstone of initial treatment. However, while ADT is initially effective, most patients ultimately develop resistance, progressing to incurable castration-resistant prostate cancer (CRPC) wherein AR activity is aberrantly restored. Oncogenic activity of AR is critically enabled by chromatin-binding regulatory proteins, among which the pioneer transcription factor FOXA1 is particularly important. FOXA1 facilitates AR's access to DNA by decompacting chromatin, thereby shaping the downstream gene expression programs. Importantly, FOXA1 is mutated in approximately 10% of primary prostate cancers in Caucasian men and over 40% of primary PCa's in the Asian population. In metastatic CRPC, FOXA1 is altered in more than 35% of cases. This positions FOXA1 as a key oncogene in PCa development.

RATIONALE: Despite the high clinical incidence of FOXA1 alterations, the molecular mechanisms underlying FOXA1-driven tumorigenesis remain unexplored in vivo. In this study, we developed and characterized genetically engineered mice with targeted knock-in of human cancer-associated FOXA1 Class 1 (i.e., Wing 2 alteration) and Class 2 (i.e., C-terminal truncation) mutant transgenes.

RESULTS: Through longitudinal histopathological evaluation, in situ immunofluorescence staining, and integrative multiomics profiling of Class 1 and Class 2 FOXA1-mutant mouse prostate tissues and derivative organoids, we uncovered mutation-specific phenotypes and oncogenic mechanisms: Truncal FOXA1 Class 1 mutations in a p53-null background triggered high-grade adenocarcinoma mimicking human disease, characterized by abnormal induction of NSD2 expression, extensive AR reprogramming to chimeric AR-half neo-enhancers, and sensitivity to androgen deprivation therapies. By contrast, the acquired FOXA1 Class 2 mutations did not drive transformation. Instead, they induced cellular reprogramming within the prostate epithelium in androgen-replete normal tissues, wherein differentiated cells acquire stemlike attributes and express markers such as TROP2, CK4, and PSCA. Notably, Class 2-mutant epithelial cells survive and continue to proliferate despite androgen withdrawal, with decompaction of the cis-regulatory circuitries of the KLF5 and AP-1 transcription factors.

CONCLUSION: Our findings establish FOXA1 mutation classes as drivers of divergent PCa clinical trajectories through distinct chromatin and transcriptional reprogramming mechanisms, with Class 1 mutations initiating prostate carcinogenesis and Class 2 mutations promoting adaptive therapy resistance in advanced stages. Furthermore, our transgenic mice provide critical preclinical models for evaluating emerging FOXA1-targeted therapies. □

Corresponding author: Arul M. Chinnaiyan (arul@med.umich.edu), Abhijit Parolia (aparolia@med.umich.edu). Cite this article as S. Eyunni *et al.*, *Science* **389**, eadv2367 (2025). DOI:10.1126/science.adv2367

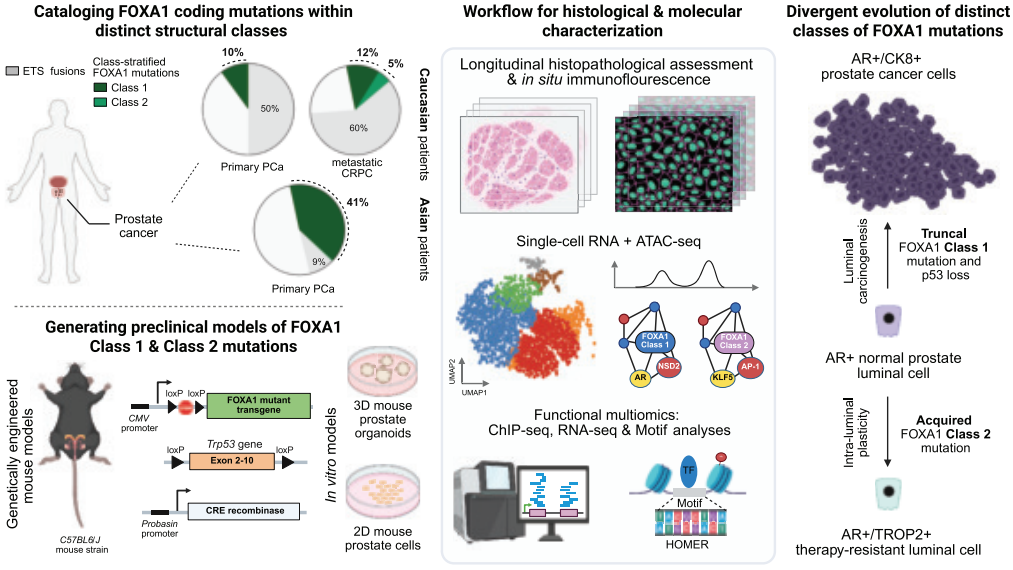

Histopathological and multiomic characterization of transgenic mice with distinct FOXA1 mutations reveals class-specific driver roles in divergent prostate cancer trajectories. Recurrence of FOXA1 alterations in prostate cancer among Caucasian and Asian men (top left). Transgenic mice and organoid models used in this study (bottom left). Methodologies and experimental workflow (middle). FOXA1 Class 1 mutations trigger prostate carcinogenesis while Class 2 mutations drive therapy-resistant intraluminal plasticity—revealing two faces of the FOXA1 oncogene (right). PCa, prostate cancer; mCRPC, metastatic prostate cancer; AR, androgen receptor; CK8, cytokeratin-8. [Figure created with BioRender.com]

RESEARCH ARTICLE SUMMARY

CELL BIOLOGY

Epithelial tension controls intestinal cell extrusion

Daniel Krueger*†, Willem Kasper Spoelstra†, Dirk Jan Mastebroek, Rutger N. U. Kok, Shanie Wu, Mike Nikolaev, Marie Bannier-Hélaouët, Nikolche Gjorevski, Matthias Lutolf, Johan van Es, Jeroen van Zon*, Sander J. Tans*, Hans Clevers*

Full article and list of author affiliations: https://doi.org/10.1126/science.adr8753

INTRODUCTION: The intestinal epithelium is a protective barrier between the body and the luminal gut content. Disruption of this barrier is a hallmark of diseases such as inflammatory bowel disease and tufting enteropathy. To preserve tissue homeostasis, the epithelium undergoes self-renewal, during which new cells are born continuously and older cells are removed through extrusion. A commonly proposed model suggests that proliferation-induced crowding triggers extrusion at the villus tip. This model, although conceptually attractive, remains untested owing to the challenges of studying mechanical forces and cellular dynamics within the intestine's complex architecture. Identifying cues that govern extrusion is essential for understanding how the intestine maintains homeostasis and how extrusion fails in disease.

RATIONALE: We hypothesized that intestinal cell extrusion is regulated by intercellular force transmission arising from crowding or other mechanical interactions. To test this, we used intestinal organoids that recapitulate key features of the native tissue while enabling real-time manipulation and observation from multicellular to subcellular levels. Our strategy combined long-term live imaging with automated cell tracking such that we could follow extrusion events in space and time. To mimic in vivo tissue topology, organoids were cultured on three-dimensionally shaped hydrogels. CRISPR-engineered fluorescent tagging and optogenetic control of myosin II enabled both visualization and induction of contractility, and laser ablation provided acute mechanical perturbations. Key findings were validated in mouse intestinal tissue. This multiscale approach allowed us to dissect the spatiotemporal force dynamics that govern extrusion.

RESULTS: We found that cells extrude from regions of the intestinal villus that are under tension. This tension is generated by a dynamically contracting actomyosin network at the cell base and reveals the "tug-of-war" behavior of cells. Optogenetic activation of contractility and mosaic organoids consisting of cells with different levels of contractility showed that highly contractile cells can drive extrusion of less-contractile neighbors. Reducing a cell's contractility genetically or disrupting its basal cortex by laser ablation also prompted extrusion, showing that the abrupt loss of the ability to generate tension triggers cell extrusion. Extrusion involved myosin II up-regulation in the extruding cell and its neighbors, reflecting a coordination at the tissue level. Lastly, in a model of congenital tufting enteropathy—caused by epithelial cell adhesion molecule (Epcam) loss and associated with hyperactive myosin II—we observed excessive contractility, which disrupted tissue architecture, increased extrusion rates, and in mosaics led to the myosin-dependent preferential elimination of less-contractile wild-type cells.

CONCLUSION: Our results support a tension-based model for the regulation of cell extrusion in the intestine. A dynamic and contractile actomyosin network generates tissue-scale tension, and cells that fail to produce sufficient force to counteract pulling by their neighbors are preferentially removed. This tug-of-war mechanism maintains mechanical integrity by eliminating the tissue's weakest links. Our findings reframe intestinal homeostasis as an active, force-regulated process. They also show how differences in contractility, such as those observed in congenital tufting enteropathy, can lead to abnormal extrusion and disrupted epithelial structure. These insights suggest that targeting force-generating pathways may provide potential therapeutic strategies for diseases in which epithelial barrier function is compromised. □

*Corresponding author. Email: h.clevers@hubrecht.eu (H.C.); s.tans@amolf.nl; (S.J.T.); j.v.zon@amolf.nl (J.V.Z.); d.krueger@hubrecht.eu (D.K.) †These authors contributed equally to this work. Cite this article as D. Krueger *et al.*, *Science* **389**, eadr8753 (2025). DOI:10.1126/science.adr8753

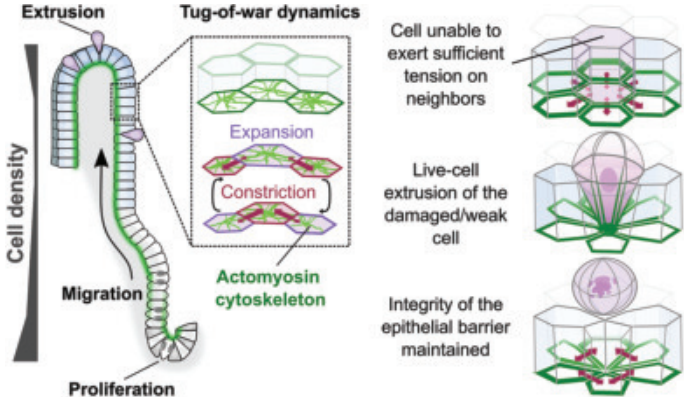

Tug-of-war–like competition between intestinal epithelial cells regulates cell extrusion. Cells in the intestinal epithelium proliferate in the crypt, migrate up the villus, and typically extrude near the villus tip. In the villus, cells exert highly dynamic tension forces on their neighbors. Mechanically compromised cells that cannot exert sufficient tension extrude in order to maintain the integrity of the intestinal epithelial barrier.

RESEARCH ARTICLE SUMMARY

PLANT PATHOLOGY

Systematic discovery and engineering of synthetic immune receptors in plants

Bruno Pok Man Ngou, Michele Wyler†, Marc W. Schmid†, Takehiro Suzuki, Markus Albert, Naoshi Dohmae, Yasuhiro Kadota*, Ken Shirasu*

Full article and list of author affiliations: https://doi.org/10.1126/science.adx2508

INTRODUCTION: Plants, like most organisms, sense external stimuli through cell surface–localized receptors composed of an ectodomain, transmembrane domain, and cytosolic domain. Environmental cues are typically detected by the ectodomain, triggering activation of the cytosolic domain and downstream signaling. Pathogen-associated molecules are recognized by a class of receptors known as pattern recognition receptors (PRRs), which initiate defense responses against pathogens and pests. Among these, leucine-rich repeat receptor-like kinases (LRR-RLKs) form one of the largest PRR families in plants.

RATIONALE: LRR-RLKs have diversified in a lineage-specific manner throughout land plant evolution. These lineage-specific PRRs can be transferred across crop species to confer broad-spectrum resistance against pathogens. Although genetic tools facilitate the identification of PRRs in model plants, characterizing them in nonmodel species, such as trees and perennial crops, remains challenging. This study aimed to map the pathogen recognition landscape of LRR-RLKs and identify uncharacterized PRRs that can be engineered to enhance disease resistance in crop species.

RESULTS: To characterize subgroup XII of LRR-RLKs (LRR-RLK-XIIs), 13,185 receptors from 285 angiosperm genomes were clustered on the basis of conserved residues in their LRR ectodomains, yielding 210 subgroups, which represent 31.7% of all identified receptors. To identify those responsive to pathogens, we expressed chimeric receptors in *Nicotiana benthamiana*, each comprising a subgroup-specific LRR ectodomain fused to the cytosolic kinase domain of a brassinosteroid receptor, enabling specific detection of PRR activation in response to pathogens. Of the 210 chimeras screened, seven were activated by *Agrobacterium*, including receptor 181 from *Citrus maxima* (pomelo), which responded to multiple bacterial species. Biochemical analysis revealed that receptor 181 recognizes cold shock proteins (CSPs), specifically the conserved peptide csp15, and was designated SCORE (selective cold shock protein receptor). SCORE differs in ligand recognition specificity from the previously characterized CSP receptor CORE. In addition, SCORE and its orthologs—primarily found in Sapindales, Malvids, and Magnoliids—exhibit diverse specificity toward csp15 variants owing to sequence polymorphisms. Protein structure predictions and domain swapping experiments identified the 10th LRR motif in SCORE as key to csp15 recognition specificity, with three variable residues modulating specificity through surface charge interactions. Guided by these insights, we engineered synthetic SCORE variants to detect CSPs from a broader range of pathogens. Several variants gained responsiveness to *Ralstonia*, *Xanthomonas*, *Candidatus Liberibacter asiaticus* (causative pathogen for citrus greening disease), and root-knot nematodes, which cannot be detected by the wild-type (WT) SCORE.

CONCLUSION: This study demonstrates a scalable approach to identifying functional immune receptors across plant lineages by integrating bioinformatics, synthetic biology, and biochemical approaches. We characterized SCORE, a receptor that evolved independently from CORE to detect CSPs and exhibits natural variation in ligand specificity. Structural insights enabled the engineering of synthetic SCORE variants capable of recognizing previously undetectable pathogens. These findings highlight the evolutionary and functional diversity of PRRs and offer a promising strategy for developing disease-resistant crops, particularly in nonmodel and perennial species, for which conventional genetic approaches remain limited. Future work may expand this platform to systematically mine and reprogram PRRs for broad-spectrum resistance across diverse crops. □

*Corresponding author. Email: yasuhiro.kadota@riken.jp (Y.K.); ken.shirasu@riken.jp (K.S.)
†These authors contributed equally to this work. **Cite this article as B. P. M. Ngou *et al.*, *Science* 389, eadx2508 (2025). DOI: 10.1126/science.adx2508**

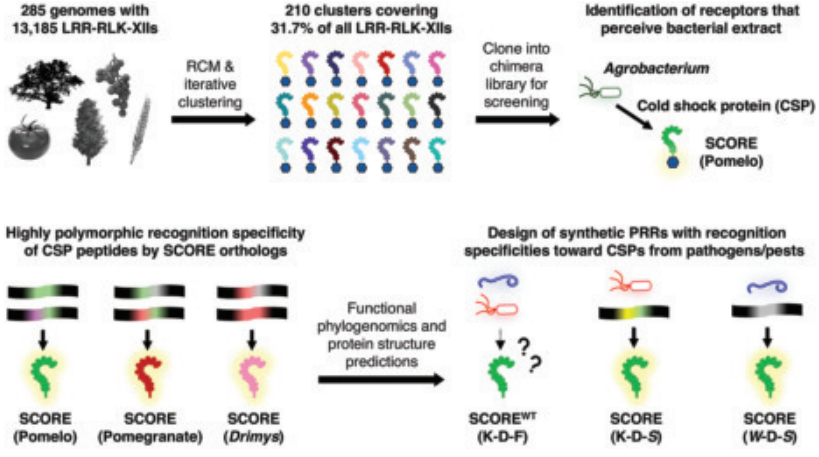

Pipeline for systematic discovery and engineering of plant immune receptors. A total of 13,185 LRR-RLK-XIIs were clustered into 210 subgroups. These receptors were expressed as chimeras and screened for *Agrobacterium*-induced activation. SCORE was identified as a cold shock protein (CSP) receptor, with orthologs showing polymorphic recognition of the conserved CSP peptide. Guided by structural and phylogenomic insights, we engineered SCORE variants to detect diverse crop pathogens and pests. RCM, repeat conservation mapping; WT, wild type.

RESEARCH ARTICLE SUMMARY

NEUROSCIENCE

Cooperative actions of interneuron families support the hippocampal spatial code

Manuel Valero*†, Pablo Abad-Perez†, Andrea Gallardo, Marta Picco, Raquel García-Hernandez, Jorge Brotons, Anel Martínez-Félix, Robert Machold, Bernardo Rudy, György Buzsáki*

Full article and list of author affiliations: https://doi.org/10.1126/science.adv5638

INTRODUCTION: The dynamic interactions between the hippocampus and its partner structures create a cognitive map that enables flexible spatial and mental navigation. Single pyramidal cells contribute to this map with their place fields. Most physiological studies assume that the recurrent excitatory system of the CA3 region or the entorhinal grid system generates place fields. In turn, flexibility and remapping are induced by plastic changes in excitatory synapses. An alternative consideration of this flexibility is the contribution of diverse inhibitory microcircuits that shape the place field properties of pyramidal neurons. The multiple interactions among the large diversity of genetically defined interneuron families and their joint effect on the pyramidal neuron can, in principle, regulate the various place field features. Testing this hypothesis requires the simultaneous recording of members from various interneuron families in behaving animals.

RATIONALE: Current optogenetic and pharmacogenetic methods typically enable the identification and manipulation of only one or, occasionally, two families in a given experiment. Our first goal was to characterize and validate the interneuron family divisions by demonstrating reliable physiological boundaries among them, using optogenetic identification of the four major interneuron families in individual mice. In turn, these physiological fingerprints allowed us to recognize members of these families in large-scale, unlabeled populations. Thus, we could examine the nature of interactions among them and their relationship to the firing of pyramidal cells in the same experiment. Optogenetic perturbation of the interneuron families, in turn, provided further support for their role in circuit control and their ability to shape the place field features of their target principal cells.

RESULTS: We combined multiple-shank silicon probe recordings with optogenetic identification of neurons expressing channelrhodopsin-2 (ChR2) in the four major interneuron families (*Pvalb*, *Sst*, *Vip*, and *Id2* neurons) and pyramidal cells expressing calcium- and calmodulin-dependent protein kinase II alpha (*CaMK2α*) in the hippocampus and neocortex. The physiological features of opto-tagged neurons collected during spontaneous behaviors in the home cage were used to train a machine learning classifier. The high accuracy of physiology-based interneuron classification (>89%) enabled the identification of members of interneuron families in large-scale recording experiments and the study of their interactions. The fractions of the predicted families in unlabeled populations showed a strong correlation with gene expression–based fractions. The identified differentiating physiological features are communicable across different experiments and laboratories. Spiking activity of the members of the four interneuron families showed distinctive correlations with place field features, such as stability, selectivity, generalization, and mutual information between firing rates and the animal's position. Our family-specific perturbation experiments validated these correlational results. Optogenetic activation of *Pvalb* neurons predominantly suppressed the first half of the place fields of pyramidal cells, whereas *Sst* and *Id2* activation suppressed place field spiking in the second half, demonstrating time-division control of pyramidal cells.

CONCLUSION: We demonstrate the reliability of physiological fingerprinting with genetically defined interneuron families. Our findings reveal a fundamental role for the cooperative function of interneuron families in the emergence of the hippocampal cognitive map. Because our physiological fingerprinting strategy is paradigm independent, it is also generalizable to nonspatial functions of the hippocampus and other brain regions. □

*Corresponding author. Email: valegarman@gmail.com (M.V.); gyorgy.buzsaki@nyulangone.org (G.B.) †These authors contributed equally to this work. **Cite this article as** M. Valero *et al.*, *Science* **389**, eadv5638 (2025). DOI: 10.1126/science.adv5638

Interneuron diversity shapes place field features of the hippocampal cognitive map. Gene expression clusters neocortical and hippocampal neurons into five families: *Pvalb*, *Sst*, *Id2*, *Vip*, and *CaMK2α*. We recorded opto-tagged neurons and trained a classifier using physiological properties across families. By combining targeted manipulation with large-scale recordings and neuron classification, we show that interneuron families differentially shape the spatial coding features of pyramidal neurons.

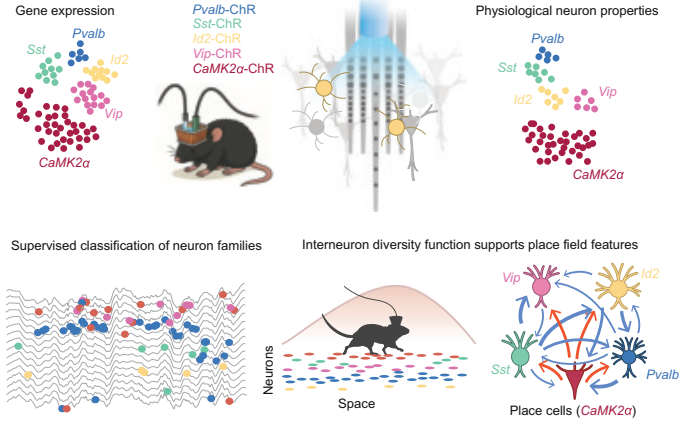

RESEARCH ARTICLE SUMMARY

NEURODEGENERATION

Lewy body dementia promotion by air pollutants

Xiaodi Zhang†, Haiqing Liu†, Xiao Wu†, Longgang Jia†, *et al.*

Full article and list of author affiliations: https://doi.org/10.1126/science.adu4132

INTRODUCTION: Lewy body dementia (LBD), comprising dementia with Lewy bodies (DLB) and Parkinson's disease (PD) with dementia (PDD), is a devastating and increasingly prevalent neurodegenerative disorder. Ambient $PM_{2.5}$ is a recognized broad dementia risk factor; however, its specific role in initiating LBD, particularly its distinct pathological trajectory versus PD without dementia, remains unaddressed. This study systematically investigates this link.

RATIONALE: Pathologic α-synuclein (αSyn) is the defining neuropathological hallmark of LBD. A leading hypothesis posits that environmental neurotoxins, such as fine particulate matter ($PM_{2.5}$), could trigger initial αSyn misfolding and propagation into the brain. However, epidemiological relationships between $PM_{2.5}$ exposure and LBD versus PD subtypes lacked large-scale substantiation. Whether $PM_{2.5}$ can induce αSyn to form pathogenic strains that drive LBD's specific clinical and pathological signatures remains unclear. Elucidating this environmental-molecular nexus is key to unravelling LBD pathogenesis and identifying targeted interventions. Our study aimed to dissect these fundamental mechanisms.

RESULTS: Convergent, multimodal evidence from large-scale human epidemiology, molecular, cellular, animal, and patient studies demonstrated a robust $PM_{2.5}$-LBD link.

First, analysis of >56 million US Medicare beneficiaries revealed that chronic $PM_{2.5}$ exposure was significantly associated with first hospitalizations for α-synucleinopathies. A key finding was that the link between $PM_{2.5}$ exposure and hospitalization risk was stronger for LBD (PDD and DLB) patients than for those with PD without dementia, implying a preferential vulnerability or pathogenic mechanism in LBD.

Second, we demonstrated an essential role of αSyn in $PM_{2.5}$-related neurological disorders. Chronic $PM_{2.5}$ exposure in wild-type (WT) mice induced brain atrophy, cognitive deficits, and widespread αSyn pathology in the brain and peripheral organs (gut, lungs) as well as concomitant tau pathology. Genetic ablation of αSyn conferred strong protection against these $PM_{2.5}$-induced detrimental effects, clearly establishing αSyn as an important mediator of this environmental neurotoxicity.

Third, we found that $PM_{2.5}$ from diverse global sources (US, China, and Europe) induced conformational change in αSyn preformed fibrils (PFFs), inducing a distinct αSyn strain (PM-PFF). PM-PFF remained stable across passages and, compared with PFF, exhibited LBD-like pathogenic features, including accelerated aggregation, degradation resistance, enhanced propagation, and increased neurotoxicity, mimicking αSyn strains found in LBD. When inoculated into humanized αSyn mice, this PM-PFF strain preferentially induced cognitive impairments, contrasting with the primarily motor deficits induced by PFF. Consistently, brain transcriptomic analyses revealed that both chronic $PM_{2.5}$ exposure and PM-PFF inoculation in humanized αSyn mice elicited gene expression signatures that mirrored those of LBD (PDD and DLB) but not those of PD without dementia, underscoring an LBD-specific pathogenic axis.

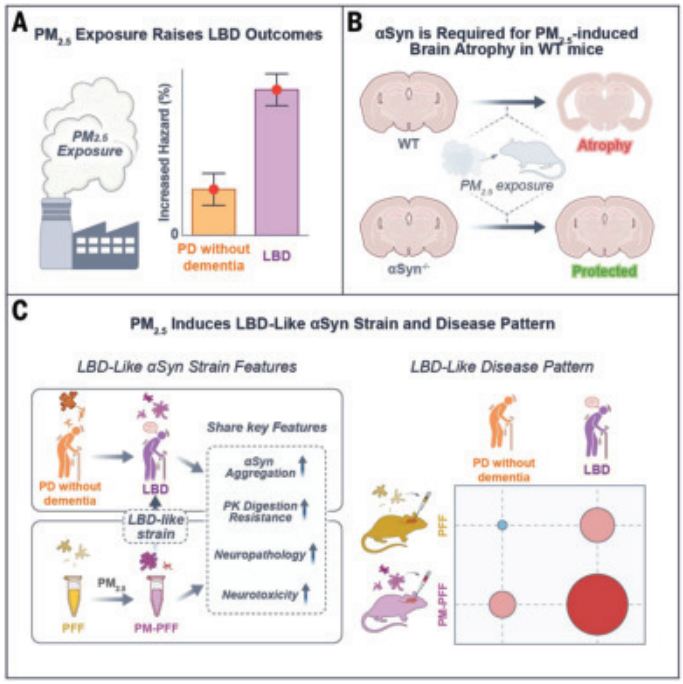

$PM_{2.5}$ promotes LBD by inducing a distinct αSyn strain. (**A**) $PM_{2.5}$ exposure is associated with a higher relative risk of LBD compared to PD without dementia. (**B**) Chronic $PM_{2.5}$ exposure leads to brain atrophy in WT mice, an effect abolished in αSyn-knockout ($\alpha Syn^{-/-}$) mice. (**C**) Mechanistically, $PM_{2.5}$ triggers an LBD-like αSyn strain and elicits a corresponding transcriptomic profile characteristic of LBD pathology.

CONCLUSION: This study provides evidence linking $PM_{2.5}$ exposure to LBD. The neurotoxic effects of $PM_{2.5}$ appear to be mediated by αSyn, with exposure generating a pathogenic strain (PM-PFF) that shares key properties with αSyn strains in human LBD. In mice, this strain induced cognitive deficits and transcriptomic changes resembling those in LBD patients, distinct from those in PD without dementia. These findings identify an environmental mechanism contributing to LBD pathogenesis and underscores the role of αSyn. The $PM_{2.5}$-induced strain represents a potential target for therapeutic intervention. Collectively, these results emphasize the importance of further research into air pollution's role in neurodegenerative diseases and its implications for public health strategies. □

Corresponding author: Xiaobo Mao (xmao4@jhmi.edu); Shizhong Han (shizhong.han@libd.org); Ted M. Dawson (tdawson@jhmi.edu); Xiao Wu (xw2892@cumc.columbia.edu)
†These authors contributed equally to this work. **Cite this article as X. Zhang *et al.*, *Science* 389, eadu4132 (2025). DOI: 10.1126/science.adu4132**

SEISMOLOGY

Very-long-range dynamic triggering of mud volcano unrest and silent magnitude-6 fault slip

Zaur Bayramov[1,2]†, Renier Viltres[1]†, Cécile Doubre[1]*†, Alessia Maggi[1]†, Romain Jolivet[3,4], Luis Rivera[1]

Seismic waves from large earthquakes are known to trigger slip on distant faults, but the underlying mechanisms remain unclear. Using interferometric synthetic aperture radar and local geodetic and seismic data, we show that the 1000-kilometer-distant, February 2023 Kahramanmaraş earthquakes in southeastern Türkiye triggered deformation and/or eruption at 56 mud volcanoes and centimeter-scale aseismic slip on seven faults over tens of kilometers within the fluid-rich Kura Basin in the West Caspian region. This transient deformation event, with an equivalent moment magnitude of 6.1, was coupled with local inflation below major hydrocarbon fields. We postulate that seismic waves led to a change in pore pressure at depth, which in turn triggered aseismic slip along several crustal faults crossing the basin and its surroundings.

The mechanism by which an initial seismic shock triggers subsequent earthquakes or seismic sequences remains a critical question in seismology. Large distant earthquakes have been found capable of affecting the seismic behavior of tectonic or hydrothermal and/or volcanic structures located several hundred kilometers away, either changing their seismic rate or producing low-amplitude seismic events (*1*, *2*). The role of crustal fluids is often invoked to explain the triggering of seismic activity and slip on distant faults, through changes in pore fluid pressure in the medium or frictional conditions along the fault plane itself, possibly mediated by the passage of appropriately polarized surface waves (*3*, *4*). However, very-long-range activation of slip on faults is not systematic, and the conditions for such triggering must be investigated.

The two destructive Pazarcık and Elbistan earthquakes of moment magnitudes (M_w) 7.8 and 7.6, respectively (hereafter called the Kahramanmaraş earthquakes), that occurred in southeastern Türkiye on 6 February 2023 remotely triggered a M_w 5.1 earthquake on the North-Anatolian fault (*5*) and repeating seismic sequences, including tremors along the Dead Sea fault (*6*) and in the western Caucasus region (*7*). In this work, we report on another consequence of the Kahramanmaraş earthquakes: the eruption and deformation of more than 50 mud volcanoes and a large-scale transient aseismic slip event on a network of strike-slip faults in and near the fluid-rich eastern Kura Basin, west of the Caspian Sea (Fig. 1).

The Kura Basin, the largest foreland basin located between the Greater and Lesser Caucasus ranges, has accommodated most of the 13 mm/year convergence between the Arabian and Eurasian plates since 5 million years ago (Ma) (*8*). Convergence-induced shortening within the Kura Basin is primarily accommodated through the development of folds and thrusts (referred to as the Kura fold-thrust belt) along the northern margin of the basin, parallel to the range front of the Greater Caucasus. Total expected deformation rates across the Kura Basin reach about 1 cm/year per 100 km (100 nanostrain/year) of transpressive motion (*8*).

The Kura fold-thrust belt and the Main Caucasus Thrust have produced historical moderate-to-large earthquakes (*9*) and show paleoseismic evidence indicating potential for a M_w >7.7 future event (*10*). Well-known historical earthquakes in the region include a sequence of magnitude 6 (*M* 6) to *M* 7 earthquakes during the past 1000 years near Shamakhi, at the junction of the West Caspian Fault (WCF) and the Greater Caucasus (Fig. 1), which prompted the transfer of the regional capital from Shamakhi to Baku (*10*). Neither the WCF nor its subparallel faults in the eastern Kura Basin, however, have been associated with large historical earthquakes or with frequent seismicity in instrumental catalogs (fig. S1), suggestive of aseismic behavior. Furthermore, little is known about the geometry of the WCF at depth, particularly its dip, because of inconsistent geodetic observations (*8*), the lack of earthquakes and hence of earthquake focal mechanisms, and the generally limited availability of geophysical data.

Regional compressive tectonics and hydrocarbon-rich crust have led to the formation of more than 400 buried, extinct, dormant, or active mud volcanoes across the West Caspian region (*11*, *12*). A mud volcano typically exhibits an edifice that is tens to hundreds of meters high and a few kilometers wide, built from multiple mud eruptions. These eruptions, which can be either explosive or effusive, involve water, oil, and large volumes of gas originating from the deep hydrocarbon systems traveling through fault zones in the overlying sediments (*11*, *13*). Such migration is driven by overpressure from rapid sedimentation and compaction, tectonic compression, and degassing and expansion of dissolved methane in the mud (*14*).

In the eastern Kura Basin, mud volcanoes are predominantly found at the eastern termination of compressive structures of the Greater Caucasus and along the strike-slip WCF system (Fig. 1). Mud volcanoes are more often associated with compressive structures (*12*, *14*), but strike-slip faulting may also influence their emplacement (*15*–*18*). The source materials for mud volcanoes in the region originate primarily from Oligocene-Miocene shales, known as the Maykop series—the main source rock for hydrocarbons in the West Caspian region. The Maykop series is up to 3-km thick at depths of 7 to 10 km in the South Caspian Basin and 0.2- to 1.2-km thick at depths of 4 to 6 km in the eastern Kura Basin (*19*). Geodetic monitoring of surface deformation indicates that, like magmatic volcanoes, mud volcanoes alternate between quiescent and active periods, the latter mainly driven by pulses of overpressured muddy material ascending from depth (*20*, *21*) and potentially accumulating in shallow mud chambers (*22*).

Moderate-to-large earthquakes have triggered mud volcanoes globally (e.g., an eruption >1000 km from the 2004 Sumatra M_w 9.1 earthquake and a new island formed ~380 km from the 2013 Balochistan M_w 7.7 event) (*23*) and in the West Caspian (e.g., eruptions within 50 km of the 1872 *M* ~5.7 and 1902 *M* ~7.0 Shamakhi earthquakes) (*24*). The largest previously documented mud volcano response in the region involved 14 delayed eruptions within an epicentral distance of 100 km during the year after the 2000 Baku doublet (M_w 6.4 and 6.2) (*24*). In this work, we report immediate unrest at more than 50 mud volcanoes in the region and aseismic slip across seven fault segments (70 to 170 km in length), triggered by the M_w 7.7 and 7.8 Kahramanmaraş earthquakes at a distance of more than 1000 km. This activity represents one of the most distant and spatially extensive dynamic responses documented to date, relative to the magnitude and location of the triggering earthquake. Large regional earthquakes of magnitude larger than 7.0, such as the 2011 Van (eastern Türkiye), the 2017 Sarpol-e Zahab (Iran-Iraq border), or the 2023 Kahramanmaraş events, represent rare but

[1]Institut Terre et Environnement de Strasbourg UMR 7063, Université de Strasbourg, CNRS, Strasbourg, France. [2]Azerbaijan State Oil and Industry University, French-Azerbaijani University, Baku, Azerbaijan. [3]Laboratoire de Géologie, Département de Géosciences, École Normale Supérieure, PSL University, CNRS, UMR 8538, Paris, France. [4]Institut Universitaire de France, Paris, France. ***Corresponding author. Email: cecile.doubre@unistra.fr** †These authors contributed equally to this work.

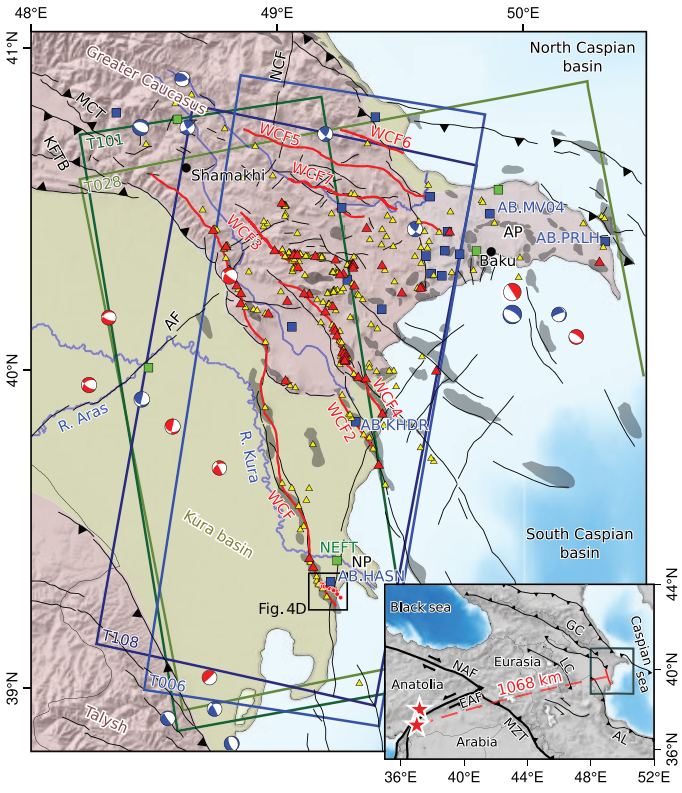

Fig. 1. Tectonic context of the WCF in the Kura Basin. The main tectono-sedimentary features are the Greater Caucasus and Talysh mountain ranges (pink) and Kura Basin (green). Black fault tracks are from (*55*), and red fault tracks are mapped using sharp phase gradients in the four interferograms and the four interferometric coherence maps covering the period under study (4 to 9 February 2023). Colored rectangles are the contours of SAR images used for InSAR processing. Yellow triangles represent mud volcanoes identified in the topography, and red triangles represent mud volcanoes active during the period under study—i.e., with eruptions deduced from interferometric coherence analysis or LOS displacement field analysis. Blue and red focal mechanisms of $M_w \geq 5.0$ earthquakes over the period of 1976 to 2024 with focal depth smaller and higher than 50 km, respectively (*56*). Blue and green squares show seismic and GNSS stations used in this study, respectively. Red dots represent single-station locations of microearthquakes during the period under study. Gray areas represent hydrocarbon fields (*57*). WCF2-to-6, secondary faults identified as activated faults from InSAR results [NB: WCF4 is also called Alat Fault (*18*)]; NCF, North Caspian Fault; AP, Absheron Peninsula; NP, Neftchala Peninsula; KFTB, Kura fold-thrust belt; MCT, Main Caucasus Thrust; AF, Aras Fault. (Inset) Regional tectonic plates and boundaries (NAF, North Anatolian Fault; EAF, East Anatolian Fault; MZT, Main Zagros Thrust). Red stars show the epicentral locations of the two large shocks on 6 February 2023 in Türkiye. LC, Lesser Caucasus; GC, Greater Caucasus; AL, Alborz.

powerful sources of dynamic perturbations in the West Caspian region, an area composed of thick, unconsolidated, and fluid-rich sediments and thus particularly susceptible to dynamic stresses.

Large-scale transient deformation in the West Caspian region

We use synthetic aperture radar (SAR) acquisitions from the Sentinel-1 constellation along two descending and two ascending tracks across the broad West Caspian region (Fig. 1) to produce four line-of-sight (LOS) displacement maps covering the 12-day time span that includes the date of the Kahramanmaraş earthquakes (6 February 2023). We observe sharp displacement gradients (Fig. 2 and fig. S3) along a network of known fault traces, indicative of slip reaching the surface along these structures with differential motion up to 2 cm in the LOS. Deformation maps covering the previous and subsequent 12-day periods do not show substantial deformation (fig. S3).

Mud volcanoes

Between 4 and 9 February 2023, we detected 22 patches of interferometric phase variations and 56 patches of loss of coherence, all associated with mud volcanoes known in the literature (*12*) and/or visible in optical satellite imagery, excluding persistent mud pools or unrelated fluid-filled depressions (Fig. 2E and figs. S6 and S8). Most of the patches are smaller than 0.5 km^2, but those associated with the larger mud volcanoes extend up to 4 km^2 (fig. S6). We ruled out rain or snow as causes of these coherence-loss patches based on data from the ERA5 atmospheric model (*25*) and Sentinel-2 optical imagery, which indicate that there was no snow cover or extreme precipitation during the study period. Furthermore, a comparative analysis of interferometric coherence during extreme wet periods does not show localized losses of coherence, similar to those documented in this work (fig. S9). We confirmed the relationship between loss of interferometric coherence and mud volcano eruptive activity by successfully recovering known eruptions from a field-based catalog (*26*) for the period of 2017 to 2019 (figs. S10 and S11) along with many undocumented events between 2017 and 2023 showing similar coherence-loss patterns (fig. S12). The mud volcanoes showing interferometric phase change also show loss of coherence. Although sector collapses have been previously reported on the mud volcanoes (*27*) and may produce loss of coherence, such collapse would result in asymmetrical phase variations, whereas the phase signals that we observe in this case are predominantly circular. Furthermore, sector collapse is geometrically implausible for the relatively flat plateau volcanoes (fig. S8, A, C, and E) and unlikely for elongated ones given the much lower recorded ground accelerations (~0.008 g at AB.PRLH seismic station; all others <0.001 g) compared with those reported in the literature (0.1 to 0.2 g) (*28*). When phase changes are measurable, they reveal subsidence up to ~17 mm (fig. S7), which suggests that observed interferometric phase and coherence signals on the surface of mud volcanoes are associated with changes of volume and pressure within the feeding system at depth. Therefore, we interpret the local low interferometric coherence as resulting from coating of the surface with newly discharged muddy materials, which modified the backscattering properties of the ground. Even if some of those signals resulted from gravitational collapse, their fluid-driven nature remains valid because such collapses are often linked to fluid escape (*27*). More than 60% of these activated mud volcanoes are located less than 5 km from the activated faults.

Activated faults

We identified seven activated faults in the region of the eruptions (Fig. 1 and fig. S5). In the eastern Kura Basin, we observed surface slip along the ~170-km-long, N160°E-trending WCF and along shorter (<60-km) N140°E-trending faults further east (WCF2, WCF3, and WCF4; Fig. 2A). Between the easternmost part of the Greater Caucasus and the Absheron Peninsula (AP in Fig. 1), we detected weaker signals for surface slip along three ~50-km-long, N120°E-trending faults (WCF5, WCF6, and WCF7; Fig. 2A). Sharp phase offsets (Fig. 2C and fig. S13D) and loss of coherence along the fault lines (fig. S5) confirm that ruptures on these faults reached the surface.

Variable surface offsets can be observed along all activated faults. This is particularly clear for the WCF from ascending and descending tracks (Fig. 2B) and from the N160° and vertical directions after decomposition (see supplementary materials and Fig. 2D). Horizontal offsets average 16 mm and increase up to 43 mm at fault bends, where push-up structures, resulting from long-term finite deformation, are visible in the topography. Activated mud volcanoes also seem to influence the slip distribution (Fig. 2D).

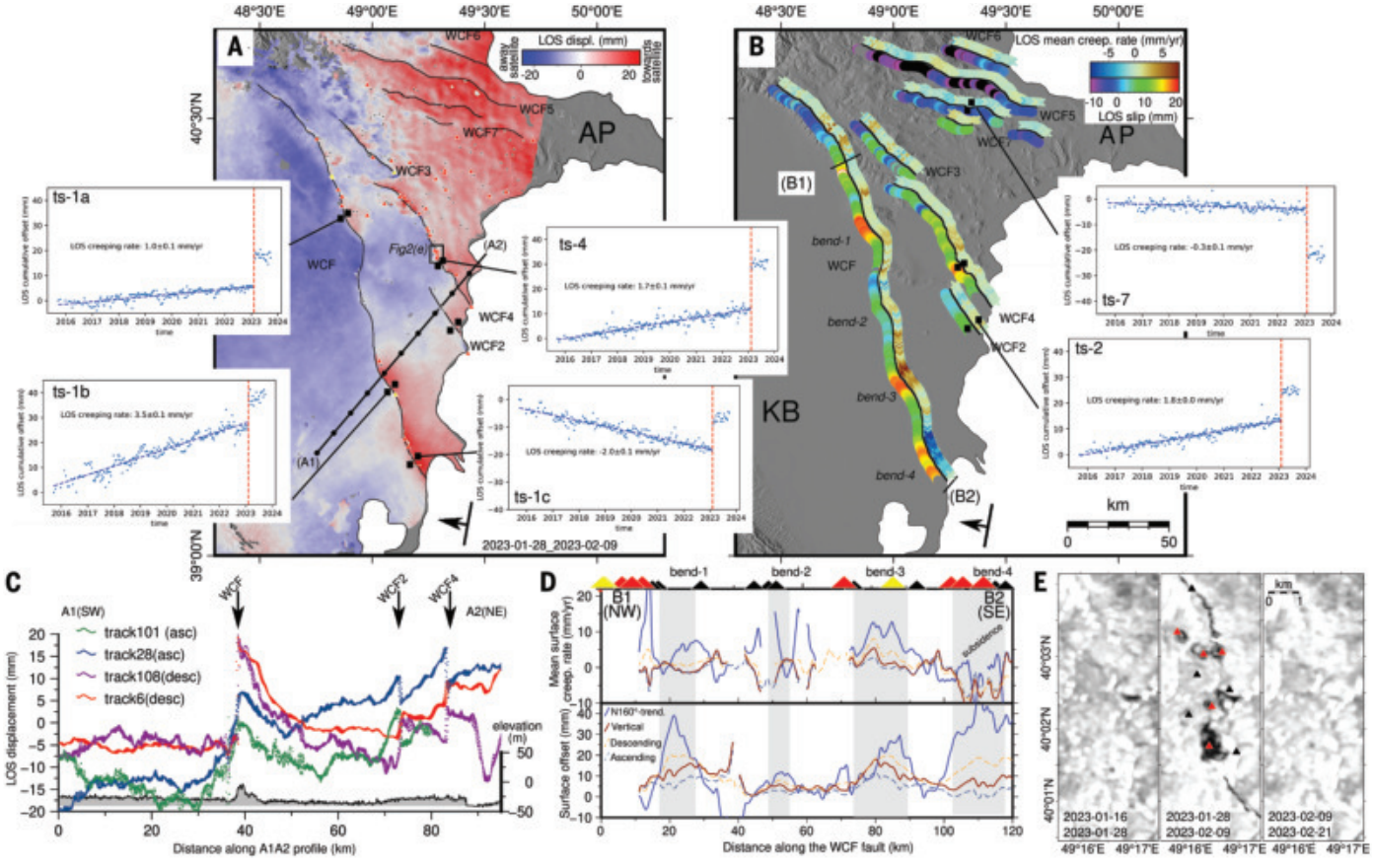

Fig. 2. SAR analysis of LOS fault displacement and mud volcanoes. (**A**) The LOS displacement field from the unwrapped interferogram was computed with SAR images acquired on 28 January 2023 (2023-01-28) and 2023-02-09 along descending track 006. (**B**) South of each fault, the amplitude of LOS offset along the activated faults between 2023-01-28 and 2023-02-09 is shown; north of each fault, the mean LOS creep rate amplitude deduced from the time series analysis resulting from the processing of the SAR images acquired along the track 006 is shown. Six examples of the relative time series of two points across the fault are presented. The relative amplitudes of the LOS offset and mean creeping rate were deduced by subtracting the values on the southern side of the fault from those on the northern side in the coseismic displacement and cumulative LOS velocity fields, respectively. (**C**) Southwest-northeast–trending profile of the LOS displacement fields obtained from the four tracks. (**D**) Variation of surface offsets associated with the 2023 aseismic event (bottom) and surface mean creep rates (top) along the WCF for the period from September 2015 to January 2023. The beginning of the profile is given in (B). Offsets and creep rates along the vertical and N106°E direction result from the decomposition, presented in the supplementary materials. (**E**) Interferometric coherence map for the period before (left; 2023-01-16 to 2023-01-28), coeval with (middle; 2023-01-28 to 2023-02-09), and after (right; 2023-02-09 to 2023-02-21) the Türkiye event. For (A), (D), and (E), the black triangles are the inactive mud volcanoes identified on Google Earth optical images, red triangles are erupted mud volcanoes identified on the interferometric coherence data for the period 2023-01-28 to 2023-02-09, and yellow triangles are deformed mud volcanoes identified on the interferograms for the period 2023-01-28 to 2023-02-09.

Transient slip at depth

Excluding ascending track 101 because of low signal-to-noise ratio, we inverted for the slip distribution at depth along the four faults with the clearest signals (WCF to WCF4). Owing to the lack of geophysical constraints on the geometry of the faults at depth, we assume that the faults are vertical down to 20-km depth with surface traces defined from interferometric synthetic aperture radar (InSAR)–derived deformation and coherence maps. Most of the displacement can be explained by pure right-lateral strike-slip faulting. However, at the southern tip of the WCF, we observed upward ground motion in both ascending and descending tracks, which suggests the presence of localized inflation sources within the hydrocarbon fields near the fault planes (fig. S5B). This fault segment exhibits the largest horizontal surface displacement in both InSAR (Fig. 2A) and global navigation satellite system (GNSS) station (Fig. 3A) estimates, as well as a near-fault microseismicity migration that may suggest fluid presence (Fig. 4).

Most slip is confined to the upper 7 km, except along the northernmost segment of the WCF (Fig. 5). However, fault slip estimations in this area may be affected by long-wavelength atmospheric phase screen residuals potentially responsible for the high slip amplitude (up to 39 mm) at the deepest part of the fault. Excluding this segment, slip reaches maxima of ~38 mm, ~27 mm, ~28 mm, and ~47 mm along WCF, WCF2, WCF3, and WCF4, respectively (see Fig. 5 for locations). The pressure change for the inflation sources in the southernmost segment of the WCF ranges between 5.1 and 9.6 MPa. The seismic moment released during the transient slip episode was equivalent to M_w 6.0, 5.1, 5.2, and 5.6 for WCF, WCF2, WCF3, and WCF4, respectively, resulting in a total seismic moment release equivalent to a M_w 6.1 earthquake.

Capturing the timing of the transient event

No signal equivalent to a M_w 6.1 is observed in the regional or teleseismic seismological data, which suggests that slip is mostly aseismic. We narrowed down the InSAR-based time period for the fault slips, initially estimated between 4 and 9 February 2023 (fig. S2A), by using position time series of several GNSS stations. An offset is visible on four of them

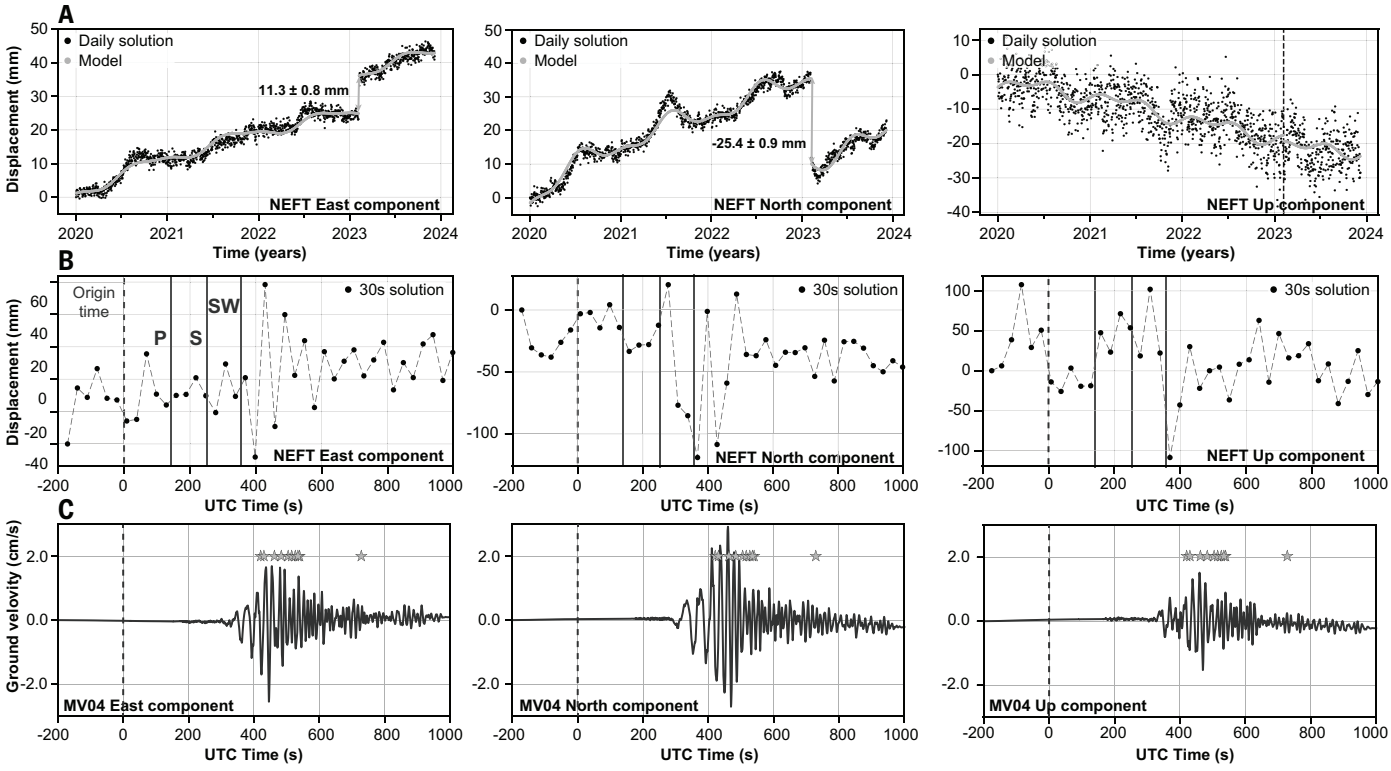

Fig. 3. Timing constraints on the occurrence of slip. (**A**) GNSS position time series using daily solution (2020 to 2024) at the NEFT site (location in Fig. 1). Offset at the time of the first Kahramanmaraş shock is estimated using the Hector software (see supplementary materials). (**B**) Same as (A), using the 30-s solution (see supplementary materials). Origin time of the first Kahramanmaraş shock is indicated as well as the arrival times of the main seismic phases in the region. P, compressional waves; S, shear waves; SW, surface waves. (**C**) Seismic constraints from velocity traces recorded at the MV04 station (location in Fig. 1), located away from the basin and selected to avoid its effects on the recordings. Surface waves from the first Kahramanmaraş shock arrive ~400 to 500 s after the origin time of 01:17:34 on 6 February. Stars indicate the times of small local triggered earthquakes detected at the AB.HASN station in the eastern Kura Basin. UTC, universal time coordinated.

on 6 February 2023 (fig. S25), particularly at the NEFT station (Fig. 3A), located 9 km from the southeastern section of the WCF (Fig. 1), where the total horizontal displacement reaches 28 ± 1 mm (fig. S25). Analysis of the 30-s solution of GNSS time series at site NEFT indicates that the largest part of the transient motion occurred at the arrival time of the surface waves of the first Kahramanmaraş event (Fig. 3, B and C).

We examine continuous records from seismometers placed close to the activated faults to identify any related microearthquakes that might further narrow down the time window for aseismic slip. Only two stations with freely available data placed close to the faults were available to us: AB.HASN near the southern part of the WCF and AB.KHDR close to WCF2 (Fig. 1). In the AB.HASN waveforms, we identified a series of high-frequency local seismic events (fig. S19) that started when surface waves from the first M_w 7.8 Kahramanmaraş shock arrived at the station (Fig. 4). The number of events increases again 2 hours later and then again when the surface waves of the second M_w 7.6 Kahramanmaraş earthquake arrived. The maximum amplitudes of these local events indicate a decay of about 1.5 magnitude units between the strongest events, which occur when the seismicity rate is highest, and the smallest detectable events. These smaller events are mainly detectable during the local nighttime, owing to substantial anthropogenic noise in the region. Cross-correlation of stacked templates from these events against continuous waveforms (from earliest available data on 28 July 2022 to 30 April 2023) did not reveal similar events at AB.HASN before the arrival of Kahramanmaraş surface waves or after 10 March 2023.

Single-station location of the larger events placed them on or very close to the WCF, at 10- to 20-km depth, which is deeper than the slip modeled from the InSAR data (Fig. 4D and table S4). The space-time evolution of microseismicity shows a southeast-trending lateral migration at a rate of ~0.3 km/hour (fig. S23A). A recent study has analyzed seismic migration sequences related to hydraulic injections, natural fluid circulation, and slow or aseismic slip transients (*29*). The migration velocity and duration of our sequence place it between slow-slip– and fluid-driven sequences, although it is slightly more consistent with a slow-slip–driven sequence (fig. S23B). This seismic sequence allows us to date the occurrence of underground activity and is synchronous with surface wave arrivals and GNSS displacements.

Long-term creep

To constrain the behavior of faults in the eastern Kura Basin before perturbations from the Kahramanmaraş earthquakes, we performed a time series analysis of SAR data along Sentinel-1 descending track 006 over the 2016 to 2023 period (table S1 and fig. S2B). The resulting time evolution of cumulative slip on the WCF (see time series in Fig. 2A) confirms the transient slip event reported above. In addition, we observe continuous creep with a mean LOS rate of ~0.2 mm/year, which represents a horizontal creep rate of ~0.7 mm/year assuming a pure right-lateral fault. From the decomposition of mean surface velocities along both the ascending and descending LOS directions into the N160° or vertical directions, we identify peaks in the along-strike creep rate profiles that exceed 12 mm/year and correlate with concentrations of mud volcanoes along some segments of the WCF (Fig. 2, A and D). Notably, bend 3 of the WCF exhibits elevated creep rates along its entire ~15-km length (Fig. 2, B and D). The southernmost section of the WCF, which slipped the most during the 2023 transient slip event, previously

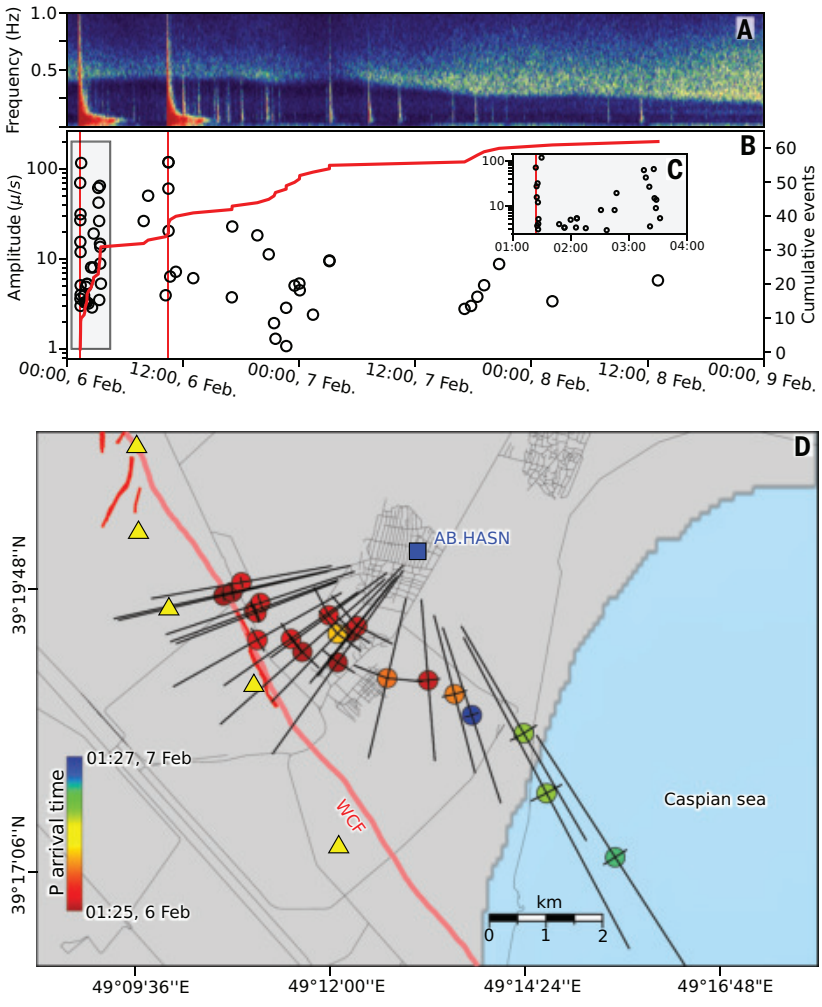

Fig. 4. Summary of the seismic data recorded at AB.HASN between 6 and 8 February 2023. (**A**) Vertical-component spectrogram at frequencies below 1 Hz showing the surface waves and aftershocks of the Kahramanmaraş events. (**B**) Amplitude versus arrival time of the local events that we detected (circles) and their cumulative number (red line). (**C**) Zoom-in on the local events occurring within the first 3 hours. (**D**) Single-station locations and horizontal uncertainties deduced from uncertainties of the incidence and back-azimuth angles (table S4) for the larger local events showing migration toward the South Caspian Basin.

accommodated subsidence of the Neftchala Peninsula (NP in Fig. 1), as shown by the InSAR and GNSS time series (Fig. 2, A and D, and fig. S25). The LOS creep rates of the other faults are slower than those of the WCF (Fig. 2B and fig. S13). We also note that, with the exception of bend 3, transient slip was largest where the fault had been previously creeping at a near-zero rate.

Long-distance triggering

Sometime between 4 and 9 February 2023, 56 mud volcanoes in the West Caspian region erupted, and 22 showed signs of localized surface deformation, far exceeding the typical 12-day interferometric coherence–derived rate of 0 to 2 cases (fig. S12) and the field-observed annual range of 1 to 11 eruptions (*26*). During the same period, the previously creeping WCF and six other faults in the West Caspian region underwent a substantial transient aseismic slip event. On 6 February, small high-frequency earthquakes located at the southern portion of the WCF occurred after the passage of the surface waves of the first Kahramanmaraş earthquake, coeval with the transient displacements measured at four GNSS stations.

These observations led us to conclude that the WCF slipped in response to long-range (~1000-km) triggering from the Kahramanmaraş earthquakes. Such long-distance triggering has been proposed to explain the increase in activity of tectonic, geothermal, and mud or magma volcanic systems (*1*, *30*) after the Landers, Hector Mine, Denali (*31*), and El Mayor–Cucapah earthquakes (*32*) as well as some instances of nonvolcanic tremor (*2*). However, to our knowledge, there is no previous account of remotely triggered aseismic slip at a comparable spatial scale (180 by 100 km^2) and at such a large distance from the triggering earthquake (~1000 km), involving multiple subparallel faults 70 to 170 km in length and tens of kilometers apart, with up to 4 cm of aseismic slip. In comparison, remotely triggered slip in Southern California from the M_w 7.2 El Mayor–Cucapah earthquake involved multiple but much shorter and discontinuous fault segments (0.1 to 29 km) at much shorter distances (6 to 172 km), with slip of 0.5 to 8.5 cm associated with only minor hydrothermal features (mud lumps) (*32*, *33*).

Transient slip on the WCF cannot have been caused by static stress changes from the Kahramanmaraş earthquakes because these did not exceed 10 Pa (*5*, *34*), even though their co- and postseismic crustal deformation spread over a much larger area than would be predicted by a seismic elastic dislocation (*35*). Although the physical mechanisms involved in dynamic triggering are still under debate, most proposed mechanisms involve long-period surface waves ($T > 30$ s) increasing shear and/or reducing frictional stresses on fault planes that are already close to failure (*2*, *31*, *36*). In our case, the estimated level of shear stress produced in the West Caspian region by the first Kahramanmaraş earthquake reached 0.15 MPa, a value that is well beyond the thresholds documented in the literature for dynamic stress triggering by surface waves (*36*, *37*).

Observations of dynamic triggering show the involvement of hydrothermal systems that in some cases were perturbed at distances >1000 km (*38*). When fluids are involved, variations of pore pressure induced by seismic waves are assumed to modify the effective normal stress across the failure planes or cracks (*39*, *40*). Several eruptions of mud volcanoes have been correlated with regional intermediate-magnitude earthquakes and are thought to result from increased fluid (water and oil) pressures and expansion of dissolved methane (*23*, *24*, *41*, *42*). The triggering of more than 50 mud volcanoes in the West Caspian, ~1000 km from the M_w 7.8 and 7.6 Kahramanmaraş earthquakes, slightly extends the upper bound of known global mud volcano responses (*43*) and represents, to our knowledge, the most distant case relative to earthquake magnitude (fig. S26).

Involvement of the deep fluid system

In this case, the coeval activity of mud volcanoes and aseismic slip along the faults in the West Caspian region points to a possible interaction between the faults and crustal fluids associated with mud volcanoes and hydrocarbon reservoirs. Our confidence in such a relationship is reinforced by the need to include inflation sources along the southernmost part of the WCF to fit the InSAR data.

However, the poor temporal resolution of our InSAR observations, the better but still insufficient temporal constraints provided by the microseismic activity and by the transient displacement measured at the local GNSS stations, together with the lack of publicly available piezometric well data, do not allow us to specify a detailed chronology

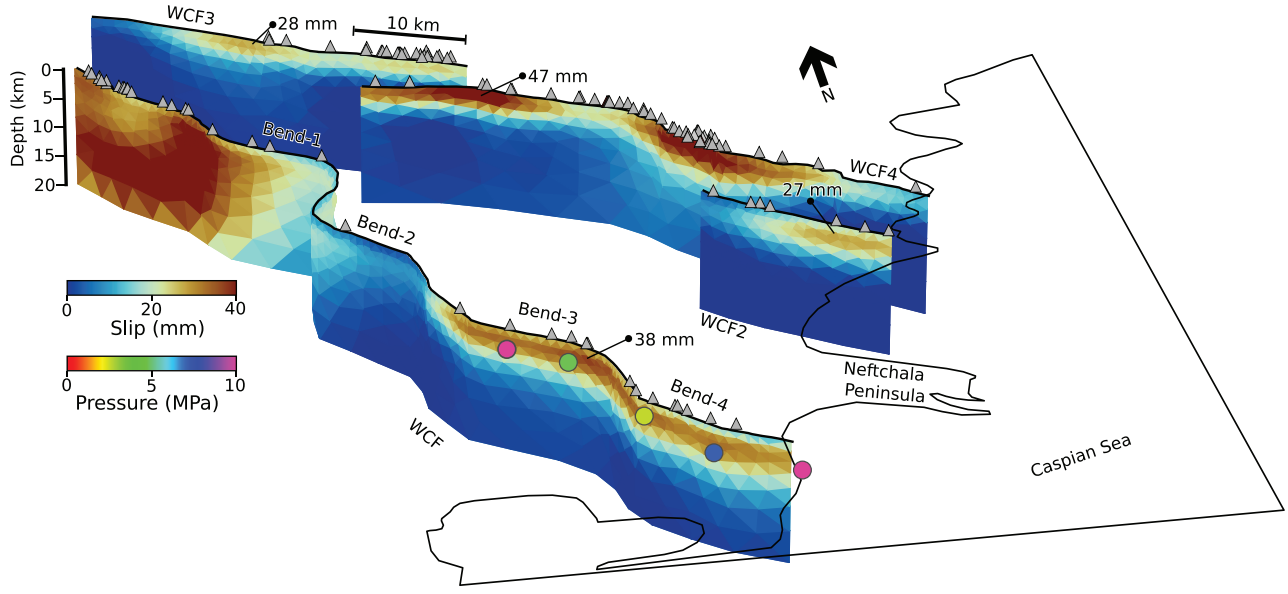

Fig. 5. Fault slip distribution and pressure changes at the inflation sources inferred from least squares inversion of the InSAR-derived surface displacement fields. Fault slip distribution (triangular patches) and inflation sources (circles) are represented in terms of their strike-slip component of motion and pressure change, with positive values depicting right-lateral strike-slip and inflation, respectively. Active mud volcanoes in the area are depicted by dark gray triangles. For visualization purposes, the size of the inflation sources has been exaggerated by a factor of 2.

of fluid-related activities. It therefore remains difficult to choose between the two following scenarios.

The first scenario is that surface waves triggered slip on the faults, which then induced changes in fluid circulation, causing the unrest of mud volcanoes and migration of mud and hydrocarbons through the crust to the surface. Slip would have been triggered dynamically by the nonlinear behavior of the fault gouge, for which the elastic modulus would have fallen abruptly as the surface waves passed (*44*). The deformation field induced by slip along the fault would change the drainage system in the surrounding environment, as observed during the short-term postseismic period of several earthquakes (*45*, *46*), and would have induced compressional and dilational processes in the crust in which fluids could circulate. Such a scenario is supported by the estimated normal stress changes induced by the M_w 6.8 2003 Chenkung earthquake on the Chihshang Fault in Taiwan, which triggered the eruptions of the Leikunghuo and Luoshan mud volcanoes by dilating and compressing their fault-controlled mud volcano reservoirs (*47*). Dynamic stress pulses promote failure almost instantly by advancing preexisting instabilities (*48*). In our case, this scenario of direct activation of slip by the passage of surface waves would require that all seven activated faults were close to their failure threshold (*49*, *50*), which seems unlikely.

The second scenario is that surface waves led to local pore pressure increase within the fluid-saturated sediments of the basin (*51*). At long distances, seismic waves are known to induce soil liquefaction and elevate pore pressures in sedimentary basins, especially at shallow depths (*52*). In our case, the entire region is a hydrocarbon-rich basin, with a thick layer of unconsolidated sediments, which would make it strongly susceptible to destabilization by seismic waves. The increase in pore pressure would lead to the inflation and/or eruption of mud volcanoes and local reduction in effective normal stress along the faults at shallow depths, allowing the faults to slip. Because the decrease of normal stress comes with an increase in the nucleation size on the faults [i.e., the size over which a slip instability can reach dynamic speeds (*53*)], this increase in pore pressure would have kept slip velocity to subseismic speeds. The short triggering delay of surface manifestations of fluids within the whole basin is consistent with a local effect of the seismic waves on pore pressure without the need for fluid migrations. Unrest of the fluid system as indicated by the activation of mud volcanoes and transient slip on the WCF fault is also observable in our InSAR data after the ~600-km-distant M_w 7.4 Sarpol-e Zahab (Iran-Iraq border) earthquake in 2017 (fig. S27).

Aseismic behavior of the WCF

This newly discovered transient slip episode affects the WCF system, a fault system directly branching into the Greater Caucasus, which is the locus of several large earthquakes (*9*). Documenting that the WCF not only creeps continuously, but also experiences substantial aseismic slip transients, must be considered when assessing seismic hazard in the east Kura Basin.

Recent average right-lateral creep rate for the WCF is low (<1 mm/year), although it reaches ~12 mm/year at fault bends and segments particularly affected by mud volcanoes. InSAR estimates are smaller than the right-lateral slip-rates of 7 to 11 mm/year inferred from GNSS measurements (*8*, *54*), which suggests that stresses may accumulate at depth, creating the potential for large earthquakes. A recent paleoseismic study has found lateral offsets reaching 2 to 3 m over five separate episodes for a long-term slip rate of about 4 mm/year over the past 3000 years (*18*). Because of the absence of documented historical earthquakes along this fault, these slip episodes were attributed to continuous creep or discrete aseismic events triggered by deeper seismic activity or fluid pressure in the sediments (*18*). This interpretation is consistent with our findings of slow, continuous creep and triggered aseismic slip transients along the WCF. However, the question of the total strain budget over the whole fault system remains unsolved, and the addition of distantly triggered slow slip events further complicates matters.

Although the precise triggering scenario remains uncertain, we have captured with satellite, geodetic, and seismicity data one of the largest crustal aseismic transients across a network of strike-slip faults, associated with the unrest of mud volcanoes. We believe that this region would be a valuable natural laboratory to explore continuous

creep and large transient slip events on well-hydrated strike-slip faults. We further postulate that the influence of large earthquakes on the dynamics of fault systems at regional and continental scales should be reevaluated.

REFERENCES AND NOTES

1. J. Gomberg, P. Johnson, *Nature* **437**, 830 (2005).
2. M. Miyazawa, J. Mori, *Geophys. Res. Lett.* **32**, 2005GL022539 (2005).
3. D. P. Hill *et al.*, *Science* **260**, 1617–1623 (1993).
4. T. Taira, P. G. Silver, F. Niu, R. M. Nadeau, *Nature* **461**, 636–639 (2009).
5. Q. Zhai, Z. Zhan, J. A. Chavarria, *J. Geophys. Res. Solid Earth* **129**, e2023JB027680 (2024).
6. A. Inbal, A. Ziv, I. Lior, R. N. Nof, A. S. Eisermann, *Geophys. Res. Lett.* **50**, e2023GL104908 (2023).
7. D. Yao *et al.*, *Geophys. Res. Lett.* **51**, e2024GL110786 (2024).
8. B. Aktuğ *et al.*, *J. Geodyn.* **67**, 40–45 (2013).
9. A. Ismail-Zadeh *et al.*, *Earth Sci. Rev.* **207**, 103222 (2020).
10. I. Pierce *et al.*, *Tectonics* **43**, e2023TC007758 (2024).
11. S. Planke, H. Svensen, M. Hovland, D. A. Banks, B. Jamtveit, *Geo-Mar. Lett.* **23**, 258–268 (2003).
12. A. A. Aliev, I. Guliev, F. Dadashov, R. Rahmanov, *Atlas of the World Mud Volcanoes* (Nafta Press Publishing House, 2015).
13. S. R. Fowler *et al.*, *J. Petrol. Sci. Eng.* **28**, 189–206 (2000).
14. M. Bonini, *Earth Sci. Rev.* **115**, 121–152 (2012).
15. C. Huguen *et al.*, *Mar. Geol.* **209**, 245–263 (2004).
16. A. Mazzini, *Mar. Pet. Geol.* **26**, 1677–1680 (2009).
17. C. Hensen *et al.*, *Geology* **43**, 339–342 (2015).
18. N. R. Marshall, thesis, University of Oxford (2023).
19. M. Bonini, F. Mazzarini, *Tectonophysics* **494**, 32–47 (2010).
20. B. Antonielli *et al.*, *Tectonophysics* **637**, 163–177 (2014).
21. K. Iio, M. Furuya, *Prog. Earth Planet. Sci.* **5**, 61 (2018).
22. F. Odonne *et al.*, *Mar. Pet. Geol.* **134**, 105315 (2021).
23. M. Bonini, M. L. Rudolph, M. Manga, *Tectonophysics* **672–673**, 190–211 (2016).
24. R. Mellors, D. Kilb, A. Aliyev, A. Gasanov, G. Yetirmishli, *J. Geophys. Res. Solid Earth* **112**, B04304 (2007).
25. H. Hersbach *et al.*, ERA5 hourly data on single levels from 1940 to present, *Copernicus Climate Change Service (C3S) Climate Data Store (CDS)* (2023); https://doi.org/10.24381/cds.adbb2d47.
26. A. A. Aliyev, I. S. Guliyev, R. R. Rahmanov, *Catalogue of Mud Volcano Eruptions of Azerbaijan (2008–2019)* (Elm Publishing, ed. 3, 2019).
27. K. S. Roberts, S. A. Stewart, R. J. Davies, R. J. Evans, *J. Geol. Soc.* **168**, 49–60 (2011).
28. O. Marc, P. Meunier, N. Hovius, *Nat. Hazards Earth Syst. Sci.* **17**, 1159–1175 (2017).
29. P. Danré, L. De Barros, F. Cappa, L. Passarelli, *Nat. Commun.* **15**, 8943 (2024).
30. M. Manga, E. Brodsky, *Annu. Rev. Earth Planet. Sci.* **34**, 263–291 (2006).
31. J. Gomberg, P. Bodin, K. Larson, H. Dragert, *Nature* **427**, 621–624 (2004).
32. M. J. Rymer *et al.*, "Triggered surface slips in southern California associated with the 2010 El Mayor-Cucapah, Baja California, Mexico, earthquake," US Geological Survey Open-File Report 2010–1333 and California Geological Survey Special Report 221 (2011); https://pubs.usgs.gov/of/2010/1333/.
33. M. Rudolph, M. Manga, *J. Geophys. Res. Solid Earth* **115**, B12211 (2010).
34. C. Liu *et al.*, *Nat. Commun.* **14**, 5564 (2023).
35. S. Ergintav *et al.*, *Science* **386**, 328–335 (2024).
36. D. P. Hill, S. G. Prejean, in *Treatise on Geophysics*, G. Schubert, Ed. (Elsevier, ed. 2, 2015), pp. 273–304.
37. E. E. Brodsky, N. J. van der Elst, *Annu. Rev. Earth Planet. Sci.* **42**, 317–339 (2014).
38. D. R. Montgomery, M. Manga, *Science* **300**, 2047–2049 (2003).
39. J. E. Elkhoury, E. E. Brodsky, D. C. Agnew, *Nature* **441**, 1135–1138 (2006).
40. J. E. Elkhoury, A. Niemeijer, E. E. Brodsky, C. Marone, *J. Geophys. Res.* **116**, B02311 (2011).
41. M. Manga, M. Brumm, M. L. Rudolph, *Mar. Pet. Geol.* **26**, 1785–1798 (2009).
42. A. Kopf *et al.*, *Int. J. Earth Sci.* **99**, 227–240 (2010).
43. C.-Y. Wang, M. Manga, *Geofluids* **10**, 206–216 (2010).
44. P. A. Johnson, X. Jia, *Nature* **437**, 871–874 (2005).
45. G. Peltzer, P. Rosen, F. Rogez, K. Hudnut, *J. Geophys. Res.* **103**, 30131–30145 (1998).
46. S. Jónsson, P. Segall, R. Pedersen, G. Björnsson, *Nature* **424**, 179–183 (2003).
47. M. Bonini, *Mar. Pet. Geol.* **128**, 105050 (2021).
48. M. E. Belardinelli, A. Bizzarri, M. Cocco, *J. Geophys. Res. Solid Earth* **108**, 2135 (2003).
49. J. Gomberg, M. L. Blanpied, N. Beeler, *Bull. Seismol. Soc. Am.* **87**, 294–309 (1997).
50. J. Gomberg, N. Beeler, M. Blanpied, P. Bodin, *J. Geophys. Res.* **103**, 24411–24426 (1998).
51. L. Goren, E. Aharonov, D. Sparks, R. Toussaint, *Pure Appl. Geophys.* **168**, 2289–2323 (2011).
52. S. Ben-Zeev, L. Goren, R. Toussaint, E. Aharonov, *Nat. Commun.* **14**, 5791 (2023).
53. J.-P. Ampuero, A. M. Rubin, *J. Geophys. Res.* **113**, B01302 (2008).
54. F. Kadirov, S. Mammadov, R. Reilinger, S. McClusky, *Proc. Azerbaijani Natl. Acad. Sci.* **1**, 82–88 (2008).
55. E. Zelenin, D. Bachmanov, S. Garipova, V. Trifonov, A. Kozhurin, *Earth Syst. Sci. Data* **14**, 4489–4503 (2022).
56. G. Ekström, M. Nettles, A. Dziewoński, *Phys. Earth Planet. Inter.* **200–201**, 1–9 (2012).
57. S. Vincent, C. Davies, K. Richards, E. Aliyeva, *Mar. Pet. Geol.* **27**, 2079–2106 (2010).
58. P. A. Rosen, S. Hensley, G. Peltzer, M. Simons, *Eos* **85**, 47 (2004).
59. M.-P. Doin *et al.*, "Presentation of the small baseline NSBAS processing chain on a case example: The Etna deformation monitoring from 2003 to 2010 using Envisat data," in Proceedings of the Fringe 2011 Workshop, Frascati, Italy, 19 to 23 September 2011 (ESA SP-697, 2011), pp. 3434–3437.
60. M.-P. Doin *et al.*, *J. Geophys. Res. Solid Earth* **120**, 5290–5310 (2015).
61. R. Jolivet, jolivetr/csi: First Release, Zenodo (2024); https://doi.org/10.5281/zenodo.14170822.
62. M. S. Bos, R. M. S. Fernandes, S. D. P. Williams, L. Bastos, *J. Geod.* **87**, 351–360 (2013).
63. D. Tian *et al.*, PyGMT: A Python interface for the Generic Mapping Tools, Zenodo (2024); https://doi.org/10.5281/zenodo.13679420.

ACKNOWLEDGMENTS

InSAR processing was carried out on the EOST-A2S (Application Satellite Survey) HPC facility of the University of Strasbourg. We are grateful to D. Miché and J.-P. Malet for their support in using the cluster. We thank F. Masson, M. P. Doin, C. Lasserre, R. Toussaint, M. Jolivet, P. Vernant, and H. Valiyev for their helpful discussions and three anonymous reviewers, whose comments helped improve the manuscript. **Funding:** Z.B.'s PhD research at ITES is supported by a scholarship from the French government. This project has received funding from the European Research Council (ERC) under the European Union's Horizon 2020 research and innovation program (grant 758210 for project Geo4D and 101125232 for project iQuake). R.J. acknowledges funding from the Institut Universitaire de France. **Author contributions:** Conceptualization: C.D., A.M.; Investigation: Z.B., R.V., C.D., A.M., R.J., L.R.; Supervision: C.D., A.M.; Writing: Z.B., R.V., C.D., A.M., R.J., L.R. **Competing interests:** The authors declare no competing interests. **Data and materials availability:** Copernicus Sentinel-1 SAR images 2015-2023 are publicly available at https://search.asf.alaska.edu/. Azerbaijan National Seismological Network (AB) waveforms are freely available at EarthScope Consortium Web Services (https://service.iris.edu/). We provide a catalog of both dormant and activated mud volcanoes as data S1. Regional GNSS data are available at http://geodesy.unr.edu/. Interferograms and time series were generated using the ROI-PAC (*58*) and NSBAS processing chain (*59*,*60*). Fault models have been produced on the software CSI (https://github.com/jolivetr/csi) (*61*). GNSS data have been postprocessed using Hector package (*62*). Maps were generated using pygmt (*63*). **License information:** Copyright © 2025 the authors, some rights reserved; exclusive licensee American Association for the Advancement of Science. No claim to original US government works. https://www.science.org/about/science-licenses-journal-article-reuse. This research was funded in whole or in part by the European Research Council (grants 758210 and 101125232); as required the author will make the Author Accepted Manuscript (AAM) version available under a CC BY public copyright license.

SUPPLEMENTARY MATERIALS

science.org/doi/10.1126/science.adv8438
Materials and Methods; Figs. S1 to S27; Tables S1 to S4; References (*64*–*101*); Data S1

Submitted 9 January 2025; accepted 2 July 2025

10.1126/science.adv8438

APOPTOSIS

Relative importance of the anti-apoptotic versus apoptosis-unrelated functions of MCL-1 in vivo

Kerstin Brinkmann[1,2]*, Kate McArthur[3]†, Shezlie Malelang[1]†, Leonie Gibson[1], Annli Tee[1,2], Sheik Nadeem Elahee Doomun[4], Caitlin L. Rowe[3], Philip Arandjelovic[1,2], Julia M. Marchingo[1,2], Damian D'Silva[1,2], Annabell Bachem[5], Simon Monard[1], Lauren G. Whelan[1], Grant Dewson[1,2], Tracy L. Putoczki[1,2], Philippe Bouillet[1,2], Nai Yang Fu[1,2,6], Kristin K. Brown[7,8,9], Andrew J. Kueh[1,2,10,11], Verena C. Wimmer[1,2], Marco J. Herold[1,2,10,11]‡, Tim Thomas[1,2]‡, Anne K. Voss[1,2]‡, Andreas Strasser[1,2]*‡

The anti-apoptotic protein MCL-1 (myeloid cell leukemia-1) is essential for embryogenesis and the survival of many cell types that tolerate loss of its relatives, BCL-XL and BCL-2. Apoptosis-unrelated roles of MCL-1 in metabolism may contribute to this requirement, although their relevance for embryogenesis and postnatal life remains unclear. We hypothesized that BCL-XL and BCL-2 may substitute MCL-1's anti-apoptotic but not its apoptosis-unrelated functions. Replacing MCL-1 with BCL-XL or BCL-2 supported embryo development by rescuing the *Mcl-1*$^{-/-}$ preimplantation lethality. *Mcl-1*$^{Bcl\text{-}xL/Bcl\text{-}xL}$ but not *Mcl-1*$^{Bcl\text{-}2/Bcl\text{-}2}$ mice were born on a mixed background, although they showed metabolic defects. Thus MCL-1's apoptosis-unrelated functions appear critical in later development, with BCL-XL, but not BCL-2, partially compensating. These findings clarify MCL-1's distinct physiological roles, critically informing MCL-1 inhibitor development as cancer therapeutics.

Apoptotic cell death is essential for morphogenesis and tissue homeostasis (*1*, *2*), with defects in apoptosis promoting cancer, autoimmune disorders, and degenerative diseases (*3*, *4*). Apoptosis is regulated by three BCL-2 (B cell lymphoma 2) protein family subgroups (*5*, *6*). Anti-apoptotic proteins (BCL-2, BCL-XL, MCL-1, A1, BCL-W) prevent apoptosis by neutralizing BH3-only proteins (e.g., tBID, BIM, PUMA, NOXA) and effectors BAX and BAK (*5*, *7*, *8*) (fig. S1A). Activated BAX and BAK cause mitochondrial outer membrane permeabilization, initiating the caspase cascade that dismantles the cell (*9*, *10*).

MCL-1 (myeloid cell leukemia-1) is critical for cell survival. Its removal or inhibition causes death of many cell types that are not affected by loss or inhibition of other anti-apoptotic BCL-2 proteins (*11*, *12*). MCL-1–deficient embryos die around embryonic day E3.5 (*13*). BCL-XL–deficient embryos die at ~E13.5 as a result of erythroid and neuronal cell death (*14*). BCL-2–deficient mice die ~4 weeks after birth from polycystic kidney disease (*15*, *16*). Removal of A1 or BCL-W causes only minor defects (*17*) (fig. S1B). Anti-apoptotic BCL-2 proteins differ in binding to their pro-apoptotic relatives, turnover, and localization (fig. S1, A, C, and D) (*18*–*20*). Some anti-apoptotic BCL-2 proteins reportedly also exert functions unrelated to apoptosis (*21*). Proteolytically processed MCL-1 (*22*–*25*) and BCL-XL (*26*, *27*), but not BCL-2 (*28*), are found in the intermitochondrial membrane space regulating mitochondrial dynamics and adenosine triphosphate (ATP) production through oxidative phosphorylation (OXPHOS). MCL-1 also controls mitochondrial fatty acid oxidation (FAO) through interaction with ACSL1 (acyl–coenzyme A synthetase long-chain family member 1) on the outer mitochondrial membrane (*29*, *30*). The physiological importance of apoptosis-unrelated roles of MCL-1 (and other BCL-2 proteins) is unclear. Notably, dying *Mcl-1*$^{-/-}$ blastocysts reportedly lack apoptosis hallmarks (*13*), prompting the hypothesis that implantation failure results from loss of an apoptosis-unrelated role of MCL-1 (*22*). Moreover, cardiomyocytes reportedly require both the anti-apoptotic and apoptosis-unrelated function(s) of MCL-1 to maintain heart function (*25*, *31*).

MCL-1 inhibitors can block both MCL-1 functions (*29*, *30*) and in some cases (AMG-176, AZD5991) cause cardiotoxicity in patients (*32*). To advance MCL-1 inhibitors for cancer therapy, we need to know whether their efficacy and toxicity stem solely from inhibiting the anti-apoptotic or also apoptosis-unrelated functions of MCL-1 (*32*, *33*). To address this and to investigate functional redundancies and differences with other anti-apoptotic BCL-2 proteins, we generated mice in which *Mcl-1* coding sequences were replaced by sequences encoding BCL-XL, BCL-2, or A1.

Validation of *Mcl-1* gene-replacement strategy

MCL-1 would only be fully substituted by another BCL-2 family member if it has no distinct essential apoptosis-unrelated function. To test this, we used cDNA sequences encoding human BCL-2 (hBCL-2; called *Mcl-1*$^{Bcl\text{-}2}$ mice), FLAG-tagged mouse BCL-XL (*Mcl-1*$^{Bcl\text{-}xL}$), or FLAG-tagged mouse A1 (*Mcl-1*^{A1}) to replace the *Mcl-1* coding exons and introns in C57BL/6 mice (Fig. 1A). This strategy maintained the 5′ and 3′ untranslated regions of the *Mcl-1* gene. As a control for loss of *Mcl-1* introns, we used a cDNA encoding human MCL-1 (hMCL-1). Heterozygous *Mcl-1*$^{hMcl\text{-}1/+}$, *Mcl-1*$^{Bcl\text{-}xL/+}$, *Mcl-1*$^{Bcl\text{-}2/+}$, and *Mcl-1*$^{A1/+}$ mice were viable and reached adulthood (fig. S2, A and B). The expression of hMCL-1, FLAG-BCL-XL, hBCL-2, and FLAG-A1 proteins was confirmed by Western blotting in E10.5 embryo lysates (Fig. 1B), mouse embryonic fibroblasts (MEFs) (fig. S2, C and D), and by flow cytometry in bone marrow cells from heterozygous gene-replacement mice (fig. S2E). Endogenous mouse MCL-1 (mMCL-1) was discriminated from the knock-in hMCL-1 by differences in molecular weight (*34*). Endogenous mouse BCL-2 (mBCL-2) was discriminated from the knock-in hBCL-2 using species-specific monoclonal antibodies. The knock-in BCL-XL and A1 were FLAG-tagged to allow discrimination from the endogenous proteins. We observed the expected reduction in endogenous MCL-1 in *Mcl-1*$^{Bcl\text{-}xL/+}$, *Mcl-1*$^{Bcl\text{-}2/+}$, and *Mcl-1*$^{A1/+}$ embryo lysates and MEFs (Fig. 1, B and G, and fig. S2, C and D). There were no major changes in the abundance of other BCL-2 family proteins, with the exception of a reduction in BCL-XL in lysates from *Mcl-1*$^{Bcl\text{-}2/+}$ and *Mcl-1*$^{Bcl\text{-}2/Bcl\text{-}2}$ E10.5 embryos as well as *Mcl-1*$^{Bcl\text{-}2/+}$ MEFs (Fig. 1, B and G, and fig. S2, C, D, F, and G).

For functional validation, we treated mitogen-activated B cells from heterozygous *Mcl-1* gene-replacement mice with BH3 mimetic drugs (Fig. 1C). Cells from *Mcl-1*$^{hMcl\text{-}1/+}$ mice were more susceptible to the MCL-1 inhibitor S63845 than were wild-type cells, consistent with the higher affinity of S63845 for hMCL-1 than mMCL-1 (*35*). B cells from *Mcl-1*$^{Bcl\text{-}xL/+}$ or *Mcl-1*$^{Bcl\text{-}2/+}$ mice expressed higher total amounts of BCL-XL (mBCL-XL plus FLAG-BCL-XL) or BCL-2 (mBCL-2 plus hBCL-2) and less MCL-1 compared with those of wild-type cells

[1]The Walter and Eliza Hall Institute of Medical Research, Melbourne, Australia. [2]Department of Medical Biology, University of Melbourne, Melbourne, Australia. [3]Department of Biochemistry and Molecular Biology, Biomedicine Discovery Institute, Monash University, Melbourne, Australia. [4]Metabolomics Australia, Bio21 Institute, University of Melbourne, Melbourne, Australia. [5]Department of Microbiology and Immunology, Peter Doherty Institute, University of Melbourne, Melbourne, Australia. [6]Cancer and Stem Cell Biology Program, Duke-NUS Medical School, Singapore. [7]Peter MacCallum Cancer Centre, Melbourne, Australia. [8]The Sir Peter MacCallum Department of Oncology, University of Melbourne, Melbourne, Australia. [9]Department of Biochemistry and Pharmacology, University of Melbourne, Melbourne, Australia. [10]Olivia Newton-John Cancer Research Institute, Melbourne, Australia. [11]School of Cancer Medicine, La Trobe University, Melbourne, Australia. ***Corresponding author. Email: strasser@wehi.edu.au (A.S.); brinkmann.k@wehi.edu.au (K.B.)** †These authors contributed equally to this work. ‡These authors contributed equally to this work.

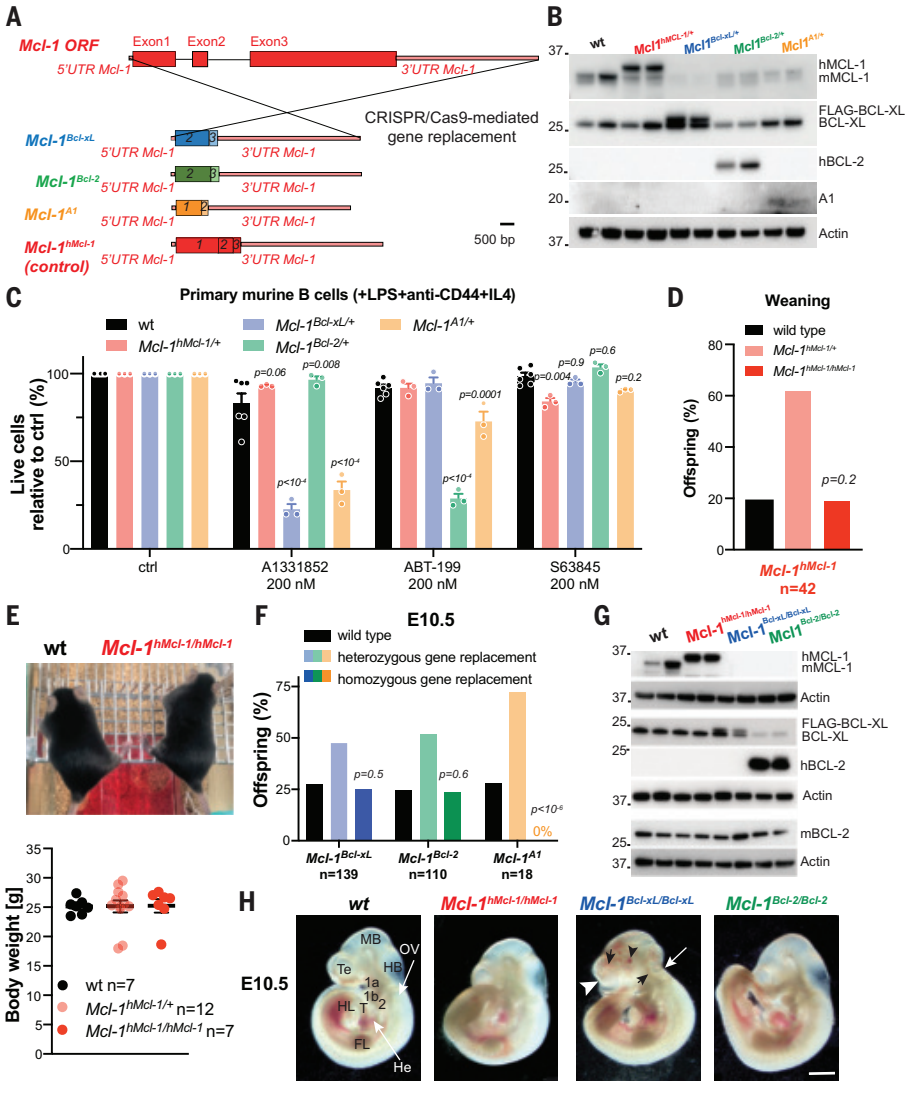

Fig. 1. Essential function of MCL-1 in preimplantation development replaced by BCL-XL or BCL-2 but not by A1. (**A**) Schematic of the *Mcl-1* gene-targeting strategy. UTR, untranslated region. (**B**) Representative (from $n \geq 2$ repeats) Western blot of wild-type (wt), *Mcl-1*$^{hMcl\text{-}1/+}$, *Mcl-1*$^{Bcl\text{-}xL/+}$, *Mcl-1*$^{Bcl\text{-}2+/}$, and *Mcl-1*$^{A1/+}$ E10.5 embryo lysates ($n = 2$ per genotype) detecting the indicated proteins. (**C**) Survival (as %AnnexinV-PI-) of mitogen-activated B cells from wild-type, *Mcl-1*$^{hMcl\text{-}1/+}$, *Mcl-1*$^{Bcl\text{-}xL/+}$, *Mcl-1*$^{Bcl\text{-}2/+}$, and *Mcl-1*$^{A1/+}$ mice treated with the indicated drugs for 24 hours. Data shown as mean ± SEM from ≥2 experiments, each performed in triplicate. Two-way ANOVA with Tukey's multiple comparison; *P* values shown. (**D**) Offspring genotype frequencies at weaning from intercrosses of *Mcl-1*$^{hMcl\text{-}1/+}$ mice. (**E**) Representative images of a wild-type and a *Mcl-1*$^{hMcl\text{-}1/hMcl\text{-}1}$ mouse aged 50 days (top) and whole-body weights of 50- to 60-day-old wild-type ($n = 7$), *Mcl-1*$^{hMcl\text{-}1/+}$ ($n = 12$), and *Mcl-1*$^{hMcl\text{-}1/hMcl\text{-}1}$ ($n = 7$) males (bottom). One-way ANOVA with Dunnett's multiple comparison. No significant differences were observed. (**F**) Offspring genotype frequencies at E10.5 from homotypic intercrosses of *Mcl-1*$^{hMcl\text{-}1/+}$, *Mcl-1*$^{Bcl\text{-}xL/+}$, *Mcl-1*$^{Bcl\text{-}2/+}$, or *Mcl-1*$^{A1/+}$ mice. [(D) and (F)] Genotype distributions analyzed using cumulative binomial probability (*P* values and *n* indicated). (**G**) Representative (from $n \geq 2$ repeats) Western blot of wild-type, *Mcl-1*$^{hMcl\text{-}1/hMcl\text{-}1}$, *Mcl-1*$^{Bcl\text{-}xL/Bcl\text{-}xL}$, and *Mcl-1*$^{Bcl\text{-}2/Bcl\text{-}2}$ E10.5 embryo lysates ($n = 2$ per genotype) detecting the indicated proteins. (**H**) Representative images of E10.5 wild-type, *Mcl-1*$^{hMcl\text{-}1/hMcl\text{-}1}$, *Mcl-1*$^{Bcl\text{-}xL/Bcl\text{-}xL}$, and *Mcl-1*$^{Bcl\text{-}2/Bcl\text{-}2}$ embryos. 1a and 1b, maxillary and mandibular portion of the first pharyngeal arch, respectively; 2, pharyngeal arch; FL, forelimb bud; HB, hindbrain; He, heart (here, beneath the tail); HL, hindlimb bud; MB, midbrain; OV, otic vesicle; T, tail; Te, telencephalon. White arrowhead and white arrow, areas of the lateral ventricles in the telencephalon and the fourth ventricle in the hindbrain, respectively, that appeared collapsed; black arrowhead, blood accumulation; black arrows, neuroepithelium forming ridges in the telencephalon and hindbrain. Scale bar, 1.34 mm.

and thus were more susceptible to the BCL-XL inhibitor A1331852 or the BCL-2 inhibitor ABT-199/venetoclax, respectively. B cells from *Mcl-1*$^{A1/+}$ mice were more susceptible to BH3 mimetic drugs compared with wild-type B cells, presumably because of the low abundance of A1 (Fig. 1, B and C). These findings demonstrate the expression and functionality of the knock-in proteins.

Intercrosses of *Mcl-1*$^{hMcl\text{-}1/+}$ mice yielded *Mcl-1*$^{hMcl\text{-}1/hMcl\text{-}1}$ offspring at the expected Mendelian frequency (Fig. 1D), and they displayed normal appearance, weight, and survival (Fig. 1E and fig. S3A). Histological analysis of the liver, kidney, and heart revealed no abnormalities (fig. S3, B to D). MEFs from *Mcl-1*$^{hMcl\text{-}1/+}$ and *Mcl-1*$^{hMcl\text{-}1/hMcl\text{-}1}$ mice showed normal responses to apoptotic stimuli (fig. S3E). These findings demonstrate that the function of the mouse *Mcl-1* gene locus can be replaced by a cDNA encoding human MCL-1, meaning that the absence of introns of the *Mcl-1* gene does not have deleterious impact.

Apoptosis-unrelated functions of MCL-1 are dispensable for early embryogenesis

We examined whether the E3.5 lethality caused by MCL-1 loss could be rescued by replacing MCL-1 with hBCL-2, FLAG-BCL-XL, or FLAG-A1. Intercrosses of *Mcl-1*$^{A1/+}$ mice did not produce homozygous *Mcl-1*$^{A1/A1}$ embryos at E10.5 or later stages (Fig. 1F and fig. S4A), possibly owing to low amounts of FLAG-A1 (Fig. 1B). Examination of preimplantation embryos (E2.5–E3.5) showed that, like *Mcl-1*$^{-/-}$ embryos, *Mcl-1*$^{A1/A1}$ embryos died before E3.5 (fig. S4, B to D). In contrast, *Mcl-1*$^{Bcl\text{-}xL/Bcl\text{-}xL}$ and *Mcl-1*$^{Bcl\text{-}2/Bcl\text{-}2}$ embryos expressing hBCL-2 or FLAG-BCL-XL instead of MCL-1 were present at E10.5 at the expected Mendelian frequency (Fig. 1F), with no compensatory changes in expression of other BCL-2 family proteins detected (Fig. 1G and fig. S4E). Early embryonic development stages include E0–E7.5, with critical developmental patterning events that result in the formation of the three germ layers, requiring precise gene regulation, occurring during gastrulation (E6–E8) (*36*). Neuronal development during early embryogenesis includes neurulation (E8.0–E8.5) and neuronal tube closure (E9.0–E9.5) (*36*). Thus, *Mcl-1*$^{Bcl\text{-}xL/Bcl\text{-}xL}$ and *Mcl-1*$^{Bcl\text{-}2/Bcl\text{-}2}$ embryos underwent preimplantation, implantation, gastrulation, and embryonic patterning without MCL-1. The presence of the forebrain, midbrain, hindbrain, and spinal cord indicated successful neurulation and neural tube patterning (Fig. 1H). Embryos had a detectable heartbeat and were within the expected size range (crown-rump length of ~2.5 to 3.5 mm at E10.5) (*36*), although *Mcl-1*$^{Bcl\text{-}2/Bcl\text{-}2}$ embryos appeared slightly smaller than wild type [analysis of variance (ANOVA): $P < 10^{-4}$] but remained within normal developmental limits (fig. S2H). However, some embryos showed

head region anomalies, including collapsed ventricles and ridged neuroepithelium (Fig. 1H). These findings demonstrate that BCL-2 and BCL-XL can replace MCL-1 during the preimplantation state when all *Mcl-1*$^{-/-}$ embryos die. Unlike MCL-1 and BCL-XL, BCL-2 does not localize to the mitochondrial intermembrane space (*28*) and does not interact with ACSL1 (*30*). Therefore, the development of *Mcl-1*$^{Bcl\text{-}2/Bcl\text{-}2}$ embryos to E10.5 demonstrates that the reported apoptosis-unrelated functions of MCL-1 (*22*, *29*, *30*) are not critical for early embryogenesis.

Comparison of *Mcl-1*$^{Bcl\text{-}2/Bcl\text{-}2}$ and *Mcl-1*$^{Bcl\text{-}xL/Bcl\text{-}xL}$ mouse development

Among offspring of intercrosses of heterozygotes, *Mcl-1*$^{Bcl\text{-}xL/Bcl\text{-}xL}$ fetuses were underrepresented from E13.5 (Fig. 2A), whereas *Mcl-1*$^{Bcl\text{-}2/Bcl\text{-}2}$ embryos were already underrepresented from E12.5 (Fig. 2B). At E14.5, 10% of offspring were *Mcl-1*$^{Bcl\text{-}xL/Bcl\text{-}xL}$, but no *Mcl-1*$^{Bcl\text{-}2/Bcl\text{-}2}$ fetuses were detected (Fig. 2, A and B). No viable *Mcl-1*$^{Bcl\text{-}xL/Bcl\text{-}xL}$ or *Mcl-1*$^{Bcl\text{-}2/Bcl\text{-}2}$ embryos were found at E15.5, and none survived to weaning on a C57BL/6 background (Fig. 2, A and B). From E11.5 to E12.5, significantly higher percentages (chi-square test: $P < 10^{-4}$) of abnormal *Mcl-1*$^{Bcl\text{-}xL/Bcl\text{-}xL}$ and *Mcl-1*$^{Bcl\text{-}2/Bcl\text{-}2}$ embryos were observed compared with those of wild-type littermates (Fig. 2, C to E; fig. S4F; and table S1). Some homozygous embryos were small and abnormal (7% *Mcl-1*$^{Bcl\text{-}xL/Bcl\text{-}xL}$, 11% *Mcl-1*$^{Bcl\text{-}2/Bcl\text{-}2}$), whereas others died (3 and 48%, respectively; Fig. 2, C to E; fig. S4F; and table S1). Anomalies included exencephaly (9% *Mcl-1*$^{Bcl\text{-}2/Bcl\text{-}2}$), other cranial abnormalities (10% *Mcl-1*$^{Bcl\text{-}xL/Bcl\text{-}xL}$, 2% *Mcl-1*$^{Bcl\text{-}2/Bcl\text{-}2}$; collapsed lateral and fourth ventricles, ridged neuroepithelium), and cranial blood accumulation, consistent with hemorrhages (17% *Mcl-1*$^{Bcl\text{-}xL/Bcl\text{-}xL}$, 7% *Mcl-1*$^{Bcl\text{-}2/Bcl\text{-}2}$; Fig. 2, C to E; fig. S4F; and table S1). Whole-mount

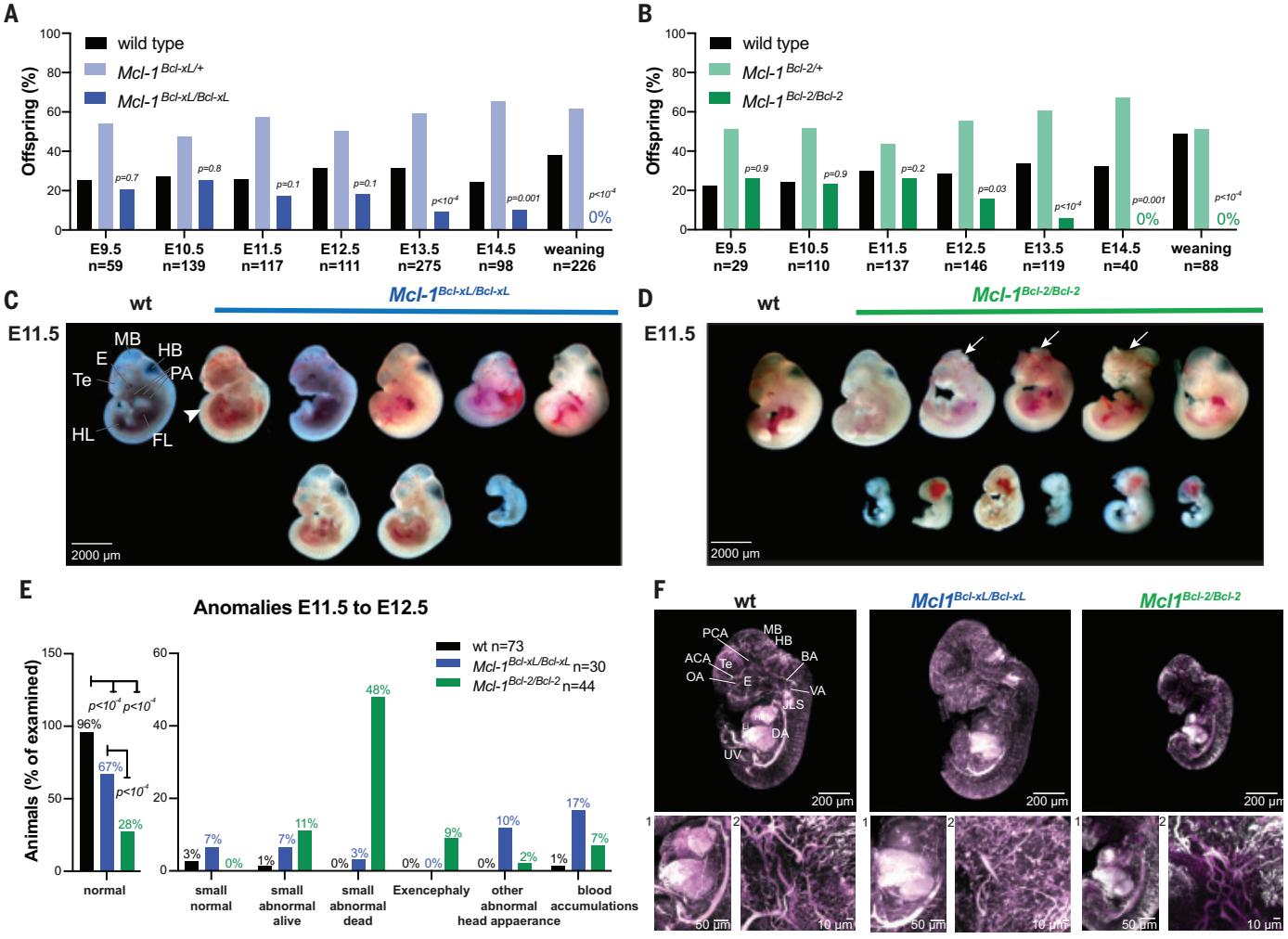

Fig. 2. *Mcl-1*$^{Bcl\text{-}xL/Bcl\text{-}xL}$ and *Mcl-1*$^{Bcl\text{-}2/Bcl\text{-}2}$ embryos are more likely than wild-type embryos to exhibit abnormalities. (**A** and **B**) Offspring genotype frequencies at indicated embryonic days from homotypic intercrosses of (A) *Mcl-1*$^{Bcl\text{-}xL/+}$ or (B) *Mcl-1*$^{Bcl\text{-}2/+}$ mice, analyzed using cumulative binomial probability (*P* values and *n* indicated). E10.5 data from Fig. 1F are included for comparison. (**C** and **D**) Representative images showing wild-type ($n = 2$), *Mcl-1*$^{Bcl\text{-}xL/Bcl\text{-}xL}$ ($n = 8$), and *Mcl-1*$^{Bcl\text{-}2/Bcl\text{-}2}$ ($n = 11$) embryos at E11.5. (**E**) Summary frequencies of the phenotypes from E11.5 to E12.5 of wild-type ($n = 73$), *Mcl-1*$^{Bcl\text{-}xL/Bcl\text{-}xL}$ ($n = 30$), and *Mcl-1*$^{Bcl\text{-}2/Bcl\text{-}2}$ ($n = 44$) embryos; percentages shown per genotype. Full breakdown in table S1. Statistical significance assessed using cumulative binomial probability (normal *Mcl-1*$^{Bcl\text{-}xL/Bcl\text{-}xL}$ and *Mcl-1*$^{Bcl\text{-}2/Bcl\text{-}2}$ embryos versus wild-type embryos); *P* values shown. (**F**) Representative (from $n \geq 2$ embryos per genotype) whole-mount images (iDISCO) showing a wild-type, a *Mcl-1*$^{Bcl\text{-}xL/Bcl\text{-}xL}$, and a *Mcl-1*$^{Bcl\text{-}2/Bcl\text{-}2}$ E12.5 embryo [vasculature (CD31/PCAM1), purple; blood cells (autofluorescence), white]. Higher magnifications highlight (1) heart and liver and (2) cephalic vasculature. ACA, anterior cerebral artery; BA, basilar artery; DA, descending aorta; FL, forelimb (forelimb bud, E11.5 and E12.5); HB, hindbrain; He, heart; HL, hindlimb (hindlimb bud, E11.5 and E12.5); JLS, jugular lymph sac (here, blood-filled); Li, liver; MB, midbrain; OA, olfactory artery; PA, pharyngeal arches; PCA, posterior communicating artery; Te, telencephalon; UV, umbilical vein; VA, vertebral artery.

three-dimensional imaging (*37*) of intact E12.5 embryos, with staining of endothelial cells and inherent blood autofluorescence, revealed no major differences in vital organs, including the heart and fetal liver, or vascularization between genotypes (Fig. 2F and movies S1 to S3). From E11.5 to E12.5, a considerably smaller proportion of living *Mcl-1*$^{Bcl\text{-}2/Bcl\text{-}2}$ embryos was observed compared with that of *Mcl-1*$^{Bcl\text{-}xL/Bcl\text{-}xL}$ embryos (chi-square test: $P < 10^{-4}$) (Fig. 2, C to E; fig. S4F; and table S1), indicating that BCL-XL compensates for MCL-1 loss more effectively than does BCL-2.

Apoptosis signaling in embryos

The defects in *Mcl-1*$^{Bcl\text{-}xL/Bcl\text{-}xL}$ and *Mcl-1*$^{Bcl\text{-}2/Bcl\text{-}2}$ embryos at later stages may result from reduced apoptosis, as both BCL-2 and BCL-XL proteins have a longer half-life than the replaced MCL-1. Accordingly, *Mcl-1*$^{Bcl\text{-}xL/+}$ or *Mcl-1*$^{Bcl\text{-}2/+}$ MEFs and mitogen-activated B cells were significantly more resistant to apoptotic stimuli than were wild-type cells (Fig. 3A and fig. S5A). *Mcl-1*$^{Bcl\text{-}xL/+}$ and *Mcl-1*$^{Bcl\text{-}2/+}$ females displayed an increased incidence of vaginal septa, indicating failure of normal apoptotic septum regression during development (Fig. 3B). Potentially consistent with this, E9.5 *Mcl-1*$^{Bcl\text{-}2/+}$ embryos exhibited reduced TUNEL$^+$ cells compared with wild-type controls. Homozygous *Mcl-1*$^{Bcl\text{-}2/Bcl\text{-}2}$ embryos exhibited increased TUNEL$^+$ cells (fig. S5B), possibly as a result of cell death associated with their developmental abnormalities (Fig. 2, C to E).

Histological analysis revealed that some E11.5–E12.5 *Mcl-1*$^{Bcl\text{-}xL/Bcl\text{-}xL}$ and *Mcl-1*$^{Bcl\text{-}2/Bcl\text{-}2}$ embryos exhibited folding of the neuroepithelium in several areas of the developing brain (fig. S5, C and D), likely owing to the collapse of the lateral and fourth brain ventricles. No defects in neural tube closure were observed in *Mcl-1*$^{Bcl\text{-}xL/Bcl\text{-}xL}$ embryos, but 9% of *Mcl-1*$^{Bcl\text{-}2/Bcl\text{-}2}$ embryos showed exencephaly (Fig. 2, C to E, and fig. S4F), a phenotype common in mice with apoptosis defects (*2*). At E11.5, neuronal differentiation has begun in the hindbrain, whereas the cortex has few differentiated cells. Proliferating cells are located in the ventricular zone (VZ), and differentiating neurons migrate to the marginal zone (MZ). The VZ-to-MZ proportion and the percentage of cells in these zones did not differ between genotypes (fig. S5E). The dorsal telencephalon, the precursor to the cerebral cortex, mainly consists of proliferating neuronal precursor cells at E11.5, with minimal cell death. No significant differences in percentages of mitotic or pyknotic nuclei were found between genotypes (fig. S5F). However, cell density was significantly reduced in the E11.5 *Mcl-1*$^{Bcl\text{-}2/Bcl\text{-}2}$ dorsal telencephalon (fig. S5F), indicating cell death or reduced proliferation at an earlier developmental stage.

The inhibition of intrinsic apoptosis during development by substituting BCL-XL or BCL-2 for MCL-1 extended survival until E14.5 at most (Fig. 2, A and B). In contrast, *Bax*$^{-/-}$*Bak*$^{-/-}$*Bok*$^{-/-}$ triple knockout (TKO) fetuses, which cannot undergo intrinsic apoptosis owing to lacking all apoptosis effectors, develop until E18.5, with 1.8% even reaching weaning (Fig. 3C) (*38*). Hence, the lethal developmental abnormalities observed in *Mcl-1*$^{Bcl\text{-}xL/Bcl\text{-}xL}$ and *Mcl-1*$^{Bcl\text{-}2/Bcl\text{-}2}$ fetuses are not due to impaired developmental apoptosis, supporting an apoptosis-unrelated function of MCL-1 at later developmental stages that cannot be substituted by BCL-XL or BCL-2.

Impact of potential apoptosis-unrelated roles of BCL-2 and BCL-XL

Apoptosis-unrelated functions have been reported for BCL-2 and BCL-XL, and their excess may contribute to defects in *Mcl-1*$^{Bcl\text{-}2/Bcl\text{-}2}$ and *Mcl-1*$^{Bcl\text{-}xL/Bcl\text{-}xL}$ embryos. The early lethality of *Mcl-1*$^{-/-}$ and *Mcl-1*$^{Bcl\text{-}2/Bcl\text{-}2}$ embryos limit the analysis of these processes in vivo. To explore potential impacts of apoptosis-unrelated functions of excess BCL-2 and BCL-XL, we created mice with one floxed *Mcl-1* allele and the other expressing FLAG-BCL-XL or hBCL-2, using *Mcl-1*$^{fl/fl}$ mice as controls. All contained the *Rosa26-CreERT2* transgene for tamoxifen-inducible *Mcl-1*^{fl} deletion (*39*). Polymerase chain reaction and Western blot analysis in MEFs confirmed *Mcl-1*^{fl} deletion upon tamoxifen treatment and expression of the gene-swap encoded proteins, producing *Mcl-1*$^{del/del}$ (control), *Mcl-1*$^{Bcl\text{-}xL/del}$, and *Mcl-1*$^{Bcl\text{-}2/del}$ MEFs (fig. S6, A and B).

BCL-XL and BCL-2 allegedly control calcium flux through various mechanisms (*21*). However, no differences in calcium flux peak amplitude were observed between genotypes in MEFs (fig. S6C). BCL-2 may inhibit cell proliferation by delaying the G1-to-S phase transition of the cell cycle (*40*, *41*). Consistently, we observed slightly reduced proliferation rates of *Mcl-1*$^{Bcl\text{-}2/fl}$ MEFs compared with those of controls (ANOVA: $P = 0.046$) (Fig. 3, D and E). CreERT2-induced *Mcl-1*^{fl} deletion significantly reduced proliferation across all lines, particularly in *Mcl-1*$^{del/del}$ MEFs (ANOVA: $P < 10^{-4}$) (Fig. 3, D and E). *Mcl-1*$^{Bcl\text{-}xL/del}$ MEFs had higher proliferation rates than did *Mcl-1*$^{Bcl\text{-}2/del}$ MEFs (ANOVA: $P < 10^{-4}$), indicating greater efficacy of BCL-XL in compensating for MCL-1 loss. The proliferation rate of *Mcl-1*$^{Bcl\text{-}2/del}$ MEFs was not significantly different than that of *Mcl-1*$^{del/del}$ MEFs, indicating that in the absence of MCL-1, inhibitory effects of BCL-2 on proliferation are negligible. These results indicate that excess apoptosis-unrelated functions of BCL-2 and BCL-XL do not contribute to the observed phenotypes in *Mcl-1*$^{Bcl\text{-}2/Bcl\text{-}2}$ and *Mcl-1*$^{Bcl\text{-}xL/Bcl\text{-}xL}$ embryos, but they do support the notion that BCL-XL is a more effective substitute for MCL-1 than is BCL-2.

Mixed genetic background *Mcl-1*$^{Bcl\text{-}xL/Bcl\text{-}xL}$ pups

One *Mcl-1*$^{Bcl\text{-}xL/Bcl\text{-}xL}$ pup (C57BL/6 background) developed to E18.5 appeared normal (Fig. 3F) with no major anomalies in brain architecture (Fig. 3G). However, specific features that might have been slightly abnormal, such as the area of the subventricular neurogenic zone and the size of the lateral ventricles, could not be statistically assessed. Because animals with mixed genetic backgrounds often better tolerate genetic mutations (*42*–*44*), we crossed *Mcl-1*$^{Bcl\text{-}2}$ and *Mcl-1*$^{Bcl\text{-}xL}$ mice to FVBxBALB/c F1 hybrids.

MCL-1 loss also caused preimplantation lethality on this background. E2.5 *Mcl-1*$^{-/-}$ embryos were compromised and rarely reached the morula stage (fig. S4, B and C). They failed to produce inner cell mass outgrowths in culture, and none developed to the E3.5 blastocyst stage (fig. S4, B and C). TUNEL$^+$ cells were detected in a dying *Mcl-1*$^{-/-}$ E2.5 morula (fig. S7), indicating that the lethality was caused by aberrant apoptosis, contrary to a previous report (*13*) but consistent with our finding that replacement of MCL-1 with BCL-2 or BCL-XL allowed development until at least E10.5.

Many *Mcl-1*$^{Bcl\text{-}xL/Bcl\text{-}xL}$ mice were born alive on the mixed genetic background, and 11% reached weaning (Fig. 4A). In contrast, no *Mcl-1*$^{Bcl\text{-}2/Bcl\text{-}2}$ mice on a mixed background were present at E19.5 or weaning (Fig. 4B). These findings further demonstrate that an apoptosis-unrelated function of MCL-1, which can be partially replaced by BCL-XL but not by BCL-2, is critical for fetal development and survival after birth.

BCL-XL cannot fully replace MCL-1 in pups

Mcl-1$^{Bcl\text{-}xL/Bcl\text{-}xL}$ pups on a mixed genetic background were abnormally small, had a hunched posture, and displayed a domed head (Fig. 4C). All died within 31 days postnatally (Fig. 4D). Histological examination revealed that the total depth of the frontal cortex and individual cortical layers showed no genotype differences (fig. S8). However, *Mcl-1*$^{Bcl\text{-}xL/Bcl\text{-}xL}$ pups had a significantly larger subventricular zone neurogenic region compared with wild-type controls (fig. S8B), and one out of five displayed enlarged lateral ventricles (fig. S8C).

In *Mcl-1*$^{Bcl\text{-}xL/Bcl\text{-}xL}$ pups, severe disruption of hepatic architecture and the reticulin network and marked steatosis were observed (Fig. 4, E to G, and fig. S9, A and B). However, *Mcl-1*$^{Bcl\text{-}xL/Bcl\text{-}xL}$ pups did not show increased concentration of serum ALT (alanine transaminase) (Fig. 4H) or immune cell infiltration in the liver (fig. S9B), indicating that the hepatocytes were not rupturing. However, *Mcl-1*$^{Bcl\text{-}xL/Bcl\text{-}xL}$ pups

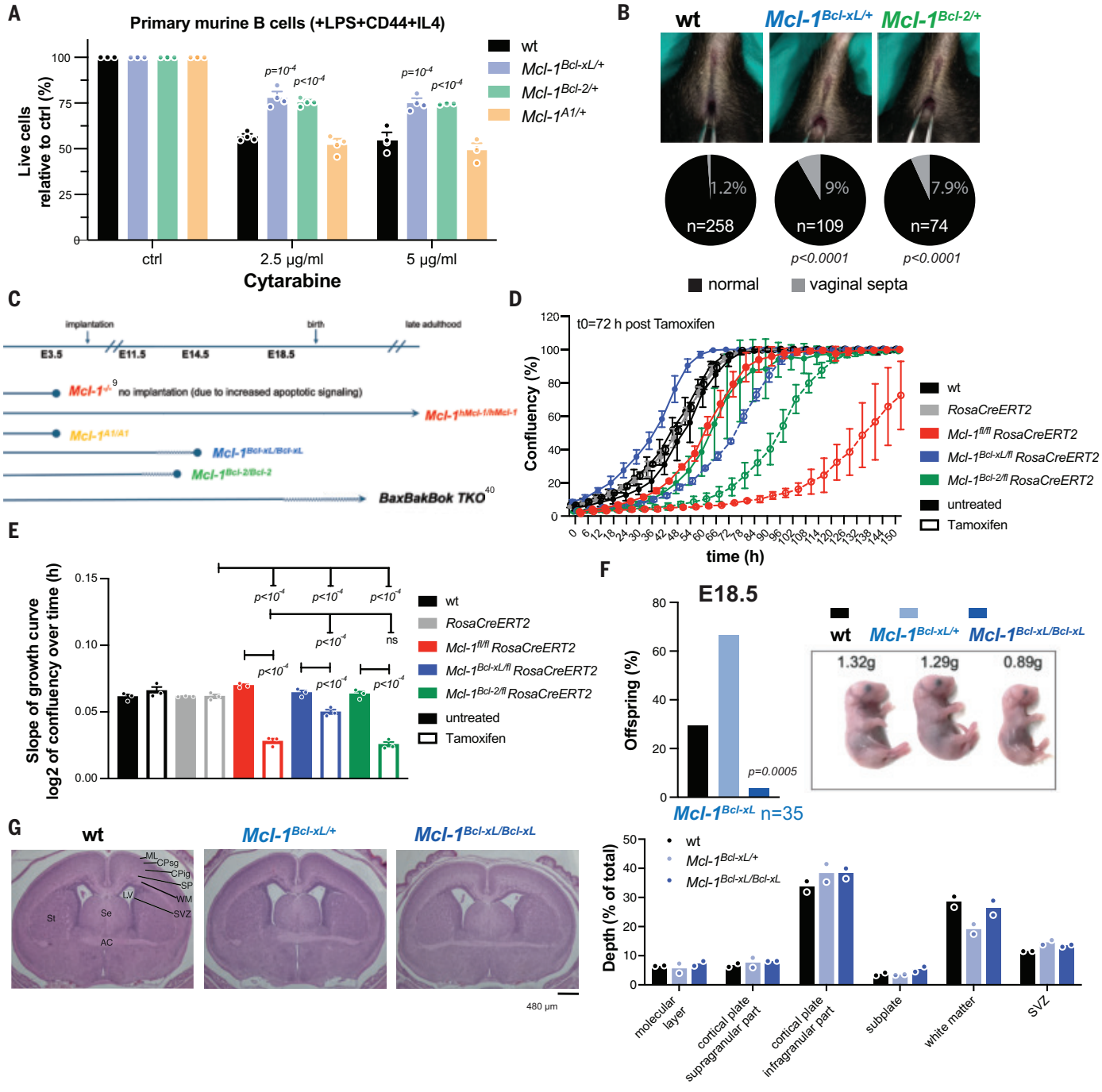

Fig. 3. Lethality of *Mcl-1*$^{Bcl\text{-}xL/Bcl\text{-}xL}$ and *Mcl-1*$^{Bcl\text{-}2/Bcl\text{-}2}$ embryos caused not only by aberrant apoptosis. (**A**) Survival (as %AnnexinV-PI-) of mitogen-activated B cells from wild-type ($n = 4$), *Mcl-1*$^{Bcl\text{-}xL/+}$ ($n = 4$), *Mcl-1*$^{Bcl\text{-}2/+}$ ($n = 4$), and *Mcl-1*$^{A1/+}$ ($n = 4$) mice treated with cytarabine for 24 hours. Data shown as mean ± SEM from ≥3 independent experiments, each performed in triplicate. Two-way ANOVA with Tukey's test; *P* values shown. (**B**) Representative images of vaginal septa in wild-type, *Mcl-1*$^{Bcl\text{-}xL/+}$, and *Mcl-1*$^{Bcl\text{-}2/+}$ females (top row) and incidence of nonperforate vaginal septa in wild-type ($n = 258$), *Mcl-1*$^{Bcl\text{-}xL/+}$ ($n = 109$), and *Mcl-1*$^{Bcl\text{-}2/+}$ ($n = 74$) females (bottom row). Chi-square test comparing observed versus expected frequencies; *P* values shown. (**C**) Schematic of developmental lethality and survival of *Mcl-1*$^{-/-}$, *Mcl-1*$^{hMcl\text{-}1/hMcl\text{-}1}$, *Mcl-1*$^{A1/A1}$, *Mcl-1*$^{Bcl\text{-}xL/Bcl\text{-}xL}$, *Mcl-1*$^{Bcl\text{-}2/Bcl\text{-}2}$, and *Bax*$^{-/-}$*Bak*$^{-/-}$*Bok*$^{-/-}$ mice. (**D**) Incucyte proliferation analysis of MEFs treated with 4-hydroxytamoxifen (1 µM) over 150 hours ($t_0 = 72$ hours post-treatment) (solid lines) or left untreated (dotted lines) ($n \geq 8$ for each genotype and condition). (**E**) Growth curve slopes from (D) analyzed with two-way ANOVA with Tukey's multiple comparison; *P* values shown. (**F**) Offspring genotype frequency at E18.5 from intercrosses of *Mcl-1*$^{Bcl\text{-}xL/+}$ mice (left) and images of a wild-type, a *Mcl-1*$^{Bcl\text{-}xL/+}$, and a *Mcl-1*$^{Bcl\text{-}xL/Bcl\text{-}xL}$ embryo at E18.5 with whole-body weights indicated (right). Genotype distributions analyzed using cumulative binomial probability (*P* values and *n* indicated). (**G**) Cresyl violet–stained coronal brain sections (E18.5) at the anterior commissure level, showing frontal cortex of wild-type, *Mcl-1*$^{Bcl\text{-}xL/+}$, and *Mcl-1*$^{Bcl\text{-}xL/Bcl\text{-}xL}$ embryos (left) with morphometric analysis of cortical layers, subventricular zone (SVZ), and lateral ventricles (LV) (right). Circles represent the left and right side of the single brain per genotype. AC, anterior commisure; CPig, cortical plate, intrage; CPsg, cortical plate, infragranular and supragranular part; ML, molecular layer; Se, subependymal zone; SP, subplate; St, striatum; SVZ, subventricular zone; WM, white matter.

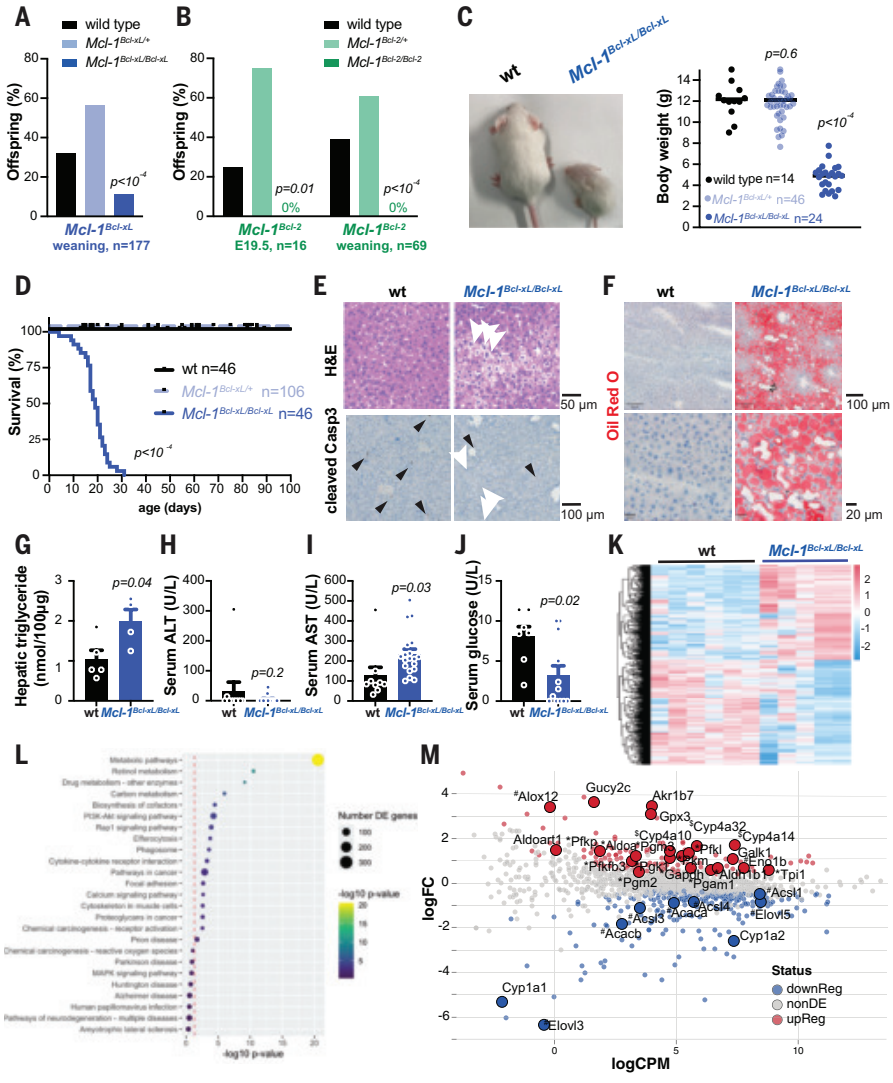

Fig. 4. Requirement of apoptosis-unrelated function of MCL-1 for survival of mice after birth. (**A**) Offspring genotype frequency at weaning from *Mcl-1*$^{Bcl\text{-}xL/+}$ ($n = 177$) intercrosses (FVBxBALB/cxC57BL/6) analyzed using cumulative binomial probability; *P* values shown. (**B**) Offspring genotype frequency from *Mcl-1*$^{Bcl\text{-}2/+}$ intercrosses (FVBxBALB/cxC57BL/6) at weaning ($n = 69$) and E19.5 ($n = 16$) analyzed using cumulative binomial probability; *P* values shown. (**C**) Representative images of a wild-type and a *Mcl-1*$^{Bcl\text{-}xL/Bcl\text{-}xL}$ mouse at postnatal day 21 (FVBxBALB/cxC57 BL/6, left), and body weights of wild-type ($n = 14$), *Mcl-1*$^{Bcl\text{-}xL/+}$ ($n = 46$), and *Mcl-1*$^{Bcl\text{-}xL/Bcl\text{-}xL}$ ($n = 24$) mice at postnatal day 21 (FVBxBALB/cxC57BL /6, male and female, right). One-way ANOVA with Dunnett's multiple comparison test; *P* values shown. (**D**) Kaplan-Meier survival curve of wild-type ($n = 46$), *Mcl-1*$^{Bcl\text{-}xL/+}$ ($n = 106$), and *Mcl-1*$^{Bcl\text{-}xL/Bcl\text{-}xL}$ ($n = 46$) mice (FVBxBALB/cxC57 BL/6). Log rank (Mantel-Cox) test; *P* values shown. (**E**) Representative (from $n \geq 3$ for each genotype) hematoxylin and eosin–stained liver sections (top row) and cleaved (activated) caspase-3–stained sections (bottom row) of wild-type (left) and *Mcl-1*$^{Bcl\text{-}xL/Bcl\text{-}xL}$ mice (right) (FVBxBALB/cxC57BL/6). Black arrowheads, apoptotic (cleaved caspase-3 positive) cells; white arrowheads, swelling hepatocytes. (**F**) Representative Oil Red O–stained liver sections (detecting lipids) from wild-type (left) and *Mcl-1*$^{Bcl\text{-}xL/Bcl\text{-}xL}$ pups (right) (FVBxBALB/cxC57BL/6). (**G**) Triglyceride content in liver extracts from wild-type ($n = 5$) and *Mcl-1*$^{Bcl\text{-}xL/Bcl\text{-}xL}$ ($n = 4$) pups (FVBxBALB/cxC57BL/6). (**H** to **J**) Serum concentration of (H) alanine aminotransferase (ALT), (I) aspartate aminotransferase (AST), (J) glucose from wild-type [wt: (H) $n = 7$, (I) and (J) $n = 9$] and *Mcl-1*$^{Bcl\text{-}xL/Bcl\text{-}xL}$ [(H) n=9, (I) and (J) $n = 19$] pups (FVBxBALB/cxC57BL/6). [(G) to (J)] Data shown as mean ± SEM analyzed by two-tailed *t* test; *P* values shown. (**K** to **M**) RNA-seq analysis in liver extracts from wild-type ($n = 6$) and *Mcl-1*$^{Bcl\text{-}xL/Bcl\text{-}xL}$ ($n = 4$) pups (FVBxBALB/cxC57BL/6). (K) Heatmap showing differentially expressed genes. (L) Enrichment plot showing the top 25 deregulated pathways using KEGG (Kyoto Encyclopedia of Genes and Genomes) analysis. (M) MA plot showing deregulated genes within metabolic pathway determined by KEGG pathway analysis. Genes involved in glycolysis (*Pfkl*, *Pfkp*, *Pfkfb3*, *Tpi1*, *Aldoa*, *Gapdh*, *Pkm*, *Pgk1*, *Pgam1*, *Pgm2*, *Pgm3*; marked with an asterisk), lipid metabolism (*Acsl1*, *Acsl3*, *Acsl4*, *Eno1b*, *Elovl5*, *Acacb*, *Acaca*, *Elovl3*, *Alox12*; marked with a hashtag), fatty acid omega oxidation (*Cyp4a32*, *Cyp4a10*, *Cyp4a14*; marked with a dollar sign), and other nonaerobic metabolic pathways that may be associated with liver damage (*Aldoart1*, *Gucy2c*, *Akr1b7*, *Gpx3*, *Galk1*) are highlighted. downReg, down-regulated; nonDE; not differentially expressed; upReg, up-regulated.

had significantly increased concentrations of serum AST (aspartate transaminase) and creatine kinase (Fig. 4I and fig. S9C), possibly because of damage in other tissues (fig. S9, D to F). The small intestine showed disorganized crypts with abnormally low cell numbers (fig. S9D), whereas kidney damage included degeneration of proximal renal tubular cells and glomeruli (fig. S9E). Cardiomyocytes appeared to undergo degeneration (fig. S9F). Staining for activated caspase-3 (Fig. 4E, bottom row, and fig. S9, D to G) and TUNEL in the liver (fig. S9H) revealed no increase in apoptosis. No hepatic (fig. S9B) or cardiac fibrosis (fig. S10A) was detected, a phenotype driven by BAX- or BAK-mediated apoptosis with cardiomyocyte-specific MCL-1 deletion (*25*). This indicates that the observed defects result from the loss of an apoptosis-unrelated function of MCL-1.

Mcl-1$^{Bcl\text{-}xL/Bcl\text{-}xL}$ pups exhibited a phenotype similar to that of *Vdac2*$^{-/-}$ pups, which also die shortly after birth with swelling hepatocytes and liver damage (*45*) (fig. S10B). Given the role of VDAC2 in ATP export from mitochondria, this phenotype was linked to metabolic defects (*45*, *46*). Thus, *Mcl-1*$^{Bcl\text{-}xL/Bcl\text{-}xL}$ pups might exhibit similar metabolic defects. Congruently, serum glucose concentrations were abnormally reduced (Fig. 4J), suggesting dysregulation of glucose metabolism pathways.

RNA sequencing (RNA-seq) analysis of livers from *Mcl-1*$^{Bcl\text{-}xL/Bcl\text{-}xL}$ pups revealed significantly altered expression of metabolic genes (Fig. 4, K and L), with up-regulation of glycolysis-related genes and down-regulation of lipid metabolism genes (Fig. 4M). Several genes involved in fatty acid omega oxidation, a compensatory process in the endoplasmic reticulum triggered by defects in mitochondrial beta oxidation (*47*), were also up-regulated. Differential gene expression analysis in MEFs (fig. S11A) revealed that *Mcl-1*$^{del/del}$ and *Mcl-1*$^{Bcl\text{-}2/del}$ MEFs exhibited substantially greater overlap in up-regulated (but not down-regulated) metabolic genes than did *Mcl-1*$^{del/del}$ and *Mcl-1*$^{Bcl\text{-}xL/del}$ MEFs (chi-square test: $P = 5 \times 10^{-6}$ and $P = 0.3$, respectively; fig. S11B and table S2). This indicates that BCL-XL compensates for the loss of MCL-1 in the regulation of metabolism better than BCL-2 does.

Metabolic defects in *Mcl-1*$^{Bcl\text{-}xL/Bcl\text{-}xL}$ pups

MCL-1 controls mitochondrial morphology and OXPHOS by regulating complex IV assembly and activity (*22*, *25*). No

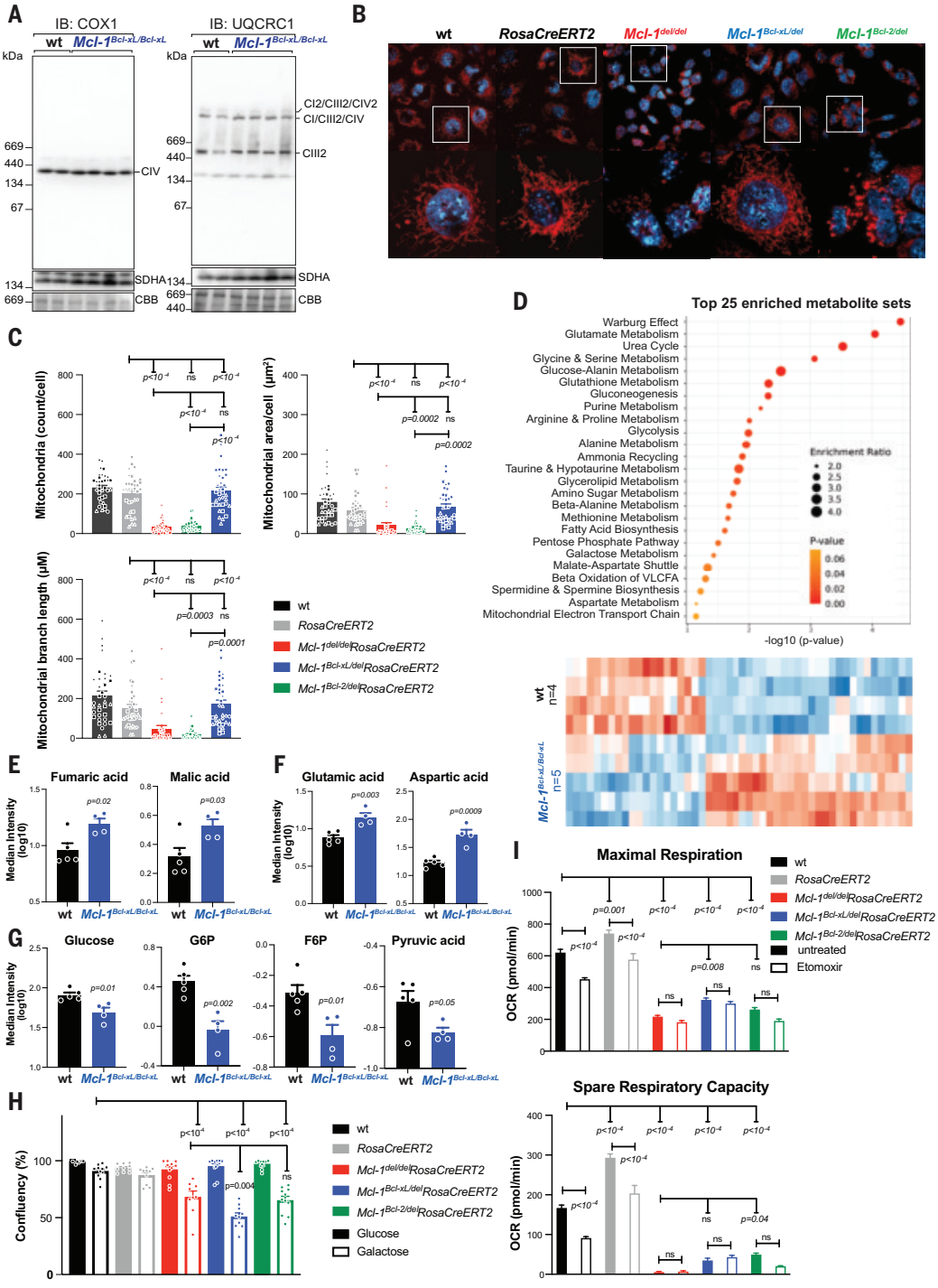

Fig. 5. The metabolic function of MCL-1 in fatty acid oxidation is critical for liver function. (**A**) Blue native PAGE and immunoblot analysis of respiratory complexes I–IV (CI–CIV) in mitochondria isolated from livers of wild-type and *Mcl-1*$^{Bcl\text{-}xL/Bcl\text{-}xL}$ pups. UQCRC1 and COX1 antibodies were used for CI-III and CIV detection, respectively. Coomassie-stained complex V (CV) serves as a loading control. (**B**) Representative immunofluorescent images of MEFs of the indicated genotypes showing mitochondria stained with MitoTracker (red) and cell nuclei stained with DAPI (4′,6-diamidino-2-phenylindole; blue). (**C**) Quantification of mitochondrial count, area, and branching in MEFs of the indicated genotypes using ImageJ. Data shown as mean ± SEM from $n = 35$ cells across four independent experiments. All data points shown with each experiment indicated by distinct symbols (e.g., circle, square, diamond, triangle). One-way ANOVA with Dunnett's multiple comparison; *P* values shown. (**D** to **G**) Metabolomics analysis in liver extracts from wild-type ($n = 5$) and *Mcl-1*$^{Bcl\text{-}xL/Bcl\text{-}xL}$ ($n = 4$) pups (FVBxBALB/cxC57BL/6). (D) Metabolite pathway analysis (top) and heatmap showing the top 25 deregulated metabolites (bottom). Metabolite levels of (E) fumaric acid (FA) and malic acid (MA), (F) glutamic acid (GA) and aspartic acid (AA), and (G) glucose (Glu), glucose-6-phosphate (G6P), fructose-6-phosphate (F6P), and pyruvic acid. Data shown as mean ± SEM, two-tailed *t* test; *P* values shown. (**H**) Incucyte proliferation analysis of MEFs cultured for 48 hours in glucose (filled bars) or galactose (hollow bars). Data shown as mean ± SEM ($n = 3$ independent experiments in triplicate; all data points shown). Two-way ANOVA with Tukey's multiple comparison; *P* values shown. (**I**) Representative Seahorse analysis in MEFs of the indicated genotypes with (hollow bars) or without (filled bars) treatment with the CPT1a inhibitor etomoxir, showing maximal respiration (top) and spare respiratory capacity (bottom). Data shown as mean ± SEM from $n \geq 6$ replicates. Two-way ANOVA with Tukey's multiple comparison; *P* values shown.

defects in complex IV, or any other electron transport chain complexes, were observed in liver extracts from *Mcl-1*$^{Bcl\text{-}xL/Bcl\text{-}xL}$ pups (Fig. 5A). Complex IV defects were only observed in *Mcl-1*$^{-/-}$ MEFs cultured without MCL-1 long term, whereas acute or medium-term induced deletion of *Mcl-1* in *Mcl-1*$^{del/del}$, *Mcl-1*$^{Bcl\text{-}2/del}$, or *Mcl-1*$^{Bcl\text{-}xL/del}$ MEFs did not affect complex IV formation or activity (fig. S12, A to D). Thus, complex IV defects may be secondary to prolonged loss of MCL-1. No complex IV defects were observed in *Mcl-1*$^{Bcl\text{-}xL/Bcl\text{-}xL}$ MEFs (fig. S12E). *Mcl-1*$^{del/del}$ and *Mcl-1*$^{Bcl\text{-}2/del}$ MEFs showed fragmented mitochondria whereas *Mcl-1*$^{Bcl\text{-}xL/del}$ MEFs had normal mitochondrial structure (Fig. 5, B and C). Electron microscopy confirmed these findings, however, normal cristae organization was seen in intact mitochondria from *Mcl-1*$^{del/del}$, *Mcl-1*$^{Bcl\text{-}2/del}$, *Mcl-1*$^{Bcl\text{-}xL/del}$, and *Mcl-1*$^{Bcl\text{-}xL/Bcl\text{-}xL}$ MEFs (fig. S13). Thus, in MEFs and hepatocytes, BCL-XL can at least partially replace the function of MCL-1 in electron transport chain assembly and mitochondrial morphology.

MCL-1 loss, akin to treatment with certain drugs (*48*), causes defects in FAO (*29*, *30*), and this may underlie the defects observed in *Mcl-1*$^{Bcl\text{-}xL/Bcl\text{-}xL}$ pups. To explore this, we conducted metabolomic analyses on liver extracts from *Mcl-1*$^{Bcl\text{-}xL/Bcl\text{-}xL}$ pups and wild-type littermates (Fig. 5, D to G, and fig. S14, A to D). This revealed significant dysregulation in key metabolic pathways (Fig. 5D). Amounts of tricarboxylic acid cycle intermediates malic and fumaric acid (Fig. 5E and fig. S14A) and the metabolites aspartic and glutamic acid (Fig. 5F) were increased, indicating dysregulation of mitochondrial metabolic pathways. Depletion of glucose and early glycolytic intermediates suggests dysregulation of glucose metabolism pathways (Fig. 5F and fig. S14B). Increased abundance of ketone bodies (e.g., 2-HB; fig. S14C) indicate activation of alternative ketogenesis pathways. Increased long-chain fatty acid (LCFA) levels and dodecanoic acid accumulation (fig. S14D) point to defects in FAO.

Together with the RNA-seq analysis (Fig. 4, K to M), these findings indicate that defects in FAO are associated with metabolic adaptations, including increased glycolysis in *Mcl-1*$^{Bcl\text{-}xL/Bcl\text{-}xL}$ pups. Steatosis in *Mcl-1*$^{Bcl\text{-}xL/Bcl\text{-}xL}$ pups is likely caused by loss of MCL-1 function in regulating FAO that cannot be replaced by BCL-XL.

Role of MCL-1 in FAO

Supporting the hypothesis that MCL-1 regulates FAO, we observed proliferation defects and reduced ATP production in *Mcl-1*$^{del/del}$, *Mcl-1*$^{Bcl\text{-}2/del}$, and *Mcl-1*$^{Bcl\text{-}xL/del}$ MEFs when cultured in galactose to promote aerobic energy production (Fig. 5H and fig. S14E). No differences were observed in *Mcl-1*$^{Bcl\text{-}2/del}$ or *Mcl-1*$^{Bcl\text{-}xL/del}$ MEFs when compared with *Mcl-1*$^{del/del}$ MEFs, thus neither BCL-2 nor BCL-XL appears to compensate for MCL-1 under nonglycolytic conditions.

Seahorse analysis revealed significant reduction in maximal respiration and spare respiratory capacity in *Mcl-1*$^{del/del}$, *Mcl-1*$^{Bcl\text{-}2/del}$, and *Mcl-1*$^{Bcl\text{-}xL/del}$ MEFs compared with those of control MEFs (*Mcl-1*$^{fl/fl}$, *Mcl-1*$^{Bcl\text{-}2/fl}$, *Mcl-1*$^{Bcl\text{-}xL/fl}$, wild type, and *RosaCreERT2*$^{+/Ki}$; fig. S14F). No significant further reduction was observed in *Mcl-1*$^{del/del}$, *Mcl-1*$^{Bcl\text{-}2/del}$, or *Mcl-1*$^{Bcl\text{-}xL/del}$ MEFs upon treatment with the carnitine palmitoyltransferase 1a (CPT1a) inhibitor etomoxir (inhibiting FAO), unlike in wild-type and *RosaCreERT2*$^{+/Ki}$ MEFs (Fig. 5I), suggesting a metabolic shift from FAO to alternative pathways. No significant differences were seen between *Mcl-1*$^{del/del}$ versus *Mcl-1*$^{Bcl\text{-}2/del}$ and *Mcl-1*$^{Bcl\text{-}xL/del}$ MEFs, indicating that the primary metabolic role of MCL-1 is regulating FAO, with no compensation from BCL-2 or BCL-XL. Notably, CPT1a and ACSL1 expression was detected by Western blotting in liver and heart lysates from heterozygous *Mcl-1*$^{hMcl\text{-}1/+}$, *Mcl-1*$^{Bcl\text{-}2/+}$, and *Mcl-1*$^{Bcl\text{-}xL/+}$mice (fig. S15, A and B) and homozygous E10.5 *Mcl-1*$^{hMcl\text{-}1/hMcl\text{-}1}$, *Mcl-1*$^{Bcl\text{-}xL/Bcl\text{-}xL}$, and *Mcl-1*$^{Bcl\text{-}2/Bcl\text{-}2}$ embryos (fig. S15C) as well as by IHC in liver and heart tissues from mixed background homozygous *Mcl-1*$^{Bcl\text{-}xL/Bcl\text{-}xL}$ pups (fig. S15, D and E).

Collectively, these findings show that in various tissues and cells during late development and after birth, MCL-1 is essential not only for inhibiting apoptosis but also for regulating critical apoptosis-unrelated processes. BCL-XL, but not BCL-2, can substitute for MCL-1 in regulating the mitochondrial electron transport chain, but neither can replace MCL-1 in controlling FAO.

Discussion

Our study using *Mcl-1* gene-replacement mice resolved the physiological importance of the anti-apoptotic versus apoptosis-unrelated function(s) of MCL-1 in pre- and postnatal development. Although *Mcl-1*$^{-/-}$ blastocysts were reported to fail implantation without apoptosis (*13*), we observed apoptotic DNA fragmentation in a *Mcl-1*$^{-/-}$ E2.5 embryo, indicating aberrant apoptosis. Congruently, replacing MCL-1 with BCL-2 or BCL-XL supported embryogenesis until E13.5. Although both MCL-1 and BCL-XL may regulate mitochondrial OXPHOS (*26*, *29*, *30*, *49*), BCL-2 does not, as it lacks intermitochondrial membrane localization (*28*, *50*). Recently, MCL-1 was shown to regulate FAO by binding to ACSL1, thereby facilitating LCFA import into mitochondria (*30*). BCL-2 does not interact with ACSL1 and thus cannot replace any of the reported metabolic functions of MCL-1 (*30*). Collectively, these findings demonstrate that only the anti-apoptotic function, but no apoptosis-unrelated functions, of MCL-1 is essential for early embryogenesis.

At later developmental stages and postnatally, the role of MCL-1 in regulating mitochondrial metabolism was essential for normal cell function and survival. *Mcl-1*$^{Bcl\text{-}xL/Bcl\text{-}xL}$ and *Mcl-1*$^{Bcl\text{-}2/Bcl\text{-}2}$ fetuses died significantly earlier than *Bax*$^{-/-}$*Bak*$^{-/-}$*Bok*$^{-/-}$ fetuses lacking all apoptotic executioners (*38*), indicating developmental defects unrelated to apoptosis. BCL-XL proved more effective than BCL-2 in compensating for MCL-1 loss, although it, too, could not fully replace the metabolic role of MCL-1. *Mcl-1*$^{Bcl\text{-}xL/Bcl\text{-}xL}$ embryos developed 1 day further on a C57BL/6 background, and only *Mcl-1*$^{Bcl\text{-}xL/Bcl\text{-}xL}$, but not *Mcl-1*$^{Bcl\text{-}2/Bcl\text{-}2}$, mice were born alive on a mixed genetic background. We propose that these differences are due to the ability of BCL-XL, but not BCL-2, to sustain OXPHOS (*26*, *49*). Consistently, we found no defects in the assembly of the electron transport chain in *Mcl-1*$^{Bcl\text{-}xL/Bcl\text{-}xL}$ pups. However, *Mcl-1*$^{Bcl\text{-}xL/Bcl\text{-}xL}$ mixed genetic background pups suffered from severe metabolic defects due to impaired FAO, presumably owing to the loss of the interaction of MCL-1 with ACSL1 (*30*). A weak interaction between BCL-XL and ACSL1 has been observed (*30*); however, our data indicate that this is insufficient for effective FAO needed for the survival of cells with high energy demand (e.g., hepatocytes).

Our findings show that both the anti-apoptotic and apoptosis-unrelated roles of MCL-1 are essential for pre- and postnatal development, with their importance varying by developmental stage and cell type. This information has implications for the efficacy and tolerability of MCL-1 inhibitors in cancer therapy.

REFERENCES AND NOTES

1. A. Glucksmann, *Biol. Rev. Camb. Philos. Soc.* **26**, 59–86 (1951).
2. A. K. Voss, A. Strasser, *F1000Res.* **9**, 148 (2020).
3. A. Strasser, L. O'Connor, V. M. Dixit, *Annu. Rev. Biochem.* **69**, 217–245 (2000).
4. C. B. Thompson, *Science* **267**, 1456–1462 (1995).
5. P. E. Czabotar, G. Lessene, A. Strasser, J. M. Adams, *Nat. Rev. Mol. Cell Biol.* **15**, 49–63 (2014).
6. R. Singh, A. Letai, K. Sarosiek, *Nat. Rev. Mol. Cell Biol.* **20**, 175–193 (2019).
7. D. R. Green, G. Kroemer, *Science* **305**, 626–629 (2004).
8. X. Luo, K. L. O'Neill, K. Huang, *F1000Res.* **9**, 935 (2020).
9. G. S. Salvesen, V. M. Dixit, *Cell* **91**, 443–446 (1997).
10. G. S. Salvesen, V. M. Dixit, *Proc. Natl. Acad. Sci. U.S.A.* **96**, 10964–10967 (1999).
11. K. Brinkmann, A. P. Ng, C. A. de Graaf, A. Strasser, *Cell Death Differ.* **29**, 1079–1093 (2022).
12. J. T. Opferman, A. Kothari, *Cell Death Differ.* **25**, 37–45 (2018).
13. J. L. Rinkenberger, S. Horning, B. Klocke, K. Roth, S. J. Korsmeyer, *Genes Dev.* **14**, 23–27 (2000).
14. N. Motoyama *et al.*, *Science* **267**, 1506–1510 (1995).
15. P. Bouillet, S. Cory, L. C. Zhang, A. Strasser, J. M. Adams, *Dev. Cell* **1**, 645–653 (2001).

16. D. J. Veis, C. M. Sorenson, J. R. Shutter, S. J. Korsmeyer, *Cell* **75**, 229–240 (1993).
17. R. L. Schenk *et al.*, *Cell Death Differ.* **24**, 534–545 (2017).
18. K. W. Adams, G. M. Cooper, *J. Biol. Chem.* **282**, 6192–6200 (2007).
19. M. J. Herold *et al.*, *J. Biol. Chem.* **281**, 13663–13671 (2006).
20. U. Maurer, C. Charvet, A. S. Wagman, E. Dejardin, D. R. Green, *Mol. Cell* **21**, 749–760 (2006).
21. A. Gross, S. G. Katz, *Cell Death Differ.* **24**, 1348–1358 (2017).
22. R. M. Perciavalle *et al.*, *Nat. Cell Biol.* **14**, 575–583 (2012).
23. M. L. Rasmussen *et al.*, *Stem Cell Reports* **10**, 684–692 (2018).
24. M. L. Rasmussen *et al.*, *iScience* **23**, 101015 (2020).
25. X. Wang *et al.*, *Genes Dev.* **27**, 1351–1364 (2013).
26. K. N. Alavian *et al.*, *Nat. Cell Biol.* **13**, 1224–1233 (2011).
27. S. B. Berman *et al.*, *J. Cell Biol.* **184**, 707–719 (2009).
28. T. Lithgow, R. van Driel, J. F. Bertram, A. Strasser, *Cell Growth Differ.* **5**, 411–417 (1994).
29. M. S. Prew *et al.*, *Cell Rep.* **41**, 111445 (2022).
30. T. Wright *et al.*, *Mol. Cell* **84**, 1338–1353.e8 (2024).
31. R. L. Thomas *et al.*, *Genes Dev.* **27**, 1365–1377 (2013).
32. S. T. Diepstraten *et al.*, *Nat. Rev. Cancer* **22**, 45–64 (2022).
33. J. Montero, A. Letai, *Cell Death Differ.* **25**, 56–64 (2018).
34. M. S. Brennan *et al.*, *Blood* **132**, 1573–1583 (2018).
35. A. Kotschy *et al.*, *Nature* **538**, 477–482 (2016).
36. K. Takaoka, H. Hamada, *Development* **139**, 3–14 (2012).
37. N. Renier *et al.*, *Cell* **159**, 896–910 (2014).
38. F. F. S. Ke *et al.*, *Cell* **173**, 1217–1230.e17 (2018).
39. J. Seibler *et al.*, *Nucleic Acids Res.* **31**, e12 (2003).
40. Y. M. Janumyan *et al.*, *EMBO J.* **22**, 5459–5470 (2003).
41. G. P. Linette, Y. Li, K. Roth, S. J. Korsmeyer, *Proc. Natl. Acad. Sci. U.S.A.* **93**, 9545–9552 (1996).
42. M. Bonyadi *et al.*, *Nat. Genet.* **15**, 207–211 (1997).
43. H. M. McRae *et al.*, *Development* **147**, dev187021 (2020).
44. H. M. McRae *et al.*, *Blood* **133**, 1729–1741 (2019).
45. H. S. Chin *et al.*, *Nat. Commun.* **9**, 4976 (2018).
46. M. Y. Liu, M. Colombini, *Biochim. Biophys. Acta* **1098**, 255–260 (1992).
47. Y. Miura, *Proc. Jpn. Acad. Ser. B Phys. Biol. Sci.* **89**, 370–382 (2013).
48. S. K. Satapathy, V. Kuwajima, J. Nadelson, O. Atiq, A. J. Sanyal, *Ann. Hepatol.* **14**, 789–806 (2015).
49. Y. B. Chen *et al.*, *J. Cell Biol.* **195**, 263–276 (2011).
50. S. Krajewski *et al.*, *Cancer Res.* **53**, 4701–4714 (1993).

ACKNOWLEDGMENTS

The authors thank WEHI Bioservices, particularly G. Siciliano, J. Gilbert, T. Baldwin, L. Spencer, L. Johnson, T. Kitson, and K. Franks for animal husbandry and help with experiments using mice; B. Helbert, R. Chan, and N. Coleman for genotyping; the WEHI Histology Centre, particularly E. Tsui, E. Pan, and A. Spence; M. Clark, G. Giner, N. Kapuruge, and A. Garnham for experimental advice; J. Opferman for sharing critical reagents and discussions; G. Kelly, A. Rose, L. Formosa, and M. Lazarou for their help with data interpretation and discussions; and L. Whitehead for imaging data processing. The generation of the gene-swap mice used in this study was supported by Phenomics Australia and the Australian Government through the National Collaborative Research Infrastructure Strategy (NCRIS) program. **Funding:** National Health and Medical Research Council (NHMRC) program grant 101671 (A.S., P.B.); NHMRC investigator grant 1020363 (A.S.); NHMRC investigator grant 1176789 (A.K.V.); NHMRC fellowship 2017971 (M.J.H.); NHMRC ideas grant 2021510 (K.B., K.M.); NNHMRC project grant 1160618 (T.T.); NHMRC ideas grant 2010711 (T.T.); Cancer Council Grant-in-Aid 2024 (A.S., K.B.); Victorian Cancer Agency MCR fellowship 23020 (K.B.); Leukemia Foundation Research Scholarship (D.D'S.); Viertel Senior Medical Research Fellowship (T.L.P.); NMRC OF-IRG MOH-000614 (N.Y.F.); Bodhi Education Fund Fellowship (G.D.). **Author contributions:** Conceptualization: K.B., M.J.H., A.S.; Methodology: K.B., K.M., A.J.K., A.T., L.G., A.B., D.D'S., L.G.W., C.L.R., S.Ma., S.N.E.D., S.Mo., V.C.W., P.A., K.K.B., T.T., A.K.V.; Investigation: K.B., K.M., M.J.H., J.M.M., T.T., G.D., K.K.B., T.L.P., N.Y.F., P.B., A.K.V., A.S.; Visualization: K.B., S.Ma., A.T., L.G., S.Mo., S.N.E.D., J.M.M., V.C.W., P.A., A.S., A.K.V.; Funding acquisition: K.B., K.M., A.S., M.J.H., A.K.V.; Project administration: K.B., A.S.; Supervision: K.B., A.S., M.J.H., A.K.V., T.T., K.M.; Writing – original draft: K.B., A.S., M.J.H., A.K.V., T.T., K.M.; Writing – review & editing: All authors. **Diversity, equity, ethics, and inclusion:** This study was conducted by researchers with a broad range of backgrounds, including early, mid-, and late career researchers from 11 different nationalities. **Competing interests:** K.B., A.J.K., A.T., S.Ma., K.M., L.G.W., D.D'S., S.Mo., J.M.M., V.C.W., L.G., P.A., N.Y.F., T.L.P., G.D., P.B., A.K.V., T.T., M.J.H., and A.S. are, or were for some time, employees of the Walter and Eliza Hall Institute. The Walter and Eliza Hall Institute receives milestone payments and royalties from the sale of venetoclax, parts of which are distributed to current and former employees. M.J.H. and A.S. collaborated with Servier on the development of MCL-1 inhibitors and received financial support for some of their research. S.Ma., S.N.E.D., A.B., K.K.B., and C.R. declare that they have no conflicts of interest. **Data and materials availability:** RNA-seq data presented in this study can be accessed through the Gene Expression Omnibus (GSE299730). Metabolomics LC-MS data presented in this study can be accessed through the Metabolomics Workbench (ID#5995). All other data are available in the main text or the supplementary materials. This research was funded in whole or in part by the National Health and Medical Research Council (101671, 1020363, 1176789, 2017971, 2021510, 1160618, 2010711), a cOAlition S organization. The author will make the Author Accepted Manuscript (AAM) version available under a CC BY public copyright license.

SUPPLEMENTARY MATERIALS

science.org/doi/10.1126/science.adw1836
Materials and Methods; Figs. S1 to S15; Tables S1 to S5; References (*51–65*); MDAR Reproducibility Checklist; Movies S1 to S3

Submitted 23 January 2025; accepted 25 June 2025; published online 3 July 2025
10.1126/science.adw1836

ASTROPHYSICS

Improving cosmological reach of a gravitational wave observatory using Deep Loop Shaping

Jonas Buchli[1]*† Brendan Tracey[1]†, Tomislav Andric[2,3]†, Christopher Wipf[4]†, Yu Him Justin Chiu[1]†, Matthias Lochbrunner[1]†, Craig Donner[1]†, Rana X. Adhikari[4]*, Jan Harms[2,3]*†, Iain Barr[1], Roland Hafner[1], Andrea Huber[1], Abbas Abdolmaleki[1], Charlie Beattie[1], Joseph Betzwieser[4], Serkan Cabi[1], Jonas Degrave[1], Yuzhu Dong[1], Leslie Fritz[1], Anchal Gupta[4], Oliver Groth[1], Sandy Huang[1], Tamara Norman[1], Hannah Openshaw[1], Jameson Rollins[4], Greg Thornton[1], George van den Driessche[1], Markus Wulfmeier[1], Pushmeet Kohli[1]*, Martin Riedmiller[1], The LIGO Instrument Team‡

Improved low-frequency sensitivity of gravitational wave observatories would unlock study of intermediate-mass black hole mergers and binary black hole eccentricity and provide early warnings for multimessenger observations of binary neutron star mergers. Today's mirror stabilization control injects harmful noise, constituting a major obstacle to sensitivity improvements. We eliminated this noise through Deep Loop Shaping, a reinforcement learning method using frequency domain rewards. We proved our methodology on the LIGO Livingston Observatory (LLO). Our controller reduced control noise in the 10- to 30-hertz band by over 30x and up to 100x in subbands, surpassing the design goal motivated by the quantum limit. These results highlight the potential of Deep Loop Shaping to improve current and future gravitational wave observatories and, more broadly, instrumentation and control systems.

The gravitational wave (GW) detectors LIGO and Virgo have revolutionized astrophysics by detecting mergers of exotic objects, such as black holes (BHs) and neutron stars (NSs) (*1*–*3*). Currently, most of the detectable signal lies in the 30- to 2000-Hz band, leaving the low-frequency band (10 to 30 Hz) largely unexplored. Enhancing sensitivity in this band could lead to a substantial increase in cosmological reach and thus in the scientific capabilities of LIGO (Fig. 1A). The 10- to 30-Hz band is also important for the early (premerger) detection of binary neutron stars (BNSs), potentially doubling the warning time, which would enable real-time observation of neutron star collisions, the subsequent creation of heavy elements, and the birth of black holes (*4*–*6*). However, such sensitivity improvements are currently partially limited by injected control noise on the interferometer mirrors. Furthermore, as the control noise is a bottleneck to overall sensitivity improvements, there is currently little to be gained from improvements to other noise sources. We addressed this challenge with a new tailored reinforcement learning (RL) method and improved the alignment control of the LIGO mirrors. We lowered the injected control noise on the most demanding feedback control loop, the common-hard-pitch (θ_{CHP}) loop of the Livingston Observatory, below the quantum back-action limit. By eliminating the harmful noise from this critical representative controller, we paved the path to improve LIGO's sensitivity.

The space-time strain associated with even the loudest GW signals produces a signal equivalent to only $\approx 10^{-19}$ meters of mirror motion. As a comparison, the environmental disturbance, due to Earth tides and seismic vibration, is roughly 13 orders of magnitude larger. To measure the weak GW signals, laser-interferometric GW detectors have hundreds of optomechanical degrees of freedom that require stabilization. Active control is used to achieve precise stabilization in the face of complex mirror dynamics and inherently unstable degrees of freedom. More specifically, the optomechanical response

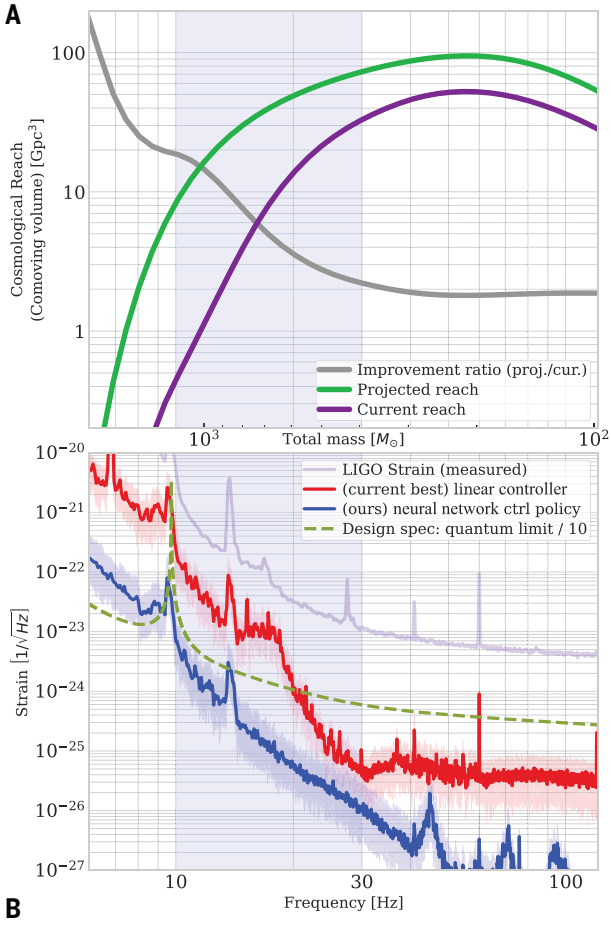

Fig. 1. Cosmological reach and strain noise from control. (**A**) The plot shows the volume in space explored with binary BH merger waveforms (*20*) for different cases of technical noise. The *x* axis in (A) is the total mass of the equal-mass binary pair. This corresponds to the *x* axis in (B), the frequency of the first quasinormal mode of a Schwarzschild BH with such a mass, as measured in the source frame. The purple trace shows the reach of LIGO as of March 2024. The green trace shows the volumetric improvement in the case where the technical noise is removed entirely. Many of the known technical noise sources are linked to controls. (**B**) LIGO's noise budget and controller performance. Lavender represents overall measured strain noise, red represents strain noise contribution from the currently operational linear controller for θ_{CHP}, and blue represents strain noise contribution from neural network RL policy as run on the LIGO Livingston Observatory on 5 Dec 2024 (mean, 10th and 90th percentiles of amplitude spectral density (ASD) of control action of neural network control policy). The dashed green line indicates the control design goal derived from the quantum back-action limit by applying a design margin of 10x; the control noise should drop below this curve. A detailed accounting of technical noise sources is available in (*21*).

[1]Google DeepMind, London, UK. [2]Gran Sasso Science Institute (GSSI), L'Aquila, Italy. [3]Laboratori Nazionali del Gran Sasso, Assergi (INFN), Italy. [4]LIGO Laboratory, Division of Physics, Math, and Astronomy, California Institute of Technology, Pasadena, CA, USA. ***Corresponding author. Email: buchli@google.com (J.B.); rana@caltech.edu (R.X.A.); jan.harms@gssi.it (J.H.); pushmeet@google.com (P.K.)** †These authors contributed equally to this work. ‡LIGO Instrument Team authors and affiliations are listed in the supplementary materials.

of the interferometer (i.e., the plant) is subject to dynamic variations: Even low absorption of the high-power laser beam (~300 to 500 kW) causes thermal distortions in the mirrors, leading to offsets in sensor signals and changes in optomechanical resonant frequencies. In addition, the high-power laser also creates substantial forces and torques on the suspended mirrors, leading to optomechanical instabilities of several mechanical eigenmodes (*7*–*9*). These resonances are stabilized using feedback control, but any noise injected by the feedback controllers into the GW readout harms the peak astrophysical sensitivity and drowns out the GW signals themselves.

In simplified terms, the main control design challenge is that larger control action in lower frequencies provides better disturbance rejection but injects higher noise into the observation band. Conversely, lowering the control action reduces injected noise but results in insufficient disturbance rejection and possible loss of stability. Linear control systems theory shows fundamental limits to this trade-off (*10*, *11*) under certain assumptions about the controller design. The ultimate aim of controller design is to shape the "closed-loop" behavior, i.e., the performance of the designed controller acting in a feedback loop with the plant.

There are many classical methods to achieve the desired closed-loop behavior. Early methods, i.e., the classic (open)–loop shaping methods, exploit the direct relationship between the open- and closed-loop transfer functions to design the controller. Since the 1980s, the focus of design has shifted from open-loop design to directly shaping closed-loop transfer functions, i.e., the sensitivity functions (*12*, *13*), usually through optimization [e.g., convex optimization (*14*), H_∞ (*15*)]. These methods are more general and can take into account a larger variety of design goals and constraints. Yet they still require strong assumptions, such as convexity and linearity. For GW detectors like LIGO, progress using traditional approaches has come to a plateau.

In this work, we present a new control design method, Deep Loop Shaping (DLS), to design controllers that satisfy specific demands on the system's frequency domain behavior (Fig. 2). DLS has no constraints regarding the use of nonlinear models and control structures. It exploits the machinery of deep reinforcement learning to directly optimize frequency domain properties and shape the closed-loop behavior. We demonstrate DLS's utility on the critical LIGO θ_{CHP} control loop, achieving state-of-the-art feedback control performance. The injected control noise was reduced by up to two orders of magnitude while maintaining mirror stability. Applying DLS more widely on LIGO can improve sensitivity. Furthermore, the method has wide applicability to control engineering; for example, highly unstable systems, vibration suppression, and noise cancellation all have strong frequency-dependent control demands.

The LIGO controls challenge

Angular sensing and control (ASC) is the challenge of maintaining the orientation of the interferometer mirrors. Stabilization is accomplished through a hybrid active-passive isolation system. Passive stabilization happens through a series of pendulums, from which the optics are suspended. These pendulums suppress seismic disturbances at frequencies above 10 Hz by several orders of magnitude. However, active stabilization is required to reject seismic disturbances at frequencies below ~3 Hz. This stabilization is accomplished by a set

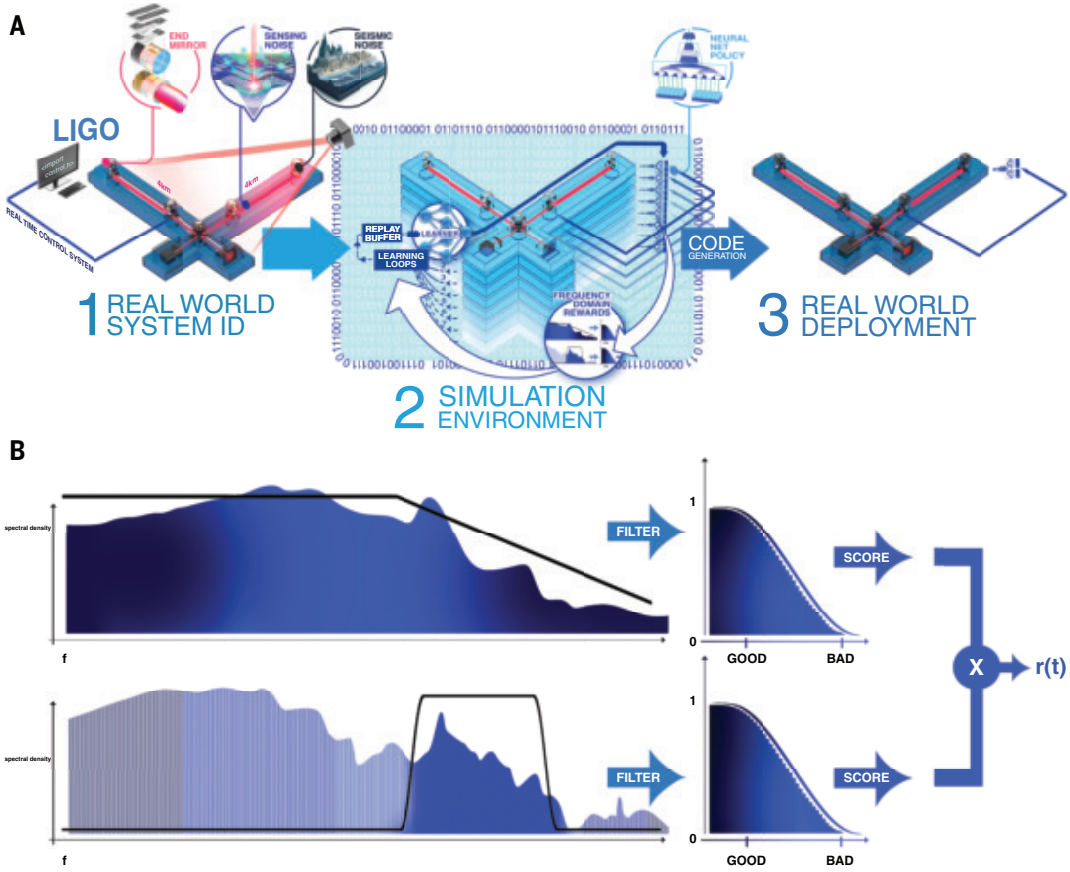

Fig. 2. DLS: Reinforcement learning with frequency domain rewards. (**A**) (1) A model is identified from plant measurements. (2) The identified model is used as a learning environment. Frequency domain rewards are used to compute rewards. (3) The optimized control policy is deployed on the plant. (**B**) Illustration of the frequency domain rewards and the multiplicative scoring.

of actuators that produce a torque on the suspended optics at the penultimate stage of the suspension system. Additionally, there are disturbances caused by the radiation-pressure forces of the high-power laser beam (*16*) that couple the angular motions of the cavity mirrors. The sensors used to measure the angular motion have a good signal-to-noise ratio at frequencies below a few hertz to enable active stabilization, but in the 10- to 30-Hz band, the sensor noise is orders of magnitude larger than the signal related to angular motion, and so motion in this band is not visible from the angular sensor and is only seen in the interferometer strain spectrum. The active controller injects sensing noise in this frequency band through the actuator to the test mass. This effect is the primary cause of test mass angular motion at frequencies above 10 Hz (*8*, *17*). Avoiding the injection of noise as much as possible and at the same time guaranteeing rejection of seismic disturbances is the main design goal for ASC controllers. We address this problem, which comprises the most challenging control loops in a GW observatory, with DLS.

The θ_{CHP} loop

In this work, we primarily focus on the ASC control loop, "common hard pitch" (θ_{CHP}). "Hard pitch" refers to the stiffer of the two optomechanical pitch eigenmodes of the arm cavities. "Common" signifies a relation of modes between the cavities of the two arms (*8*). The θ_{CHP} degree of freedom is the most difficult of the entire ASC system to stabilize and optimize. Reducing the control noise in this loop well below the quantum limit would remove this source of noise as a blocking issue for improved astrophysical sensitivity.

Closed-loop shaping as a reinforcement learning problem

In this work, we formulated the θ_{CHP} closed-loop control as an optimal control problem and found approximate solutions through reinforcement learning (RL). ASC requirements are naturally expressed as functions of the system response in the frequency domain, i.e., as desired spectra of state-space signals. We introduced a new reward scheme based on frequency domain behavior to enforce the desired closed-loop shaping of the control policy in such a way that RL could discover an effective control policy. It is similar to traditionally used methods of shaping sensitivity functions, but RL removes restrictions on the reward definition and system dynamics. RL can also discover nonlinear policies represented with deep neural networks that can serve as drop-in replacements for the existing hand-crafted controllers and enables improved performance without compromising robustness.

RL designs controllers by adapting a parameterized state-action mapping. Our specific choice of learning algorithm is maximum a posteriori policy optimization (MPO) (*18*). We used a small multilayer perceptron (MLP) with a dilated convolution input layer for the policy network, which executes sufficiently fast for control. The critic network is a long-short-term-memory (LSTM) network with input and output MLPs, as the critic is not needed for deployment.

Frequency domain rewards

RL naturally lends itself to reward descriptions formulated in the time domain, e.g., scoring events that happen at certain times. Instead, we directly formulated the ASC requirements as rewards in the frequency domain (Fig. 2B). To do so, we designed linear filters for the θ_{CHP} response signal whose transfer functions each select a certain frequency band of the signal. We used a low-pass filter to reward pitch alignment, a band-pass filter to reduce control action in the 8- to 30-Hz band, and an additional band-pass filter for frequencies >40 Hz to avoid high-frequency artifacts. A high output from a filter at a given timestep corresponds to a large historic response in the measured frequency band. These per-timestep response measures can then be used to construct a reward for RL. Specifically, we computed the RL reward by passing the filter outputs through a sigmoid function to compute a (per-filter) score in [0,1], with a value of 1 when the specification was fulfilled and fading to 0 as the response worsened. These individual filter scores were multiplied to yield the per-timestep reward, then used by the RL method to choose a policy that minimizes the discounted sum of this reward over time. This formulation of multiplying rewards can loosely be understood as a soft logical-AND; i.e., we wanted all properties to be fulfilled for high reward.

Training and deployment

We trained nonlinear control policies with RL against a linear stochastic state-space simulation of the plant dynamics (i.e., optomechanical response of the interferometer) identified from measurement data of the plant. We used domain randomization to add robustness to the learned policies. Specifically, at the beginning of each episode, we randomized the angular instability pole frequency and sampled variations in the seismic noise, including the overall noise strength.

At the conclusion of training, we performed several steps to ready the policy for hardware testing. First, a deterministic policy was created by using only the mean of the policy Gaussian. Second, we validated this deterministic policy across a selected set of disturbances and nonnominal plant parameters. We examined the reward achieved as well as measured key performance criteria, such as root mean square of the control effort in the observation band (10 to 30 Hz), and visually inspected the error and control spectra. With performance confirmed, we "exported" the policy for the hard real-time control required for execution on LIGO without further training or adaptation on the plant.

We deployed the control policies directly in the existing control infrastructure of the interferometer (*19*). As such, the RL-trained policies were drop-in replacements of the existing single-input, single-output (SISO) controllers. In particular, the LIGO control system uses somewhat arbitrary "counts" as the units for ASC inputs and outputs, and we adopted these conventions for the controller and the controller-simulator interface. We have also reported our results in these units for technical reasons.

Deployment on gravitational wave observatory hardware

We ran the deployed policies on the LIGO Livingston Observatory (LLO). In the experiments, the control of θ_{CHP} was under the sole authority of a neural network–based control policy. We measured the ASC noise during policy execution as well as comparison spectra from the standard controller before and after the nonlinear policy. In Fig. 1B we compare the performance of the neural network policy against the standard controller for a >10 min stretch on 12 December 2024. The figure shows the projection of the measured angular control noise into the GW readout. Additional details of this experiment are shown in the supplementary materials.

We found excellent performance for the neural network policy. In the crucial 3- to 30-Hz band, we see a reduction of noise of up to two orders of magnitude. At the same time, the neural network policy shows similar control authority as the linear controller in the control band (<3 Hz). The control noise added by the neural network policy is well below the fundamental thermodynamic noise and quantum back-action noise in the whole band of interest. These results show that the neural network policy has effectively removed the issue of noise injected by active control as a limit to the astrophysical sensitivity.

In the supplementary materials, we present additional results from April and August 2024, with total time on the instrument of well over 1 hour. The sustained control of the unstable θ_{CHP} mode demonstrates robustness of the neural network policy to normal seismic activity. We saw a good match between the training simulation and the real plant

under the tested conditions for frequencies >0.1 Hz, which increases confidence in our results. We additionally compared the control policy against the incumbent linear controller in terms of statistical measures, such as non-Gaussianity and nonstationarity. We found that, although the policy does exhibit some nonstationarity, the overall reduction in noise still leads to a clear benefit for signal detection.

For comparison, we derived controllers with convex optimization and show a series of simulation-based results in the supplementary materials. Although these optimized linear controllers have similar predicted performance, they are not fit for deployment in the high-stakes environment of the real observatory. In particular, they are open-loop unstable, and their disturbance rejection behavior is highly aggressive, in contrast to the neural network policies. In addition to experiments on LLO, we used the same methodology on the mode-cleaner of the Caltech prototype and similarly found that DLS is capable of reducing noise in a band of interest while maintaining overall control.

REFERENCES AND NOTES

1. LIGO Scientific Collaboration; Virgo Collaboration; *Phys. Rev. Lett.* **116**, 061102 (2016).
2. LIGO Scientific Collaboration; Virgo Collaboration; *Phys. Rev. Lett.* **119**, 161101 (2017).
3. LIGO Scientific Collaboration; Virgo Collaboration; KAGRA Collaboration; *Phys. Rev. X* **13**, 041039 (2023).
4. H. Yu, R. X. Adhikari, R. Magee, S. Sachdev, Y. Chen, *Phys. Rev. D* **104**, 062004 (2021).
5. B. Banerjee *et al.*, *Astron. Astrophys.* **678**, A126 (2023).
6. A. Tohuvavohu *et al.*, *Astrophys. J. Lett.* **975**, L19 (2024).
7. J. A. Sidles, D. Sigg, *Phys. Lett. A* **354**, 167–172 (2006).
8. L. Barsotti, M. Evans, P. Fritschel, *Class. Quantum Gravity* **27**, 084026 (2010).
9. V. Braginsky, S. Strigin, S. Vyatchanin, *Phys. Lett. A* **287**, 331–338 (2001).
10. K. J. Aström, R. Murray, *Feedback Systems: An Introduction for Scientists and Engineers* (Princeton Univ. Press, ed. 2, 2021); https://books.google.com/books?id=I50DEAAAQBAJ.
11. G. Stein, *IEEE Control Syst.* **23**, 12–25 (2003).
12. H. W. Bode, *Network Analysis and Feedback Amplifier Design* (D. Van Nostrand Company, 1945).
13. G. Zames, *IEEE Trans. Automat. Contr.* **26**, 301–320 (1981).
14. C. Barratt, S. Boyd, in *Control and Dynamical Systems: Digital and Numeric Techniques and Their Applications in Control Systems, Part 1*, vol. 55, C. T. Leondes, Ed. (Academic Press, 1993), pp. 1–24.
15. J. C. Doyle, K. Glover, P. P. Khargonekar, B. A. Francis, *IEEE Trans. Automat. Contr.* **34**, 831–847 (1989).
16. K. L. Dooley *et al.*, *J. Opt. Soc. Am. A Opt. Image Sci. Vis.* **30**, 2618–2626 (2013).
17. H. Yu *et al.*, *Phys. Rev. Lett.* **120**, 141102 (2018).
18. A. Abdolmaleki *et al.*, Maximum a Posteriori Policy Optimisation, *International Conference on Learning Representations*, Vancouver, CA, 30 April to 3 May 2018. (ICLR, 2018).
19. R. Bork *et al.*, *SoftwareX* **13**, 100619 (2021).
20. S. Khan *et al.*, *Phys. Rev. D* **93**, 044007 (2016).
21. E. Capote *et al.*, Advanced LIGO Detector Performance in the Fourth Observing Run. [gr-qc] (2024).
22. M. Hoffman *et al.*, Acme: A research framework for distributed reinforcement learning. arXiv:2006.00979 [cs.LG] (2020).
23. F. Yang *et al.*, Launchpad: A Programming Model for Distributed Machine Learning Research (2021) [cs.DC], arXiv:2106.04516.
24. google-deepmind, dm env: A python interface for reinforcement learning environments, GitHub (2019); https://github.com/deepmind/dm_env.
25. T. Hennigan, T. Cai, T. Norman, L. Martens, I. Babuschkin, Haiku: Sonnet for JAX (2024); https://github.com/deepmind/dm-haiku.
26. A. Cassirer *et al.*, Reverb: A Framework For Experience Replay. arXiv:2102.04736 [cs.LG] (2021).
27. J. Harms, Lightsaber, https://github.com/janosch314/Lightsaber (2025).
28. LIGO Scientific Collaboration, Identified Plant Model & Selected ASC Experimental Data of LIGO Livingston, Zenodo (2025); https://doi.org/10.5281/zenodo.15793015.

ACKNOWLEDGMENTS

We thank J. Dean for strategic help and inspiration at the start of the project. **Funding:** The authors gratefully acknowledge the support of the US National Science Foundation (NSF) for the construction and operation of the LIGO Laboratory and Advanced LIGO as well as the Science and Technology Facilities Council of the UK and the Max Planck Society for support of the construction of Advanced LIGO. Additional support for Advanced LIGO was provided by the Australian Research Council. LIGO was constructed by the California Institute of Technology and Massachusetts Institute of Technology with funding from the NSF and operates under cooperative agreement no. PHY-18671764464. Advanced LIGO was built under grant no. PHY-18680823459. **Author contributions:** R.X.A., J.Bu., S.C., J.H., M.R., and B.T. conceived the project. R.X.A., J.Bu., C.D., A.H., J.H., and B.T. led the project. T.A., R.X.A., I.B., J.Bu., J.Be., C.D., G.v.d.D., J.D., A.G., J.H., M.L., B.T., G.T., and C.W. developed the physics simulations. T.A., I.B., J.Bu., Y.H.J.C., C.D., J.D., M.L., B.T., and C.W. integrated the physics simulations with the learning framework. A.A., J.Bu., R.H., S.H., M.L., M.W., and B.T. developed the learning framework and performed learning experiments. C.D., T.N., J.R., and C.W. developed the real-time neural network interface. R.X.A., J.Be., J.Bu., C.D., A.G., B.T., and C.W. integrated the real-time neural network with the control system and ran experiments on LLO and the California Institute of Technology 40m prototype. C.B., J.Bu., Y.H.J.C., C.D., Y.D., O.G., M.L., and C.W. developed data curation tools. R.X.A., I.B., J.Bu., Y.H.J.C., B.T., and C.W. developed and ran the data analysis. L.F., P.K., H.O., and M.R. consulted for the project. T.A., R.X.A., J.Bu., J.H., B.T., and C.W. wrote the manuscript. The LIGO Instrument Team maintains and runs the LIGO Observatory. **Competing interests:** The authors declare that they have no competing interests. **Data and materials availability:** The learning algorithm used in the actor-critic RL method is MPO (*18*), a reference implementation of which is available under an open-source license (*22*). Additionally, the software libraries launchpad (*23*), dm env (*24*), Jax/Haiku (*25*), and reverb (*26*) were used, which are also open source. Simulations were implemented in Lightsaber (*27*) and advLigoRTS (*19*). The identified LLO model and experimental data are available at (*28*).

SUPPLEMENTARY MATERIALS

science.org/doi/10.1126/science.adw1291
Supplementary Text; Figs. S1 to S16; Tables S1 to S3; References *(29–69)*

Submitted 28 January 2025; accepted 7 July 2025

10.1126/science.adw1291

NEPHROLOGY

Estrogen-regulated renal progenitors determine pregnancy adaptation and preeclampsia

Carolina Conte[1], Maria Lucia Angelotti[1], Benedetta Mazzinghi[2], Maria Elena Melica[1], Giulia Antonelli[1], Giulia Carangelo[1], Samuela Landini[3], Valentina Raglianti[1], Fiammetta Ravaglia[4], Luigi Cirillo[2], Camilla Fantini[1], Tommaso Dafichi[1], Martin Klaus[5], Ersilia Lucenteforte[6], Alice Molli[1], Letizia De Chiara[1], Anna Julie Peired[1], Elena Lazzeri[1], Hans-Joachim Anders[5], Laura Lasagni[1], Paola Romagnani[1,2]*

The global burden of kidney disease displays marked sexual dimorphism. Lineage tracing and single-cell RNA-sequencing revealed that starting from puberty, estrogen signaling in female mice supports self-renewal and differentiation of renal progenitors to increase filtration capacity, reducing sensitivity to glomerular injury compared with that of males. This phenomenon accelerated as female kidneys adapted to the workload of pregnancy. Deletion of estrogen receptor α in renal progenitors disrupted this adaptation, leading to preeclampsia, fetal growth restriction, and increased maternal risk of hypertension and chronic kidney disease. Offspring from affected mothers had fewer nephrons, resulting in early-life hypertension and greater susceptibility to kidney disease. These results highlight the fundamental role of kidney fitness and renal progenitors for pregnancy and preeclampsia and as a determinant of sexual dimorphism in kidney disease.

Chronic kidney disease (CKD) affects >10% of the global population and is a leading health concern (*1*). Beyond kidney failure—a condition with high morbidity and mortality—CKD also increases cardiovascular disease (CVD) risk (*1*). By 2040, CKD is projected to be the fifth leading cause of death, with CKD-related CVD even more prevalent (*2*).

Male sex is a known risk factor for CKD progression (*3*, *4*). The increased incidence of CKD and CVD in postmenopausal or ovariectomized women supports a protective role of female sex hormones (*5*). However, female sex hormones are also implicated in preeclampsia—a hypertensive, proteinuric disorder that complicates ~5% of pregnancies (*6*, *7*). Its consequences extend far beyond pregnancy, increasing the risk for hypertension and CKD for both mother and offspring later in life (*6*–*8*).

Injury to podocytes—specialized epithelial cells essential for the filtration barrier—is a key driver of proteinuria and CKD progression (*9*) because the kidney has limited capacity to replace lost podocytes from renal progenitor cells (RPCs) in adult glomeruli (*10*, *11*). We hypothesized that sex differences in CKD progression originate from the greater capacity of female kidneys to structurally adapt to the increased workload imposed by pregnancy.

Results

RPCs show sexual dimorphism during kidney homeostasis

To assess role of RPCs in kidney disease dimorphism, we used the *Pax2.rtTA;tetO.cre;R26.Confetti* transgenic model, which labels RPCs with one of four fluorescent proteins (YFP, yellow; CFP, cyan; RFP, red; or GFP, green) upon doxycycline (dox) induction, enabling single-cell and clonal tracking of $Pax2^+$ cells. Mice received 10 days of dox at different ages, starting after glomerular development was complete (fig. S1A) (*12*). RPC numbers were similar in male wild-type (M-WT) and female wild-type (F-WT) mice at day 20, but female mice showed more glomerular RPCs than did males from day 30, after puberty (Fig. 1, A and B, and fig. S1B).

Tracking $Pax2^+$ cells over time with lineage tracing (fig. S1C) showed that RPCs generated longer clones along the Bowman capsule in male compared with female mice (Fig. 1C and fig. S1D). Most $Pax2^+$ clones in males showed tubular cell morphology (Fig. 1, D and E, and fig. S1E) and stained positive with the tubular marker *Lotus tetragonolobus* lectin (fig. S1E). By contrast, 11.6 ± 2.9% of glomeruli in female mice—compared with only 1.1 ± 0.3% in male mice—showed migration of RPCs into the glomerular tuft (Fig. 1, D and E), where they began to coexpress the podocyte markers synaptopodin (Syn) and nephrin, indicating podocyte differentiation (fig. S1E). Male and female mice had similar podocyte numbers up to day 30, whereas at day 120, female mice had more podocytes compared with that of males (fig. S1, F and G), a difference enhanced by normalization for the glomerular size, podocyte density (fig. S1, H and I). These results suggest that during fertile life, female mice have more RPCs to generate more podocytes, which results in a higher podocyte density compared with that of males.

Female sex hormones promote RPC proliferation and differentiation into podocytes in vitro

Because RPC dimorphism emerges after puberty, we examined the effects of estrogen [17β-estradiol (17βE)], progesterone (PG), and testosterone (TS) on primary human RPCs (hRPCs). Male and female age-matched hRPCs expressed estrogen receptor α (*ER*α), estrogen receptor β (*ER*β), G protein–coupled estrogen receptor 1 (*GPER*), progesterone receptor (*PGR*), and androgen receptor (*AR*) similarly (fig. S1J). 17βE and, to a lesser extent, PG—but not TS—promoted hRPC proliferation (Fig. 1F), with 17βE and PG showing an additive effect (Fig. 1F). Both hormones also enhanced hRPC differentiation into podocytes, increasing *nephrin* mRNA and protein levels (Fig. 1G and fig. S1K). 17βE effects were observed only at 10 to 100 nM, levels reached in females during ovulation and pregnancy (*13*, *14*), whereas PG effects appeared only at concentrations typical of late pregnancy. Use of specific agonists of estrogen receptors showed that hRPC proliferation (fig. S1L) and differentiation (Fig. 1H) induced by 17βE were mostly mediated by ERα. PG had no effect on *ER*α expression by hRPCs (fig. S1M). Together, female sex hormones promote hRPC proliferation and differentiation into podocytes.

ERα promotes RPC differentiation into podocyte during kidney homeostasis in vivo

To evaluate the role of estrogen in the generation of new podocytes from RPCs in vivo, we first confirmed the mRNA expression of *ER*α in sorted GFP^+ RPCs of *Pax2.rtTA;tetO.cre;R26.mT/mG* mice (fig. S2, A to C). Then, we deleted *ER*α in the RPCs in females of this strain (F-ERαKO), permitting tracking of RPCs with GFP and visualization of podocyte foot processes while depleting *ER*α upon exposure to dox (fig. S2, D to F). F-WT and F-ERαKO mice appeared normal and had similar reproductive capability, weight, diuresis, and osmolarity as well as potassium, sodium, and glucose levels (fig. S2, G to L). RPCs in F-WT mice generated new podocytes in 11.2 ± 1.1% of glomeruli in the first 120 days of adult life, whereas in M-WT mice, this phenomenon after puberty was negligible (1.9 ± 0.3%) (Fig. 1, I and J, and fig. S2M). Upon *ER*α depletion from RPCs, the percentage of glomeruli with RPC-derived podocytes was no longer different from that of male mice (Fig. 1, I and J, and fig. S2M). RPC-derived podocytes showed a fully differentiated phenotype interdigitating with other podocytes (Fig. 1K and fig. S2N). Optical clearing of kidney tissue, immunofluorescence staining for nephrin, and three-dimensional (3D) reconstruction (fig. S2O) revealed a reduction in foot process coverage observed with stimulated emission depletion (STED)

[1]Department of Biomedical, Experimental and Clinical Sciences "Mario Serio," University of Florence, Florence, Italy. [2]Nephrology and Dialysis Unit, Meyer Children's Hospital IRCCS, Florence, Italy. [3]Medical Genetics Unit, Meyer Children's Hospital, IRCCS, Florence, Italy. [4]Nephrology and Dialysis Unit, Santo Stefano Hospital, Prato, Italy. [5]Division of Nephrology, Department of Medicine IV, LMU University Hospital, Munich, Germany. [6]Department of Statistics, Computer Sciences and Applications "G. Parenti," University of Florence, Florence, Italy. *Corresponding author. Email: paola.romagnani@unifi.it

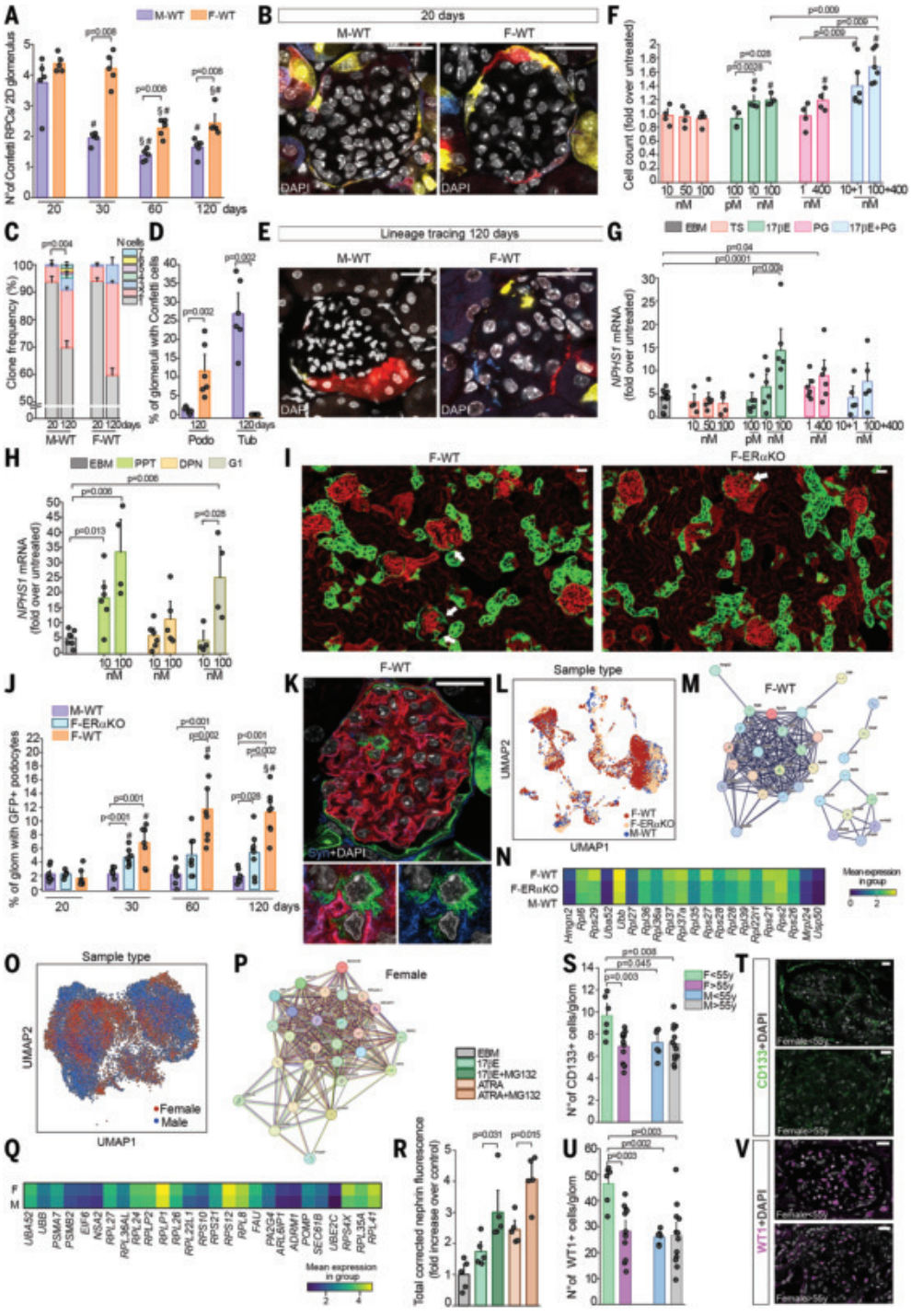

Fig. 1. RPCs show sexual dimorphism during kidney homeostasis, and female sex hormones promote RPC proliferation and differentiation into podocytes.
(**A**) Number of Confetti RPCs per glomerulus ($n = 5$ mice) and (**B**) representative images (10-μm-thick slices). #, significance versus 20 days; §, significance versus 30 days; all $P \leq 0.01$. (**C**) Clone frequency of Confetti RPCs per glomerulus ($n = 6$ mice). (**D**) Percentage of glomeruli with Confetti-derived tubular and podocyte cells ($n = 6$ mice) and (**E**) representative images. DAPI, 4′,6-diamidino-2-phenylindole. (**F** and **G**) hRPCs stimulated with TS, 17βE, PG, and 17βE $^{+}$ PG. (F) Cell count. (G) *NPHS1* mRNA. #, significance versus control; all $P \leq 0.01$. EBM, endothelial basal medium. (**H**) *NPHS1* mRNA in hRPCs stimulated with ERα agonist {4′,4″- [4-Propyl-(1H)- pyrazole-1,3,5-triyl] trisphenol (PPT)}, ERβ agonist [2,3-Bis(4-hydroxyphenyl)propionitrile (DPN)], or GPER agonist (G1). (**I**) Representative images of *Pax2.mT/mG.WT* and *ERαKO* female mice (glomeruli with GFP^{+} podocytes, arrows). (**J**) Percentage of glomeruli with GFP^{+} podocytes (30-μm-thick slices) ($n = 8$ mice). #, significance versus 20 days; all $P < 0.001$; §, Significance versus 30 days; $P = 0.01$. (**K**) Representative glomerulus with a GFP^{+} podocyte. (**L**) UMAP plot of cell populations in mouse glomeruli annotated by sample name. (**M**) Functional association networks and (**N**) matrix plot of the top differentially expressed genes of F-WT RPCs (Pax2^{+}Fluo^{+}). (**O**) UMAP plot of hRPC culture annotated by sample name. (**P**) Functional association networks and (**Q**) matrix plot of the top differentially expressed genes of female hRPCs. (**R**) Nephrin quantification in hRPCs. ATRA, all-trans retinoic acid. (**S** and **T**) Human kidney biopsies from healthy females and males. (S) Number of CD133^{+} cells per glomerulus. (T) Representative images. (**U**) Number of WT1^{+} cells per glomerulus and (**V**) representative images. Data are expressed as mean ± SEM. Each dot indicates a biological replicate. Statistical significance was assessed by means of a Mann-Whitney test; $P < 0.05$ is considered statistically significant. Scale bars, 25 μm.

microscopy in M-WT in comparison with F-WT mice (fig. S2, O and P). F-ERαKO mice also showed reduced foot process coverage (fig. S2, O and P). Moreover, in contrast to F-WT, M-WT mice developed microalbuminuria and showed a higher blood pressure, which is consistent with previous reports that showed sexual dimorphism in albuminuria and arterial pressure in mice (fig. S2, Q and R) (*15*). F-ERαKO showed values comparable with those of M-WT and higher than those of F-WT mice (fig. S2, Q and R). In addition, RPCs distributed along the tubule generated new tubular cells in the S2 segment, particularly in females, through an estrogen receptor (ER)–dependent mechanism (fig. S2, S and T). Together, in contrast to fertile male mice, fertile female mice generated new podocytes through ERα signaling, which protects from albuminuria and hypertension.

Next, we performed single-cell RNA-sequencing (scRNA-seq) on glomeruli from *Pax2.rtTA;tetO.cre;R26.Confetti* M-WT and F-WT and *Pax2.rtTA;tetO.cre;R26.Confetti;ERαKO* female mice after starting with dox induction at 20 days of age and lineage tracing until 90 days of age (fig. S3A). Unsupervised clustering revealed clusters with distinct expression patterns of different kidney cell types (fig. S3, B and C) and sex distribution (Fig. 1L). RPC subclusters reflected different stages of podocyte differentiation (fig. S3, D to G). Gene differences among M-WT, F-WT, and F-ERαKO mice in uncommitted RPCs, podocyte-committed RPCs, and mature podocytes are listed in table S1. Uniform manifold approximation and projection (UMAP) distribution of fluorochromes (fig. S3H) and Pax2 (fig. S3I) also identified RPCs ($Pax2^+Fluo^+$) and newly generated podocytes ($Pax2^-Fluo^+$) in F-WT, F-ERαKO, and M-WT mice (fig. S3J). An interactome of the most characteristic transcripts of F-WT RPCs ($Pax2^+Fluo^+$) (Fig. 1M) highlighted activation of ribosomal and ubiquitinase systems, *Uba52* (Fig. 1N and fig. S3, K to M), and up-regulation of *Usp50*, compared with M-WT and F-ERαKO RPCs (Fig. 1, M and N, and fig. S3, K to N). Similar RNA signatures were observed in hRPC cultures obtained from male and female subjects (Fig. 1, O to Q, and fig. S4, A to C). Consistently, proteasome inhibition with MG132 enhanced hRPC differentiation into podocytes induced by 17βE as well as by retinoic acid (Fig. 1R and fig. S4D). Coherently, in human kidneys, RPCs were more abundant and produced a higher number of podocytes in young women compared with postmenopausal women and men of any age (Fig. 1, S to V, and table S2). Together, 17βE promotes hRPC proliferation and differentiation into podocytes through ERα and by inhibition of the proteasome, permitting better podocyte endowment in fertile females.

Sexual dimorphism of RPCs influences severity of glomerular injury in mice

Male mice are more susceptible than female mice to glomerular injury (*16*, *17*). To verify whether this is related to a lower number of RPCs and podocytes, we induced podocyte injury. *Pax2.rtTA;tetO.cre;R26.mT/mG* M-WT and F-WT and *Pax2.rtTA;tetO.cre;R26.mT/mG;ERαKO* female mice received dox at 5 weeks of age to induce the transgene. After dox washout, we induced nephropathy using doxorubicin and followed the mice for 30 days (fig. S5A). Optical clearing of kidney tissue, immunofluorescence staining for nephrin, 3D reconstruction, and STED microscopy revealed less podocyte injury in female and loss of foot processes in male versus female mice (Fig. 2, A to C). Consistently, proteinuria was lower (Fig. 2D) and kidney function better (Fig. 2E and fig. S5B) in F-WT and F-ERαKO mice. In M-WT mice, estradiol treatment improved both proteinuria and kidney function (fig. S5, C to E). This was associated with a difference in the capacity of RPCs to regenerate podocytes as demonstrated by a lower percentage of glomeruli with GFP^+ podocytes inside the tuft after *ERα* deletion in F-ERαKO versus F-WT mice (4.9 ± 1.1% versus 11.4 ± 1.2%) (Fig. 2F and fig. S5, F and G). Similar results were obtained in anti–glomerular basement membrane (anti-GBM) glomerulonephritis (Fig. 2, G to J, and fig. S5, H to J). In this model, F-WT mice showed less proteinuria, better kidney function, smaller crescents, and increased RPC differentiation into podocytes (Fig. 2, G to J, and fig. S5, I and J). Thus, estrogen signaling in RPCs modulates glomerular disease severity and outcomes through enhanced podocyte regeneration in female mice.

RPCs generate new podocytes and extend the glomerular filtration barrier during pregnancy

Pregnancy requires an increase in glomerular filtration rate (GFR) of 40 to 50% (*18*). To test whether RPCs generate new podocytes in response to increased filtration demand, we induced *Pax2.rtTA;tetO.cre;R26.Confetti* and *Pax2.rtTA;tetO.cre;R26.Confetti;ERαKO* females at 5 weeks with dox and mated them after washout (fig. S6A). Lineage tracing revealed that in pregnant WT mice (P-WT), RPCs underwent clonal expansion along the Bowman capsule and migrated inside the glomerular tuft, a phenomenon that was not observed in age-matched nulliparous controls (N-WT) (Fig. 3, A and B) and started already in the early stages of pregnancy (fig. S6, B to D). ERα deletion reduced RPC expansion and migration inside the tuft during pregnancy (Fig. 3, A and B). The podocyte phenotype, characterized in *Pax2.rtTA;tetO.cre;R26.mT/mG* and *Pax2.rtTA;tetO.cre;R26.mT/mG;ERαKO* mice, showed Syn- and nephrin-positive fully differentiated foot processes (Fig. 3, C and D). However, ERα deletion in RPCs reduced the percentage of glomeruli showing new podocytes in pregnant ERαKO mice (P-ERαKO) versus P-WT mice (7.7 ± 2% versus 18.9 ± 1.8%) (Fig. 3E and fig. S6E). This was associated with a reduction in foot process coverage observed by STED microscopy in P-ERαKO mice versus P-WT mice (Fig. 3, F and G). To assess human pregnancy, urine RPC cultures (uRPCs) were successfully established from pregnant women but not from healthy controls (*19*), suggesting RPC activation specifically during pregnancy (Fig. 3H). scRNA-seq revealed activation of ribosomal and ubiquitinase systems, increased proteasome activity, *UCHL1* overexpression, and elevated production of pro-angiogenic factors such as *VEGF-A*, compared with kidney tissue–derived RPCs (Fig. 3, I to K, and fig. S6, F to H). Proteasome inhibition in uRPCs from pregnant women induced their differentiation into podocytes (Fig. 3, L and M). Together, these findings show that pregnancy induces de novo generation of podocytes from RPCs as part of the structural adaptation process.

Inefficient generation of new podocytes from RPCs promotes preeclampsia

What are the possible consequences of ERα deficiency in RPCs during pregnancy? P-ERαKO mice lacked the physiologic drop in blood pressure observed in P-WT mice and developed hypertension and progressive proteinuria (Fig. 3, N and O)—in other words, preeclampsia (*6*, *7*). Similarly, ERα deletion in RPCs attenuated the pregnancy-related increase in GFR (Fig. 3P) and increased blood urea nitrogen (BUN) (Fig. 3Q), demonstrating impaired kidney function in late pregnancy.

GFP expression in other mouse organs excluded the expression of Pax2 outside the kidney, with the exception of rare cells in the heart and the uterus (fig. S7, A to G) that were not amplified during pregnancy (fig. S7, E and F). To further exclude a contribution of the $Pax2^+$ cells in collecting ducts, we generated conditional ERαKO mice under the control of the promoter Pax8, *Pax8.rtTA;tetO.cre;R26.mT/mG;ERαKO* (P-Pax8 ERαKO) (fig. S8, A and B). Overall, Pax8 protein labeled <14% of RPCs within glomeruli and was lost during RPCs' commitment toward podocyte progenitors (fig. S8, C to F). Pax8 closely mirrored Pax2 expression in the renal collecting ducts and outside the kidney, as shown with confocal microscopy analysis (fig. S8, G to I) as well as with scRNA-seq in the Human Protein Atlas (figs. S7G and S8J) (*20*). Last, P-Pax8 ERαKO pregnant mice did not develop hypertension or proteinuria (fig. S8, K and L). Overall, estrogen signaling in RPCs stimulates production of new podocytes in females to adapt to pregnancy-related hyperfiltration, and preeclampsia develops when adaptation remains insufficient.

RPC dysfunction, not endothelial damage, causes maternal CKD after preeclampsia

We compared our preeclampsia model with a classical model of preeclampsia related to endothelial dysfunction induced by injection of the vasoconstrictor N(ω)-nitro-L-arginine methyl ester (L-NAME) in *Pax2.rtTA;tetO.cre;R26.mT/mG* (P-WT L-NAME) mice (fig. S9A). Both models showed similar hypertension and proteinuria severity at gestational

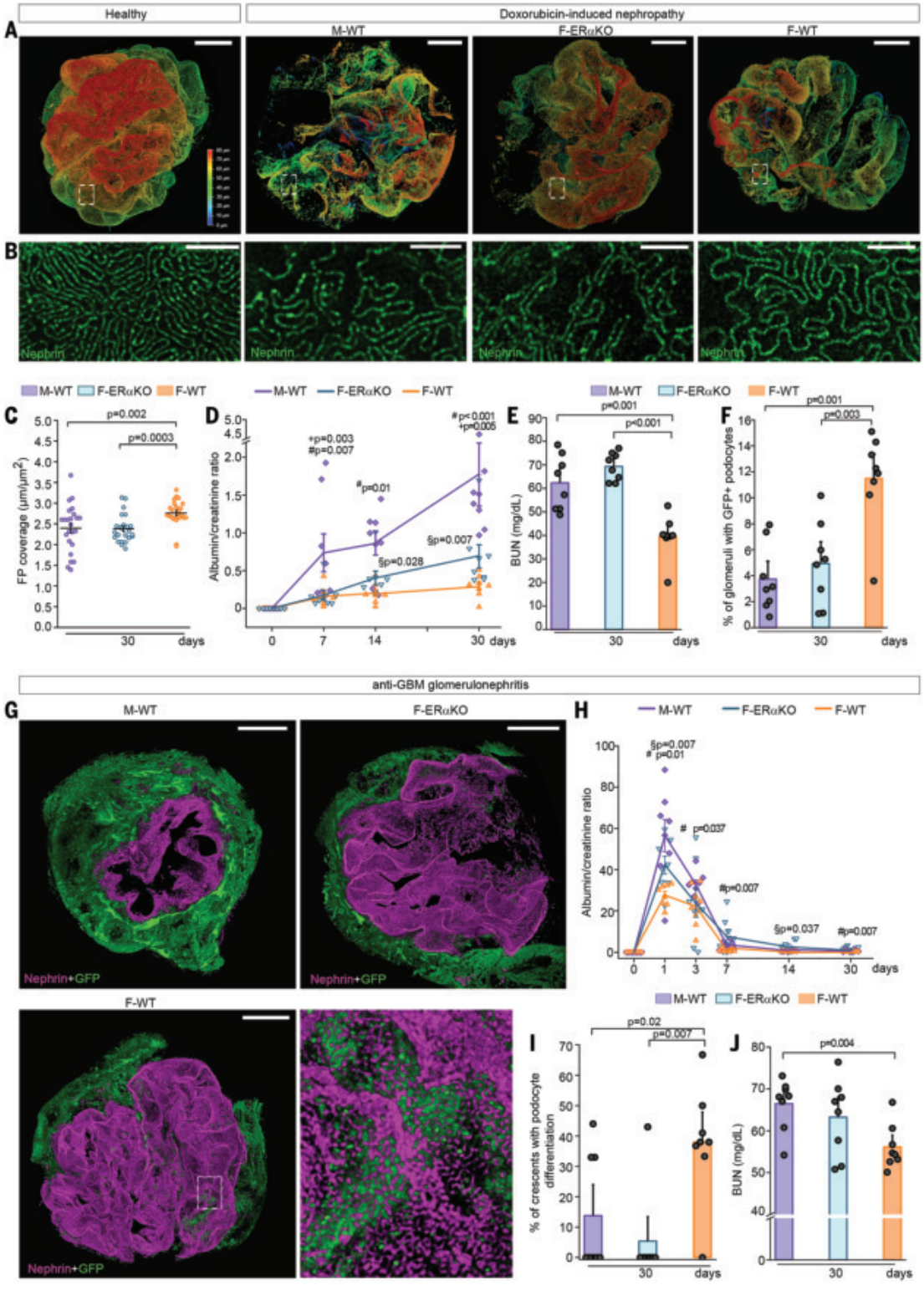

Fig. 2. Sexual dimorphism of RPCs influences severity of glomerular injury in male and female mice. (**A** to **F**) Doxorubicin-induced nephropathy. (A) 3D reconstructions of whole glomeruli after optical tissue clearing stained for nephrin. Nephrin expression is shown with a depth coding profile. Scale bars, 20 µm. (B) Representative images of podocyte foot processes created with STED microscopy in nephrin-stained kidney sections. Scale bars, 2 µm. (C) Quantification of foot process (FP) density ($n = 4$ mice). Each dot indicates one glomerulus. (D) Time course of urine albumin/creatinine ratio ($n = 8$ mice). (E) BUN ($n = 8$ mice). (F) Percentage of glomeruli with GFP$^+$ podocytes (30-µm-thick slices) ($n = 8$ mice). (**G** to **J**) Anti-GBM glomerulonephritis. (G) 3D reconstructions of whole glomeruli after optical tissue clearing stained for nephrin and GFP. Scale bars, 20 µm. Higher magnification of the boxed area in the female glomerulus is shown. (H) Time course of urine albumin/creatinine ratio ($n = 8$ mice). (I) Percentage of crescents with GFP$^+$ cells showing morphological features of podocytes (30-µm-thick sections) ($n = 8$ mice). (J) BUN ($n = 8$ mice). Data are expressed as mean ± SEM. Each dot indicates a biological replicate, except in (C). #, significance M-WT versus F-WT; §, significance F-WT versus F-ERαKO; +, significance M-WT versus F-ERαKO. Statistical significance was assessed by means of a Mann-Whitney test; $P < 0.05$ is considered statistically significant.

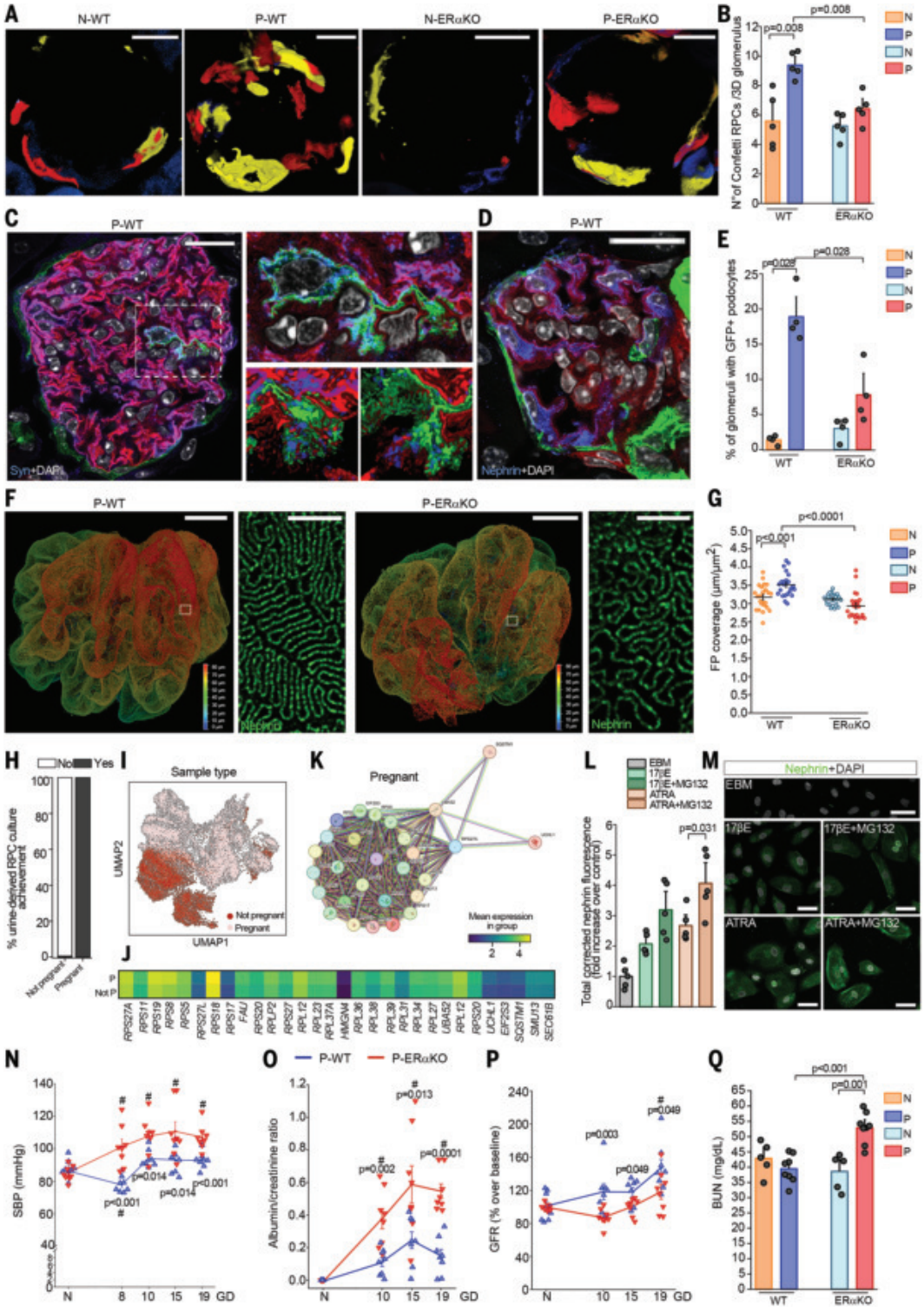

Fig. 3. RPCs generate new podocytes and extend the glomerular filtration barrier during pregnancy. (**A**) 3D glomeruli from *Pax2-Confetti WT* and *ERαKO* mice at delivery (P-WT and P-ERαKO) and N-WT and N-ERαKO ("N"). Scale bars, 20 µm. (**B**) Number of Confetti RPCs per glomerulus (30-µm-thick slices) ($n = 5$ mice). (**C** and **D**) Representative glomeruli with GFP$^+$ podocytes, stained for (C) synaptopodin (Syn) and (D) nephrin. Scale bar, 20 µm. (**E**) Percentage of glomeruli with GFP$^+$ podocytes (30-µm-thick slices) ($n = 4$ mice). (**F**) 3D reconstructions of whole mouse glomeruli after optical tissue clearing stained for nephrin. Nephrin expression is shown with a depth coding profile. Scale bars, 20 µm. Representative images of podocyte foot processes created with STED microscopy in nephrin-stained sections. Scale bars, 2 µm. (**G**) Quantification of foot process density ($n = 4$ mice). Each dot indicates one glomerulus. (**H**) Success in achieving human uRPC culture. (**I**) UMAP plot of human uRPC cultures annotated by sample name. (**J**) Matrix plot and (**K**) functional association networks of the top differentially expressed genes of pregnant human uRPCs. (**L**) Nephrin quantification in human uRPCs and (**M**) images of nephrin expression. Scale bars, 25 µm. (**N** to **P**) Time course during pregnancy ($n = 8$ mice) of (N) systolic blood pressure (SBP) (N), (O) urine albumin/creatinine ratio, and (P) GFR. GD, gestational day. #, significance versus N-WT and N-ERαKO: $P \leq 0.01$ in (N); $P \leq 0.001$ in (O) and (P). (**Q**) BUN. Data are expressed as mean ± SEM. Each dot indicates a biological replicate, except in (G). Statistical significance was assessed by means of a Mann-Whitney test; $P < 0.05$ is considered statistically significant.

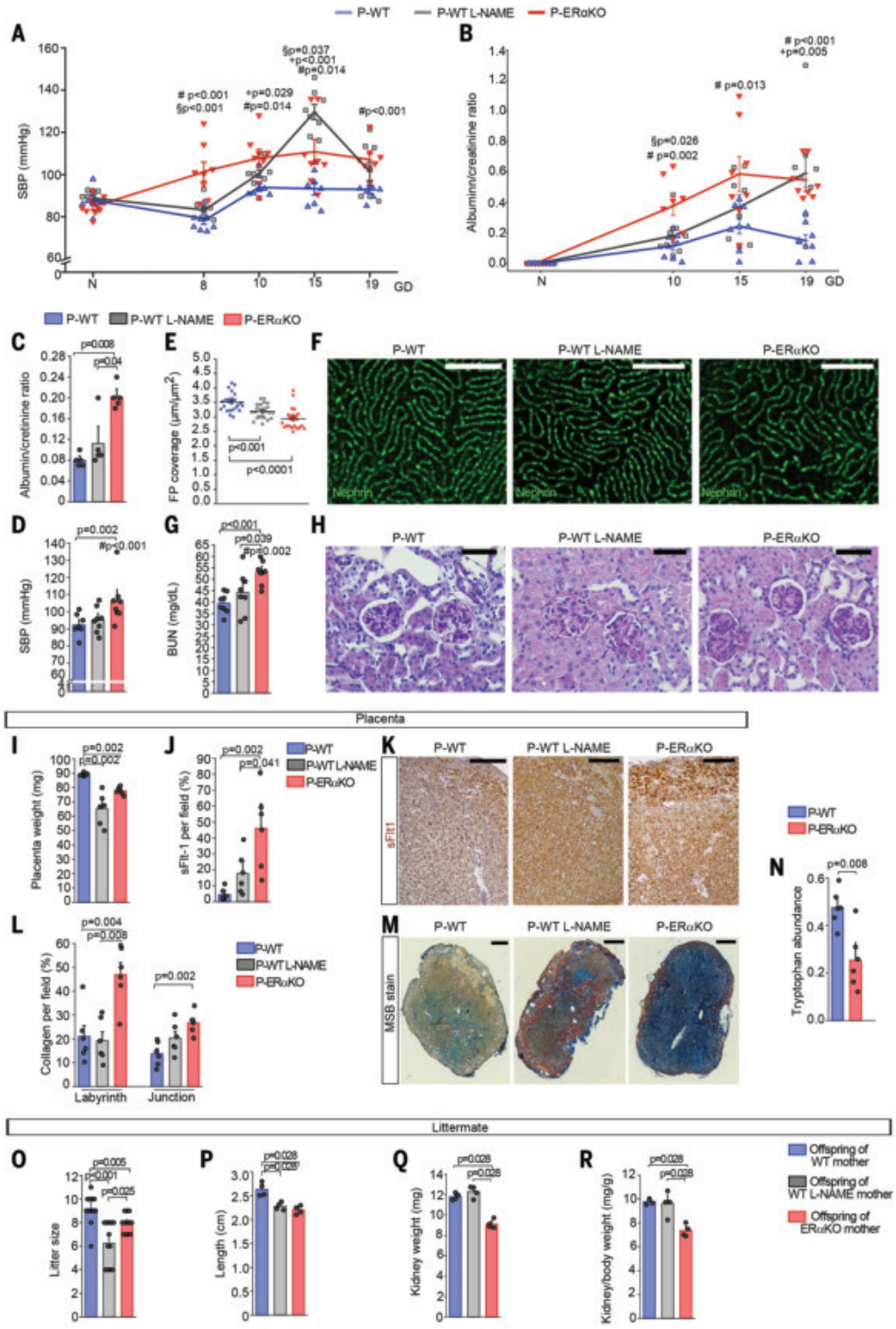

Fig. 4. Inefficient generation of new podocytes from RPCs promotes preeclampsia and affects placentation and neonatal outcome. (**A** and **B**) Time course of (A) SBP and (B) urine albumin/creatinine ratio during pregnancy ($n = 8$ mice). #, significance P-WT versus P-ERαKO; +, significance P-WT versus P-WT L-NAME; §, significance P-ERαKO versus P-WT L-NAME. (**C** to **H**) Analysis of P-WT, P-WT L-NAME, and P-ERαKO mice at delivery. (C) Urine albumin/creatinine ratio ($n = 5$ mice) and (D) SBP ($n = 8$ mice). (E) Quantification of foot process density ($n = 4$ mice). Each dot indicates one glomerulus. (F) Representative images of podocyte foot processes created with STED microscopy in nephrin-stained sections. Scale bars, 2 µm. (G) BUN ($n = 8$ mice). (H) Kidney sections stained with periodic acid–Schiff (PAS). Scale bars, 50 µm. (**I** to **M**) Placenta analysis at gestational day (GD) 18. (I) Weight. Each dot indicates the mean of four placenta per mice ($n = 6$ mice). (J) Percentage of sFlt-1–stained area ($n = 6$ mice). (K) Representative images. Scale bars, 200 µm. (L) Percentage of collagen area (blue) per field in the placental labyrinth and junction area. (M) Representative images. Scale bars, 1000 µm ($n = 6$ mice). MSB, Martius Scarlet Blue. (**N**) Relative tryptophan abundances ($n = 6$ mice). (**O**) Litter size. Each point indicates a litter ($n = 12$). (**P** to **R**) Offspring analysis at the delivery. (P) Length. (Q) Kidney weight. (R) Kidney weight/body weight ratio. Each dot indicates the mean of pups from $n = 4$ mothers per group. Data are expressed as mean ± SEM. Statistical significance was assessed by means of a Mann-Whitney test; $P < 0.05$ is considered statistically significant.

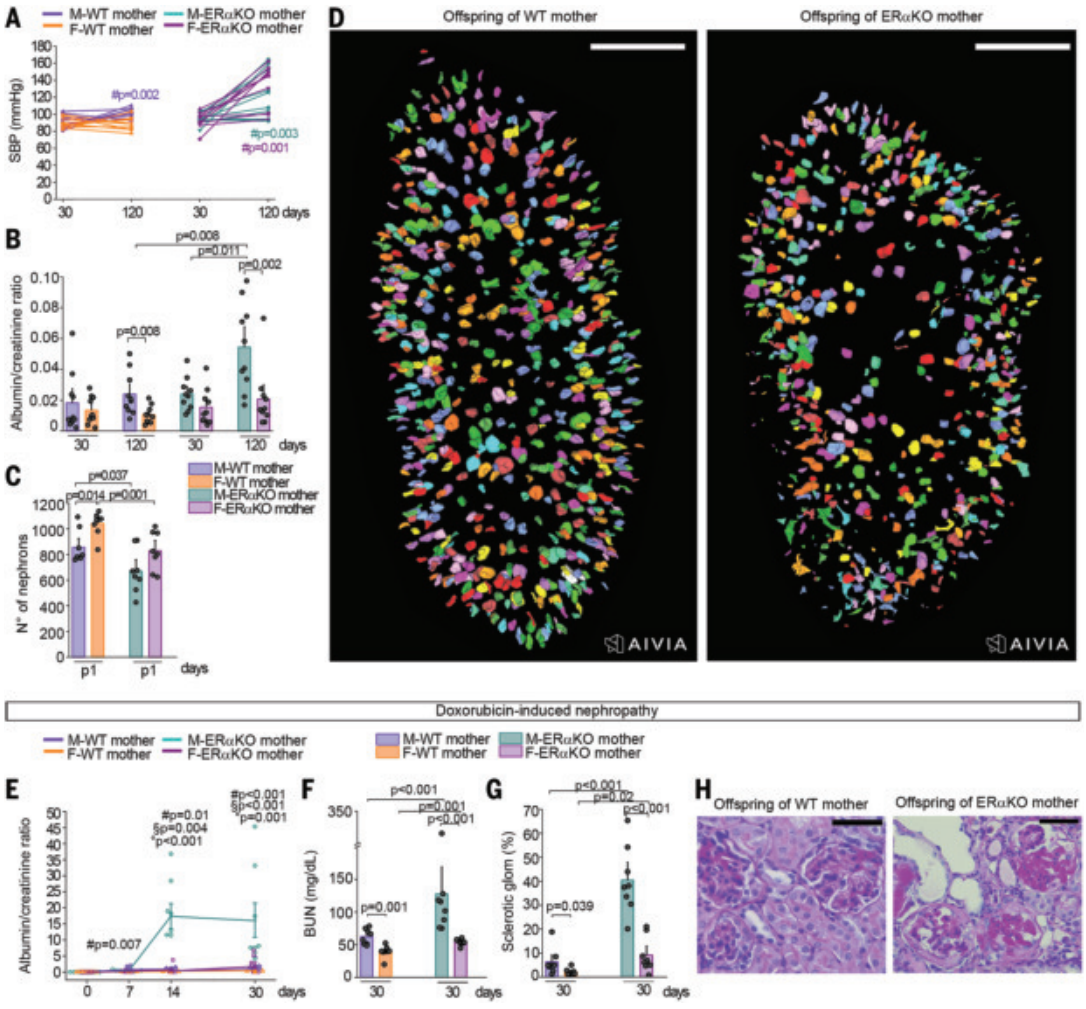

Fig. 5. Inefficient podocyte generation increases hypertension and CKD risk in the offspring. (**A** to **D**) In the offspring (male and female mice) of WT and ERαKO mothers at 30 and 120 days. (A) SBP ($n = 10$ mice). (B) Urine albumin/creatinine ratio ($n = 10$ mice). #, significance versus 30 days. (C) Total nephron number at birth [postnatal day 1 (p1)] as assessed with Aivia (Leica Microsystems) artificial intelligence software ($n = 8$ mice). (D) 3D reconstructions of optically cleared kidneys labeled for nephrin obtained with the artificial intelligence software Aivia to detect glomeruli as objects and create surface reconstructions of all detected objects. Scale bars, 500 μm. (**E** to **H**) In mice with doxorubicin-induced nephropathy. (E) Time course of urine albumin/creatinine ratio ($n = 8$ mice). #, significance male versus female of WT-mother; circle, significance male versus female of ERαKO mother; §, significance male of WT mother versus male of ERαKO mother. (F) BUN ($n = 8$ mice). (G) Percentage of sclerotic glomeruli ($n = 8$ mice). (H) Images of PAS-stained kidney sections. Scale bars, 50 μm. Data are expressed as mean ± SEM. Each dot indicates a biological replicate. Statistical significance was assessed by means of a Mann-Whitney test; $P < 0.05$ is considered statistically significant.

days 15 and 19 (Fig. 4, A and B). However, in L-NAME mice, albuminuria and hypertension resolved postpartum (Fig. 4, C and D) as previously reported (*21*), whereas P-ERαKO mice exhibited persistent proteinuria and hypertension (Fig. 4, C and D), reduced slit diaphragm density (Fig. 4, E and F), increased BUN (Fig. 4G), glomerulosclerosis, and thrombotic microangiopathy (Fig. 4H and fig. S9B)—in other words, CKD. These findings indicate that podocytopenia-driven, not endothelial dysfunction-driven, preeclampsia causes postpartum maternal hypertension and CKD.

Inefficient generation of new podocytes from RPCs affects placentation and neonatal outcome

Preeclampsia is associated with a smaller and fibrotic placenta as well as abortion or low birth weight in the newborn (*6*, *7*). Consistently, placentas of pregnant mice exposed to L-NAME as well as placentas of P-ERαKO mice were smaller and produced more soluble FMS-like tyrosine kinase-1 (sFlt-1) in comparison with those of untreated P-WT mice (Fig. 4, I to K). Placentas of P-ERαKO mice were more fibrotic in comparison with those of P-WT mice (Fig. 4, L and M, and fig. S9, C to E). No GFP^+ Pax2-tracked cells were observed in the placenta (fig. S7D), indicating that inefficient placentation was not a consequence of ERα deletion in this organ. However, mass spectrometry revealed that compared with WT mice, P-ERαKO mice (Fig. 4N) showed reduced blood concentration of L-tryptophan levels that impair utero-placental development, linking inadequate podocyte endowment to preeclampsia (*22*–*25*), as already reported for nephrectomy (*26*). As a further characteristic common to human preeclampsia, P-ERαKO mice gave birth to smaller litters (Fig. 4O), with pups showing a reduced body size and kidney weights (Fig. 4, P to Q) in comparison with those of WT mice, even though we observed no differences in gestational length between WT and P-ERαKO mice (fig. S9F). Kidney weight remained smaller even when normalized for body weight (Fig. 4R). Together, inefficient generation of new podocytes from RPCs affects placentation and neonatal outcome.

Inefficient maternal podocyte generation increases hypertension and CKD risk in the offspring

Children of mothers with preeclampsia have an increased risk of developing hypertension and proteinuria later in life (*6*, *7*). Consistently, offspring of P-ERαKO preeclamptic mice developed hypertension in adulthood and had greater proteinuria at day 120 than offspring of WT

mothers (Fig. 5, A and B). Deep learning–assisted 3D imaging of optically cleared kidneys showed a lower nephron count at birth in offspring of ERαKO mothers compared with offspring of WT mothers (Fig. 5, C and D). Male offspring exhibited more severe hypertension and proteinuria than females, which is consistent with their lower nephron count at birth (Fig. 5, A to D). Moreover, in the adult offspring of ERαKO mothers, induction of doxorubicin-induced nephropathy was associated with a more severe proteinuria in comparison with offspring of WT mothers, an effect that was more pronounced in males (Fig. 5E). Only the offspring of ERαKO mice developed subsequent CKD, as shown by worse kidney function and tissue damage with increased glomerulosclerosis at day 30 after induction of doxorubicin-induced nephropathy (Fig. 5, F to H). The clinical phenotype was more severe in male offspring. Thus, insufficient maternal podocyte generation during pregnancy limits nephron formation in offspring, reducing their kidney reserve and resilience to injury later in life.

Discussion

These results show that (i) in female mice, kidneys have a greater number and regenerative capacity of RPCs through ERα signaling; (ii) this advantage lowers females' risk of CKD and hypertension during their reproductive years; (iii) failure of RPCs to generate new podocytes contributes to preeclampsia and increases the risk of CKD and hypertension in affected mothers after delivery; and (iv) preeclampsia caused by RPC dysfunction also impairs nephron development in offspring, increasing their lifelong risk for hypertension and CKD.

Our study reveals that female mice have a higher podocyte production reserve to accommodate the 40 to 50% increase in GFR during pregnancy, which was previously attributed to adaptive podocyte hypertrophy (*18*). Women with reduced podocyte reserve (for example, from diabetes, obesity, or CKD) and even some otherwise healthy pregnancies are at higher risk for preeclampsia (*1*, *6*, *9*). Although placental hypoxia and sFlt-1 upregulation are considered primary causes of preeclampsia (*6*), our findings suggest that in some cases, preeclampsia may stem from inadequate estrogen-driven podocyte generation by RPCs, which is essential for physiologic pregnancy and healthy fetal growth (*1*, *6*, *9*). To explore mechanisms, we measured plasma L-tryptophan levels—which are essential for placental development and vascularization (*23*–*26*)—and found them reduced in P-ERαKO mice. Similarly, nephrectomy lowers L-tryptophan metabolite levels, impairing placentation and increasing sFlt1 (*26*). These findings suggest that RPC dysfunction, by limiting podocyte endowment, may reduce L-tryptophan metabolite levels much like low nephron mass does, linking placental failure and preeclampsia to underlying kidney dysfunction (*22*, *23*, *26*). Insufficient podocyte endowment in conditions of hyperfiltration promotes podocyte detachment, perpetuating and amplifying injury, as happens in adaptive forms of focal segmental glomerulosclerosis (FSGS) (*9*). Supporting this hypothesis, urinary podocyte loss and increased $Ki67^+$ parietal epithelial cells have been reported in women with preeclampsia (*27*–*30*), suggesting that in some patients, preeclampsia may represent a form of FSGS due to RPC failure (*31*).

The model may also explain why many, but not all, women with preeclampsia develop long-term hypertension and CKD. Accordingly, this occurs in the P-ERαKO but not in the L-NAME model of endothelial dysfunction-driven preeclampsia (*21*, *32*). These findings may suggest that preeclampsia is heterogeneous, with distinct kidney- and endothelium-driven subtypes requiring tailored follow-up and treatment (*6*). In addition, the model may explain why the offspring of mothers with preeclampsia are at increased risk of developing hypertension, CKD, and CVD later in life (*6*, *7*, *33*). Preeclampsia caused by RPC failure also led to fetal growth restriction, low birth weight, and poor nephron endowment.

These findings suggest that pregnancy may have exerted evolutionary pressure on the female kidney to enhance podocyte regeneration through estrogen-driven proteasome activity in RPCs. As shown by Guhr *et al.* (*34*), RPCs maintain low podocyte gene expression, with proteasomes preventing protein buildup and differentiation. This brake appears more easily released in female RPCs, particularly during pregnancy.

Although sex differences in RPC function and podocyte number, as well as increased proteasome activity during pregnancy, were confirmed in human tissues, a limitation of this study is the inability to analyze all parameters in humans as comprehensively as in mice. Still, these results shed light on mechanisms underlying preeclampsia, CKD, and hypertension and point to potential therapeutic opportunities.

REFERENCES AND NOTES

1. P. Romagnani *et al.*, *Nat. Rev. Dis. Primers* **3**, 17088 (2017).
2. K. J. Foreman *et al.*, *Lancet* **392**, 2052–2090 (2018).
3. N. C. Chesnaye, J. J. Carrero, M. Hecking, K. J. Jager, *Nat. Rev. Nephrol.* **20**, 7–20 (2024).
4. A. C. Ricardo *et al.*, *J. Am. Soc. Nephrol.* **30**, 137–146 (2019).
5. A. G. Kattah *et al.*, *Clin. J. Am. Soc. Nephrol.* **13**, 1649–1658 (2018).
6. E. Dimitriadis *et al.*, *Nat. Rev. Dis. Primers* **9**, 8 (2023).
7. V. D. Garovic, G. B. Piccoli, *Kidney Int.* **104**, 213–217 (2023).
8. H. R. Turbeville, J. M. Sasser, *Am. J. Physiol. Renal Physiol.* **318**, F1315–F1326 (2020).
9. J. B. Kopp *et al.*, *Nat. Rev. Dis. Primers* **6**, 68 (2020).
10. M. E. Melica *et al.*, *Sci. Transl. Med.* **14**, eabg3277 (2022).
11. S. Romoli *et al.*, *Kidney Int.* **94**, 1111–1126 (2018).
12. H. A. Hartman, H. L. Lai, L. T. Patterson, *Dev. Biol.* **310**, 379–387 (2007).
13. W. Rosner, S. E. Hankinson, P. M. Sluss, H. W. Vesper, M. E. Wierman, *J. Clin. Endocrinol. Metab.* **98**, 1376–1387 (2013).
14. N. Santoro *et al.*, *J. Clin. Endocrinol. Metab.* **102**, 2218–2229 (2017).
15. G. Barsha, K. M. Denton, K. M. Mirabito Colafella, *Biol. Sex Differ.* **7**, 57 (2016).
16. C. N. Bairey Merz *et al.*, *Nat. Rev. Nephrol.* **15**, 776–783 (2019).
17. L. L. Yanes, J. C. Sartori-Valinotti, J. F. Reckelhoff, *Hypertension* **51**, 976–981 (2008).
18. K. L. Cheung, R. A. Lafayette, *Adv. Chronic Kidney Dis.* **20**, 209–214 (2013).
19. E. Lazzeri *et al.*, *J. Am. Soc. Nephrol.* **26**, 1961–1974 (2015).
20. M. Karlsson *et al.*, *Sci. Adv.* **7**, eabh2169 (2021).
21. N. de Alwis *et al.*, *Life Sci. Alliance* **5**, e202201517 (2022).
22. Z. A. Jasim, H. K. Al-Hakeim, S. Zolghadri, A. Stanek, *Biomolecules* **13**, 1447 (2023).
23. S. K. M. van Zundert *et al.*, *Placenta* **158**, 105–112 (2024).
24. M. Løset *et al.*, *Am. J. Obstet. Gynecol.* **204**, 84.e1–84.e27 (2011).
25. Y. Kudo, C. A. Boyd, I. L. Sargent, C. W. Redman, *Am. J. Obstet. Gynecol.* **188**, 719–726 (2003).
26. V. Dupont *et al.*, *J. Clin. Invest.* **132**, e158346 (2022).
27. V. D. Garovic *et al.*, *Nephrol. Dial. Transplant.* **28**, 1555–1561 (2013).
28. I. M. Craici *et al.*, *Hypertension* **61**, 1289–1296 (2013).
29. B. Jim *et al.*, *J. Pregnancy* **2012**, 984630 (2012).
30. M. E. Penning *et al.*, *Clin. J. Am. Soc. Nephrol.* **9**, 1377–1385 (2014).
31. V. D. Garovic, *Clin. J. Am. Soc. Nephrol.* **9**, 1337–1340 (2014).
32. C. Motta *et al.*, *Reprod. Domest. Anim.* **50**, 611–616 (2015).
33. V. D. Garovic, P. August, *J. Am. Soc. Nephrol.* **27**, 2921–2924 (2016).
34. S. S. Guhr *et al.*, *Kidney Int.* **84**, 532–544 (2013).

ACKNOWLEDGMENTS

We thank A. Santi for her technical assistance for gas chromatography–mass spectrometry analysis, B. Schäfer and A. Burger for the *Pax2.rtTA* mouse model, and S. Khan for the Flox-*ER-alpha* mouse model, which are available under a materials transfer agreement with the University of Cincinnati. **Funding:** This study was funded by the European Research Council (ERC) under the European Union's Horizon 2020 research and innovation program (grant agreement 101019891), acronym SIMPOSION (to PR). **Author contributions:** P.R. designed the study and wrote the manuscript. C.C. performed or supervised all the experiments. M.L.A. and G.A. designed and performed all immunofluorescence confocal and STED microscopy as well as 3D imaging analysis. B.M. carried out all scRNA-seq and assisted with data analysis. G.C. analyzed the data from the scRNAseq analysis. S.L. validated and sequenced the single-cell libraries. M.E.M., G.A., and L.D.C. carried out mouse experiments for scRNA-seq. M.E.M. performed in vitro culture experiments. V.R., F.R., L.C., and M.K. performed histologic and morphometric analysis. E.L. revised the statistical analysis. C.F., T.D., and A.M. performed mouse genotyping and assisted with mouse experiments. C.C., M.L.A., L.D.C., A.J.P., E.L., H.-J.A., L.L., and P.R. critically revised and edited the manuscript and advised on data interpretation. All authors read and approved the final manuscript. **Competing interests:** H.-J.A. reports paid consulting for AstraZeneca, Bayer, GSK, Novartis, Kezar, and Vifor. All other authors declare that they have no competing interests. **Data and materials availability:** The authors declare that all data needed to evaluate the conclusions in this study are available in the main text or the supplementary materials. Processed and raw mouse scRNA-seq libraries produced in this study are available from the Gene Expression Omnibus (GEO) with accession nos. GSE261615, GSE292001, and GSE291924.

SUPPLEMENTARY MATERIALS

science.org/doi/10.1126/science.adp4629
Materials and Methods; Figs. S1 to S9; Tables S1 and S2; References (*35*–*51*); MDAR Reproducibility Checklist

Submitted 2 April 2024; resubmitted 3 April 2025; accepted 18 June 2025

10.1126/science.adp4629

NANOMATERIALS

Rapid, low-temperature nanodiamond formation by electron-beam activation of adamantane C–H bonds

Jiarui Fu[1], Takayuki Nakamuro[1]*, Eiichi Nakamura[1,2]*

Diamond and adamantane (**Ad**) share a T_d-symmetric carbon skeleton, but converting **Ad** to diamond has been challenging because it requires selective carbon-hydrogen (C–H) bond cleavage and monomer assembly into a diamond lattice. Our approach differs from the conventional high-temperature, high-pressure diamond syntheses. We electron-irradiated **Ad** submicrocrystals at 80 to 200 kilo–electron volts and 100 to 296 kelvin in vacuum for tens of seconds. This process yielded defect-free nanodiamonds (NDs) of cubic crystal structure, accompanied by hydrogen gas evolution. Time-resolved transmission electron microscopy revealed the initial formation of **Ad** oligomers transforming into spherical NDs. A sizable kinetic isotope effect indicates that C–H cleavage was rate-determining, and other hydrocarbons tested failed to form NDs.

Diamond synthesis typically requires extreme conditions—pressures of tens of gigapascals and temperatures of thousands of kelvin (K)–in which diamond is thermodynamically stable (*1*). Synthesis from adamantane (**Ad**; $C_{10}H_{16}$) is a theoretically feasible alternative approach because of its shared T_d-symmetry with diamond and the substantial enthalpic gains from H_2 formation (~3000 kJ mol^{-1}) (Fig. 1A). However, this transformation has yet to be realized (*2*, *3*) because it faces two fundamental chemical hurdles: One is the selective cleavage of 16 C–H bonds to form 16 new C–C bonds while preserving the **Ad** cage structure, and the other is the ordered assembly of these monomers into the three-dimensional diamond lattice (Fig. 1A). Traditional thermal approaches have yielded limited success (*4*) because C–C bonds are homolytically weaker and cleave more readily than do the C–H bonds (Fig. 1B) (*5*). Reports on synthesis and mass spectrometry have shown that removal of a single electron from an **Ad** molecule (single-electron oxidation or ionization) generates the adamantane radical cation ($\mathbf{Ad}^{\bullet+}$), which undergoes C–H bond cleavage faster than C–C cleavage, yielding a stable adamantyl cation ($\mathbf{Ad}^{+}$) and a hydrogen radical (*6*, *7*).

These results prompted us to explore electron-impact ionization of solid **Ad** as a route to diamond synthesis (*8*, *9*). We describe the synthesis of nanodiamonds (NDs) through electron irradiation (80 or 200 keV) of **Ad** microcrystals in a vacuum, on the order of seconds, at a temperature as low as 100 to 296 K (Fig. 1C) (*10*). We monitored the reaction at the level of single-molecule, atomic-resolution, time-resolved observation using transmission electron microscopy (SMART-EM), which enabled us to study the structures and the kinetics of the growth of the **Ad** oligomers ($\mathbf{Ad_n}$) within an amorphous **Ad** matrix (*11*–*14*). These molecules subsequently transformed into defect-free, single-crystalline cubic NDs, 2 to 4 nm in diameter, with a circularity exceeding 90%. Concurrently, vigorous gas evolution was observed from the **Ad** matrix. Prolonged irradiation induced fusion of single-crystalline NDs, producing twin crystals 8 to 20 nm in diameter.

[1]Department of Chemistry, The University of Tokyo, Bunkyo-ku, Tokyo, Japan. [2]Frontiers Science Center for New Organic Matter, State Key Laboratory and Institute of Elemento-Organic Chemistry, College of Chemistry, Nankai University, Tianjin, P. R. China. *Corresponding author. Email: muro@chem.s.u-tokyo.ac.jp (T.N.); nakamura@chem.s.u-tokyo.ac.jp (E.N.)

We performed a variable-temperature, variable-voltage quantitative kinetic study based on a statistical analysis of the time course of the growth of ND particles and found a notable H(D) kinetic isotope effect (KIE = 2.0) for perdeuterated adamantane (**Ad-d**) throughout the ND formation. This result indicated that C–H cleavage was the rate-determining step and that the surfaces of the **Ad** oligomers and the NDs were covered with hydrogen atoms (Fig. 1C). Hence, the NDs formed under high vacuum from **Ad** are massive hydrocarbons. By contrast, D_{3d}-symmetric diamantane (**Da**) yielded defective NDs (*15*), whereas 1,1′-biadamantane (**Ad–Ad**), 1-phenyladamantane (**PhAd**), coronene ($C_{24}H_{12}$), and paraffin ($C_{44}H_{90}$) failed to produce NDs (Fig. 1D). These results highlight that the T_d-symmetric **Ad** skeleton was the best building block for the diamond synthesis.

Given the accessibility of **Ad** from petroleum and natural gases (*16*) and the scalability of nano- to large-scale electron beam (e-beam) engineering (*17*, *18*), this method has potential for applications in materials science, quantum technologies, and biomedical research (*19*, *20*). Moreover, this reaction differs from the conventional high-temperature, high-pressure (HTHP) approach to diamonds (*21*, *22*), exemplifying the value of controlled C–H activation (*23*, *24*).

Reciprocal and real-space analysis of ND formation

The bottom-up synthesis under e-beam irradiation of defect-free cubic single-crystalline NDs from **Ad** crystals has characteristics not found in previously reported diamond syntheses (*25*). It was achieved at low temperatures under vacuum conditions without catalysts, additives, or support medium (fig. S1 and movie S1). We observed in situ ND formation during the interactions between an 80-keV e-beam and **Ad** submicrocrystals, placed on a 20-nm-thick amorphous carbon film at 296 K. Upon initiating the irradiation, electron diffraction (ED) signals from the **Ad** crystal were visible (Fig. 2A) but rapidly disappeared because of e-beam–induced amorphization (Fig. 2B, fig. S2, and movie S2) (*26*). Continued e-beam irradiation revealed Debye-Scherrer rings originating from cubic diamond (Fig. 2C), with strong spots occasionally visible corresponding to larger ND crystals (fig. S3 and movie S3). The electron dose rate (EDR) had negligible effects on the reaction rate if it was $>0.5 \times 10^5$ e$^-$ nm^{-2} s^{-1}.

Under identical conditions, prolonged e-beam irradiation of **PhAd**, coronene, and **Ad–Ad** microcrystals produced no NDs, and that of paraffin microcrystals resulted in melting. The results of 25-min irradiation of **PhAd** [total electron dose (TED) = 2.2×10^8 e$^-$ nm^{-2}] are shown in Fig. 2, D to F. As indicated by the fast Fourier transform (FFT) images in Fig. 2E, the product generated after e-beam irradiation lacked periodic structures, and TEM images suggested the formation of particles ~1 nm in size that lacked periodicity (Fig. 2F). These results have several implications. The phenyl group was not detached from the **Ad** skeleton and obstructed the growth of diamond structures, despite the single-molecule-level chemical reactivity of **PhAd** under e-beam irradiation having to resemble that of **Ad**. Results of coronene irradiation (TED = 4.1×10^9 e$^-$ nm^{-2}) are shown in Fig. 2, G to I. The FFT pattern with a diffusive ring of 2.1 Å and the high-resolution TEM image (Fig. 2I) indicated that coronene underwent an expansion of its sp^2 network upon electron irradiation (*27*, *28*). We compared the reactivity of an **Ad–Ad** particle (Fig. 2J), irradiated side by side with an **Ad** particle (Fig. 2, K and L), and found that the latter afforded NDs, whereas the former did not change its appearance.

We next analyzed the temporal evolution of the ND structure using high-resolution TEM. Amorphous **Ad** supported on carbon nanohorn (CNH) aggregates were first used to observe ND growth (fig. S4). Representative TEM images at 80 keV and 296 K taken with a frame rate of 50 frames per second (fps; 20 ms frame^{-1}) are shown in Fig. 2M. Graphitic structures originating from CNH were visible in the frame at 0 s, with little contrast attributable to **Ad**. At 3.56 s (TED = 10^7 e$^-$ nm^{-2}), many NDs had already formed, reaching ~5 nm in size by 14.30 s as **Ad** molecules were consumed, halting the growth.

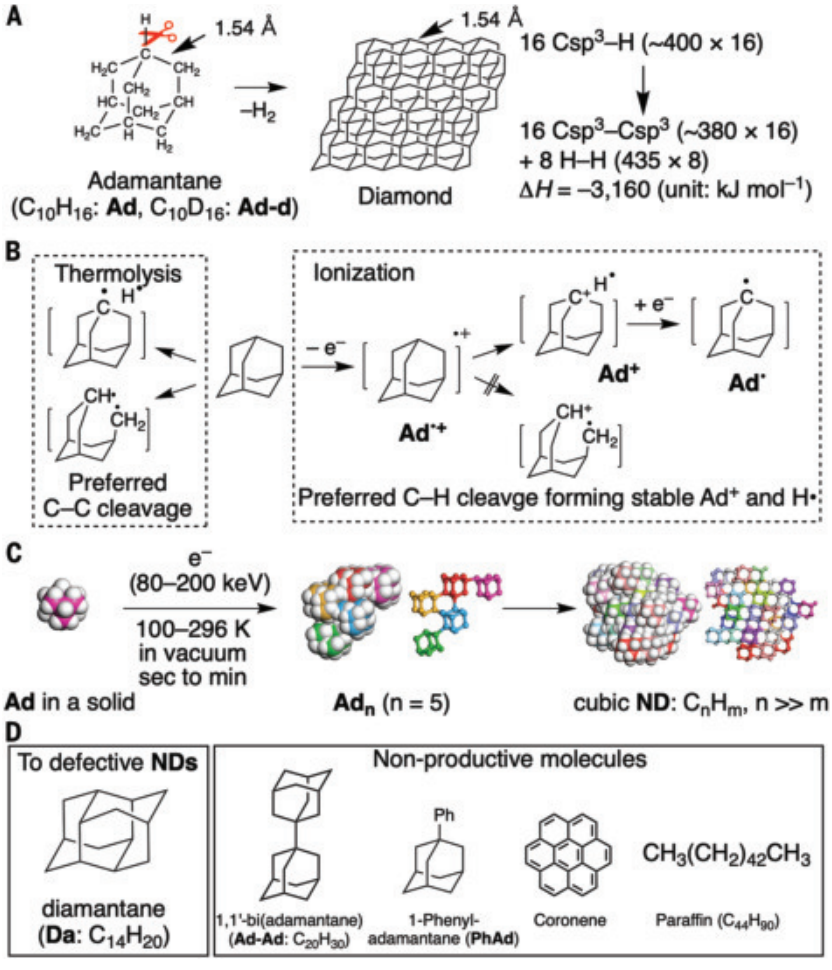

Fig. 1. Ad-to-diamond reactions enabled with electron irradiation. (**A**) Ad to ND and its energetics. (**B**) Thermolysis versus ionization of **Ad**. (**C**) Conversion of **Ad** to NDs by means of **Ad** oligomers. To illustrate the incomplete diamond structure of $\mathbf{Ad_5}$, it is shown here from an angle different from the one in Fig. 4A in a ball-and-stick representation. (**D**) Less symmetrical **Da**, which gave defective NDs, and nonproductive molecules.

We estimated the rate of the increase in the volume of single ND particles to be reaction rate constant (k) = 3.4×10^{-8} nm^2 (e$^-$)$^{-1}$ (fig. S4C). This value aligned with the rate measured on an amorphous carbon substrate [$k = 3.3 \times 10^{-8}$ to 3.8×10^{-8} nm^2 (e$^-$)$^{-1}$], indicating that the reaction rate was independent of the substrate that supports the solid **Ad**. However, the vibration of CNH aggregates and rotation of the NDs hindered atomic-resolution observations (*12*), prompting us to use 20-nm-thick amorphous carbon films to suppress the mechanical vibrations (*29*).

We next studied the temporal evolution of the ND structure on a stable carbon surface. In Fig. 3A, we present four representative frames from low-magnification TEM imaging (×120,000; EDR = 0.1×10^5 to 5.6×10^5 e$^-$ nm^{-2} s^{-1}) recorded with 20-ms frame intervals (fig. S5 and movie S4). The reaction progress depended solely on TED, not EDR. Initially, a low-contrast **Ad** solid was observed on the amorphous carbon substrate. After 1 min, numerous oligomers formed 1 to 2 nm in size, floating in a matrix of **Ad** (7.92 to 63.42 s), showing ND structures. As TED increased and **Ad** was consumed, the NDs started fusing with each other (124.84 to 154.58 s), ceasing reaction progress at ~3 min (TED = ~3×10^7 e$^-$ nm^{-2}). The formation of larger NDs in the center of the image with smaller NDs on the periphery reflected the thicker central and thinner peripheral **Ad** matrix (fig. S6).

A particularly intriguing observation was the formation and bursting of nanometer-sized hydrogen bubbles (Fig. 3A, white dotted box). A video of this phenomenon is available in the supplementary materials (movie S5). Magnified views of the boxed region are shown in Fig. 3B and fig. S5. From 89.58 to 118.90 s, the particle sizes increased in the central area, followed by an explosive formation of hydrogen bubbles of ~10 nm in diameter by 118.90 s, displacing NDs seen as dark spots (*30*). The hole disappeared between 122.96 and 126.84 s, resembling gas bubble eruptions in geothermal mud pools. ND particle arrangement reverted to near-original configuration by 128.82 s. We can view the polymerization of **Ad** as a variant of well-known e-beam–driven polymerization of polyethylene that forms interpolymer C–C bonds with concomitant formation of hydrogen gas (*31*).

We tracked the progress of C–H activation using carbon K-edge core-loss electron energy loss spectroscopy (EELS) in scanning transmission electron microscopy (STEM), with both imaging and spectral acquisition performed simultaneously by means of beam scanning (Fig. 3, C and D). The signal from the carbon support grid (Fig. 3D, †) served as an internal standard to monitor the reaction. In the low-conversion spectrum (Fig. 3D, spectrum a), we observed distinct signals for the C–C skeleton (Fig. 3D, $) and the C–H bonds of **Ad** (Fig. 3D, ‡). As the reaction progressed, the **Ad**'s C–C skeleton signal disappeared in spectrum b, whereas the C–H signal persisted, assigned to C–H bonds on the surface of **Ad** oligomers and small NDs (Fig. 1C). As the size of the NDs increased, the C–H signal vanished in spectrum d, giving rise to two broad features above 296 eV, almost identical to the reported spectrum e of HTHP diamonds (*32*).

Fast and atomic-resolution imaging of ND formation

At higher magnification (×1,000,000 to 2,000,000; EDR = 0.1×10^7 to 2.0×10^7 e$^-$ nm^{-2} s^{-1}), we observed individual **Ad** oligomers (Fig. 4). Real-time imaging at 50 fps captured oligomer growth (figs. S7 and S8 and movie S6) and defect-free cubic ND formation (fig. S9 and movie S7). The translational and rotational motions of the molecules in the **Ad** matrix allowed us to determine their atomic structure by viewing individual particles from various directions (*33*). $\mathbf{Ad_n}$ oligomers were unambiguously characterized on the basis of the multislice method (fig. S10). The stepwise growth of **Ad** oligomers are shown in Fig. 4, A to G, culminating in defect-free cubic NDs (Fig. 4, I to L). Toward the completion of the reaction, NDs fused to yield large NDs (8 to 20 nm, >90% circularity) (Fig. 4, M and N), primarily as multitwin crystals (*34*). We found no polymorphs other than cubic structure, unlike in the diamond synthesis under harsher conditions (*35*).

TEM images of two groups of **Ad** oligomers are provided in Fig. 4, A to D. In Fig. 4A, we show the image from the <110> axis direction. Comparison with the TEM image with the simulations generated with the multislice method for oligomers of various sizes strongly suggests that this is an **Ad** pentamer. In Fig. 4B, we show a parallelogram-like oligomer assigned to be an octamer and a model of $\mathbf{Ad_8}$. The observation indicated that during a period of 0.92 s, approximately three **Ad** molecules were attached to $\mathbf{Ad_5}$. We calculated the growth rate for the addition of carbon atoms per TED as $k = 9 \times 10^{-8}$ nm^2 (e$^-$)$^{-1}$, which agreed with the one measured for an average of numerous NDs. In Fig. 4, C and D, we show a ~17-nucleotide oligomer ($\mathbf{Ad_{\sim 17}}$) observed growing into a ~26-nucleotide oligomer ($\mathbf{Ad_{\sim 26}}$). The degree of oligomerization was also estimated by comparison of the TEM images with the simulation of model oligomers. We calculated the growth rate of carbon atoms per TED to be $k = 12 \times 10^{-8}$ nm^2 (e$^-$)$^{-1}$ during 2.66 s observations, which agreed with the one for the $\mathbf{Ad_5}$-to-$\mathbf{Ad_8}$ case.

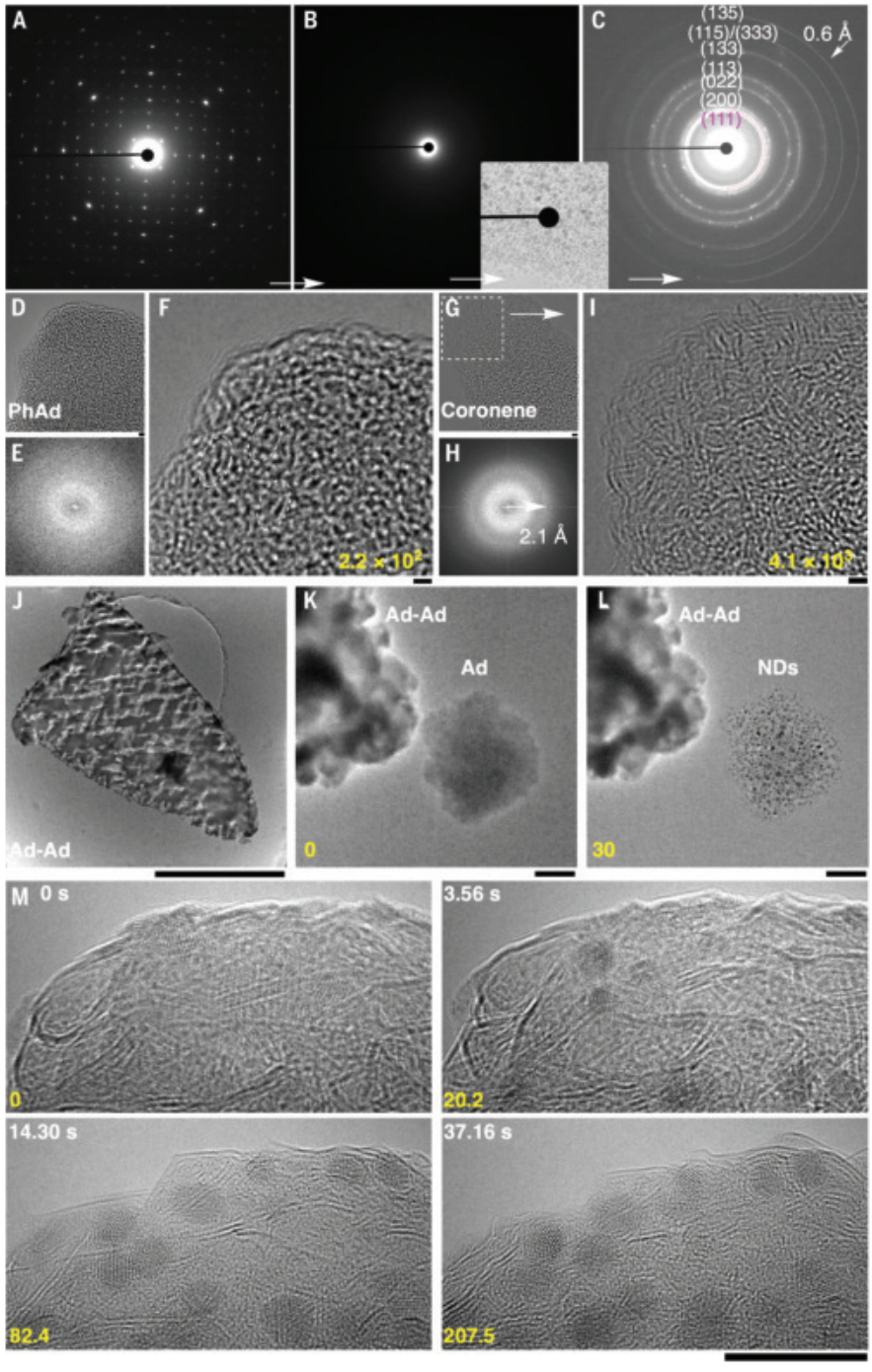

Fig. 2. Monitoring Ad-to-ND transformations in reciprocal space and comparisons between nonproductive molecules and Ad at 80 keV and 296 K. (**A**) An ED pattern of a crystalline face-centered-cubic (fcc) **Ad** microcrystal. (**B**) Quick disappearance of the ED signals caused by amorphization after irradiation with TED of ~5×10^5 $e^- nm^{-2}$. (**C**) The appearance of an ED pattern characteristic of a cubic ND powder with TED of ~1×10^8 $e^- nm^{-2}$. (Inset) TEM image. (**D**) TEM image of amorphous material after irradiation of **PhAd** with TED = 2.2×10^8 $e^- nm^{-2}$. TED (yellow) is shown with a unit of $\times 10^6$ $e^- nm^{-2}$. (**E**) FFT of (D), indicating lack of periodicity. (**F**) Magnified TEM image of (D) showing dark-contrast objects of a diameter <1 nm, which is suggestive of **PhAd** oligomers. (**G**) TEM images after irradiation of coronene with TED = 4.1×10^9 $e^- nm^{-2}$. (**H**) FFT of (G), showing a diffused ring at 2.1 Å, which is indicative of graphitic structures. (**I**) Magnified TEM images of (G), revealing graphitic features. (**J**) TEM image of **Ad–Ad** particle at 80 keV and 296 K. (**K**) **Ad–Ad** and **Ad** particles side by side. (**L**) **Ad** converted to NDs, whereas **Ad–Ad** unchanged in appearance after TED of 3×10^7 $e^- nm^{-2}$. (**M**) Growth of NDs on the surface of CNHs, with time in white, TED in yellow, and EDR = 5.7×10^6 $e^- nm^{-2} s^{-1}$. Frame rate = 50 fps. Time 0 was set arbitrarily. Scale bars, 1 nm (D), (F), (G), and (I); 10 nm (M); 100 nm (K) and (L); and 1000 nm (J).

In Fig. 4, E to G, we show NDs with diameters of ~2 nm viewed from the <100>, <110>, and <112> axes, respectively, made from 40 to 60 **Ad** molecules. We include in the supplementary materials 110 pairs of TEM and FFT images of defect-free, single-crystalline cubic NDs like those depicted in Fig. 4, A to G (figs. S11 to S14). Larger cubic NDs that grew further are illustrated in Fig. 4, I to L. The TEM images of the single-crystalline cubic ND particles showed a circularity of 93.6%, averaged over 100 NDs (fig. S15).

Plotting the lattice sizes of **Ad** oligomers and NDs revealed an intriguing trend (Fig. 4H). For NDs > ~2 nm (Fig. 4I), the (111) lattice spacing matched that of bulk diamond (2.1 Å). By contrast, smaller structures ~1 nm in size (Fig. 4A) exhibited expanded lattice spacings—up to 2.7 Å for the (111) plane. Careful analysis of the structures of putative **Ad** pentamers revealed that the isomers with incomplete diamond lattices, such as $\mathbf{Ad_5}$ (Fig. 1C), reproduced the experimental 2.7-Å FFT signal (Fig. 4A). The diamond structure in $\mathbf{Ad_5}$ was not yet formed, in that two adamantane units were linked by only a single C–C bond to a central trimer, so each adamantane unit connected through only two C–C bonds. This result raises the question of why such a weakly bonded dimer appears rigid under TEM. We attribute this rigidity to Schreiner's finding that long single bonds connecting diamondoids are stabilized by attractive dispersion interactions between closely aligned H···H contact surfaces. The atomic models shown in Figs. 1C and 4, A to D, constructed on the basis of this principle (*36*), successfully reproduced the observed 2.7- and 2.5-Å FFT patterns (fig. S10) (*37*).

Further irradiation caused the merging of single-crystalline NDs to produce twin NDs > 8 nm in diameter. Examples of these are shown in Fig. 4, M and N. Figure 4M features a quintuple twin cubic diamond

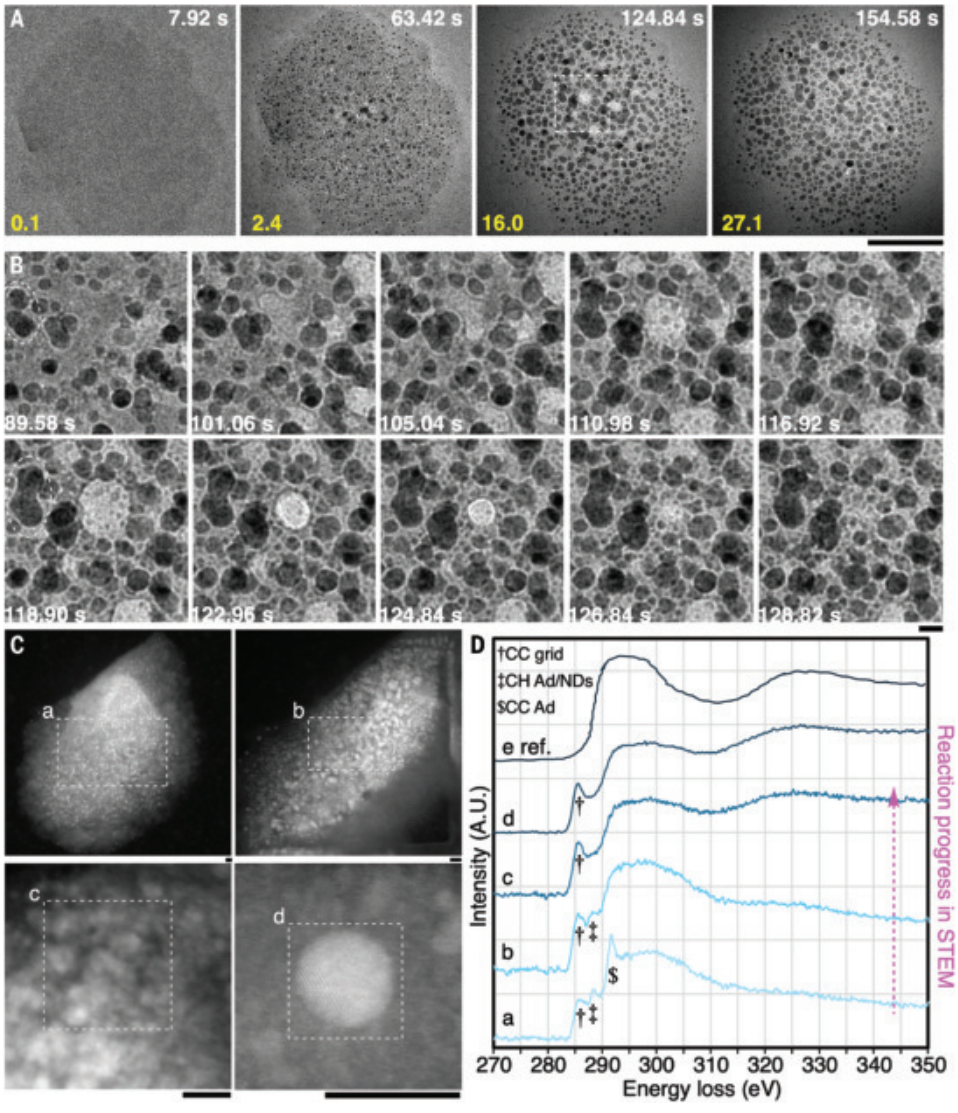

Fig. 3. Ad-to-ND transformations evidenced by evolution of H_2 and EELS at 296 K. (**A**) Low-magnification images of **Ad**-to-ND transformation with time in white, TED in yellow, and EDR = 0.1×10^5 to 5.6×10^5 $e^- nm^{-2} s^{-1}$. 50 fps; voltage, 80 keV. Dark particles are NDs, and light areas indicate hydrogen bubbles. The area of a dotted square is magnified in (B). (**B**) Magnified images of (A). The frames at 118.90, 122.96, and 124.84 s illustrate the process of the hydrogen gas escape from a viscous matrix of **Ad** oligomers, which caused the motion of nearby ND particles (50 fps). Two NDs merged into one, as seen in the circled area. (**C**) Reaction progress of **Ad**-to-ND transformation recorded in the STEM mode under 200 keV at 296 K. The images (a) to (c) roughly correspond to 5, 40, and 100% yield in Fig. 5B, respectively. The image (d) is for a single ND. (**D**) The reaction progress (a) to (d) illustrated by the carbon K-edge EELS spectra measured for the square regions in (C). The spectrum (e) is a reference spectrum of HTHP diamonds taken from (*32*). The signal at 285.5 eV (†) arose from the amorphous carbon on the TEM grid, serving as a reference. The signal at 288 eV (‡) is from the 1s-σ* (C–H) in **Ad** and NDs. The signal at 292 eV ($) is characteristic of the 1s-σ* (C–C) of the **Ad** skeleton. The broad peak centered at 296 eV corresponds to the 1s-σ* (C–C) signal from NDs, and the broad peak that emerged later at 325 eV corresponds to multiple scattering resonances, an indicator of long-range order. Scale bars, 10 nm (B) and (C), and 100 nm (A).

with four mirror planes, whereas Fig. 4N shows a cubic diamond with a pentafold twin with fivefold symmetry. These nanotwinned structures formed from single-crystalline cubic diamonds (*38*).

Da also produced NDs upon e-beam irradiation but yielded inefficient reactions and a mixture of defective crystals and less-crystalline regions. In Fig. 4, O and P, we illustrate an example of the ND growth starting from **Da** microcrystal. The disordering of **Da** crystals was slower than for **Ad** crystal disordering; the ND growth began before the entire amorphization of the **Da** crystals, as shown by the presence of **Da** crystal lattice (Fig. 4O). The image observed in the early stages of the reaction depicts an amorphous aggregate with partial diamond periodicity. Continued irradiation formed a multiple twin (Fig. 4P). Single-molecule-level measurements indicated that the volume increased by ~35% after 3.56 s, showing an approximate growth rate of $k = 4 \times 10^{-8}$ nm^2 $(e^-)^{-1}$. This rate was about 2.5 times slower than that observed in the single-molecule-level analysis described above for the **Ad** growth, agreeing with assessments of the sluggishness. Thus, D_{3d}-symmetric **Da** serves less efficiently than **Ad** for ND formation, which again showcases the different mechanisms of ND formation by using the e-beam and HTHP (*4*).

Quantitative kinetic analysis of ND formation

Next, we examined the mechanism of the new ND synthesis through particle-by-particle statistical analysis of the ND growth, particle size, and particle count relative to the EDR and TED (Fig. 5, A to C, and fig. S16). We also examined the effects of the starting materials, substrates, acceleration voltage, temperature, and the H(D) KIE (Fig. 5, D to I, and figs. S17 to S22). The KIE data indicated that C–H bond cleavage is the rate-determining step of ND formation.

In Fig. 5A, we show the time evolution of **Ad**-to-ND conversion at 100 K and 200 keV e-beam irradiation with EDR = 2.6×10^5 $e^- nm^{-2} s^{-1}$. In Fig. 5A, inset, we show a rapid loss of the **Ad** crystal diffraction signals with a very small half-life of TED = 0.16×10^6 $e^- nm^{-2}$ (*26*). After complete amorphization in a few seconds, the ND growth started to produce NDs in ~10% yield after 23 s (TED = 6×10^6 $e^- nm^{-2}$) and stopped after ~100 s. The final yield after 107 s (TED = 30×10^6 $e^- nm^{-2}$) was estimated to be quantitative on the basis of the calculated total volume of the NDs with an assumption that **Ad** molecules have not been lost in a vacuum (fig. S16). **Ad** oligomerization occurred in the zeroth order as to TED with an **Ad** half-life of TED = 21×10^6 $e^- nm^{-2}$—130 times larger than the ED decay half-life of TED = 0.16×10^6 $e^- nm^{-2}$. The conversion became faster after the yield exceeded ~40%, and the growth ended at TED ~3.0×10^7 $e^- nm^{-2}$. The particle count (Fig. 5, blue dot) and the particle volume per particle (Fig. 5, orange dot) indicate that the accelerated growth was caused by the fusion of ND particles after ~40% conversion, as was visually seen in the TEM images of individual particles (Fig. 3B) (*39*). Continuing irradiation after

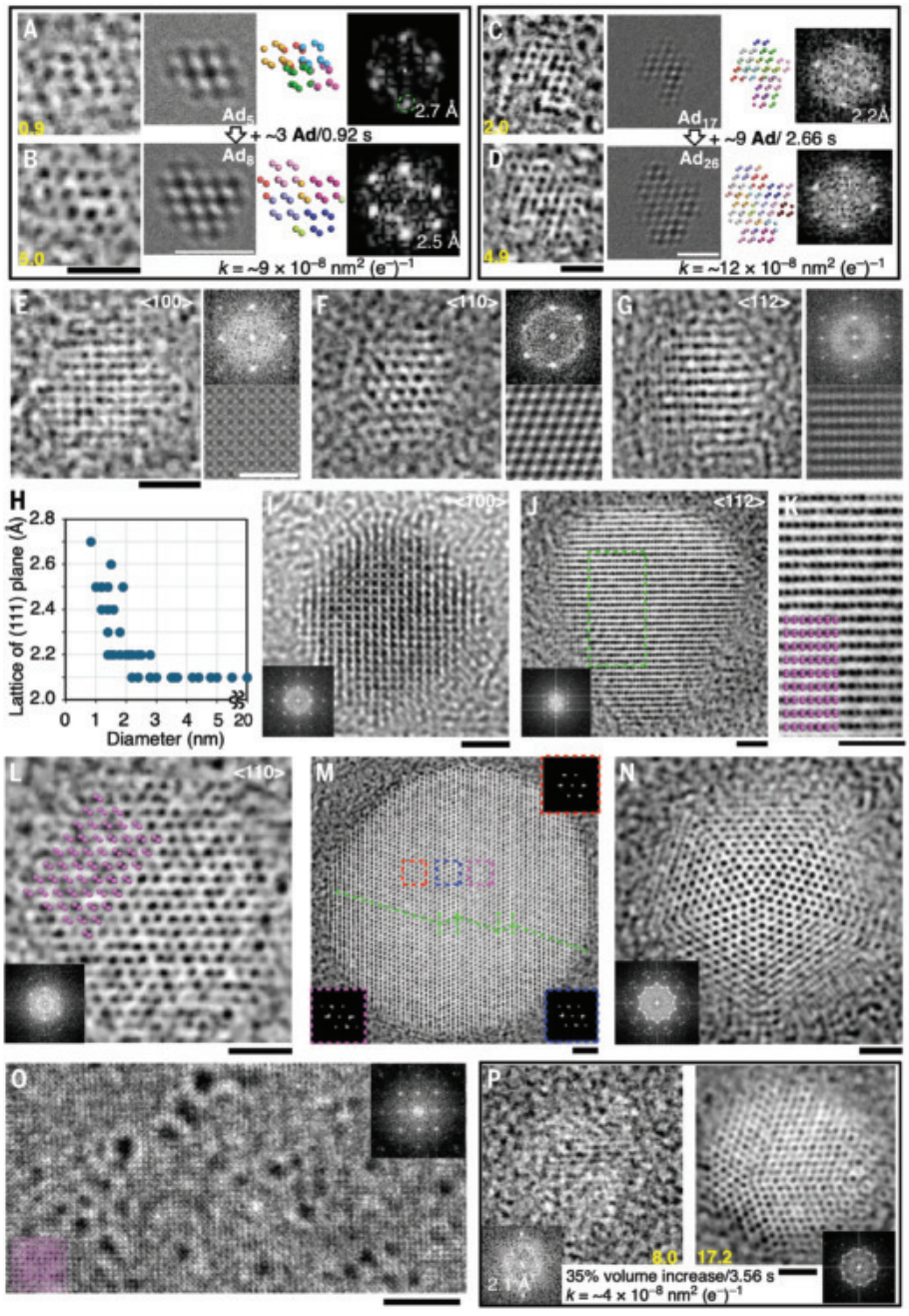

Fig. 4. Representative images of NDs formed from Ad and Da at 80 keV, 296 K, and 50 fps. (**A**) Experimental, simulated, and FFT images of the smallest observable **Ad** oligomer, viewed along the <110> axis, shown together with a *Z*-correlated high-noise (ZC_{HN}) depiction of $\mathbf{Ad_5}$, the smallest size to reproduce the TEM image. Each **Ad** molecule is shown in different colors. (**B**) The ZC_{HN} depiction for $\mathbf{Ad_8}$. A larger oligomer grew from the oligomer in (A) during 0.92 s observations (EDR = 4.5×10^6 e^- nm^{-2} s^{-1}). This oligomer rotated during observation and exposed the same face as in (A). The values in yellow are TED (unit, $\times 10^6$ e^- nm^{-2}). The TEM frame shown in (A) was created by stacking two consecutive images for visibility. (**C**) An oligomer whose TEM image can be reproduced by $\mathbf{Ad_{17}}$, a ZC_{HN} model, and an experimental FFT pattern. (**D**) $\mathbf{Ad_{26}}$ after 2.66 s from (C) (EDR = 1.1×10^6 e^- nm^{-2} s^{-1}). For (C) and (D), five consecutive frames were stacked for visibility. (**E** to **G**) Three ~2.0 nm NDs viewed along the <100>, <110>, and <112> axes and their FFT patterns. Simulated TEM images of cubic NDs (ICSD: 44101) are shown for comparison. The scale bars in (E) apply also to (F) and (G). (**H**) Decrease in the (111)-plane *d*-spacing with an increase of the ND diameter, indicating that the skeletal vibration stops for diameters >2 nm. Details are provided in figs. S11 to S14; single crystals 2 to 4 nm in diameter were the most abundant. (**I** to **L**) Representative single NDs (4 to 8 nm in diameter) seen along the <100>, <112>, and <110> axes, with their FFT patterns. (**M**) Large crystal with planar defects and the FFT patterns. FFT analyses were performed for the areas indicated with boxes to show the twin structures. (**N**) Fivefold twinning crystal and its FFT pattern. (**O**) Coexistence of **Da** crystalline domains, amorphous domains, and NDs (black dots). The image was generated by stacking 260 frames for visibility. EDR = 2.1×10^4 e^- nm^{-2} s^{-1}. A ZC_{HN} model and FFT of crystal domains are also shown. (**P**) The growth of an ND crystal into a multitwin crystal, highlighted by the slower growth rates (*k*, determined by volume). This ND from **Da** is evidently more defective than the single-crystalline NDs formed from **Ad**. EDR = 2.6×10^6 e^- nm^{-2} s^{-1}. Scale bars, 1 nm (A) to (G), (I) to (N), and (P); 10 nm (O).

100% conversion (Fig. 5C, 100*) led to further NDs' fusion until they formed spherical NDs as large as 20 nm at TED ≈ 10^8 e^- nm^{-2} (Fig. 4, M and N). The results shown in Fig. 5C indicate that defect-free single crystals with diameters of 2 to 4 nm formed with a selectivity of 63% at 20% conversion of **Ad**.

As the first step of the quantitative kinetic study, we determined the zeroth-order *k* at 80 keV at 296 K over a 100-fold variation in EDR, yielding highly insightful results (Fig. 5D). Specifically, with EDR = 0.1×10^5 e^- nm^{-2} s^{-1}, we saw no conversion of ND even after 45 min, TED ≈ 2×10^7 e^- nm^{-2}. The induction period became shorter at EDR > 0.5×10^5 e^- nm^{-2} s^{-1} and became much shorter at EDR = 10.7×10^5 e^- nm^{-2} s^{-1} (TED ≈ 0.5×10^7 e^- nm^{-2}). Then, the reaction rate *k* at EDR > 0.5×10^5 e^- nm^{-2} s^{-1} was EDR-independent [$k = 3.3$–3.8×10^{-8} nm^2 $(e^-)^{-1}$]. These rate constants that were measured up to 40% conversion align with the ones measured at single-molecule levels for $\mathbf{Ad_5}$ and $\mathbf{Ad_{\sim 17}}$ [k = ~10×10^{-8} nm^2 $(e^-)^{-1}$, 80 keV, 296 K] (Fig. 5, A to D). The observed small difference rate may indicate that the structurally flexible small oligomers (Fig. 4H) are slightly more reactive than the larger and rigid NDs.

The rate constants *k* shown in Fig. 5E are identical despite a large variation in acceleration voltage and temperature. The rate *k* was temperature-independent for 80 keV electrons, and the Arrhenius activation energies (E_a) were close to zero for both 80 and 200 keV conditions (E_a = 0.2 to 0.7 kJ mol^{-1}), indicating that the energy provided by the electrons is enough to cause the C–H cleavage and subsequent reactions without the supply of thermal energy from the surroundings (Fig. 5F). Because of rapid structural disordering at the onset of irradiation, we observed no substantial difference in reaction rates starting from crystalline and amorphous **Ad** particles (figs. S23 and 24).

The frequency factors ln(*A*) at 80 and 200 keV shown in Fig. 5F are essentially identical: –17.0 and –16.8, respectively. They are very similar (1/3 as to *A*) to the one for the previously reported C_{60} dimerization through radical cation [ln(*A*) = –15.9, E_a = 1.7 kJ mol^{-1}] (*40*), suggesting

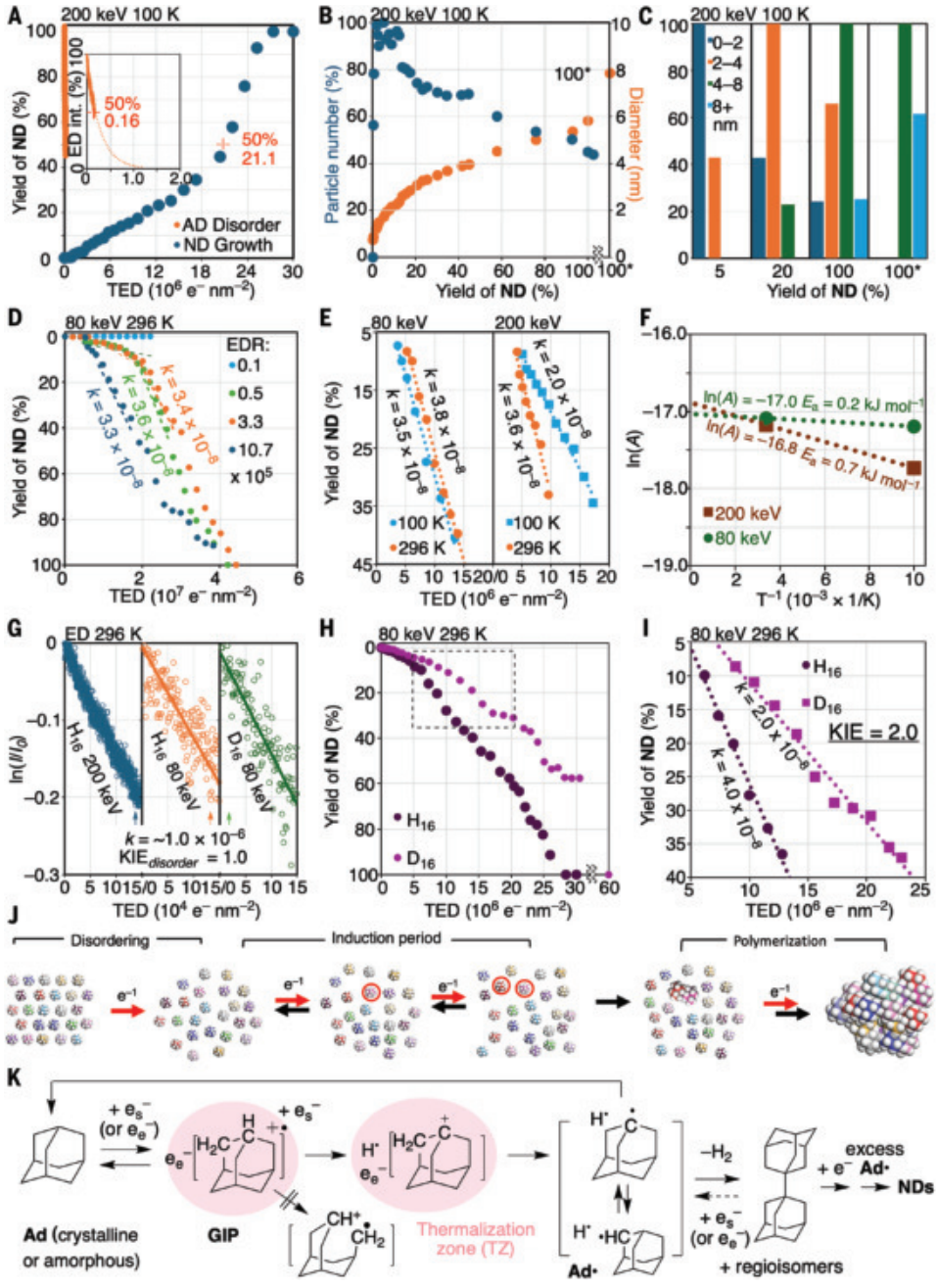

Fig. 5. Kinetic and statistical analyses on Ad-to-ND conversion. (**A**) (Inset) Electron-induced disordering of **Ad** crystals, and the conversion to **Ad**-to-NDs at 200 keV, 100 K, and EDR = 2.6×10^5 e$^-$ nm^{-2} s^{-1}. The volume of each ND particle was estimated from the area of each particle image and was integrated over all observed ND particles at each TED (supplementary materials). The yield of ND is based on the increase in the total volume of ND particles relative to that at the end of the reaction. Both the disorder rate and the ND formation rate depend only on TED and not on EDR shown in (D). (**B**) Plots of particle number (blue) and average diameter (orange) against normalized reaction progress at 200 keV and 100 K. Decrease in particle number reflects ND fusion, particularly after the yield exceeding 80%. (**C**) Change in diameter distributions against reaction progress. 100* refers to the data after further irradiation beyond 100% conversion of **Ad**-to-NDs (TED of ~10^8 e$^-$ nm^{-2}). (**D**) Reaction progress plots at 80 keV and 296 K with EDRs of 0.1×10^5, 0.5×10^5, 3.3×10^5, and 10.7×10^5 e$^-$ nm^{-2} s^{-1}. We determined k through linear fitting in the range of up to ~40% conversion. (**E**) Reaction rates at different temperatures and voltages. (**F**) Arrhenius plots for electron-mediated **Ad**-to-ND reactions, presenting activation energies (E_a) and frequency factors (A). (**G**) KIE = 1.0 for disordering of **Ad** and **Ad-d** crystals at 296 K. EDR = 0.3×10^3 e$^-$ nm^{-2} s^{-1} for **Ad** at 200 keV, 4.5×10^4 e$^-$ nm^{-2} s^{-1} for **Ad** at 80 keV, and 5.8×10^4 e$^-$ nm^{-2} s^{-1} for **Ad-d** at 80 keV. (**H**) A large KIE for **Ad** and **Ad-d** at 80 keV and 296 K. We examined the TED range indicated with a box to study the reaction after steady state was achieved. (**I**) KIE = 2.0 for **Ad** and **Ad-d** determined at low conversion. (**J**) Induction period in which a low concentration of radicals causes regeneration of **Ad**, and the growth period in which many radicals form and polymerize. (**K**) A mechanistic rationale involving GIP formation and its recombination within the thermalization zone (pink) in an **Ad**. Scattered electron, e_s^-; ejected electron, e_e^-.

their mechanistic similarity. On the other hand, the values are vastly smaller than the ln(A) values for the e-beam–induced disordering of organic crystals [ln(A) = −6 to −8] (*26*). This large discrepancy highlights the mechanistic distinction between electron-induced ionization and the vibration-induced disordering of organic molecules in crystals (*26*).

Next, we found that the ND formation shows a sizable H(D)KIE but not the ED signal decay, indicating that the former includes C–H bond cleavage as a rate-determining step, whereas the latter did not, as we expected (*41*). In Fig. 5G, we show that the ED signal decay shows neither KIE nor dependence on the acceleration voltage (*42*). The voltage independence of the ED signal decay rate was also reported previously (*26*). However, the ND growth exhibited sizable H(D)KIE. In Fig. 5H, we present the whole kinetic profiles for **Ad** and **Ad-d** at 80 keV and 296 K, demonstrating that the reaction proceeded more slowly for **Ad-d** than **Ad** through the entire reaction. The H(D)KIE calculated for the initial rate of the growth (Fig. 5I) was 2.0, indicating that C–H bond cleavage in **Ad** and its oligomers was involved in the rate-determining step. This result indicates that the surfaces of the **Ad** oligomers and the ND particles were covered by hydrogen atoms; that is, they are considered massive hydrocarbons. Therefore, the H_2 formation provides a major driving force throughout the entire ND growth (Fig. 1A).

Mechanistic studies

The EDR-dependent induction period and the subsequent zeroth-order kinetics are two characteristics of our ND synthesis (Fig. 5D), and such kinetic behavior is frequently observed in the photo-controlled radical polymerization in solution (*43*) but rarely reported in electron microscopy studies. Drawing from abundant photochemical precedents, we propose an outline of the ND formation (Fig. 5J). In this model, electrons initially induce rapid crystal disordering and, with prolonged irradiation, generate short-lived reactive species in equilibrium with

the starting **Ad** molecule (Fig. 5J, induction period, red circle). Irreversible ND formation starts once a sufficient equilibrium concentration of the reactive species is achieved (growth period).

A detailed model (Fig. 5K) offers further insights into the chemistry underlying ND formation. Electron impact mass spectrometry studies of organic molecules using a 70-eV electron beam in vacuum (*7*) showed that the primary event is the single-electron oxidation forming a radical cation and an ejected (secondary) electron (e_e^-). We propose that the radical cation of **Ad** (**Ad**$^{\bullet+}$) decomposed to generate an adamantyl cation (**Ad**$^+$) through selective cleavage of C_1–H bond, despite it being stronger than the C–C bond (Fig. 1A).

Radiation chemistry in condensed phase has shown that the radical cation and the ejected electron in the crystal form a geminate ion-pair (GIP), which recombines within the thermalization zone (TZ) (Fig. 5K, pink) (*44*). In the present ND synthesis, when an electron entered an **Ad** crystal (ionization energy = 9.25 eV, comparable with that of benzene), it created GIPs within the TZ, comprising an ejected electron (e_e^-), hydrogen radical, **Ad**$^{\bullet+}$, and **Ad**$^+$. Beyond ionization of a single molecule, the secondary electron (e_e^-) could initiate a cascade of reactions among neighboring **Ad** molecules within the TZ until it lost most of its energy. This ionization mechanism does not operate in inorganic solids such as metal oxides, which have much higher ionization energies and extremely small thermalization zones (*45*).

The observed near-zero E_a aligns with this scenario (Fig. 5F), in which the first intermediate, **Ad**$^{\bullet+}$, represents the highest energy state along the pathway. Ad$^{\bullet+}$ would undergo C–H bond fission, producing a hydrogen radical (H$^\bullet$) and **Ad**$^+$. **Ad**$^+$ is an exceptionally stable carbocation because of its strong hyperconjugative stabilization (*6*). GIP recombination within the TZ generates a tertiary adamantyl radical (**Ad**$^\bullet$) and H$^\bullet$, leading to the formation of an adamantyl dimer and molecular hydrogen (H_2). This process will also regenerate **Ad** (Fig. 5K, top arrow). Additionally, hydrogen atom migration between 1- and 2-adamantyl radicals (Fig. 5K, right) contributes to structural equilibria among **Ad** oligomers, which is essential for the ordered three-dimensional assembly of diamond structures. Last, the inability of **Ad**–**Ad** to yield NDs (Fig. 1D) suggests that a minute amount of **Ad**–**Ad** formed in situ from **Ad** reacts with surrounding excess **Ad** monomers and grows into larger structures under continued electron irradiation (Fig. 5K, right).

Discussion

Several key chemical characteristics of the system contributed to the clean and selective **Ad**-to-ND conversion: a substantial enthalpic driving force driven by H_2 formation, effective ionization by secondary electrons, the high thermodynamic stability of the adamantyl cation, GIP recombination within the TZ, and an overall reaction cascade initiated by scattered electrons ejected from the TZ. We found that quantitative kinetic analysis under variable-temperature, variable-voltage conditions is essential for deciphering the chemical mechanism of organic substances under electron irradiation (*40*). Kinetic studies of the **Ad**-to-ND conversion indicate that e-beam irradiation induces a chemical reaction governed by chemical principles, surpassing the conventional notion of e-beam–induced damage to organic matter (*46*).

These findings open a new paradigm for understanding and controlling chemistry (*47*, *48*) in the fields of electron lithography, surface engineering, and electron microscopy. The observed lack of ND formation at a high EDR (0.1×10^5 e$^-$ nm^{-2} s^{-1}) and TED ($\approx 2 \times 10^7$ e$^-$ nm^{-2}), as well as the previously reported C_{60} dimerization reactions (*40*), indicates that chemical reactions of organic molecules occur far less frequently than bond rotations and conformational changes of organic and protein molecules that occur frequently, even at TED $< 10^3$ e$^-$ nm^{-2} (*26*). Last, the above results provide experimental support for the long-standing hypothesis that the diamond formation in extraterrestrial meteorites and uranium-bearing carbonaceous sedimentary rocks may have been driven by high-energy particle irradiation (*49*, *50*).

REFERENCES AND NOTES

1. F. P. Bundy *et al.*, *Carbon* **34**, 141–153 (1996).
2. R. C. Fort, P. R. Schleyer, *Chem. Rev.* **64**, 277–300 (1964).
3. E. A. Ekimov, O. S. Kudryavtsev, N. E. Mordvinova, O. I. Lebedev, I. I. Vlasov, *ChemNanoMat* **4**, 269–273 (2018).
4. S. Park *et al.*, *Sci. Adv.* **6**, eaay9405 (2020).
5. T. Newhouse, P. S. Baran, *Angew. Chem. Int. Ed.* **50**, 3362–3374 (2011).
6. G. A. Olah *et al.*, *J. Am. Chem. Soc.* **107**, 2764–2772 (1985).
7. J. Bouwman, S. Horst, J. Oomens, *Chemphyschem* **19**, 3211–3218 (2018).
8. N. Nunn, M. Torelli, G. McGuire, O. Shenderova, *Curr. Opin. Solid State Mater. Sci.* **21**, 1–9 (2017).
9. S. L. Y. Chang, P. Reineck, A. Krueger, V. N. Mochalin, *ACS Nano* **16**, 8513–8524 (2022).
10. Y. Gong *et al.*, *Nature* **629**, 348–354 (2024).
11. M. Koshino *et al.*, *Science* **316**, 853–853 (2007).
12. H. Frey, A. Beck, X. Huang, J. A. van Bokhoven, M. G. Willinger, *Science* **376**, 982–987 (2022).
13. K. Harano, T. Nakamuro, E. Nakamura, *Microscopy* **73**, 101–116 (2024).
14. Y. Kratish *et al.*, *Chem* 102541 (2025).
15. S. Banerjee, P. Saalfrank, *Phys. Chem. Chem. Phys.* **16**, 144–158 (2014).
16. J. E. Dahl, S. G. Liu, R. M. K. Carlson, *Science* **299**, 96–99 (2003).
17. M. Zhang *et al.*, *J. Am. Chem. Soc.* **142**, 9169–9174 (2020).
18. J. Park, S. Lee, O. F. Jafter, J. Cheon, D. Lungerich, *Phys. Chem. Chem. Phys.* **26**, 8051–8061 (2024).
19. Y. Wu, F. Jelezko, M. B. Plenio, T. Weil, *Angew. Chem. Int. Ed.* **55**, 6586–6598 (2016).
20. E. Böhler, J. Warneke, P. Swiderek, *Chem. Soc. Rev.* **42**, 9219–9231 (2013).
21. V. N. Mochalin, O. Shenderova, D. Ho, Y. Gogotsi, *Nat. Nanotechnol.* **7**, 11–23 (2011).
22. V. V. Danilenko, *Phys. Solid State* **46**, 595–599 (2004).
23. H. Yi *et al.*, *Chem. Rev.* **117**, 9016–9085 (2017).
24. R. Shang, L. Ilies, E. Nakamura, *Chem. Rev.* **117**, 9086–9139 (2017).
25. S. Ferro, *J. Mater. Chem.* **12**, 2843–2855 (2002).
26. D. Liu *et al.*, *Science* **384**, 1212–1219 (2024).
27. J. Zhang *et al.*, *ACS Nano* **6**, 8674–8683 (2012).
28. E. Meirzadeh *et al.*, *Nature* **613**, 71–76 (2023).
29. K. Naydenova, P. Jia, C. J. Russo, *Science* **370**, 223–226 (2020).
30. T. Yamazaki *et al.*, *Microsc. Microanal.* **29**, 1940–1949 (2023).
31. H. A. Khonakdar, S. H. Jafari, U. Wagenknecht, D. Jehnichen, *Radiat. Phys. Chem.* **75**, 78–86 (2006).
32. H. Tang *et al.*, *Nature* **599**, 605–610 (2021).
33. P. A. Crozier *et al.*, *Science* **387**, 949–954 (2025).
34. Y. Shen *et al.*, *Nano Lett.* **23**, 9602–9608 (2023).
35. M. L. Frezzotti, *Nat. Commun.* **10**, 4952 (2019).
36. J. Xing *et al.*, *Proc. Natl. Acad. Sci. U.S.A.* **119**, e2114432119 (2022).
37. P. R. Schreiner *et al.*, *Nature* **477**, 308–311 (2011).
38. Q. Huang *et al.*, *Nature* **510**, 250–253 (2014).
39. J. Yang, B. J. McCoy, G. Madras, *J. Chem. Phys.* **122**, 064901 (2005).
40. D. Liu *et al.*, *Proc. Natl. Acad. Sci. U.S.A.* **119**, e2200290119 (2022).
41. E. M. Simmons, J. F. Hartwig, *Angew. Chem. Int. Ed.* **51**, 3066–3072 (2012).
42. H. J. A. Dale, A. G. Leach, G. C. Lloyd-Jones, *J. Am. Chem. Soc.* **143**, 21079–21099 (2021).
43. M. Chen, M. Zhong, J. A. Johnson, *Chem. Rev.* **116**, 10167–10211 (2016).
44. T. Kondoh, J. Yang, K. Norizawa, K. Kan, Y. Yoshida, *Radiat. Phys. Chem.* **80**, 286–290 (2011).
45. M. Sakakibara, M. Hanaya, T. Nakamuro, E. Nakamura, *Science* **387**, 522–527 (2025).
46. R. F. Egerton, *Micron* **194**, 103819 (2025).
47. H. Schwertfeger, A. A. Fokin, P. R. Schreiner, *Angew. Chem. Int. Ed.* **47**, 1022–1036 (2008).
48. D. Lungerich *et al.*, *ACS Nano* **15**, 12804–12814 (2021).
49. T. L. Daulton, M. Ozima, *Science* **271**, 1260–1263 (1996).
50. T. Henning, F. Salama, *Science* **282**, 2204–2210 (1998).

ACKNOWLEDGMENTS

We appreciate the thorough feedback provided by W. Sato, D. Lungerich, X. Fu, C. Gao, and C. Liu. We thank W. Zhang and F. Feng for assisting in acquiring EELS spectra and reproducibility experiments. J.F. thanks the Fellowship (JSPS and IGPEES). **Funding:** This work was supported by JSPS KAKENHI JP24H00447 JP24K21232 (E.N.), JST PRESTO program JPMJPR23Q6 (T.N.), and JSPS KAKENHI JP23H04874 (T.N.). **Author contributions:** Conceptualization: J.F., E.N., T.N. Data acquisition: J.F. Data analysis: J.F., T.N., E.N. Validation: J.F. Funding acquisition: E.N., T.N. Project administration: E.N., T.N. Project supervision: E.N. Writing – original draft: E.N. Writing – review & editing: E.N., T.N., J.F. **Competing interests:** Patent pending; details are not yet publicly available. **Data and materials availability:** All of the data necessary for evaluating the conclusions of the study are included in the main text or the supplementary materials.

SUPPLEMENTARY MATERIALS

science.org/doi/10.1126/science.adw2025
Materials and Methods; Supplementary Text; Figs. S1 to S24; Reference (*51*); Movies S1 to S7

Submitted 22 January 2025; resubmitted 14 May 2025; accepted 30 June 2025
10.1126/science.adw2025

CHIRAL MATERIALS

Spin-selective transport through chiral ferromagnetic nanohelices

Yoo Sang Jeon[1,2]†, Eunjin Jeong[2]†, Sang Won Im[3], Min Jun Ko[4], Jin Seo Lee[5], Jun Hwan Moon[2], Min Hyeok Lee[2], Jeong Kyu Lee[2], Sung Jong Yoo[6], Ki Tae Nam[3]*, Young Keun Kim[1,2]*

Chiral crystals with well-defined handedness in atomic arrangements exhibit properties such as spin selectivity, asymmetric magnetoresistance, and skyrmions. Although similar geometry-induced phenomena in chiral organic molecule-based systems were observed, synthesizing uniform inorganic nanostructures with desired chirality using a scalable method remains challenging. We electrochemically synthesized chiral ferromagnetic cobalt-iron nanohelices from nanoparticles in anodized aluminum oxide templates. The spiral directions and the number of strands were regulated by incorporating chiral molecules and applying an appropriate potential. We demonstrate the observation of Faraday's law of induction at the nanoscale and show how chiral nanohelices regulate the electron flow direction. The implications of our findings extend to the technological realm, with chirality- and ferromagnetism-based spin-tunable devices.

Chiral spintronics (*1*–*3*), in which spin transport could enable device energy lower than that of charge-based electronics, includes processes such as chirality-induced magnetotransport and movement of chiral domain walls (*1*, *3*–*7*). Inorganic ferromagnetic nanomaterials could potentially overcome the limits in organic chiral molecule-based performance regarding high resistive-capacitive delay, power consumption, and poor stability for industrial implementation (*8*, *9*). Conventional solvothermal and seed-mediated methods have been successfully used to fabricate chiral inorganic nanomaterials by regulating the surface energy of the materials using chiral coordinating ligands (*4*, *10*–*12*). Other attempts to encode chirality using amino acids, micelles, and polarized light during the synthesis (*11*–*14*) or to control the chiral crystallization process of inorganic materials (*15*–*20*) have been extensively studied. The electrodeposition method has shown potential in controlling the chirality of inorganic deposits (*21*). Although several trials have reported the formation of electrodeposited nonmagnetic racemic (rac) helices (*22*, *23*), deliberate chirality induction into helical nanostructures, particularly when coupled with additional functionalities such as ferromagnetism, is still challenging.

We report the use of nanoporous anodized aluminum oxide (AAO) template-assisted electrodeposition, a well-known method for fabricating nanowires of magnetic elements of Co, Ni, Fe, and their alloys (*24*–*26*). In conventional nanowire synthesis, metallic ions are reduced and deposited isotropically and conform to the symmetrical shape of a cylindrical pore. Our mechanistic understanding of electric fields in nanopores and precise tuning of the interplay between the nanotemplate wall and electrolytes enabled the creation of nanostructures beyond simple nanowires (NWs), such as nanohelices, through the controlled assembly of CoFe nanoparticles (NPs). This morphological control took advantage of the surface conduction (SC) effect when electrons were transported along the electrical double layer between the insulating wall surface and electrolyte solution. The SC changed the electrochemical reduction site from the typical cathode surface to the surrounding insulating nanotemplate wall. This effect came into operation when two conditions were met (*27*): One was applying an excessively high electrical potential (several tens of volts) to these high-aspect-ratio nanochannels, which exceeded 250 volts in this study. The other was obtaining a diffusion-limited condition of metallic ions around the cathode, leading to regions of constant current density with applied voltage.

Despite numerous efforts in recent studies, the resulting helical nanostructures formed in nanoporous templates have always been racemic mixtures (*28*). We obtained chiral magnetic nanohelices (c-MNHs) by using $VO(ascorbate)_2$ as a helical ligand and cinchonine (CN) or cinchonidine (CD) as a chiral ligand. We used cinchona alkaloids, widely applied in chiral hydrogenation reactions, because of their strong interactions with inorganic surfaces (*29*, *30*). Their three-dimensional (3D) chiral structures induced steric hindrance during electrodeposition (*14*, *31*), which influenced the kinetics governing the spiral-direction guidance.

We chose the cobalt-iron ($Co_{50}Fe_{50}$) alloy for this study because of its highly positive spin-exchange integral energy, which resulted in high magnetic moments and spin-exchange interaction, to study chirality-induced spin transport (*32*). The tunability of this method also enabled the synthesis of more intricate nanostructures, such as ferromagnetic double and multiple nanohelices. We describe an electromotive force (emf) measurement method to quantify the inherent enantioselective 3D helical structure and a spin-tunable solid-state device exhibiting chirality-based switchable transport properties.

Microstructural evolution of chiral magnetic nanohelices

The SC effect allowed us to tune NW morphology through kinetic parameters. The crucial step was identifying a singularity at which the strength of the electrical field reached the necessary condition for SC operation. We adopted linear sweep amperometry (LSA), in which the current was unidirectionally swept from 0 to 100 mA while we measured the voltage at 0.1 mA intervals with a sweep delay of 0.5 s. This method was chosen as a suitable and practical tool because the SC effect induced rapid changes in the electrical field distribution inside the template (Fig. 1). With LSA, we could observe changes in ionic resistance in response to variations in current density. As the current density increased, the emergence of a diffusion-limited condition near the cathode caused an overlimiting current, leading to an increase in electrical resistance. To alleviate the high resistance, SC was initiated to facilitate additional reduction reactions to occur at the surface of

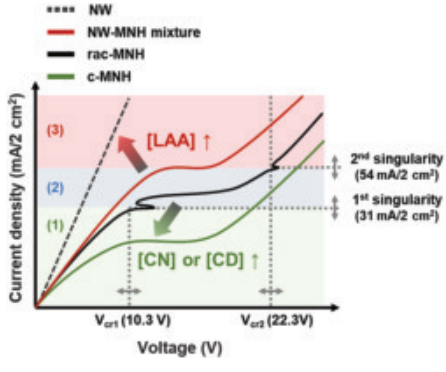

Fig. 1. LSA analysis for electrosynthesis of homochiral MNHs. Schematic LSA behaviors of standard conditions from NW and rac-MNH to c-MNH and their differences according to the addition of helical and chiral ligands.

[1]Institute of Engineering Research, Korea University, Seoul, Republic of Korea. [2]Department of Materials Science and Engineering, Korea University, Seoul, Republic of Korea. [3]Department of Materials Science and Engineering, Seoul National University, Seoul, Republic of Korea. [4]Department of Radiology, Feinberg School of Medicine, Northwestern University, Chicago, IL, USA. [5]Department of Semiconductor Systems Engineering, Korea University, Seoul, Republic of Korea. [6]Hydrogen-Fuel Cell Research Center, Korea Institute of Science and Technology, Seoul, Republic of Korea. ***Corresponding author. Email: nkitae@snu.ac.kr (K.T.N.); ykim97@korea.ac.kr (Y.K.K.)** †These authors contributed equally to this work.

the AAO wall. This potential change appeared in LSA as the first singularity (31 mA/2 cm^2 for rac-MNHs) (*28*), thereby we could easily find the optimized condition to fabricate MNHs instead of NWs (details on singularities and their relationships with microstructural control are available in fig. S1).

The electrosynthesis of homochiral inorganic nanohelices in the right- (R-) and left- (L-) handedness was verified with scanning electron microscopy (SEM) images (Fig. 2A and fig. S2, A and B). The synthesized c-MNHs had a diameter of 200 nm and a pitch of approximately 60 nm. Each of the R- and L-chiral directions, obtained by using optimized 10 μM of CN and CD, respectively (*13*, *33*–*35*), was evident in transmission electron microscopy (TEM) images with the 30° tilting of an electron beam detector for a stereoscopic analysis (inset of Fig. 2A; fig. S2C).

We encoded the chirality into MNHs by guiding the twisting direction of helical ligands (vanadyl ascorbate) with chiral ligand insertion (*30*). Notably, the evolution of double and even quadruple ferromagnetic nanohelices was observed when the concentration of chiral reagents was increased to 0.1 and 0.2 mM, respectively (Fig. 2, B and C). These results confirmed the regulation of spiral directions and the number of strands of inorganic nanohelices through electrosynthesis.

These nanohelices were assembled from CoFe NPs, as shown in the high-resolution TEM image in Fig. 2D. The size of these NPs did not change depending on the reaction time, indicating that they did not follow the conventional nucleation and growth mechanism (fig. S3). They formed preferentially at the early stage and then assembled into helical nanostructures. This crystallization pathway enabled the intervention of a new ligand amid the assembly process to regulate and achieve uniform chirality during the electrodeposition (*36*, *37*).

The key parameter in dynamic morphological change was the concentration of the chiral ligand that adsorbed on the surface of primary particles. Therefore, we investigated the reaction behavior and crystallization alteration corresponding to the amount of chiral ligand. Figure 2E is the first derivative graph of the inverse function of LSA curves in fig. S4. As mentioned earlier in Fig. 1 and fig. S1, the first singularity (peak), indicates the onset potential of the SC mode operation. The increment of chiral ligands during the synthesis caused the shifting of the peaks in Fig. 2E toward a lower current and eventually vanished. This observation means that the addition of CN or CD made the reduction of metallic ions presented at the bottom electrode more difficult, which in turn required the SC to take place in a lower current region. Meanwhile, excess chiral ligands adsorbed and eventually covered the particle surfaces, hindering the reduction and attachment (assembly) of each particle and increased cathodic resistance, as shown in fig. S5.

To alleviate the overly strong SC effect, we added L-ascorbic acid, which provided a high coverage of the alumina surface and increased the potential to compensate for the retarding of SC onset potential (*28*). Likewise, we established the optimum condition for chiral nanostructures concerning the correlation between chirality and the key parameters for electrosynthesis (current intensity and precursor/additive concentration).

Fourier-transform infrared spectroscopy confirmed the existence of helical ligands in the vicinity of 1400 and 1049 cm^{-1} in rac-MNHs, while those peaks flattened as chiral ligands were added to create c-MNHs (fig. S6A). Both near-edge x-ray absorption fine-structure spectroscopy and x-ray photoelectron spectroscopy showed the N 1*s* relevant peaks of chiral ligands.

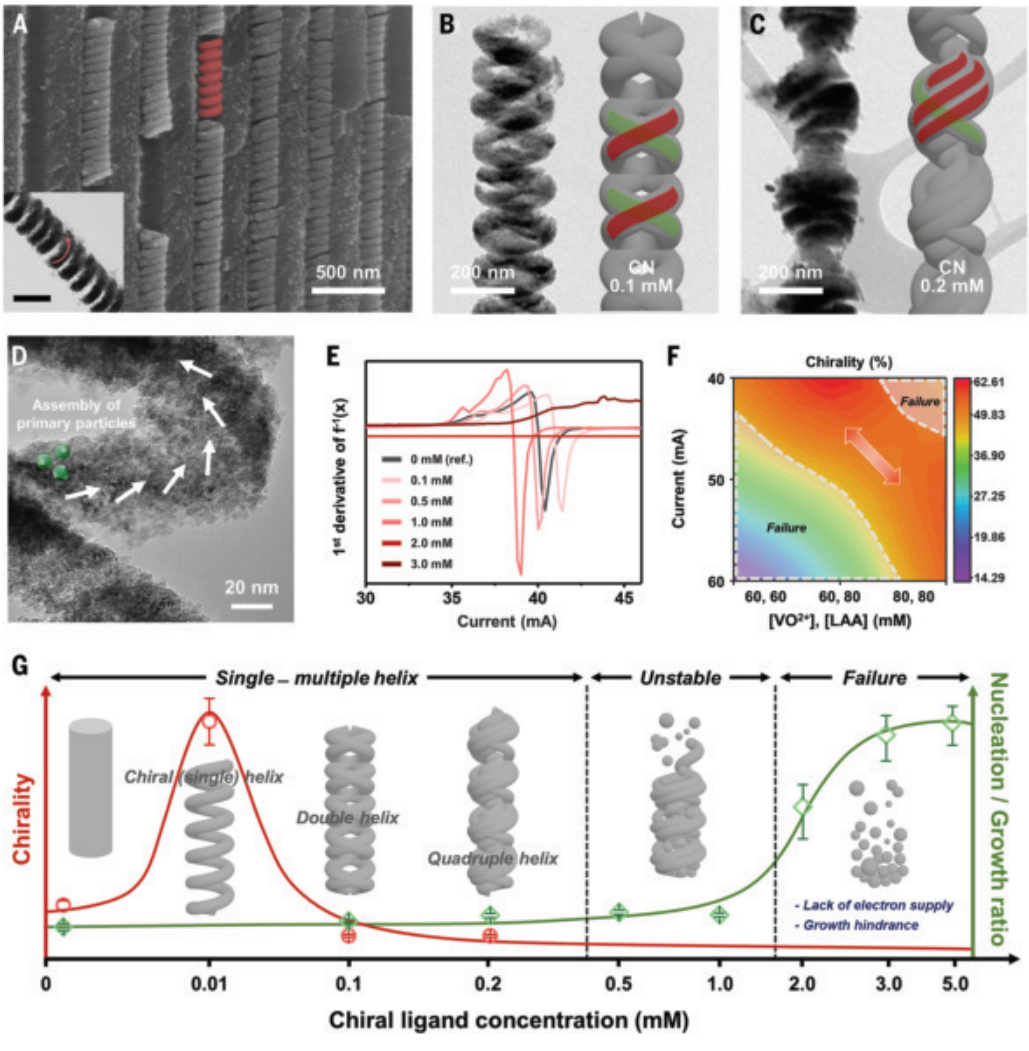

Fig. 2. Chirality control of ferromagnetic nanohelices with electrochemical optimization and cinchona alkaloids. (**A**) SEM images of R-MNHs embedded in the nanotemplate. The inset shows a 30°-tilted R-MNH image obtained using TEM. Scale bar, 200 nm. (**B** and **C**) TEM images of nanostructures with excessive chiral ligands compared with those in the c-MNH synthesis condition. Double (B) and quadruple (C) ferromagnetic nanohelices were obtained by adding 0.1 and 0.2 mM of chiral ligands, respectively. (**D**) TEM image of a free-standing L-MNH composed of primary particles with a size of 2.55 ± 0.04 nm, electrodeposited along the nanopore wall. (**E**) First derivative of the inverse function of LSA with CN concentration variations (original LSA curve in fig. S4). (**F**) Color map representing R-handed percentages observed when adjusting the applied current and concentrations of VO^{2+} and LAA in the electrolyte solution, with a fixed 10 μM of CN amount. The results were obtained from 1426 samples. (**G**) Schematic of chirality (red circles, matches with Fig. 3F and fig. S18) and nucleation/growth ratio (green diamonds, same as in fig. S5) of nanostructures versus CN or CD concentration. Additionally, corresponding SEM and LSA data for L-MNHs are shown in fig. S12.

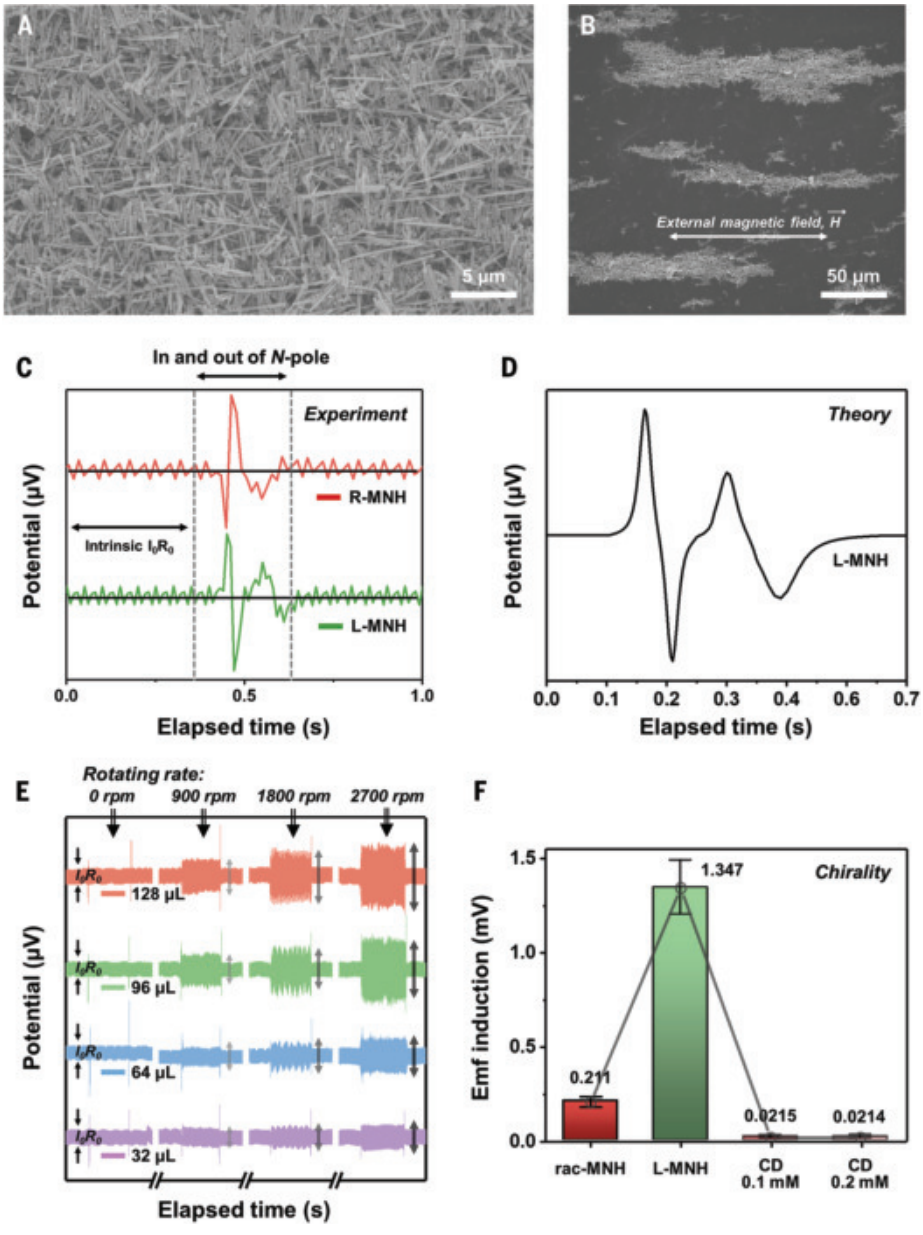

Fig. 3. Generation of emf through chiral nanoinductor. (**A** and **B**) SEM images of c-MNHs drop-casted on the glass substrate after dissolving the AAO template (A). With the easy axis parallel to the length direction of c-MNHs, a bundle of c-MNHs is aligned with the external magnetic field (B). (**C** and **D**) Experimental emf induction of each R- and L-MNH in the opposite direction of electron flow (C) and corresponding theoretical calculation using Eq. 1 (D). (**E**) Quantitative analysis of induced emf magnitude, considering parameters in Eq. 3 (amount of loaded R-MNHs, *n*; applied external magnetic field, B_0; rotating rate of the RRDE, *f*). Meanwhile, no emf was generated with the control group (only carbon without c-MNHs, fig. S15). (**F**) Amount of emf induced in each shape-controlled nanostructure with CD concentrations of 0 (rac-MNH), 0.01 (L-MNH), 0.1 (double MNH), and 0.2 mM (multiple MNH), quantifying each of their chirality.

and additive ratio. High chirality was achieved only under optimized conditions. The obtained chirality is >62% for R-MNHs and similar to that of L-MNHs (fig. S10).

The overall results are summarized, along with the actual data, in Fig. 2G and table S2. An increase in the chiral ligand from 0.01 to 0.2 mM increased electrical resistance, which increased nucleation while hindering the continuous growth of seeds and altering the morphology of the c-MNHs, double, and multiple MNHs (*28*, *38*). However, an excess of chiral ligands failed to form nanostructures. We also explored several other chiral ligand candidates, such as quinine, histidine, and glutathione, to enhance reactivity at targeted sites (fig. S11). Considering their structures and functional groups, we expected quinine to induce a similar reaction with CN. We considered histidine and glutathione because they have carboxyl groups, which have a strong affinity with metal sites and the ability to bond with helical ligands through van der Waals forces. However, only CN and CD were the effective reagents for synthesizing c-MNHs with high homochirality due to the sophisticated behavior of hydrated metallic ions and additives at the cathode and AAO wall surfaces. Thus, we propose optimized conditions for the CN- or CD-guided electrodeposition system.

Chiral nanoinductor and chirality analysis

The metallic c-MNHs exhibited minimal plasmonic effects attributable to their size, dimensions, and composition. They did not exhibit circular dichroism within the ultraviolet visible spectrum range, which posed challenges in characterizing chirality through conventional spectroscopic methods (*39*–*41*). We developed approaches for precisely measuring emf that enabled the quantification of inherent enantioselective 3D helical structures.

Faraday's law of induction is well-known in solenoid structures. The law posits that a time-varying external magnetic flux influences the emf generation. The intensity of the emf is calculated using the following equation:

$$\oint_{\partial\Sigma} E \cdot dl = \frac{-d}{dt}\int_{\Sigma} B \cdot dA \text{ and } \varepsilon = -N\frac{d\varphi}{dt} \quad (1)$$

It verified that the –N= bond in the quinoline ring of the CN or CD formed coordination bonds with the unshared electron pair located near the metal sites of the NPs (figs. S6B and S7A). Moreover, C 1*s* peaks demonstrated that the ratio of C=O bonds in the helical ligand decreased from 12.2 to 7.9% as the chiral ligands adsorbed on the NP surfaces (fig. S7B and table S1). More discussions, including the microstructure of MNHs (fig. S8) and specific interactions between NPs and chiral and helical ligands, are included in the Supplementary Materials (SM).

We quantified the R- and L-MNHs, which totaled 1426 c-MNHs from SEM (fig. S9; Fig. 2F depicts three-axis color maps of R-chiral structures, indicating the percentage of chirality at each applied current

where Σ, *E*, *dl*, *dt*, *B*, *dA*, ε, *N*, and *dφ* indicate the wire loop encircling a surface, electric field, unit of length, unit of time, magnetic field density, unit of area, emf, number of turns, and variation of magnetic flux, respectively.

We hypothesized that the helical structure of MNHs could induce emf at the nanoscale and devised an analytical method to characterize the chirality based on the emf measurement. We prepared large-scale c-MNHs after dissolving the template (Fig. 3A). We aligned them in parallel on a rotating ring disk electrode (RRDE) as shown in Fig. 3B, by utilizing their magnetic shape anisotropy (figs. S13 and S14, and Materials and Methods).

This assembly led to constructive interference between neighboring c-MNHs. They responded to the magnetic flux variation as a cosine function with the rotating external magnetic field B_0, rotation frequency f, and passing time t. The A is assumed to be constant and calculated as 6.65×10^{-3} μm^2, and N can be substituted by n, which refers to the loading amount of c-MNHs on the electrode.

$$\varepsilon(t) \approx -n\frac{AB_0 \cdot d(\cos 2\pi ft)}{dt} \quad (2)$$

Subsequently, the emf as a function of time followed a sine function and showed a vertically symmetric graph following the chiral asymmetry of the MNHs:

$$\varepsilon(t) \approx nAB_0(2\pi f)\sin(2\pi ft) \quad (3)$$

The c-MNHs of each handedness showed opposite emf signals as a sinusoidal waveform (Fig. 3C). This result demonstrated the possibility of regulation of the electron flow direction depending on the chirality of the MNHs. Within our experimental conditions, the emf with the maximum magnitude of 1.35 mV was induced with 0.42 mg of c-MNHs. A theoretical calculation of emf generation supported this observation by regulating the parameter, $d\varphi/dt$ of Eq. 1 with a constant value N (Fig. 3D).

To quantify the emf generation from c-MNHs, we regulated the loading amount (n), the rotating rate of the RRDE (f), and the external magnetic field strength (B_0). We loaded 0.105 to 0.42 mg of c-MNHs (32 to 128 μL of ink) at the variable rotating rate and 480 mT of constant magnetic field (Fig. 3E; raw data in fig. S16). The overall magnitude of the induced emf gradually increased with an increment of n. We also observed that Δ potential increased along with f (fig. S17A) and B_0 (fig. S17B).

Regardless of how the sample was exposed to 480 mT, no change in potential was observed before the electrode started rotating (0 rpm). However, there was an additional sharp potential oscillation when we turned on the magnetic field. Although it was challenging to discern whether the polarity of this abrupt emf generation induced by this rapid magnetic flux change was positive or negative, we could keep track of the chirality of MNH by observing the initial wave (fig. S17C).

We analyzed the chirality of the c-MNHs with designed RRDE-based equipment and corresponding emf equations, which previously could only be statistically counted using SEM. Our experimental system could determine the nanostructure chirality by applying the following equation, incorporating an emf to chirality conversion factor denoted as k. The unit chirality (percent) is defined as enantiomeric excess, which is widely used to indicate the degree of purity of chiral substances.

$$Chirality\ (\%) = k\frac{\varepsilon R_0}{nABf} \quad (4)$$

According to Eq. 3 and the experimental findings, emf varied proportionally to the parameters, including n, A, B, f, and inversely with the resistance R_0 of the nanomaterials. In addition to those parameters, the chirality of the nanostructures also affected the emf intensity. We assessed the chirality using the conversion factor k, a constant, as outlined in Eq. 4. We derived the k value as approximately $4.96\times10^{-11} \pm 0.041\,\mathrm{g}\cdot\mathrm{m}^2\cdot\mathrm{T}\cdot\frac{\mathrm{rpm}}{\mathrm{V}\cdot\mathrm{ohm}}$ through the measurement of emf intensities and corresponding chirality. The calculated value from Eq. 4 indicates the percentage of enantiomerically prevailing species.

We compared the emf-generation performances concerning the morphological alterations (Fig. 2G, Fig. 3F, and fig. S18). The

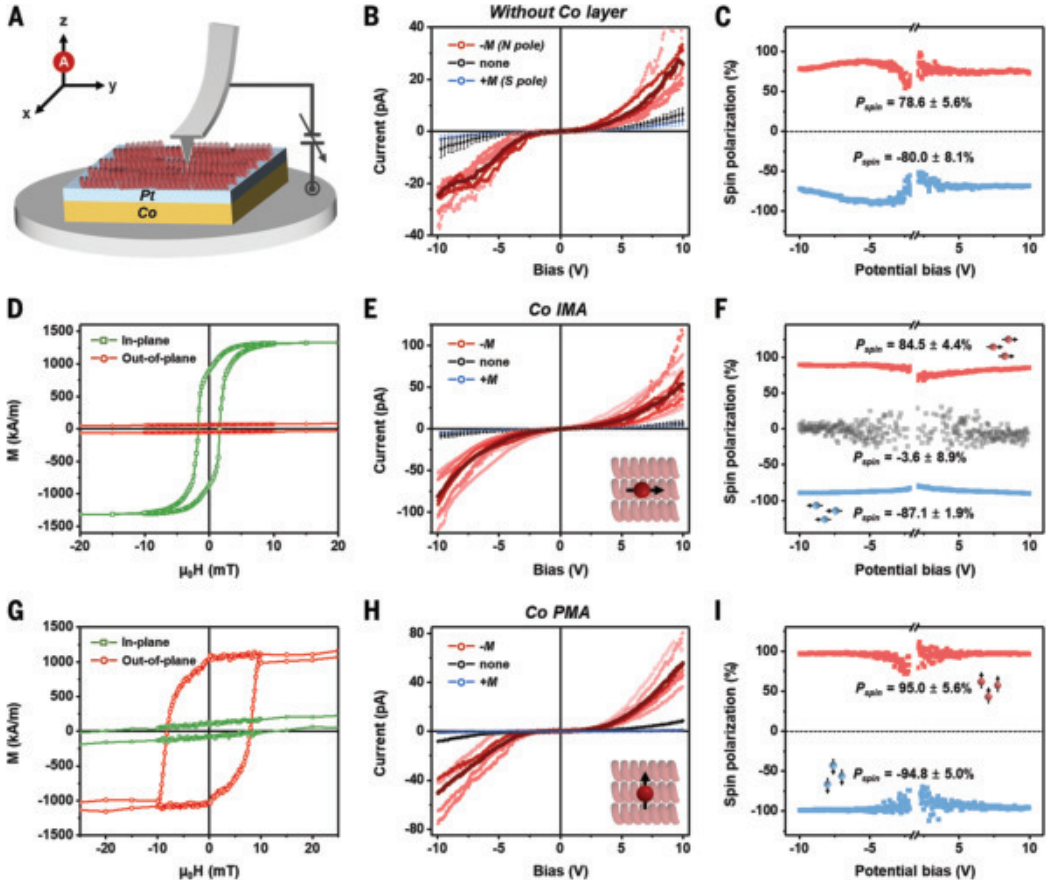

Fig. 4. Spin-dependent transport of c-MNHs with in-plane and out-of-plane spin injection. (**A**) Schematic of *I-V* measurement method with conductive atomic force microscopy. (**B**) *I-V* characteristics of R-MNHs on the Ti/Au stack (nonmagnetic substrate) while c-MNHs were either demagnetized or magnetized with *N* or *S* poles. (**C**) Corresponding spin polarization values acquired from $100\times\frac{(I_{-M}-I_{+M})}{(I_{-M}+I_{+M})}$ for R-MNHs (red, top) and L-MNHs (blue, bottom). (**D**) Hysteresis loop of a prepared Co/Pt bilayer with an in-plane magnetic anisotropy (IMA). (**E** and **F**) *I-V* characteristics of R-MNHs regarding in-plane magnetization (±*M*) direction of Co layer (E), and calculated spin polarization values of R-MNHs (red, top), rac-MNHs (black, middle), and L-MNHs (blue, bottom) (F). (**G**) Hysteresis loop of a prepared Co PMA bilayer. (**H** and **I**) *I-V* characteristics of R-MNHs regarding out-of-plane magnetization direction of Co layer (H) and the calculated spin polarization values of R-MNHs (red, top) and L-MNHs (blue, bottom), when the magnetization orientation of the Co layer was perpendicular to the length direction of MNHs (I). Statistically, a total of 65, 93, and 111 *I-V* curves were scanned for each without magnetic layer conditions (B), parallel (E), and perpendicular (H) spin injection conditions. For the −*M* state in (B), (E), and (H), the average value of the error bars in each scanned point was 8.81, 3.24, and 5.45 pA, respectively, while the darkest red curves represented the mean values. Independent of the statistics, representative curves (in bright red) were selected for the display to show the variations of the higher current state. However, for "none" and +*M* curves in lower current states, the error bars were inserted for all the scanned points with relatively small sizes.

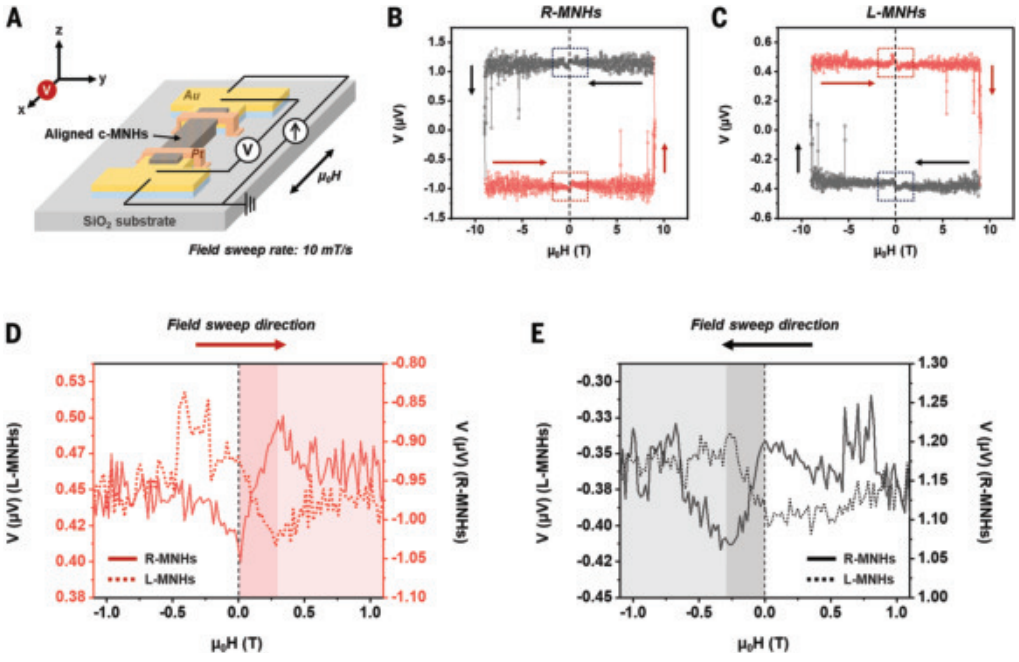

Fig. 5. Spin-tunable device made from c-MNHs. (**A**) Schematic illustration of a lateral-type solid-state device for 4-point probe measurement. The source and drain Au electrode gap patterns with 1.5 μm are connected with the aligned c-MNHs. A deposition of Pt through a focused ion beam achieved better ohmic contact between c-MNHs and the electrodes (fig. S26). (**B** and **C**) The magnetic field sweeps with a step rate of 10 mT/s to measure the potential changes. A constant 50 nA was applied to (B) R-MNH- and (C) L-MNH-based devices. (**D** and **E**) The magnified results within the range of −1 to 1 T, from negative to positive scan direction (D), and from positive to negative scan direction (E). Each *y*-axis on the left and right indicates the measured potential of L-MNH-based devices and R-MNH-based devices, respectively.

measured emf values of the nanostructures were reduced from 1.35 mV to 0.022 and 0.021 mV for the CD 0.1 and 0.2 mM containing samples, respectively, even though we only regulated the quantity of CN or CD in the electrolyte. Because double and multiple MNHs were twisted in mixed directions, the net electrical potential was negated and eliminated the effect of emf, thereby generating 1/200 of the emf signal compared with that of c-MNHs.

Spin-selective transport through chiral ferromagnetic helices

We successfully designed the 3D ferromagnetic inorganic body in which the twisted direction of the helix is controlled. Its chirality was verified with statistics (directly counted by SEM) and an emf induction signal to have an absolute population rather than a racemic mixture. Depending on the results, we explored the spin-dependent electrical properties of ferromagnetic R- or L-MNHs. We deposited the c-MNH solution onto the Co ferromagnet substrate capped with a noble metal, Pt (in thicknesses <2 nm), to avoid unwanted oxidation while preserving the spin transport properties (Fig. 4A and the Materials and Methods section in the SM) (*42*, *43*).

Before investigating the spin-selective effect with multilayered c-MNHs on the magnetic substrate, we first characterized the intrinsic properties of our ferromagnetic nanohelices. We deposited c-MNHs onto the Ti/Au stack without any magnetic layer and aligned them with a directional magnetic field of 400 mT during the deposition process. As a result, we observed the spin imbalance charge transport manifested solely depending on the magnetization (*M*) state (demagnetized or magnetized with *N* or *S* pole) of R-MNHs (Fig. 4, B and C, and fig. S19 for L-MNHs).

We conducted the same experiment with a magnetic substrate after these initial observations. To match the chiral axis and the magnetization orientation of the Co layer, we checked ~80% of remanence compared with the saturation magnetization (M_s) in the in-plane direction of the Co/Pt stack (Fig. 4D). A stable magnetized Co layer linked with ferromagnetic chiral nanostructures exhibited exceptional chirality-based spin transport behavior depending on each chirality and magnetized direction of spin injecting layer.

When the injected spin was aligned to the −*M* direction (magnetized with *N* pole), R-MNHs showed the highest current state compared with that measured with the spin aligned to the +*M* (*S* pole) and even demagnetized state (none) (Fig. 4E). Conversely, L-MNHs showed the highest current state when the Co layer was magnetized in the +*M* direction (fig. S20). We attributed the difference between the current states depending on the magnetization orientation of the magnetic layer to spin polarity. The resulting spin polarization values can be expressed as:

$$\frac{(I_{-M}-I_{+M})}{(I_{-M}+I_{+M})}\times 100\% \qquad (5)$$

Notably, the R- and L-MNHs exhibited spin polarization of 84.5 to 87.1% whereas rac-MNHs exhibited 3.6% (Fig. 4F and fig. S21).

Figure 4 highlights the chirality and ferromagnetism of c-MNHs, which are the key factors in the observed high spin-selective effects. These results can be explained from a perspective similar to chirality-induced spin selectivity (CISS), which has been extensively tested and explored in chiral organic molecules. Although the origin of the conventional CISS effect remains unclear, several recent studies reported that the orbital filter of chiral organic molecules could be transmitted into spin-dependent scattering at the interface between heavy metal substrates through their strong spin-orbit coupling (*43*–*45*). In other words, this interaction is inherently tied to the short-range exchange interaction and the dephasing of spins when they go through the chiral substances, making it difficult to adopt CISS phenomena in the relatively macro-scaled metallic chiral nanostructures. Meanwhile, ferromagnetic CoFe exhibited strong exchange energy and parallel alignment of neighboring spins. When spins were transmitted through c-MNHs, local magnetic moments of the c-MNHs could maintain the spin direction through exchange interactions (*46*). As a result, the chiral ferromagnetic system enabled the CISS-like spin-dependent transport even in inorganic nanomaterials.

To further understand the role of the ferromagnetic components encoded into chiral nanostructures, we prepared gold (Au) chiral nonmagnetic NHs (c-NMNHs) (fig. S22). They did not exhibit spin-selective behavior (fig. S23), but the emf signal could still be monitored because of their helicity (fig. S24). The spin exchange interaction was also observed when the perpendicularly magnetized spin passed through c-MNHs. We introduced another Pt layer under the Co/Pt bilayer to promote the perpendicular magnetic anisotropy (PMA) (Fig. 4G). The same spin-selective response was observed independent of the spin injection direction. Corresponding *I-V* characteristics of R- and L-MNHs with out-of-plane spin injection are shown in Fig. 4H and fig. S25, respectively. Spin polarization values comparably high with those of the in-plane spin injection condition were observed (Fig. 4I).

The compatibility for spin alignment in both parallel and perpendicular directions was caused by the high spin exchange energy and small magnetic anisotropy of the ferromagnetic c-MNHs (fig. S13).

Spin-tunable solid-state device

We sought to observe and verify the above phenomena in a device configuration distinct from the previous measurement apparatus. As shown in the scheme of Fig. 5A, we implemented a c-MNHs-based solid-state device in its simplest form for industrial applications. Unlike the conductive atomic force microscopy measurements conducted in the vertical (z) direction perpendicular to the longitudinal (x) direction of the c-MNHs, this lateral-type device was fabricated to enable measurements in the x-direction. We aimed to observe spin transport results using a four-point probe setup under varying external magnetic fields applied parallel to the chiral axis of the c-MNHs.

Using a physical property measurement system, we performed magnetic field sweeping from 9 to −9 T and back to 9 T at room temperature, with a constant applied current of 50 nA. We swept the magnetic field with a step rate of 10 mT/s to measure the voltage changes. Figure 5B demonstrates the R-MNH-based device exhibiting square-shaped *V-B* behaviors in a counterclockwise direction sweeping pattern as the sign of $d\varphi/dt$ changed at 9 and −9 T. We observed the same but a clockwise sweeping pattern in an L-MNH-based device (Fig. 5C). The voltages with opposite signs were measured depending on the chirality, confirming the robust emf signals in opposite directions as observed in Fig. 3C and fig. S17C.

We also measured the resistance changes in the range near 0 T, where the direction of magnetization changes (Fig. 5, D and E). For R-MNHs in Fig. 5D, we observed chirality-based spin transport right after the external magnetic field direction changed from negative to positive. An instantaneous increase in resistance resulted (Fig. 4E), in which the conductivity of R-MNHs was lower in the $+M$ state than in the $-M$ state. Furthermore, ferromagnetism-based spin filtering was demonstrated with increased magnetic field strength. The resistance gradually decreased again after about 0.3 T, in which the c-MNHs reached $\mu_0 M_s$ (fig. S13). We provided an additional explanation about ΔV behaviors around $\mu_0 H = 0$ based on the nonreciprocal conductance model in fig. S28 and the supplementary text section in the SM.

By contrast, L-MNHs showed the opposite behaviors of a decreased resistance by chirality-based spin transport (fig. S20) and an increase by filtered spins. In Fig. 5E with opposite field sweep scan direction from positive to negative, R- and L-MNH-based devices showed a switched trend with that of Fig. 5D. Moreover, we conducted the same measurements at the lower temperature (100 K) and with a magnetic field sweeping of ±4 T to highlight the stability of the devices (fig. S27).

Discussion

We obtained R- and L-MNHs through electrosynthesis using CN and CD as chiral ligands. The chirality of the MNHs in each handedness was directly confirmed by observing emf induction in the opposite sign, which also allows electron motion manipulation. The spin-selective behavior with high spin polarization value and spin-tunable transport features was robust across both vertical and lateral-type devices, verified by depositing the c-MNHs onto the electrodes with different configurations. Compared with existing chiral organic molecule-based systems, our inorganic c-MNHs-based device offers enhanced conductivity, scalability, and performance stability operating at room temperature. Moreover, the use of emf in our system suggests that it represents a new class of spintronics devices capable of rapidly switching conduction signals in opposite directions during spin-dependent transport processes. By bridging the gap between chiral chemistry and ferromagnetism at the nanoscale, we hope this work lays a robust foundation for the nanoarchitecture of chiral magnetic nanomaterials and advancing the chirality-associated spintronics.

REFERENCES AND NOTES

1. S.-H. Yang, R. Naaman, Y. Paltiel, S. S. P. Parkin, *Nat. Rev. Phys.* **3**, 328–343 (2021).
2. R. Naaman, Y. Paltiel, D. H. Waldeck, *Nat. Rev. Chem.* **3**, 250–260 (2019).
3. F. Evers *et al.*, *Adv. Mater.* **34**, e2106629 (2022).
4. Q. Qian *et al.*, *Nature* **606**, 902–908 (2022).
5. F. Calavalle *et al.*, *Nat. Mater.* **21**, 526–532 (2022).
6. S. Mühlbauer *et al.*, *Science* **323**, 915–919 (2009).
7. Y.-H. Kim *et al.*, *Science* **371**, 1129–1133 (2021).
8. J. H. Moon *et al.*, *Adv. Sci.* **10**, e2207321 (2023).
9. T. Yokouchi *et al.*, *Nature* **586**, 232–236 (2020).
10. R. M. Kim *et al.*, *Nature* **612**, 470–476 (2022).
11. H.-E. Lee *et al.*, *Nature* **556**, 360–365 (2018).
12. G. González-Rubio *et al.*, *Science* **368**, 1472–1477 (2020).
13. J. Lv *et al.*, *Nat. Rev. Chem.* **6**, 125–145 (2022).
14. N. H. Cho *et al.*, *Nat. Rev. Bioeng.* **1**, 88–106 (2023).
15. S. Eslami *et al.*, *ACS Photonics* **1**, 1231–1236 (2014).
16. J. Yeom *et al.*, *Science* **359**, 309–314 (2018).
17. P. Kumar *et al.*, *Nature* **615**, 418–424 (2023).
18. I. Song *et al.*, *Nature* **617**, 92–99 (2023).
19. Q. Zhang *et al.*, *Science* **365**, 1475–1478 (2019).
20. O. Oki *et al.*, *Science* **377**, 673–678 (2022).
21. J. A. Switzer, H. M. Kothari, P. Poizot, S. Nakanishi, E. W. Bohannan, *Nature* **425**, 490–493 (2003).
22. D. Yang, J. Carpena-Núñez, L. F. Fonseca, A. Biaggi-Labiosa, G. W. Hunter, *Sci. Rep.* **4**, 3773 (2014).
23. Y. Wu *et al.*, *Nano Lett.* **4**, 2337–2342 (2004).
24. J. H. Moon *et al.*, *Small* **17**, e2103575 (2021).
25. Y. S. Jeon, S. H. Kim, B. C. Park, D. Y. Nam, Y. K. Kim, *Chem. Commun.* **53**, 1825–1828 (2017).
26. A. Y. Samardak *et al.*, *Small* **18**, e2203555 (2022).
27. S. Nam *et al.*, *Phys. Rev. Lett.* **114**, 114501 (2015).
28. Y. S. Jeon *et al.*, *Nano Today* **42**, 101348 (2022).
29. T. Kaczorowski, I. Justyniak, T. Lipińska, J. Lipkowski, J. Lewiński, *J. Am. Chem. Soc.* **131**, 5393–5395 (2009).
30. A. Baiker, *Chem. Soc. Rev.* **44**, 7449–7464 (2015).
31. S. Yang *et al.*, *Energy Environ. Sci.* **17**, 1095–1106 (2024).
32. M. H. Lee *et al.*, *Sci. Rep.* **11**, 21081 (2021).
33. W. Gong, Z. Chen, J. Dong, Y. Liu, Y. Cui, *Chem. Rev.* **122**, 9078–9144 (2022).
34. T. P. Yoon, E. N. Jacobsen, *Science* **299**, 1691–1693 (2003).
35. A. Ben-Moshe *et al.*, *Science* **372**, 729–733 (2021).
36. S. Zhou *et al.*, *Nature* **612**, 259–265 (2022).
37. G. Singh *et al.*, *Science* **345**, 1149–1153 (2014).
38. A. Pei, G. Zheng, F. Shi, Y. Li, Y. Cui, *Nano Lett.* **17**, 1132–1139 (2017).
39. S. Jiang, N. A. Kotov, *Adv. Mater.* **35**, e2108431 (2023).
40. W. Ma *et al.*, *Chem. Rev.* **117**, 8041–8093 (2017).
41. Y. Duan, S. Che, *Adv. Mater.* **35**, e2205088 (2023).
42. E. Y. Tsymbal, I. Zutic, Eds., *Handbook of Spin Transport and Magnetism*, 21–46 (CRC Press, 2012).
43. K. Banerjee-Ghosh *et al.*, *Science* **360**, 1331–1334 (2018).
44. Y. Liu, J. Xiao, J. Koo, B. Yan, *Nat. Mater.* **20**, 638–644 (2021).
45. Y. Adhikari *et al.*, *Nat. Commun.* **14**, 5163 (2023).
46. D. Go *et al.*, *Phys. Rev. Res.* **2**, 033401 (2020).

ACKNOWLEDGMENTS

Funding: This work was funded by the following: National Research Foundation of Korea funded by the Ministry of Science and ICT grant RS-2023-00258680 (to Y.K.K.); National Research Foundation of Korea funded by the Ministry of Science and ICT grant RS-2024-00347718 (to Y.K.K.); National Research Foundation of Korea funded by the Ministry of Science and ICT grant RS-2024-00409405 (to K.T.N.) **Author contributions:** Conceptualization: Y.S.J. and Y.K.K. Methodology: Y.S.J., E.J., M.J.K. Validation: K.T.N. and Y.K.K. Formal analysis: Y.S.J., E.J., J.S.L., M.H.L., and S.J.Y. Investigation: Y.S.J., E.J., S.W.I., J.K.L., and J.H.M. Resources: S.J.Y., K.T.N., and Y.K.K. Data curation: E.J. Writing – original draft: Y.S.J., E.J., K.T.N., and Y.K.K. Writing – review & editing: Y.S.J., E.J., K.T.N., and Y.K.K. Visualization: Y.S.J. and E.J. Supervision: K.T.N. and Y.K.K. Project administration: Y.K.K. Funding acquisition: K.T.N. and Y.K.K. **Competing interests:** Y.K.K., E.J., S.J.Y., Y.S.J., K.T.N., and S.W.I. are inventors on an invention disclosure of the patent filed by Korea University, Korea Institute of Science and Technology, and Seoul National University (KR10-2023-0011456, filed on 30 January 2023; US18/390,703, filed on 20 December 2023; JP2023-219797, filed on 26 December 2023; EP24153637.4, filed on 24 January 2024). The authors declare that they have no other competing interests. **Data and materials availability:** All data are available in the manuscript and/or the SM.

SUPPLEMENTARY MATERIALS

science.org/doi/10.1126/science.adx5963
Materials and Methods; Supplementary Text; Figs. S1 to S28; Tables S1 and S2; References (*47*–*49*)

Submitted 20 March 2025; accepted 3 July 2025

10.1126/science.adx5963

PHOTOCATALYSIS

Photochemical H_2 dissociation for nearly quantitative CO_2 reduction to ethylene

Ping Jin[1,2], Pu Guo[1], Nengchao Luo[1,2]*, Hui Zhang[3,4], Chenwei Ni[1,2], Ruotian Chen[1], Wei Liu[1], Rengui Li[1], Jianping Xiao[1], Guoxiong Wang[5], Fuxiang Zhang[1], Paolo Fornasiero[6]*, Feng Wang[1,2]*

Producing olefins by carbon dioxide (CO_2) hydrogenation is a long-standing goal. The usual products are multicarbon mixtures because the critical step of heterolytic hydrogen (H_2) dissociation at high temperatures complicates selectivity control. In this study, we report that irradiating gold–titanium dioxide at 365 nanometers induces heterolytic H_2 dissociation at ambient temperature. This process likely relies on interfacial electric dipoles from photogenerated electrons and holes situated on the metallic gold nanoparticles and interfacial gold–oxygen–titanium scaffolds. The heterolytic H_2 dissociation is further promoted by light-induced coating of gold nanoparticles with a titanium oxide layer. The resulting nucleophilic hydrogen species reduce CO_2 to ethane in >99% yield under light irradiation in a flow apparatus. Furthermore, cascading with a subsequent photocatalytic ethane dehydrogenation generates ethylene in >99% yield over 1500 hours of irradiation.

CO_2 reduction powered by sustainable energy is a prospectively appealing method of decreasing carbon emissions and harvesting sustainable chemicals (*1*). However, CO_2 is inherently inert, with a reduction potential of −1.91 V [versus a standard hydrogen electrode (SHE)] for a one-electron process (*2*), making its reduction thermodynamically challenging (*3*). The proton-coupled electron reduction of CO_2, which operates similarly to CO_2 hydrogenation (*4*), has a reduced potential of −0.58 V (*5*), providing an accessible pathway for CO_2 reduction that leverages the reactive hydrogen species derived from H_2 dissociation. The large-scale production of green H_2 through electrochemical water splitting, powered by electricity from photovoltaic or wind sources (*4*, *5*), presents opportunities for sustainable CO_2 reduction to value-added C_{2+} chemicals. Moreover, the mature thermocatalytic industry offers the potential to scale up CO_2 hydrogenation. Efficient CO_2 hydrogenation requires heterolytic H_2 dissociation (*6*) to produce C_{2+} compounds such as ethane (*7*), propane (*8*), and ethanol (*9*). However, these processes typically require elevated temperatures or specifically designed catalysts (*10*); otherwise, CO_2 is primarily hydrogenated to C_1 compounds such as CH_3OH (*11*) and CO (*12*) or to mixtures of C_{2+} products. Therefore, developing a paradigm for heterolytic H_2 dissociation, particularly at ambient temperatures, is crucial for CO_2 reduction to a single C_{2+} compound.

[1]State Key Laboratory of Catalysis, Dalian National Laboratory for Clean Energy, Dalian Institute of Chemical Physics, Chinese Academy of Sciences, Dalian, China. [2]University of Chinese Academy of Sciences, Beijing, China. [3]Shanghai Synchrotron Radiation Facility, Shanghai Advanced Research Institute, Chinese Academy of Sciences, Shanghai, China. [4]National Key Laboratory of Materials for Integrated Circuits, Shanghai Institute of Microsystem and Information Technology, Chinese Academy of Sciences, Shanghai, China. [5]Department of Chemistry, Fudan University, Shanghai, China. [6]Department of Chemical and Pharmaceutical Sciences, Center for Energy, Environment and Transport Giacomo Ciamician, INSTM Trieste Research Unit and ICCOM-CNR Trieste Research Unit, University of Trieste, Trieste, Italy. ***Corresponding author. Email: ncluo@dicp.ac.cn (N.L.); pfornasiero@units.it (P.F.); wangfeng@dicp.ac.cn (F.W.)**

H_2 dissociation can occur by multiple mechanisms (fig. S1) (*13*). Homolytic H_2 dissociation over noble-metal nanoparticles (NPs) occurs with high efficiency because these metal NPs can populate the antibonding orbital (σ*) of H_2 with electrons from their *d* bands (*14*). However, this mechanism generates neutral H (H•) with insufficient nucleophilicity, confining CO_2 reduction to elevated temperatures (>250°C) and frequently resulting in CO formation (*15*). H_2 dissociation at frustrated Lewis pairs (FLPs) presents a valuable approach for generating nucleophilic $H^{\delta-}$ (fig. S1) (*16*). Therefore, sterically hindered acid-base pairs on catalysts such as $In_2O_{3-x}(OH)_y$ (*17*, *18*) and defect-rich c-TiO_2@a-$TiO_{2-x}(OH)_y$ (*19*) enable heterolytic H_2 dissociation, facilitating CO_2 reduction to CH_3OH or CO at ambient temperature (*20*, *21*). Moreover, H_2 dissociation can occur at interfacial acid-base pairs consisting of Au and coordinatively unsaturated hydroxyl on the metal oxide at temperatures as low as 50°C (*22*, *23*); however, efficient dissociation typically requires additional heating (*24*). These pioneering studies of CO_2 hydrogenation have underscored the benefits of nucleophilic $H^{\delta-}$ species generated from heterolytic H_2 dissociation. Nevertheless, this process is characterized by slow reaction kinetics, necessitating the precise control of the catalytic site and elevated temperatures to generate nucleophilic hydrogen species for the selective reduction of CO_2 to C_{2+} compounds.

Here, we demonstrate a photochemical approach for heterolytic H_2 dissociation on Au/TiO_2 at ambient temperature. Ultraviolet (UV) light excitation of TiO_2 generated electrons and holes trapped by metallic Au NPs and interfacial Au–O–Ti scaffolds, respectively. The light-induced coating of the Au NPs with a thin TiO_x layer enhanced the density of the Au–O–Ti defect states, resulting in improved concentration of electron-hole pairs. The excited-state negative and positive charge centers separated by a few nanometers enable heterolytic H_2 dissociation, generating $H^{\delta-}$ species that can selectively reduce CO_2 to C_2H_6 in a flow photochemical apparatus. A cascade with photocatalytic ethane dehydrogenation then selectively affords C_2H_4.

Light-induced heterolytic H_2 dissociation

The hydrogen/deuterium (H/D) exchange reaction over Au/TiO_2 exhibited H_2 dissociation in the dark (fig. S2). Irradiation with 365-nm light that excited the TiO_2 support increased the average HD formation rate from 3.0 to 94 micromoles of HD per gram of catalyst per hour ($\mu mol_{HD}\ g_{catal.}^{-1}\ hour^{-1}$). Au/$TiO_2$ was the most active catalyst among the metal oxide–supported Au NPs for the H/D exchange reaction (fig. S3). Furthermore, the Au NP–TiO_2 composite is necessary for H_2 dissociation because TiO_2 and Au/SiO_2 are inert for the H/D exchange reaction (fig. S3). The H/D exchange reaction can occur under irradiation by 525-nm light owing to plasmonic effects (Fig. 1A) (*25*, *26*), which induce a remarkable local temperature rise (fig. S4). To mitigate thermal effects associated with the plasmonic excitation of the Au NPs, experiments were conducted in acetonitrile, which facilitated heat dissipation (fig. S5). In this case, the H/D exchange reaction showed activity marginally decreased to 91 $\mu mol_{HD}\ g_{catal.}^{-1}\ hour^{-1}$ under irradiation by 365-nm light, whereas the activity almost disappeared when using 525-nm light (Fig. 1A). This result suggests that H_2 dissociation enabled by 365-nm light originates from light-induced charge separation. Consistent with this hypothesis, the H/D exchange activity scaled linearly with light intensity (Fig. 1B). Notably, the HD formation rate initially decreased and then increased at a low light intensity (Fig. 1B, inset). This phenomenon is the overall result of the thermocatalytic and light-induced mechanisms that counteract each other (fig. S6).

The features of the hydrogen species adsorbed on Au/TiO_2 were studied through infrared spectroscopy (Fig. 1C). When the Au/TiO_2 sample was irradiated by 365-nm light under a H_2 atmosphere, the Fourier transform infrared (FTIR) spectra showed two absorption peaks at 3265 and 3670 cm^{-1}, ascribed to the asymmetric stretching vibration (ν_{as}) of adsorbed water and terminal hydroxyl (OH_t), respectively (*27*).

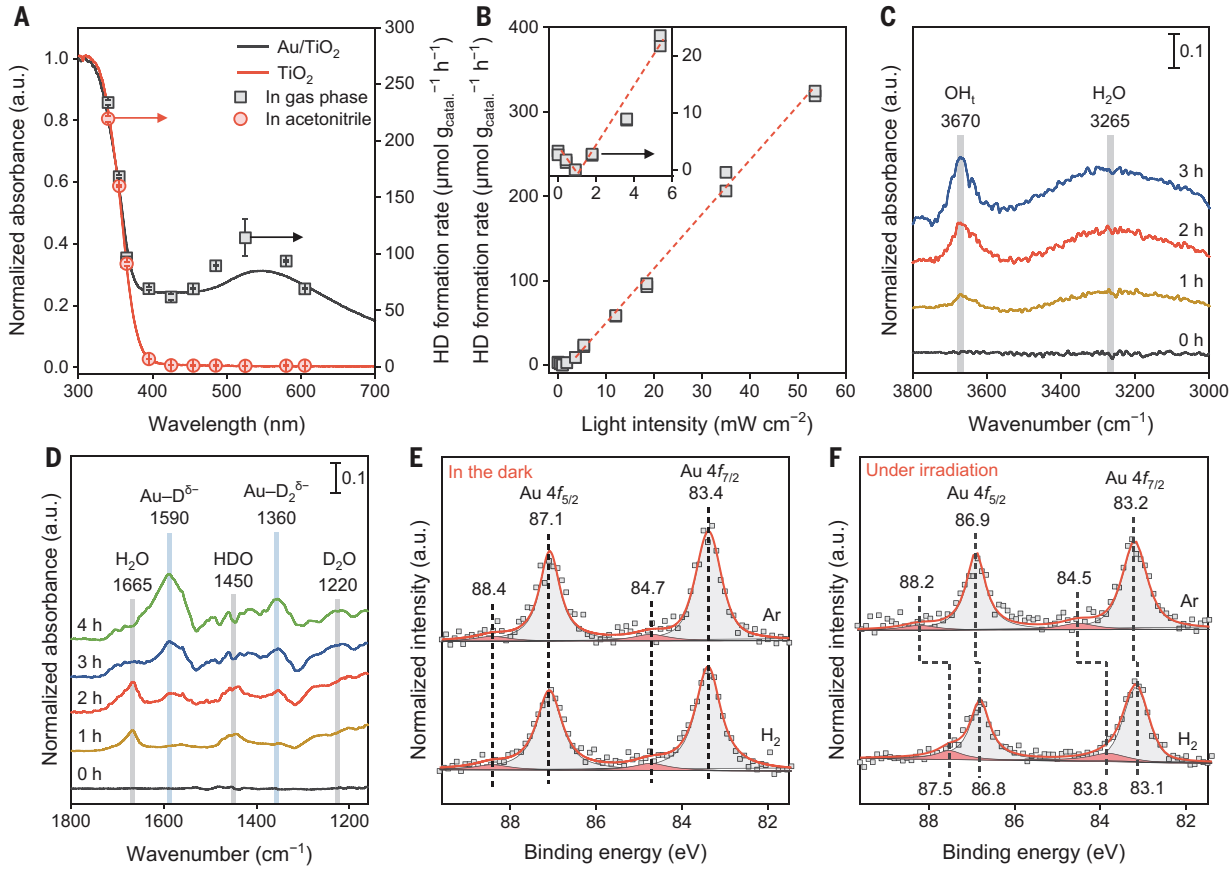

Fig. 1. Investigation of heterolytic H_2 dissociation over Au/TiO_2 under light irradiation. (**A**) Wavelength dependence of H/D exchange activity under light irradiation. The solid lines are UV-visible absorption spectra of the catalysts. The dots are the average HD formation rates obtained from reactions in a gas phase or 1.0 ml of acetonitrile. The light intensities were kept at 17.3 ± 1.3 mW cm^{-2}. (**B**) Influence of light intensity on H/D exchange reaction. The inset shows the HD formation rate with a light intensity <6 mW cm^{-2}. FTIR spectra of Au/TiO_2 collected in an atmospheric H_2 (**C**) and D_2 atmosphere (**D**) under irradiation (365 ± 5 nm, 40 W). FTIR spectroscopy was collected in the atmospheric D_2 atmosphere with the sample kept at liquid N_2 temperature. Synchrotron AP-XPS of Au/TiO_2 collected at the Au 4*f* edge in the dark (**E**) and under irradiation (**F**) with an x-ray beam energy of 700 eV. Standard reaction conditions: 5.0-ml mixture of H_2 and D_2 (1:1 v/v), 10 mg of catalyst, under irradiation (365 ± 5 nm, 10 W) or in the dark. The Au NP size and loading were 4.9 ± 0.9 nm and 1.0 wt %, respectively, unless otherwise specified. The error bars were obtained from three parallel reactions; otherwise, each data point was plotted out.

The developing protons in water and OH_t were derived from H_2 as the corresponding signals of D_2O and OD_t were observed at 2370 and 2730 cm^{-1}, respectively, under a D_2 atmosphere (fig. S7A). Moreover, the signals corresponding to H_2O and HDO gradually decreased, whereas those corresponding to D_2O increased with irradiation time (Fig. 1D). FTIR spectroscopy indicates that H_2 dissociates with the formation of $H^{\delta+}$. The dependence of the H_2 dissociation on photo-irradiation was evident because the FTIR signals remained unchanged without light irradiation (fig. S7, B and C). The results were validated through the temperature-programmed reduction of Au/TiO_2 under light irradiation, in which signals with mass/charge ratios of 19 and 20 were attributed to HDO and D_2O, respectively (fig. S8) (*28*–*30*). Furthermore, the FTIR spectra collected under a D_2 atmosphere showed signals at 1590 and 1360 cm^{-1} (Fig. 1D), corresponding to Au–$D^{\delta-}$ and Au–$D_2^{\delta-}$, respectively (*31*). Consistent with this, the gemel signals of $H^{\delta-}$ were observed under a H_2 atmosphere (fig. S7D).

The formal hydride adsorbed on the Au NPs was confirmed by synchrotron ambient pressure x-ray photoelectron spectroscopy (AP-XPS) (fig. S9), because the binding energy of Au 4*f* varies when hydrogen species are adsorbed (*32*, *33*). The Au 4*f* XPS spectra collected in the dark and under an Ar atmosphere showed two peaks attributed to Au $4f_{7/2}$ and $4f_{5/2}$ (Fig. 1E). The deconvolution of Au 4*f* signals identified peaks at binding energies of 83.4 and 84.7 eV for Au $4f_{7/2}$ and 87.1 and 88.4 eV for Au $4f_{5/2}$ signals. The peaks at 83.4 and 87.1 eV were attributed to metallic Au (Au^0), and the others were associated with $Au^{\delta+}$ at the interface (*34*). Moreover, transitioning to a H_2 atmosphere resulted in a marginal change in the binding energy of the Au 4*f* signals in the dark.

The inherent shift in the Au 4*f* binding energy due to light irradiation was assessed before studying the nature of H_2 dissociation (Fig. 1F). Upon irradiation of the Au/TiO_2 sample under an Ar atmosphere, the Au 4*f* spectrum shifted 0.2 eV toward a lower binding energy. This observation is consistent with the electron transfer from TiO_2 to Au NPs after TiO_2 excitation (*35*). When Ar was replaced with H_2, the peaks associated with $Au^{\delta+}$ redshifted by 0.7 eV. This redshift became more prominent (0.9 eV) when an x-ray beam energy of 400 eV was used to obtain further surface characterization (fig. S10A) (*36*). By contrast, the binding energy of Au shows a negligible shift when Ar is replaced by N_2 (fig. S10B). These results indicate that the redshift is attributable to $H^{\delta-}$ adsorption on $Au^{\delta+}$. The AP-XPS and FTIR results confirmed the heterolytic H_2 dissociation process occurring on Au/TiO_2 upon TiO_2 excitation.

H_2 dissociation site

H_2 may dissociate through oxidation by photogenerated holes or reduction by electrons that generate protons and hydrides (*25*, *26*). Direct H_2 reduction by electrons is not likely because the one-electron

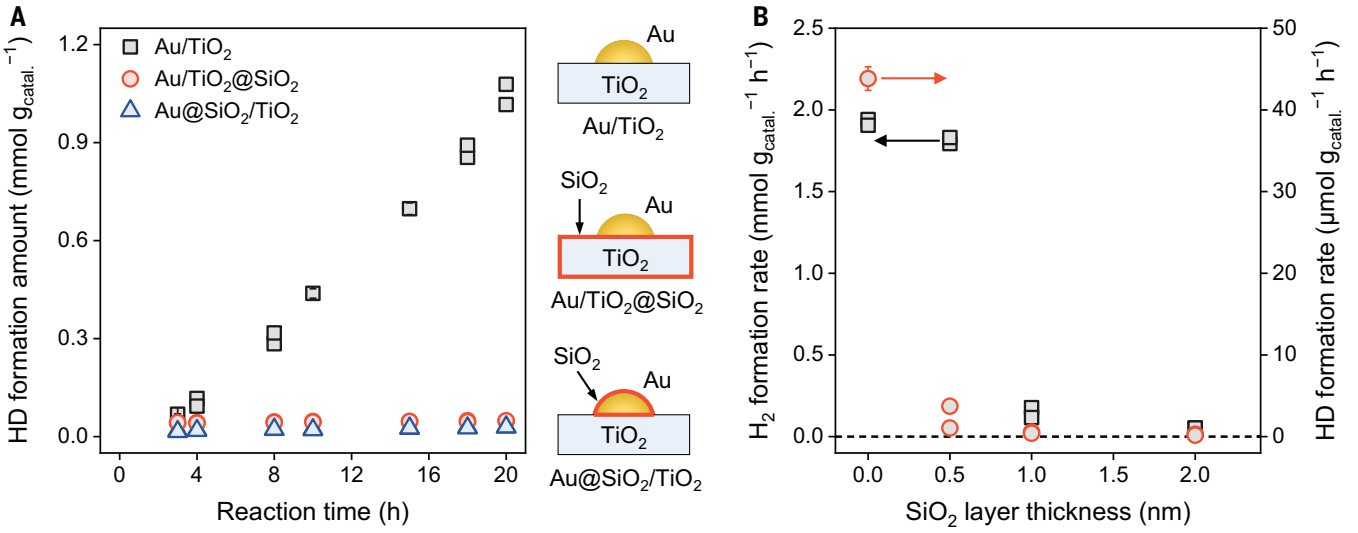

Fig. 2. Investigation of the H_2 dissociation site. (**A**) Reaction results of H/D exchange reaction over Au/TiO_2 and that with Au NPs or TiO_2 support coated by a SiO_2 layer. The schematic structures of the catalysts are shown in the right-hand panels. a.u., arbitrary units. (**B**) Influence of SiO_2 layer thickness on H/D exchange reaction and methanol dehydrogenation over Au@SiO_2/TiO_2 catalyst. Reaction conditions for H/D exchange reaction: 5.0-ml mixture of H_2 and D_2 (1:1 v/v), 10 mg of catalyst, irradiated by LEDs (365 ± 5 nm, 10 W), 10 hours. Ten milligrams of Au@SiO_2/TiO_2 was dispersed in 1.0 ml CH_3OH under an Ar atmosphere for the methanol dehydrogenation reaction. The Au NP size and loading were 5 nm and 1.0 wt %, respectively. The error bars were obtained from three parallel reactions; otherwise, each data point was plotted out.

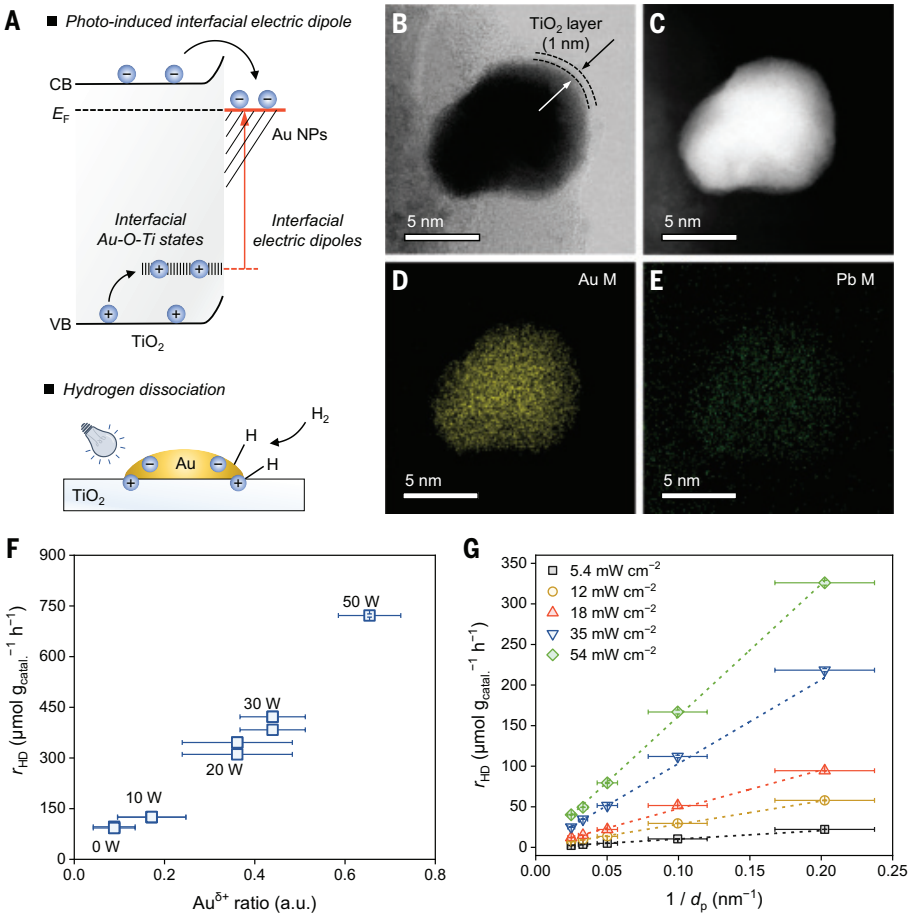

Fig. 3. Investigation of the H_2 dissociation mechanism. (**A**) The hypothesized mechanism of H_2 dissociation at Au NP–TiO_2 interface under light irradiation. The H_2 dissociation on Au/TiO_2 is driven by the IEDs derived from electrons and holes situated at Au NPs and interfacial Au–O–Ti scaffolds, respectively. (**B**) Representative TEM image and (**C**) HAADF-STEM image of the Au/TiO_2 pretreated by irradiation with green LEDs (525 ± 5 nm, 50 W) under a H_2 atmosphere. Energy-dispersive x-ray spectroscopy mappings showed the spatial distribution of Au (**D**) and Pb (**E**) for the Au/TiO_2 sample that was pretreated by irradiation with green LEDs (525 ± 5 nm, 50 W) in a H_2 atmosphere then used for the photodeposition of PbO_2 using UV LEDs (365 ± 5 nm, 100 W). (**F**) Relationship between r_{HD} and the ratio of $Au^{δ+}$ at the Au NP–TiO_2 interface. The $Au^{δ+}$ ratio was varied through pretreatment of the Au/TiO_2 by irradiation with LEDs (525 ± 5 nm, 0 to 50 W) under a H_2 atmosphere. The $Au^{δ+}$ ratios were obtained from CO-FTIR spectra. (**G**) Correlating r_{HD} with the reciprocal of the average Au NP diameter ($1/d_p$) at varied light intensities. The short dashed lines are the linear fitting curves. Standard reaction conditions: 5.0-ml mixture of H_2 and D_2 (1:1 v/v), 10 mg of Au/TiO_2, irradiated by LEDs (365 ± 5 nm, 10 W). The error bars were obtained from three parallel reactions; otherwise, each data point was plotted out.

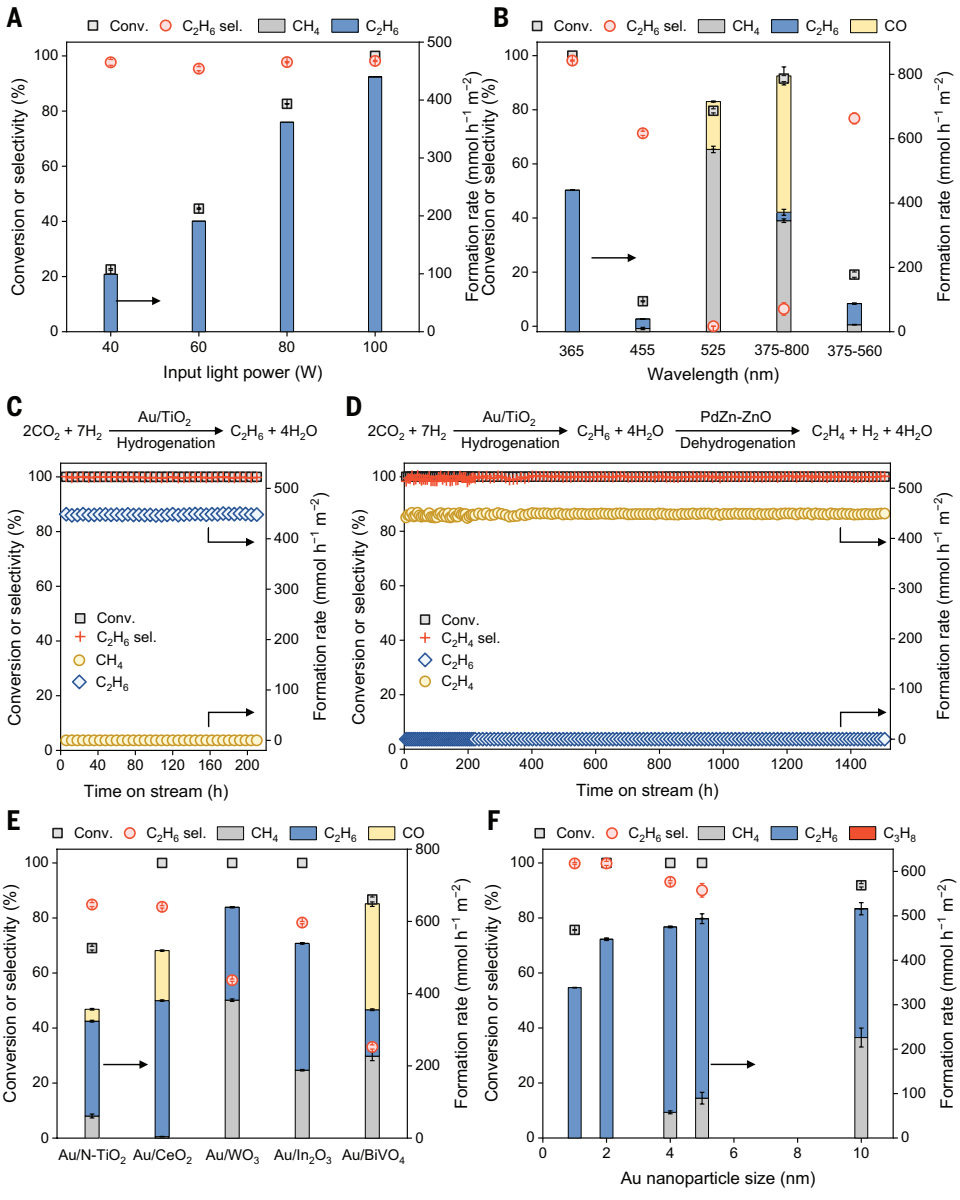

Fig. 4. CO_2 hydrogenation enabled by the light-induced H_2 dissociation. Influence of input light power (**A**) and wavelength (**B**) on the light-induced CO_2 hydrogenation over Au/TiO_2. Fifteen grams of Au/TiO_2 and 15 g of quartz sand were used to study the influence of input light power. (**C**) Continuous light-induced CO_2 hydrogenation over Au/TiO_2. (**D**) Photochemical CO_2 reduction to ethylene through light-induced CO_2 hydrogenation to C_2H_6, followed by a second-step C_2H_6 dehydrogenation. Standard reaction conditions over Au/TiO_2: 200 ml $hour^{-1}$ of CO_2, 800 ml $hour^{-1}$ of H_2, 5 g of Au/TiO_2, 25 g of quartz sand (40 to 60 meshes, diluting the catalyst), irradiated by LEDs (365 ± 5 nm, 100 W). Ten grams of PdZn–ZnO and 20 g of quartz sand were used for C_2H_6 dehydrogenation. The light intensity for CO_2 hydrogenation was 151 ± 6 mW cm^{-2}. (**E**) Extending the study to supported Au catalysts with visible-light responsive supports for CO_2 hydrogenation irradiated by blue LEDs (455 ± 5 nm, 100 W). (**F**) Optimization of the average Au NP size of the Au/N-TiO_2 catalyst. Reaction conditions: 200 ml $hour^{-1}$ of CO_2, 800 ml $hour^{-1}$ of H_2, 5 g of supported Au catalyst, 25 g of quartz sand (40 to 60 meshes, diluting the catalyst), irradiated by white LEDs with an optical filter (named 375 to 560 nm, 160 W). The spectrum of the 375- to 560-nm light is shown in fig. S47A, and the light intensity was 139 mW cm^{-2}. Supported Au catalysts with Au NPs coated by a TiO_x layer were used for CO_2 hydrogenation. The Au NP size and loading were 5 nm and 1.0 wt %, respectively, unless otherwise specified. The error bars were obtained from four parallel reactions.

reduction potential of H_2 is very negative (−2.2 eV versus SHE) (*26*). H_2 dissociation induced by holes in TiO_2 can be investigated if a sacrificial reagent is used to effectively extract electrons. This condition permits a rate-limiting step involving holes (*37*). Photogenerated holes can oxidize ethanol when 2-phenoxy-1-phenylethan-1-one (PP-one) is used to extract electrons from TiO_2. When H_2 was used to replace ethanol to react with the holes, TiO_2 could not reduce PP-one. By contrast, Au/TiO_2 effectively catalyzed the PP-one reduction, producing phenol in 92% yield (fig. S11), confirming that the photogenerated holes on TiO_2 could not oxidize H_2.

The catalytic sites for H_2 dissociation were studied by using SiO_2-coated Au/TiO_2 as a comparison (Fig. 2A). For the Au/TiO_2 catalysts, the TiO_2 was protected with a thin SiO_2 layer (Au/TiO_2@SiO_2) (fig. S12) or the Au NPs were shielded with a thin SiO_2 layer (Au@SiO_2/TiO_2) (fig. S13). The catalytic activities of the two catalysts were compared with those of uncoated Au/TiO_2. The Au/TiO_2@SiO_2 catalyst enabled PP-one reduction (fig. S11B), whereas Au@SiO_2/TiO_2 catalyzed H_2 evolution from methanol (Fig. 2B), suggesting that electrons can be extracted from the two catalysts although coated by a SiO_2 layer of ~0.5 nm in thickness. Similarly, holes were transferred to the Au/TiO_2@SiO_2 surface because PbO_2 was deposited on TiO_2 from the Pb^{2+} solution (fig. S14). However, when either the Au NPs or TiO_2 were coated with a SiO_2 layer, the H_2 dissociation reaction was inhibited, irrespective of the SiO_2 layer thickness (Fig. 2B and fig. S11C). These results also rule out the H_2 dissociation process facilitated by electrons, because the photogenerated electrons can be extracted from the two SiO_2-coated Au/TiO_2 catalysts and initiate reduction half-reactions. Moreover, the active site for H_2 dissociation should be the Au NP–TiO_2 interface because the interfaces of the two catalysts were both shielded. Furthermore, light-induced H_2 dissociation is distinct from the thermocatalytic processes occurring at the interface where the SiO_2 layer on the Au NPs promotes H_2 dissociation in the dark (fig. S15).

H_2 dissociation mechanism

The charge separation behavior pertinent to the light-induced H_2 dissociation was investigated by Kelvin probe force microscopy, using a model Au/r-TiO_2 sample (fig. S16). Upon light irradiation, the photogenerated electrons were transferred to the Au NPs, as demonstrated by the mapping of the surface photovoltage (fig. S17). According to the simulated density of states in a previous study (*38*), holes in

Au/r-TiO_2 and Au/TiO_2 are trapped at the Au NP–TiO_2 interface. In this regard, electrons situated on the Au NPs and holes trapped at the interfacial Au–O–Ti scaffolds were spatially close (Fig. 3A). The positive and negative charge centers, separated by a few nanometers, are interfacial electric dipoles (IEDs) that resembled FLPs for heterolytic H_2 dissociation. Photodeposition of PbO_2 from a Pb^{2+} solution is a common method for determining the location of holes (*38*). However, owing to their close spatial location, photogenerated electrons transferred to the Au NPs interfere with the photodeposition process of PbO_2 induced by holes. Here, the electron interference in PbO_2 photodeposition was suppressed by coating the Au NPs with a thin TiO_x layer. The advantage is that new interfacial Au–O–Ti scaffolds are formed between the TiO_x layer and the Au NPs. Moreover, electron interference in PbO_2 photodeposition can be alleviated because the Au–O–Ti scaffolds are situated outside Au NPs. Consequently, PbO_2 was deposited on the TiO_x layer when the interfacial Au–O–Ti defect states trapped holes.

In this experiment, Au NPs were coated with a TiO_x layer by using a light-induced method. When the Au/TiO_2 sample was pretreated by irradiation with 525-nm light-emitting diodes (LEDs) under a H_2 atmosphere, the Au NPs were covered by an amorphous layer with a thickness of ~1.0 nm, as observed by high-resolution transmission electron microscopy (HRTEM) and high-angle annular dark field scanning transmission electron microscopy (HAADF-STEM) (Fig. 3, B and C). The amorphous layer was identified as TiO_2 because a Ti L signal was observed in the electron energy loss spectra collected from the Au NP region (fig. S18). This confirms that the light-induced method resulted in a TiO_x layer covering the Au NPs. The ratio of $Au^{\delta+}$ increased after the coating by a TiO_x layer, which is consistent with the binding energy shift of the Au $4f_{7/2}$ XPS signal from 83.2 to 83.4 eV (fig. S19). The Au/TiO_2 composite, comprising Au NPs coated with a TiO_x layer, was used for the photodeposition of PbO_2 from a Pb^{2+} solution under irradiation at 365 nm. The notable overlap of the Au M and Pb M signals indicated the presence of interfacial hole trap states (Fig. 3, D and E, and figs. S20, A to C, and S21, A to D). Consistent with this finding, the Pb M signal was significantly weaker for uncoated Au NPs (figs. S22; S20, D to F; and S21, E to H). These results indicate that some holes and electrons were effectively trapped at the interfacial Au–O–Ti scaffolds and Au NPs, respectively, with a maximum distance corresponding to the Au NP radius.

The electron-hole pairs forming the IEDs are expected to function similarly to FLPs in heterolytic H_2 dissociation. Considering that the concentration of holes trapped at the Au–O–Ti scaffolds is lower than that of electrons transferred to Au NPs (*39*), the rate of H_2 dissociation depends primarily on the availability of trapped holes at the Au–O–Ti scaffolds. The light-induced method was used to modulate the concentration of Au–O–Ti scaffolds because the input power of the 525-nm LEDs influences the coverage of the TiO_x layer on the Au NPs (Fig. 3F). The concentration of interfacial Au–O–Ti scaffolds was determined by carbon monoxide FTIR (CO-FTIR) spectroscopy, which semiquantifies the $Au^{\delta+}$ that comprises the interfacial Au–O–Ti scaffolds. CO-FTIR spectra showed three peaks at 2106, 2071, and 2027 cm^{-1} (fig. S23), attributed to linearly adsorbed CO on metallic Au, $Au^{\delta+}$, and an unidentified signal (*40*), respectively. Moreover, the signal of $Au^{\delta+}$ increased with the intensity of the pretreating 525-nm light. Deconvolution of the CO-FTIR spectra enabled quantitative analysis of the $Au^{\delta+}$ ratio (fig. S24). A nearly linear relationship was observed between the r_{HD} and the $Au^{\delta+}$ ratio (Fig. 3F), corroborating that the concentration of Au–O–Ti scaffolds, which trap holes, limits the rate of H_2 dissociation reaction.

Given that the concentration of Au–O–Ti scaffolds is related to Au NP diameter (d_p), the light-induced H_2 dissociation mechanism enabled by IEDs was studied by establishing the relationship between the H/D exchange activity and the average d_p (eq. 20 in supplementary materials). In the kinetic study, the average Au NP sizes varied from 5 to 40 nm, and the Au loading was kept at 1.0 wt % (fig. S25 and table S1). According to the H_2 dissociation mechanism, the HD formation rate (r_{HD}) should be linearly proportional to the product of the light intensity (I) and the reciprocal of the Au NP diameter ($1/d_p$) (Fig. 3G). The good linear fit between r_{HD} and $1/d_p$ at a given light intensity is consistent with the H_2 dissociation process enabled by the IEDs. Moreover, the slope of the fit ($r_{HD} \times d_p$) scaled linearly with the light intensity (fig. S26), corroborating the predominant contribution from IEDs to H_2 dissociation. Notably, thermocatalytic H_2 dissociation at the Au NP-TiO_2 interface is minor; otherwise, r_{HD} should be linearly correlated with $1/d_p^2$ (eq. 22 in supplementary materials) (*41*).

CO_2 hydrogenation by dissociated H_2

The Au/TiO_2 photocatalyst with Au NPs coated by a TiO_x layer was used for CO_2 hydrogenation because its H_2 dissociation activity was notably higher than that of Au/TiO_2 (fig. S27). The Au/TiO_2 catalyst filled the annular space in the quartz tube (fig. S28). Light irradiation and CO_2, H_2, and the Au/TiO_2 catalyst were necessary for the reaction (fig. S29). When the input power of the 365-nm LEDs was increased from 40 to 100 W, CO_2 conversion was elevated from 23 to near 100% (Fig. 4A). Compared with thermocatalysis, which afforded a mixture of CH_4 and CO at 160°C (fig. S30), the major product of the light-induced CO_2 hydrogenation was C_2H_6 because the distinctive TiO_x coating layer on the Au NPs and the abundant reductive hydrogen species on the Au/TiO_2 catalyst (fig. S31). The formation of C_2H_6 necessitates irradiation with 365-nm light; the involvement of the plasmonic effect preferentially produces methane and CO (Fig. 4B) (*42*, *43*). ^{13}C labeling experiments (figs. S32 and S33) confirmed that the C_2H_6 was derived from CO_2.

Under optimized reaction conditions, CO_2 conversion reached nearly 100%, and the formation rate and selectivity of C_2H_6 were 440 mmol $hour^{-1}$ m^{-2} and 99%, respectively (figs. S34 and S35). Au/TiO_2 loading was lowered from 15 to 5 g without an apparent decrease in the C_2H_6 formation rate (fig. S36). The apparent quantum efficiency (AQE) for CO_2 conversion improved from 37.1 to 58.5% by decreasing the Au NP size from 5 to 2 nm (fig. S37), surpassing the AQEs reported in the literature (tables S2 to S4). The high activity and selectivity can be attributed to the preferential formation of HCOO* intermediate rather than COOH* due to the hydridic character of the dissociated hydrogen (tables S5 to S7). Moreover, the CH_3* self-coupling mechanism also ensures a high selectivity of C_2H_6 (fig. S51, B to D). CO_2 hydrogenation was conducted for 210 hours with a single-pass CO_2 conversion of nearly 100% (Fig. 4C). The formation rate and selectivity of C_2H_6 were 446 mmol $hour^{-1}$ m^{-2} and >99%, respectively, and the carbon balance remained between 98 and 101% (fig. S38). The stability of the Au/TiO_2 catalyst was evaluated by using a CO_2 flow rate of 419 ml $hour^{-1}$ to decrease CO_2 conversion. In this case, the CO_2 conversion remained at 88% after 210 hours of light irradiation (fig. S39). The structure of Au/TiO_2 remains almost unchanged after the reaction (figs. S40 to S42). CO_2 can also be hydrogenated at a concentration similar to that in air [400 parts per million (ppm)]. The CO_2 conversion and C_2H_6 selectivity were 79 and >99% at a 400-ppm CO_2 flow rate of 15,648 ml $hour^{-1}$ (fig. S43). CO_2 hydrogenation was integrated with subsequent photocatalytic dehydrogenation by using a previously reported PdZn–ZnO catalyst to afford C_2H_4 (fig. S44) (*44*). This approach is practically desirable given the substantial demand for C_2H_4 as a commodity chemical for manufacturing polymers and other high-value compounds. Throughout the 1500 hours reaction, the CO_2 conversion remained >99% (Fig. 4D). The cascade CO_2 reduction afforded C_2H_4 at a formation rate of 447 mmol $hour^{-1}$ m^{-2}, with selectivity exceeding 99% at the outlet of the tandem reactor (table S2). In addition, the carbon and hydrogen balances remained between 98 and 101% (fig. S45).

The CO_2 hydrogenation was extended to Au catalysts with visible light–responsive supports such as N-TiO_2, nano CeO_2, In_2O_3, WO_3, and

$BiVO_4$ materials. N-TiO_2 absorbs visible light from 400 to 600 nm, whereas the other materials have absorption edges between 429 and 510 nm (fig. S46, A and B). Au/N-TiO_2 enabled CO_2 hydrogenation under 455-nm light irradiation, affording 69% CO_2 conversion and C_2H_6 with 85% selectivity (Fig. 4E). Notably, Au/CeO_2 and Au/In_2O_3 afforded C_2H_6 with 84 and 78% selectivities, respectively, at >99% CO_2 conversion. CO_2 hydrogenation was powered by white LEDs, using Au/N-TiO_2 as an example (fig. S47). The C_2H_6 selectivity exceeded 99% after optimizing the input power of the LEDs (fig. S48A) and decreasing the average size of the Au NPs to <2 nm (Fig. 4F). When coupling with a subsequent C_2H_6 dehydrogenation process, the Au_{2nm}/N-TiO_2 afforded C_2H_4 with a formation rate of 447 mmol $hour^{-1}$ m^{-2} and was stable for more than 800 hours (fig. S48, B and C). Notably, CO_2 hydrogenation over Au_{2nm}/N-TiO_2 was powered by solar energy with >90% selectivity (fig. S49).

Overall, the light-induced CO_2 hydrogenation produces C_2H_6 and C_2H_4 with formation rates two orders of magnitude higher than the previous best result for C_2H_4/C_2H_6 production (8.9 μmol $hour^{-1}$) by photocatalysis (tables S2 and S3). Although the C_2H_4 formation rate is lower than those of thermal catalysis and electrocatalysis (tables S8 and S9), this CO_2 hydrogenation circumvents the trade-off between conversion and product selectivity. The scale-up prospect of CO_2 hydrogenation will be improved by using LEDs to power the process and referring to the mature gas-solid thermal catalysis. However, owing to the low electricity-to-light efficiency of UV LEDs and the 14-electron reduction feature of CO_2 to C_2H_6, realizing practical demonstration necessitates efforts to improve energy efficiency. Future efforts should concentrate on optimizing the catalyst structure, refining the catalyst molding method, and increasing light intensity by using solar concentrators.

REFERENCES AND NOTES

1. G. Centi, E. A. Quadrelli, S. Perathoner, *Energy Environ. Sci.* **6**, 1711–1731 (2013).
2. V. Andrei *et al.*, *Nature* **608**, 518–522 (2022).
3. S. Kattel, P. J. Ramírez, J. G. Chen, J. A. Rodriguez, P. Liu, *Science* **355**, 1296–1299 (2017).
4. C. Hepburn *et al.*, *Nature* **575**, 87–97 (2019).
5. X. Li, J. Yu, M. Jaroniec, X. Chen, *Chem. Rev.* **119**, 3962–4179 (2019).
6. J. Jia *et al.*, *Chem. Soc. Rev.* **46**, 4631–4644 (2017).
7. H. Ou *et al.*, *J. Am. Chem. Soc.* **144**, 22075–22082 (2022).
8. Y. Shen *et al.*, *Nat. Commun.* **14**, 1117 (2023).
9. W. Gao, Y. Xu, L. Fu, X. Chang, B. Xu, *Nat. Catal.* **6**, 885–894 (2023).
10. J. Sun, W. Sun, L. Wang, G. A. Ozin, *Acc. Mater. Res.* **3**, 1260–1271 (2022).
11. Z. Zhang *et al.*, *Nat. Commun.* **13**, 1512 (2022).
12. L. Wang *et al.*, *Nat. Commun.* **11**, 2432 (2020).
13. D. R. Aireddy, K. Ding, *ACS Catal.* **12**, 4707–4723 (2022).
14. B. Hammer, J. Norskov, *Nature* **376**, 238–240 (1995).
15. M. Cai *et al.*, *Nat. Energy* **6**, 807–814 (2021).
16. D. W. Stephan, *Science* **354**, aaf7229 (2016).
17. L. Wang *et al.*, *Angew. Chem. Int. Ed.* **58**, 9501–9505 (2019).
18. L. B. Hoch *et al.*, *Adv. Sci.* **1**, 1400013 (2014).
19. Z. Li *et al.*, *Nat. Commun.* **13**, 7205 (2022).
20. Y. F. Xu *et al.*, *Nat. Commun.* **11**, 5149 (2020).
21. L. Wan *et al.*, *Nat. Catal.* **2**, 889–898 (2019).
22. T. Fujitani, I. Nakamura, T. Akita, M. Okumura, M. Haruta, *Angew. Chem. Int. Ed.* **48**, 9515–9518 (2009).
23. A. Mahdavi-Shakib *et al.*, *Nat. Catal.* **6**, 710–719 (2023).
24. A. Grirrane, A. Corma, H. García, *Science* **322**, 1661–1664 (2008).
25. G. González-Rubio *et al.*, *Science* **358**, 640–644 (2017).
26. S. Mukherjee *et al.*, *J. Am. Chem. Soc.* **136**, 64–67 (2014).
27. A. Mahdavi-Shakib, L. C. Rich, T. N. Whittaker, B. D. Chandler, *ACS Catal.* **11**, 15194–15202 (2021).
28. M. A. Henderson, W. S. Epling, C. H. F. Peden, C. L. Perkins, *J. Phys. Chem. B* **107**, 534–545 (2003).
29. M. A. Henderson, *Langmuir* **12**, 5093–5098 (1996).
30. M. A. Henderson, *Surf. Sci.* **355**, 151–166 (1996).
31. H. Schmidbaur, H. G. Raubenheimer, L. Dobrzańska, *Chem. Soc. Rev.* **43**, 345–380 (2014).
32. N. Kruse, S. Chenakin, *Appl. Catal. A Gen.* **391**, 367–376 (2011).
33. R. Radnik, C. Mohr, P. Claus, *Phys. Chem. Chem. Phys.* **5**, 172–177 (2003).
34. H.-G. Boyen *et al.*, *Science* **297**, 1533–1536 (2002).
35. L. Luo *et al.*, *J. Am. Chem. Soc.* **144**, 740–750 (2022).
36. F. Tao *et al.*, *Science* **322**, 932–934 (2008).
37. N. Luo *et al.*, *ACS Catal.* **6**, 7716–7721 (2016).
38. S. Wang *et al.*, *J. Am. Chem. Soc.* **139**, 11771–11778 (2017).
39. X. Zou *et al.*, *J. Phys. Chem. C Nanomater. Interfaces* **126**, 21467–21475 (2022).
40. X. Du *et al.*, *Nat. Commun.* **11**, 5811 (2020).
41. T. Whittaker *et al.*, *J. Am. Chem. Soc.* **140**, 16469–16487 (2018).
42. M. Aresta, A. Dibenedetto, A. Angelini, *Chem. Rev.* **114**, 1709–1742 (2014).
43. X. Cui *et al.*, *J. Am. Chem. Soc.* **140**, 16514–16520 (2018).
44. P. Wang *et al.*, *Nat. Commun.* **15**, 789 (2024).
45. P. Jin *et al.*, Photochemical H_2 dissociation for nearly quantitative CO_2 reduction to ethylene, Zenodo (2025); https://doi.org/10.5281/zenodo.15626990.

ACKNOWLEDGMENTS

We thank the instrumental support of the Liaoning Key Laboratory of Biomass Conversion for Energy and Materials. We acknowledge the Shanghai Synchrotron Radiation Facility for providing beamtime at the BL02B01 (31124.02.SSRF.BL02B01). We thank Z. Feng and Z. Li at the State Key Laboratory of Catalysis for the help in Raman spectroscopy and preparation of the Au/TiO_2@SiO_2 sample by atomic layer deposition, respectively. We also thank Y. Wang at XAFS Beamline (31124.02.SSRF.BL14W1) for the help in local temperature measurement. **Funding:** This work was supported by the National Natural Science Foundation of China (22025206 to F.W.), the National Key R&D Program of China (2022YFA1504900), the National Natural Science Foundation of China (22172157 to N.L.), the Dalian Innovation Support Plan for High Level Talents (2022RG13), the Department of Science & Technology of Liaoning Province (2024021100-JH3/102), DICP (grant DICP I202326), the Youth Innovation Promotion Association (YIPA) of the Chinese Academy of Sciences (2023192), and the European Union (HORIZON-WIDERA-2021-ACCESS-03-01; grant 01079384; HORIZON-EIC-2023-PATHFINDEROPEN-01; grant 101130717). **Author contributions:** Conceptualization: F.W., P.F., N.L., P.J.; Funding acquisition: N.L., P.F., F.W.; Investigation: P.J., C.N., H.Z., W.L.; Methodology: P.J., P.G., N.L., R.C., R.L., J.X., G.W., F.Z.; Project administration: N.L., F.W.; Supervision: P.F., F.W.; Visualization: P.J.; Writing – original draft: P.J., N.L.; Writing – review & editing: P.J., N.L., P.F., F.W. **Competing interests:** The authors declare that they have no competing interests. **Data and materials availability:** All data are available on Zenodo (*45*).

This research was funded in whole or in part by the European Commission (HORIZON-WIDERA-2021-ACCESS-03-01; grant 01079384; HORIZON-EIC-2023-PATHFINDEROPEN-01; grant 101130717), a cOAlition S organization. The author will make the Author Accepted Manuscript (AAM) version available under a CC BY public copyright license.

SUPPLEMENTARY MATERIALS

science.org/doi/10.1126/science.adq3445
Materials and Methods; Supplementary Text; Figs. S1 to S51; Tables S1 to S9; References (*46–178*)

Submitted 9 May 2024; resubmitted 5 February 2025; accepted 11 July 2025

10.1126/science.adq3445

CARDIOLOGY

Resistin-like molecule γ attacks cardiomyocyte membranes and promotes ventricular tachycardia

Nina Kumowski[1,2,3], Steffen Pabel[1,2,3,4], Jana Grune[1,2], Noor Momin[1,2], Van K. Ninh[5], Laura Stengel[4,6], Kyle I. Mentkowski[1,2,3], Yoshiko Iwamoto[1,2], Yi Zheng[2], I-Hsiu Lee[1,2,3], Jessica Matthias[7], Jan O. Wirth[7], Fadi E. Pulous[1,2], Hana Seung[1,2,3], Alexandre Paccalet[1,2,3], Charlotte G. Muse[1,2,3], Kenneth K. Y. Ting[1,2,3], Paul Delgado[1,2], Andrew J. M. Lewis[8], Vaishali Kaushal[9], Antonia Kreso[9], Dennis Brown[10], Sikander Hayat[11], Rafael Kramann[11,12], Filip K. Swirski[13], Kamila Naxerova[1,14], Daniel C. Propheter[15], Lora V. Hooper[15,16], Michael A. Moskowitz[1,2,3], Kevin R. King[5], Nadia Rosenthal[17,18], Maarten Hulsmans[1,2], Matthias Nahrendorf[1,2,3,19,20]*

Ventricular tachycardia disrupts the heart's coordinated pump function, leading to sudden cardiac death. Neutrophils, which are recruited in high numbers to the ischemic myocardium, promote these arrhythmias. Comparing neutrophils with macrophages, we found that resistin-like molecule γ (*Retnlg* or RELMγ) was the most differentially expressed gene in mouse infarcts. RELMγ is part of a pore-forming protein family that defends the host against bacteria by perforating their membranes. In mice with acute infarcts, leukocyte-specific *Retnlg* deletion reduced ventricular tachycardia. RELMγ elicited membrane defects that allowed cell exclusion dyes to enter the cardiomyocyte interior and also caused delayed afterdepolarizations and later cardiomyocyte death, both of which are strong arrhythmogenic triggers. Human resistin likewise attacked membranes of liposomes and mammalian cells. We describe how misdirected innate immune defense produces membrane leaks and ventricular arrhythmia.

Ischemic heart disease killed nine million people in 2021 globally and remains the main cause of death worldwide (*1*). Myocardial infarction (MI) and sudden cardiac death are the most lethal complications of ischemic heart disease (*2*). Although ventricular arrhythmias have been studied for decades, their treatment remains difficult (*3*). Typically, stenosis or occlusion of a coronary artery leads to cardiomyocyte hypoxia, which compromises energy-dependent ion handling. This gives rise to ventricular tachycardia (VT) and ventricular fibrillation (VF), fast irregular rhythms that reduce the provision of oxygenated blood to the organs. Most arrhythmias occur within the first 48 hours after MI (*4*), when myocardial ischemia triggers massive immune cell recruitment (*5*, *6*). Recent studies have highlighted the role of leukocytes in normal conduction and arrhythmogenesis (*7*–*10*). Shortly after MI, neutrophils mobilize from hematopoietic organs and migrate to the heart (*5*, *11*–*14*). Cell depletion studies indicate that neutrophils incite post-MI arrhythmia (*9*).

Neutrophils highly express *Retnlg/RETN* after MI

To explore how neutrophils elicit arrhythmia, we analyzed previously published single-cell RNA-sequencing (scRNA-seq) data (*15*) to contrast gene expression in neutrophils and macrophages 24 hours after MI. *Retnlg* (resistin-like molecule γ) was the most differentially expressed gene in neutrophils (Fig. 1, A to C). In healthy mice, *Retnlg* is the most highly expressed in bone marrow granulocytes according to the *Tabula Muris* (*16*). In contrast to MI, the normal myocardium harbors no neutrophils (*5*) and does not express *Retnlg* (*16*). RELMγ is part of the resistin protein family (RELMs) (*17*), the members of which share high structural and sequence homology (*18*). Neutrophils store RELMs in granules and secrete them during bacterial infection (*18*, *19*).

Using quantitative reverse transcription polymerase chain reaction (qRT-PCR) in fluorescence-activated cell sorting (FACS)–purified innate immune cells from blood and heart (fig. S1, A and B), we found that neutrophils expressed *Retnlg* at high and rising levels within the first 24 hours after MI (Fig. 1, D and E). Monocytes expressed *Retnlg* to a lesser extent (Fig. 1, D and E). RELMγ colocalized with $Ly6G^+$ neutrophils in bone marrow (Fig. 1F), spleen (fig. S1C), and in the infarcted heart (Fig. 1G), but not with $CCR2^+$ bone marrow cells (fig. S1D). As expected, RELMγ was absent in $Retnlg^{-/-}$ mice (fig. S1E). These data suggest neutrophils as a major source of RELMγ in ischemic mouse myocardium.

Reanalysis of spatial transcriptomics in the mouse heart 24 hours after MI (*20*) revealed that *Retnlg* is expressed in the ischemic zone of the myocardium (Fig. 1, H and I), where VTs typically arise (*3*). Resistin (*RETN*) is the human homolog to mouse RELMγ (*21*, *22*). Consistent with our findings in mice, human neutrophils also express *RETN* (*19*, *23*, *24*), and resistin protein is more abundant in human neutrophils compared with monocytes (fig. S1F). Spatial transcriptomics (*25*) indicated that infarcted human myocardium expresses more *RETN* compared with noninfarcted heart tissue (Fig. 1, J and K), similar to mice.

Deleting *Retnlg* reduces VT 12-fold

To study the actions of RELMγ, we transplanted either C57Bl/6 $Retnlg^{+/+}$ or $Retnlg^{-/-}$ bone marrow into lethally irradiated C57Bl/6 recipient mice to create $Retnlg^{+/+}$ and $Retnlg^{-/-}$ bone marrow chimeras [$Retnlg^{+/+}$ and $Retnlg^{-/-}$ bone marrow transplantation (BMT)], respectively, in which bone marrow–derived cells lack RELMγ. After transplantation, blood leukocyte counts were comparable in both cohorts (fig. S2A), which showed no arrhythmia in the absence of ischemia (fig. S2B). Diet-induced hypokalemia elicited spontaneous VT in awake mice after acute MI (*9*) (Fig. 2A). We confirmed that permanent coronary ligation induced similarly distributed infarct sizes in both groups (fig. S2, C to E) because infarct size may influence arrhythmogenesis (*26*). Infarcted $Retnlg^{-/-}$ BMT mice had 12-fold lower VT burden compared with control $Retnlg^{+/+}$ BMT with MI (Fig. 2, B to D). In $Retnlg^{+/+}$ BMT mice, VT burden was particularly high around 4 to 5 hours and 16 hours after MI, and these peaks were absent in $Retnlg^{-/-}$ BMT mice (Fig. 2E). This timeline resembles human pathology (*4*, *27*). $Retnlg^{-/-}$ BMT mice

[1]Center for Systems Biology, Massachusetts General Hospital and Harvard Medical School, Boston, MA, USA. [2]Department of Radiology, Massachusetts General Hospital and Harvard Medical School, Boston, MA, USA. [3]Center for Inflammation Imaging, Massachusetts General Hospital and Harvard Medical School, Boston, MA, USA. [4]Department of Internal Medicine II, University Hospital Regensburg, Regensburg, Germany. [5]University of California, San Diego Department of Medicine and Bioengineering, La Jolla, CA, USA. [6]Department of Cardiology, Kerckhoff Heart Center, Bad Nauheim, Germany. [7]Abberior Instruments America, Bethesda, MD, USA. [8]Radcliffe Department of Medicine, NIHR Biomedical Research Centre, University of Oxford, and British Heart Foundation Centre of Research Excellence, Oxford, UK. [9]Division of Cardiac Surgery, Massachusetts General Hospital and Harvard Medical School, Boston, MA, USA. [10]Program in Membrane Biology, Nephrology Division, Department of Medicine, Massachusetts General Hospital and Harvard Medical School, Boston, MA, USA. [11]Department of Medicine 2 (Nephrology, Rheumatology, Clinical Immunology Hypertension), RWTH Aachen, Medical Faculty, Aachen, Germany. [12]Department of Internal Medicine, Nephrology and Transplantation, Erasmus Medical Center, Rotterdam, Netherlands. [13]Cardiovascular Research Institute and Department of Medicine, Icahn School of Medicine at Mount Sinai, New York, NY, USA. [14]Blavatnik Institute, Department of Genetics, Harvard Medical School, Boston, MA, USA. [15]Department of Immunology, University of Texas Southwestern Medical Center, Dallas, TX, USA. [16]The Howard Hughes Medical Institute, The University of Texas Southwestern Medical Center, Dallas, TX, USA. [17]The Jackson Laboratory, Bar Harbor, ME, USA. [18]National Heart and Lung Institute, Imperial College, London, UK. [19]Cardiovascular Research Center, Massachusetts General Hospital and Harvard Medical School, Boston, MA, USA. [20]Department of Internal Medicine I, University Hospital Wuerzburg, Wuerzburg, Germany. ***Corresponding author. Email: mnahrendorf@mgh.harvard.edu**

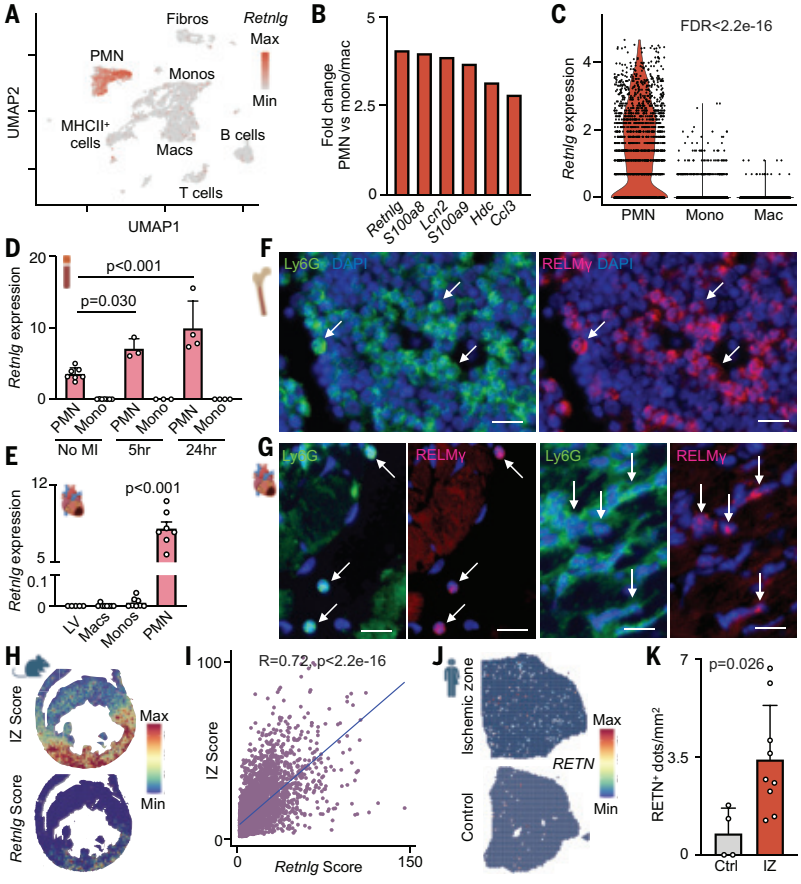

Fig. 1. Mouse *Retnlg* and human *RETN* are up-regulated in neutrophils after MI. (**A**) scRNA-seq was previously performed (*20*) in three mice 24 hours after MI and reanalyzed here. *Retnlg* expression labeled (red) in cellular subsets [polymorphonuclear neutrophils (PMNs)]. (**B**) Fold change of the most up-regulated genes in neutrophils compared with macrophages/monocytes. (**C**) *Retnlg* expression in neutrophils (PMN), monocytes (Mono), and macrophages (Mac) from the infarct area 24 hours after MI [$n = 3$ mice; false discovery rate (FDR) $< 2.2 \times 10^{-16}$]. (**D**) *Retnlg* expression relative to *Gapdh* measured by qRT-PCR in circulating neutrophils (PMN) and monocytes at baseline ($n = 7$ mice) and 5 hours ($n = 3$ mice) and 24 hours ($n = 4$ mice) after MI. Data were analyzed by one-way ANOVA and Tukey's post hoc test. (**E**) *Retnlg* expression relative to *Gapdh* determined by qRT-PCR in the left ventricle (LV; $n = 5$ mice), macrophages (Mac; $n = 8$ mice), monocytes (Mono; $n = 8$ mice), and neutrophils (PMN; $n = 8$ mice) 5 hours after MI. (**F**) Immunofluorescent staining of neutrophils (Ly6G), RELMγ, and nuclei [4′,6-diamidino-2-phenylindole (DAPI)] in the femurs of C57Bl6 mice; arrows indicate colocalization of Ly6G and RELMγ. Scale bar, 20 μm. (**G**) Immunofluorescent staining of Ly6G$^+$ neutrophils, RELMγ, and nuclei (DAPI) in the heart 24 hours after MI. Arrows indicate colocalization of Ly6G and RELMγ. Scale bar, 20 μm. (**H**) Spatial transcriptomics of mouse heart cross-section for ischemic zone (IZ) score and *Retnlg* 24 hours after ischemic injury. (**I**) Pearson correlation for *Retnlg* and IZ gene set score colocalizations. Each dot represents a spatial transcriptomics spot. (**J**) Single-nucleus RNA-sequencing (snRNA-seq) and spatial transcriptomics were previously performed in infarcted human hearts and controls (*25*) and reanalyzed here. Spatial plot of the ischemic zone after MI and control tissue of a human heart. (**K**) RETN$^+$ dots per square millimeter in the IZ ($n = 9$) and control tissue (Ctrl, $n = 4$) of human hearts. Data were analyzed by two-sided unpaired *t* test and are shown as mean ± SD. [Figure created with BioRender.com]

also had a lower VT burden after ischemia followed by reperfusion injury (IRI), which here was accompanied by reduced infarct size (fig. S2, F to I). Given that our data identified neutrophils as a major RELMγ source in MI, we pursued cell-specific gene deletion in *Ly6G*^{Cre}*Retnlg*$^{fl/fl}$ mice (fig. S2J). When exposed to the STORM model, *Ly6G*^{Cre}*Retnlg*$^{fl/fl}$ mice showed a lower spontaneous VT burden compared with *Retnlg*$^{fl/fl}$ controls (Fig. 2, F to H, and fig. S2, K and L).

To determine whether there are direct proarrhythmic properties of RELMγ, we performed patch-clamp experiments with ventricular mouse cardiomyocytes exposed to 1 μM RELMγ. Because this concentration is likely higher than what can be expected in vivo, we also incubated cardiomyocytes with medium that contained lysed neutrophils. Both RELMγ and neutrophil lysates triggered delayed afterdepolarizations (DADs) in most cardiomyocytes at a higher incidence than in vehicle-treated control cardiomyocytes (Fig. 2, I to K, and fig. S2, M to O), whereas the resting membrane potential and action potential duration were comparable in control and RELMγ-treated cells (fig. S2, P and Q). DADs can trigger ectopic beats that give rise to reentry in the presence of the arrhythmogenic substrate commonly found in the ischemic myocardium (*28*). These data support that neutrophil-derived RELMγ facilitates ventricular arrhythmia.

RELMγ causes membrane defects in liposomes and cardiomyocytes

Next, we sought to determine the mechanism by which RELMγ elicits arrhythmia. Known RELM functions can be divided into two categories: (i) enhancing inflammation (*18*, *29*, *30*) and (ii) defending against bacteria by attacking their membranes (*18*, *30*). We first studied whether infarct leukocyte frequencies, which may modulate arrhythmogenesis (*31*), were altered in *Retnlg*$^{-/-}$ BMT. Using flow cytometry of acute infarcts, remote myocardium, and blood, we found no differences in circulating and recruited leukocytes between *Retnlg*$^{-/-}$ BMT mice and *Retnlg*$^{+/+}$ BMT mice (fig. S3, A to C), nor were there differences in stromal cell numbers (fig. S3D). These data were confirmed by histology, which also revealed comparable myocardial fibrosis and vascularization (fig. S4, A to S). Cardiomyocyte size and left ventricular weight were similar in the two cohorts (fig. S4, E to G, and fig. S4M). Comparing the inflammatory response to ischemia in *Retnlg*$^{-/-}$ BMT and *Retnlg*$^{+/+}$ BMT mice with MI, we detected no differences (figs. S4, N to S, and S5). *Retnlg* deletion did not affect other inflammatory neutrophil functions such as provision of oxidative stress or NETosis (fig. S6). Therefore, we subsequently focused on the membrane pore–forming properties of RELMγ.

Mouse RELMγ and human resistin are structurally similar to other antimicrobial peptides that also inflict membrane damage, specifically a hydrophobic alpha helix and a positively charged beta sheet that enable electrostatic interactions (fig. S7A) (*30*, *32*, *33*). These properties allow RELMs to bind negatively charged lipids in the bacterial membrane within the acidic environment of infection or on normal skin, which has a pH of 5 (*30*, *34*–*36*). Several mechanisms likely prevent membrane attacks on steady-state cardiomyocytes, including the absence of neutrophils, the lack of negatively charged lipids in the outer leaflet of intact mammalian cells, and a neutral pH. However, after MI, many neutrophils enter the myocardium (*5*), and distressed cardiomyocytes flip negatively charged phosphatidylserine to their outer membrane layer (*37*). The myocardial pH drops to 5.5 after 50 min of ischemia (*38*). We thus hypothesized that in acute infarcts, RELMγ first binds to cardiomyocytes that display negatively charged phosphatidylserine on their surface and then damages cardiomyocyte membranes. Membrane breaches may allow extracellular cations to enter the cell along concentration gradients. Such

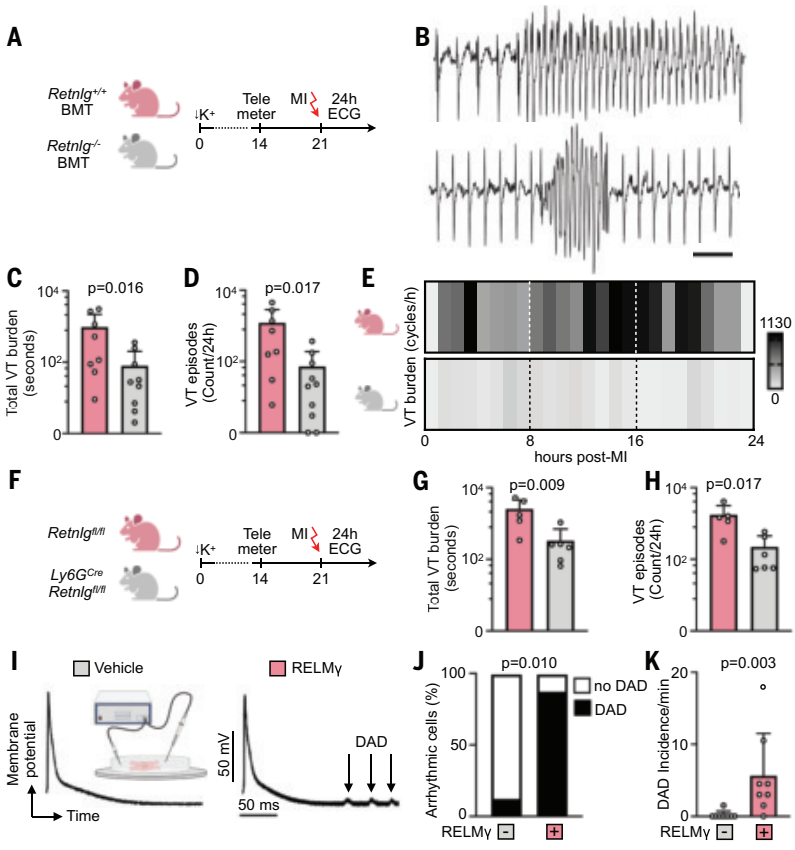

Fig. 2. RELMγ deficiency reduces arrhythmia. (**A**) Experimental outline. Bone marrow donors were either C57Bl/6 *Retnlg*$^{+/+}$ BMT mice or *Retnlg*$^{-/-}$ BMT mice. Transplant recipients were C57Bl/6 wild-type mice ($n = 10$ *Retnlg*$^{+/+}$, $n = 10$ *Retnlg*$^{-/-}$) that subsequently underwent the STORM protocol. ↓K^+, hypokalemic diet. (**B**) Electrocardiogram (ECG) from *Retnlg*$^{+/+}$ BMT control and *Retnlg*$^{-/-}$ BMT. Scale bar, 500 ms. (**C**) VT burden evaluated 24 hours after MI ($n = 9$ *Retnlg*$^{+/+}$ BMT, $n = 10$ *Retnlg*$^{-/-}$ BMT). Data were analyzed with Mann-Whitney *U* test. (**D**) Arrhythmia 24 hours after MI ($n = 9$ *Retnlg*$^{+/+}$ BMT, $n = 10$ *Retnlg*$^{-/-}$ BMT). Data were analyzed with Mann-Whitney *U* test. (**E**) VT burden expressed as cardiac cycles in VT per hour. (**F**) Experimental outline. *Ly6G*^{Cre}*Retnlg*$^{fl/fl}$ mice and *Retnlg*$^{fl/fl}$ control mice underwent the STORM protocol of hypokalemia and MI. (**G**) VT burden 24 hours after MI ($n = 5$ *Retnlg*$^{fl/fl}$, $n = 6$ *Ly6G*^{Cre}*Retnlg*$^{fl/fl}$). Data were analyzed with Mann-Whitney *U* test. (**H**) Arrhythmia 24 hours after MI ($n = 5$ *Retnlg*$^{fl/fl}$, $n = 6$ *Ly6G*^{Cre}*Retnlg*$^{fl/fl}$). Data were analyzed with Mann-Whitney *U* test. (**I**) Stimulated action potential recordings (whole-cell current-clamp) of mouse cardiomyocytes after incubation with RELMγ or vehicle for 30 min. (**J**) Percentage of arrhythmic cells with DADs (control, $n = 8$ cardiomyocytes from $n = 5$ mice; RELMγ, $n = 8$ cardiomyocytes from $N = 3$ mice). Data were analyzed with Fisher's exact test. (**K**) DAD incidence per minute (control, $n = 8$ cardiomyocytes from $n = 5$ mice; RELMγ, $n = 8$ cardiomyocytes from $n = 3$ mice). Data were analyzed with Mann-Whitney *U* test and are shown as mean ± SD. [Figure created with BioRender.com]

nonspecific ion leaks, we hypothesized, may cause electrical instability in cardiomyocytes.

Pore formation and membrane disruption in mammalian cells have been shown for several antimicrobial peptides (*39*, *40*), but not for mouse RELMγ or human resistin. Therefore, we began by examining these peptides in model systems. We performed negative-stain electron microscopy on liposomes that contained phosphatidylserine, thus mimicking the cell membrane of distressed cardiomyocytes. Pore-like membrane defects occurred in the liposomes after incubating with mouse RELMγ (Fig. 3, A and B) and human resistin (Fig. 3, C and D), with mean pore diameters of 37.0 ± 2.3 and 32.7 ± 2.2 nm, respectively. To confirm membrane permeabilization, we next pursued disruption assays on liposomes encapsulating calcein, which is released from the liposomes if their membrane becomes porous. RELMγ and resistin induced dose-dependent dye release (Fig. 3, E and F, and fig. S7, B and C) only under acidic conditions (fig. S7D), results that are consistent with prior findings for other RELMs (*35*, *36*). A control immunoglobulin G protein did not trigger more dye release than vehicle control (fig. S7E) and did not form membrane defects (fig. S7F).

We next incubated primary mouse cardiomyocytes with RELMγ in acidic conditions. Using confocal microscopy, we found that fluorescently labeled RELMγ bound to the surface of cardiomyocytes. RELMγ attached to the membrane in areas that externalized phosphatidylserine, which we identified using Apotracker (Fig. 3G and fig. S8, A and B). Spreading from focal areas of colocalized RELMγ and Apotracker signal, a dextran cell exclusion dye entered the cell and expanded from the entry point into the entire cell interior over time (Fig. 3, H and I, and fig. S8, C and D). In a control experiment that incubated cells with fluorescently labeled ovalbumin, we observed no colocalization with Apotracker, and the cell exclusion dye did not enter cells through focal areas (fig. S8, E and F). Using identical acquisition parameters, unstained cells exhibited low autofluorescence at the wavelengths used (fig. S8G).

After we identified areas of joint Apotracker and RELMγ signal at sites of membrane leakage, we used minimal photon fluxes (MINFLUX) super-resolution microscopy to investigate the structural organization of RELMγ during membrane binding (*41*). Primary mouse cardiomyocytes were labeled using the same protocol as described above for confocal imaging, including incubation with fluorescently labeled RELMγ (fig. S8H). We detected well-demarcated areas of densely packed RELMγ molecules on the surface of cardiomyocytes (Fig. 3J and fig. S8, H and I) that were 1.7 ± 1.25 μm^2 in size (Fig. 3K). Scanning electron microscopy showed similar cell surface deposits (Fig. 3L). In the vicinity of RELMγ binding, we detected enhanced staining for the membrane repair protein MG53 (fig. S9, A and B). These data are consistent with the interpretation that RELMγ binds to and then permeabilizes cardiomyocyte membranes. The observed liposome defects and RELMγ patterns align with the "carpet model" of membrane pores (*33*, *42*). Like dextran (Fig. 3H), ions should be able to traffic through such lesions, movement that would give rise to the electrical instability that we observed by patch clamp in RELMγ-exposed cardiomyocytes. To test this hypothesis directly, we pursued confocal microscopy of cardiomyocytes that were loaded with a calcium sensor, assaying calcium signal changes as a function of RELMγ membrane binding, which we tracked using fluorescently labeled RELMγ. In time-lapse observations, we recorded intracellular calcium waves. High calcium sensor signal initiated at the binding site of RELMγ before traveling through the entire cell (fig. S9C). When we focused on the cytoplasm adjacent to the RELMγ binding, we found a persistently enhanced intracellular signal (fig. S9D). This observation is consistent with extracellular calcium leaking into the cell interior through sites of RELMγ-induced membrane damage. Such leaks may give rise to cell depolarization documented by the traveling imaging signal wavefront that initiated at the RELMγ-binding site.

Using microscopy in cardiomyocytes exposed to RELMγ or vehicle, we also quantified the fluorescent signal arising from the calcium indicator. This assay showed an increasing systolic calcium transient amplitude over time in cardiomyocytes treated with RELMγ

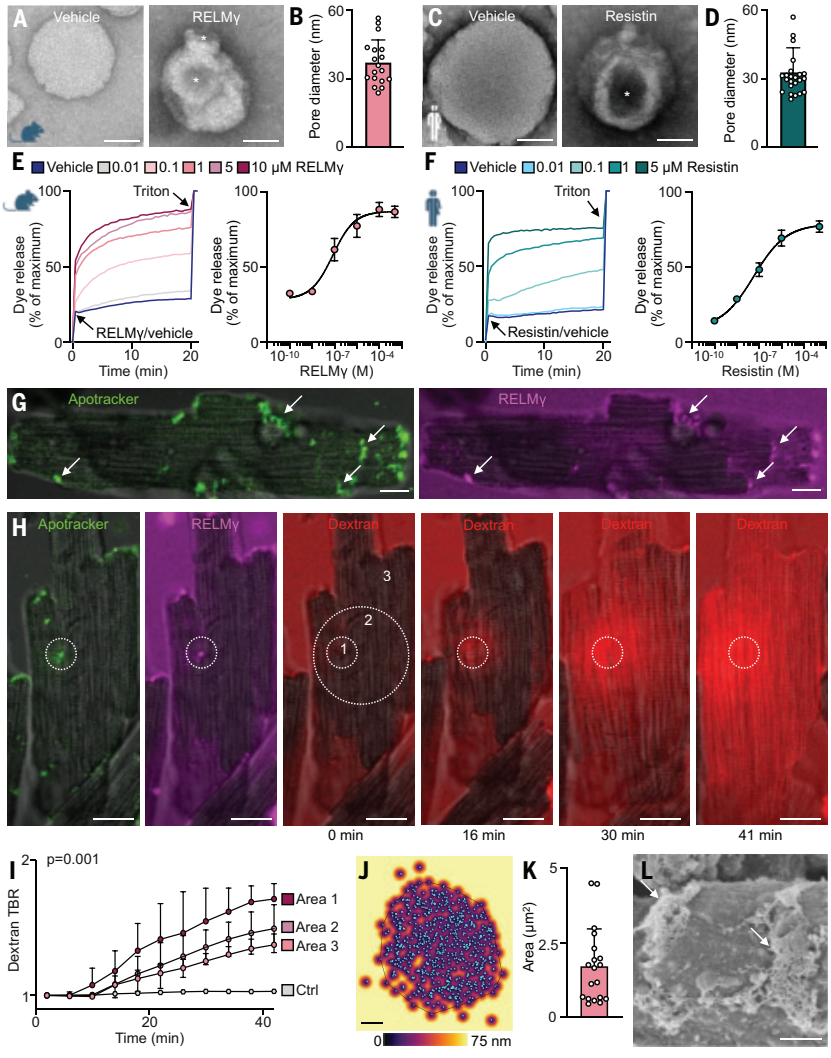

Fig. 3. RELMγ attacks lipid membranes. (**A**) Electron microscopy of liposomes in the presence of vehicle or recombinant RELMγ. Asterisks indicate pores. Scale bar, 50 nm. (**B**) Pore diameter in liposomes after exposure to RELMγ. (**C**) Electron microscopy of liposomes in the presence of either vehicle or human RETN. Scale bar, 50 nm. (**D**) Pore diameter after exposure to RETN. (**E**) Calcein-loaded liposomes treated with RELMγ. Dye efflux is expressed as percentage of maximal release after administration of Triton X-100. Lower panel shows dose response. Results shown are the average of at least three independent experiments. (**F**) Calcein-loaded liposomes were treated with different concentrations of RETN. Lower panel shows concentration curves. Results shown are the average of three independent experiments. (**G**) Confocal microscopy of a mouse cardiomyocyte. Arrows indicate colocalization of phosphatidylserine staining (Apotracker) and RELMγ. Scale bar, 10 μm. (**H**) Confocal microscopy of a mouse cardiomyocyte showing phosphatidylserine (Apotracker), RELMγ, and dextran. Circles indicate colocalization of phosphatidylserine, RELMγ, and dextran cell entry. Numbers indicate areas that are proximal (1), intermediate (2), and distant to (3) the dextran entry. Scale bar, 20 μm. (**I**) Target to baseline ratio (TBR) of fluorescence intensity indicating dextran influx in areas 1 to 3 and control cardiomyocytes (no dextran influx). $n = 4$ cells per group. Data were analyzed with two-way ANOVA for repeated measurements. (**J**) MINFLUX image of RELMγ. Cyan dots indicate RELMγ molecules (on-events), black outline indicates convex hull area, and look-up table reflects distance to nearest center of on-event (0 to 75 nm). Scale bar, 200 nm. (**K**) Carpet area in super-resolution imaging ($n = 19$ areas in $n = 19$ cardiomyocytes). (**L**) Scanning electron microscopy of a mouse cardiomyocyte showing carpet-like deposits (white arrows). Scale bar, 2 μm. Data are shown as mean ± SD. [Figure created with BioRender.com]

(fig. S10, A to I). Such data constellation is consistent with calcium influx through a membrane leak that is compensated by the cells' calcium pumps.

Finally, we pursued a cell culture assay with Neuro-2a cells that were loaded with a calcium indicator. Before adding RELMγ, the fluorescence intensity was similar in all groups (fig. S10J). Cells that were treated with RELMγ developed a higher fluorescence signal (fig. S10K), indicating rising cytosolic calcium.

RELMγ and resistin promote mammalian cell death

Membrane defects can trigger cell death, which is appropriate when pore-forming peptides encounter bacteria (*30*, *35*, *36*, *39*). Using a flow cytometry assay and the H9c2 rat cardiomyoblast cell line, we found that cells exposed to RELMγ had reduced survival compared with vehicle-treated cells in an acidic environment (Fig. 4, A and B). Denatured RELMγ did not affect cell survival (fig. S11, A and B). Further, RELMγ decreased the survival of human EXPI293 cells (Fig. 4, C and D). Recombinant human resistin also increased cell death (Fig. 4E). In mouse cardiomyocytes, RELMγ exposure lowered cell integrity (Fig. 4F). Finally, we assayed cell death in vivo 5 hours after inducing MI or IRI in *Retnlg*$^{+/+}$ BMT and *Retnlg*$^{-/-}$ BMT mice. Mice that lacked RELMγ had fewer terminal deoxynucleotidyl transferase–mediated deoxyuridine triphosphate nick end labeling (TUNEL)–positive cells (Fig. 4, G to J).

These observations raise the question of which type of cell death RELMγ may promote. We found no differences in caspase 3 activity, indicating apoptosis (*43*, *44*), in infarcts of Retnlg$^{+/+}$ BMT mice and Retnlg$^{-/-}$ BMT mice (fig. S11C). Neither did we find differences in the necroptosis markers (*43*, *44*) *Ripk1*, *Ripk3*, or *Mlkl* (fig. S11, D and E). Expression of the pyroptosis markers (*43*, *44*) *Gsdmd* and *Nlrp3* and caspase 1 activity were likewise unchanged, as was that of cleaved gasdermin-D (fig. S11, F and G). We did detect increased HMGB1 in supernatant derived from isolated mouse cardiomyocytes exposed to RELMγ (fig. S11H). Thus, our data provide no indication that RELMγ affects programmed cell death; rather, they show that RELMγ may enhance externally caused necrosis.

RELMγ in ischemic stroke

To explore RELMγ functions in a different disease setting, we reanalyzed previously published single-cell data (*45*) obtained in mice 24 hours after stroke (Fig. 5A). Neutrophils are absent from the healthy brain. *Retnlg* was highly expressed in neutrophils recruited to the ischemic brain (Fig. 5, A and B). In a qRT-PCR analysis of blood cells, *Retnlg* expression was 11-fold higher in wild-type mice with stroke compared with naïve mice (Fig. 5C), likely because neutrophil frequencies increase after stroke. Motivated by this finding, we induced ischemic stroke in *Retnlg*$^{-/-}$ and wild-type control mice (fig. S12, A to E). After 24 hours, brain infarcts were smaller in *Retnlg*$^{-/-}$ mice, a finding that indicated more widespread neuronal death in RELMγ-competent mice (Fig. 5, D and E). A flow cytometry assay of a neuroblast-derived cell line showed lower survival among cells that were exposed to RELMγ (Fig. 5, F and G). Using confocal microscopy, we observed RELMγ signal surrounding membrane defects in neuronal cells (Fig. 5H) and entry of fluorescently labeled dextran indicating membrane breaches (Fig. 5I). Neighboring intact cells were negative for both dyes. We speculate that larger brain infarcts and the neuronal cell membrane defects in the presence of RELMγ are caused by pore formation.

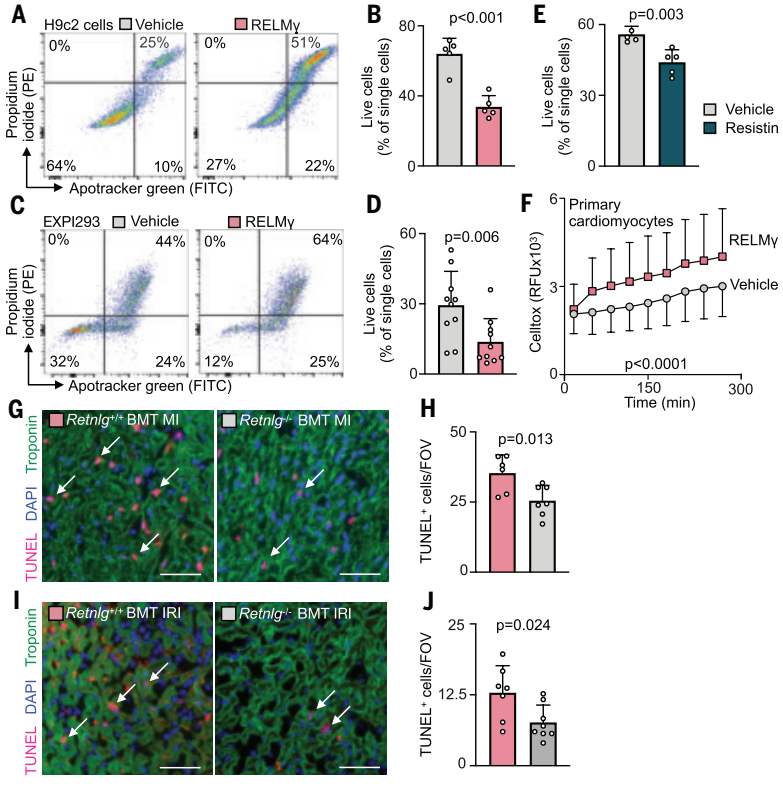

Fig. 4. RELMγ and resistin promote mammalian cell death. (**A**) Apoptosis assay of H9C2 cells exposed to 10 μM RELMγ or vehicle control in acidic pH (see the materials and methods) using propidium iodide [phycoerythrin (PE)] and Apotracker green [fluorescein isothiocyanate (FITC)]. (**B**) Live cell fraction as determined by flow cytometry. $n = 5$ replicates per group. Data were analyzed with two-sided unpaired *t* test. (**C**) Apoptosis assay of EXPI293 cells exposed to RELMγ or vehicle control in acidic pH using propidium iodide (PE) and Apotracker green (FITC). (**D**) Live cell fraction as determined by flow cytometry. $n = 10$ replicates per group. Data were analyzed with two-sided unpaired *t* test. (**E**) Apoptosis assay with 10 μM human RETN ($n = 5$ replicates) or vehicle ($n = 4$ replicates). Live cell fraction was determined by flow cytometry. Data were analyzed with two-sided unpaired *t* test. (**F**) Cell death assay measuring relative fluorescent units (RFUs) of CellTox bound to primary isolated cardiomyocytes incubated with 0.5 μM staurosporine with and without 1 μM RELMγ over 300 min. $n = 5$ replicates per group. Data were analyzed with two-way ANOVA for repeated measurements. (**G**) Immunofluorescence staining of infarct region 5 hours after MI in C57BL/6 *Retnlg*$^{+/+}$ BMT and *Retnlg*$^{-/-}$ BMT mice. Shown is staining of cardiomyocytes (troponin), apoptotic cells (TUNEL), and nuclei (DAPI). Arrows indicate apoptotic cells. Scale bar, 50 μm. (**H**) Analysis of TUNEL^{+} cells ($n = 6$ *Retnlg*$^{+/+}$ BMT, $n = 7$ *Retnlg*$^{-/-}$ BMT). Ten fields of view per MI were analyzed. Data were analyzed with two-sided unpaired *t* test. (**I**) Immunofluorescence staining of infarcted region in *Retnlg*$^{+/+}$ BMT mice and *Retnlg*$^{-/-}$ BMT mice 24 hours after IRI. Shown is staining of cardiomyocytes (troponin), apoptotic cells (TUNEL), and nuclei (DAPI). Arrows indicate apoptotic cells. Scale bar, 50 μm. (**J**) Analysis of TUNEL^{+} cells ($n = 7$ *Retnlg*$^{+/+}$ BMT, $n = 8$ *Retnlg*$^{-/-}$ BMT). Three fields of view per mouse were analyzed. Data were analyzed with two-sided unpaired *t* test and are shown as mean ± SD.

Discussion

RELMs are pore-forming peptides that attack bacterial membranes (*30*, *32*, *35*, *36*). Our study indicates that RELMγ causes membrane defects in distressed cardiomyocytes. These defects allow dextran dyes to enter the cell interior and are thus large enough for passive influx of positively charged ions, whereas the cardiomyocyte membrane potential is deeply negative. The cation influx may lead to the afterdepolarizations that we detected by patch clamp when cardiomyocytes were exposed to RELMγ. Afterdepolarizations promote electrical instability, and ventricular arrhythmia may arise from ectopic foci (*28*). In addition to aberrant cell depolarization, RELMγ may later promote arrhythmia by killing cardiomyocytes. Our data are consistent with the model that RELMγ-inflicted membrane damage accelerates the transition from cardiomyocyte apoptosis to nonprogrammed necrosis. Dead cardiomyocytes are electrically silent and may induce local conduction and repolarization heterogeneities, which favor electrical reentry and VT (see summary cartoon in fig. S13).

After 15 min of ischemia, cardiomyocytes externalize phosphatidylserine (*37*). Within 6 hours after ischemia, most cardiomyocytes are still viable, have intact cell membranes, and are potentially salvageable (*46*). Our data suggest that RELMy binds such phosphatidylserine-exposing cells. Once bound, RELMγ disrupts the membrane from the outside. Ions freely travel through the pore, ultimately leading to cytoplasmatic swelling and death. This is RELMγ's appropriate function during killing of bacteria, which feature negatively charged lipids in their cell membrane even if they are not apoptotic. These findings support that RELMγ externally elicits nonprogrammed cell death. The signs of accidental, nonprogrammed necrosis include membrane integrity loss, HMGB1 release from the cell, and the binding of cell membrane-impermeable DNA dyes to the nucleus (*43*, *44*), all of which we documented after RELMγ exposure.

Proteins can generate membrane pores through various mechanisms (*33*, *42*). Our super-resolution microcopy observations of RELMγ patterns on the cardiomyocyte membrane align best with the carpet model (*33*, *42*). In this scenario, positively charged peptides bind to the negatively charged head groups of phospholipids through electrostatic interactions, covering the membrane like a carpet. Once a critical threshold concentration is surpassed, the peptide's hydrophobic alpha helix inserts into the hydrophobic core of the membrane, leading the peptide to disrupt the membrane without necessarily oligomerizing into superstructures.

RELMs' autoaggression in ischemic tissue likely stems from a combination of three infection hallmarks: acidosis, negatively charged lipid exposure on the outer cardiomyocyte membrane, and recruitment of neutrophils, an abundant mobile source of RELMγ. In ischemia, anaerobic metabolism causes acidosis (*38*). An acidic environment facilitates membrane permeabilization by RELMs (*35*, *36*), similar to other antimicrobial proteins that form pores in bacterial membranes (*30*, *39*, *47*). Low pH may change protein conformation and protonation of amino acid residues (*47*), thereby fostering RELMs' ability to bind negatively charged membrane components and thus attack the membrane.

RELMγ action is not limited to MI, because deleting RELMγ reduced brain IRI. This result aligns with the neuronal cell death that we observed after in vitro RELMγ exposure. We speculate that RELMγ may inflict membrane defects in many inflammatory conditions. An acidic environment, neutrophil recruitment, and early apoptosis occur in numerous pathologies and may account for various neutrophil effects in tissue (*48*, *49*).

Human resistin is the functional analog to mouse RELMγ (*21*, *22*). Both human resistin and mouse RELMγ depend on the transcription factor CEBPE and are produced by neutrophils (*19*, *21*, *23*, *24*). Elevated RETN serum levels in patients after MI and stroke are associated with unfavorable outcomes (*50*–*53*). We show here that human RETN expedites mammalian cell death, and that pore formation is a conserved function across human RETN and mouse RELMγ. Thus, neutrophil production and the release of RELMs may be therapeutic targets to alleviate arrhythmia and mammalian cell death in neutrophil-rich inflammation.

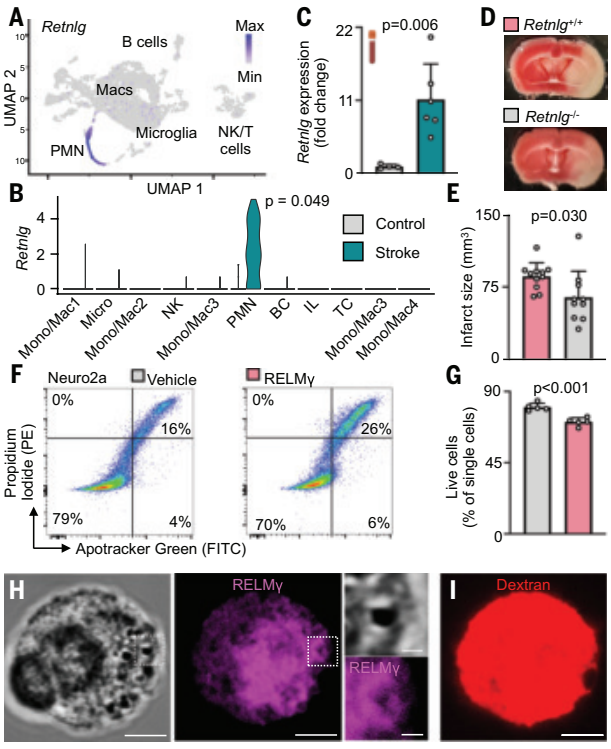

Fig. 5. RELMγ in ischemic stroke. (**A**) scRNA-seq of the brain was previously performed in $n = 3$ mice 24 hours after stroke (*45*) and reanalyzed here for *Retnlg* expression in brain leukocyte clusters (PMN, neutrophils). (**B**) *Retnlg* expression in brain after stroke in neutrophils (PMN) and other cell clusters. Mono/Mac, monocytes/macrophages; Micro, microglia; NK, natural killer cells; PMN, neutrophils; BC, B cell; IL, innate lymphoid cell; TC, T cell. (**C**) Fold change of *Retnlg* as determined by qRT-PCR in whole blood 24 hours after stroke ($n = 6$ mice) compared with naïve mice ($n = 4$). Data were analyzed with two-sided unpaired *t* test. (**D**) Triphenyltetrazolium chloride staining of brain after middle cerebral artery occlusion in *Retnlg*$^{-/-}$ ($n = 11$) and *Retnlg*$^{+/+}$ mice ($n = 10$). (**E**) Quantification of stroke size. Data were analyzed with two-sided unpaired *t* test. (**F**) Apoptosis assay of Neuro2a cells exposed to 10 μM RELMγ or vehicle control in acidic pH using propidium iodide (PE) and Apotracker green (FITC). (**G**) Live cell fraction as determined by flow cytometry. $n = 5$ replicates per group. Data were analyzed with two-sided unpaired *t* test. (**H** and **I**) Confocal microscopy of a Neuro2a cell at pH 5 incubated with fluorescently labeled RELMγ (H) and fluorescently labeled dextran (I). Scale bar, 5 μm. Magnification box scale bar, 1 μm. Data are shown as mean ± SD. [Figure created with BioRender.com]

REFERENCES AND NOTES

1. M. Vaduganathan, G. A. Mensah, J. V. Turco, V. Fuster, G. A. Roth, *J. Am. Coll. Cardiol.* **80**, 2361–2371 (2022).
2. E. J. Benjamin *et al.*, *Circulation* **135**, e146–e603 (2017).
3. J. Bhar-Amato, W. Davies, S. Agarwal, *Arrhythm. Electrophysiol. Rev.* **6**, 134–139 (2017).
4. R. H. Mehta *et al.*, *Am. J. Cardiol.* **109**, 805–812 (2012).
5. M. Nahrendorf *et al.*, *J. Exp. Med.* **204**, 3037–3047 (2007).
6. S. Epelman *et al.*, *Immunity* **40**, 91–104 (2014).
7. S. D. Francis Stuart, N. M. De Jesus, M. L. Lindsey, C. M. Ripplinger, *J. Mol. Cell. Cardiol.* **91**, 114–122 (2016).
8. M. Hulsmans *et al.*, *Cell* **169**, 510–522.e20 (2017).
9. J. Grune *et al.*, *Nat. Cardiovasc. Res.* **1**, 649–664 (2022).
10. M. Hulsmans *et al.*, *Science* **381**, 231–239 (2023).
11. D. M. Calcagno *et al.*, *J. Am. Heart Assoc.* **10**, e019019 (2021).
12. S. L. Puhl, S. Steffens, *Front. Cardiovasc. Med.* **6**, 25 (2019).
13. O. Soehnlein, S. Steffens, A. Hidalgo, C. Weber, *Nat. Rev. Immunol.* **17**, 248–261 (2017).
14. M. Horckmans *et al.*, *Eur. Heart J.* **38**, 187–197 (2017).
15. D. M. Calcagno *et al.*, *Sci. Immunol.* **5**, eaaz1974 (2020).
16. Tabula Muris Consortium, *Nature* **562**, 367–372 (2019).
17. C. Fan, B. A. Johns, Q. Su, I. A. Kolosova, R. A. Johns, *Histochem. Cell Biol.* **139**, 605–613 (2013).
18. G. M. Pine, H. M. Batugedara, M. G. Nair, *Cytokine* **110**, 442–451 (2018).
19. E. A. Boström, A. Tarkowski, M. Bokarewa, *Biochim. Biophys. Acta* **1793**, 1894–1900 (2009).
20. D. M. Calcagno *et al.*, *Nat. Cardiovasc. Res.* **1**, 1039–1055 (2022).
21. A. M. Chumakov, T. Kubota, S. Walter, H. P. Koeffler, *Oncogene* **23**, 3414–3425 (2004).
22. I. Nagaev, M. Bokarewa, A. Tarkowski, U. Smith, *PLOS ONE* **1**, e31 (2006).
23. L. Johansson *et al.*, *J. Immunol.* **183**, 4047–4054 (2009).
24. T. S. Kapellos *et al.*, *Cell Rep.* **42**, 112525 (2023).
25. C. Kuppe *et al.*, *Nature* **608**, 766–777 (2022).
26. M. Majidi *et al.*, *Eur. Heart J.* **30**, 757–764 (2009).
27. J. R. Harkness *et al.*, *Am. J. Cardiol.* **108**, 1373–1381 (2011).
28. V. Ducceschi *et al.*, *Clin. Cardiol.* **19**, 325–331 (1996).
29. S. Jiang *et al.*, *J. Immunol.* **192**, 4795–4803 (2014).
30. Y. Li *et al.*, *Front. Immunol.* **12**, 699807 (2021).
31. J. Grune, M. Yamazoe, M. Nahrendorf, *Nat. Rev. Cardiol.* **18**, 547–564 (2021).
32. K. Matsuzaki, *Biochim. Biophys. Acta* **1462**, 1–10 (1999).
33. Y. Shai, *Biochim. Biophys. Acta* **1462**, 55–70 (1999).
34. H. Lambers, S. Piessens, A. Bloem, H. Pronk, P. Finkel, *Int. J. Cosmet. Sci.* **28**, 359–370 (2006).
35. D. C. Propheter, A. L. Chara, T. A. Harris, K. A. Ruhn, L. V. Hooper, *Proc. Natl. Acad. Sci. U.S.A.* **114**, 11027–11033 (2017).
36. T. A. Harris *et al.*, *Cell Host Microbe* **25**, 777–788.e8 (2019).
37. E. A. Dumont *et al.*, *Circulation* **102**, 1564–1568 (2000).
38. H. Hirche *et al.*, *J. Mol. Cell. Cardiol.* **12**, 579–593 (1980).
39. S. Mukherjee *et al.*, *Nature* **505**, 103–107 (2014).
40. R. Miao *et al.*, *Immunity* **56**, 2523–2541.e8 (2023).
41. F. Balzarotti *et al.*, *Science* **355**, 606–612 (2017).
42. B. Bertrand, R. Garduño-Juárez, C. Munoz-Garay, *Biochim. Biophys. Acta Biomembr.* **1863**, 183551 (2021).
43. P. K. Mishra *et al.*, *Am. J. Physiol. Heart Circ. Physiol.* **317**, H891–H922 (2019).
44. G. E. Yan, M. Elbadawi, T. Efferth, *World Acad. Sci. J.* **2**, 39–48 (2020).
45. C. Beuker *et al.*, *Nat. Commun.* **13**, 945 (2022).
46. D. E. Sosnovik *et al.*, *Circ. Cardiovasc. Imaging* **2**, 460–467 (2009).
47. E. Malik, S. R. Dennison, F. Harris, D. A. Phoenix, *Pharmaceuticals (Basel)* **9**, 67 (2016).
48. F. V. S. Castanheira, P. Kubes, *Blood* **133**, 2178–2185 (2019).
49. S. Steffens *et al.*, *Cardiovasc. Res.* **116**, 1850–1862 (2020).
50. H. B. Erer *et al.*, *Kardiol. Pol.* **72**, 181–186 (2014).
51. X. Z. Qiao, Y. M. Yang, Z. R. Xu, L. A. Yang, *J. Zhejiang Univ. Sci. B* **8**, 875–880 (2007).
52. K. O. Lee *et al.*, *Neurologist* **27**, 41–45 (2021).
53. H. B. Lee *et al.*, *Thromb. Res.* **134**, 686–692 (2014).

ACKNOWLEDGMENTS

We thank the HSCI-CRM Flow Cytometry Core for assistance with cell sorting and K. Joyes for editing the manuscript. Electron Microscopy Imaging was performed in the HMS Electron Microscopy Facility. Imaging was performed in the Microscopy Core of the Program in Membrane Biology. We acknowledge Servier Medical Art (smart.servier.com) and Biorender (IH23GLWC6I) for cartoon components. The authors thank the members of the Mikael Pittet laboratory for providing *Ly6g*$^{tm2621(cre)Arte}$ mice. **Funding:** This work was supported by the Leducq Foundation (M.N.), the National Institutes of Health (NIH grants HL155097 and HL149647 to M.H., grants HL142494 and HL176359 to M.N., grant NS136068 to M.M. and M.N., grant T32HL007444 to V.K.N., and grant DP2AR075321 to K.R.K.); the Deutsche Forschungsgemeinschaft (DFG) Walter Benjamin Programm (grant 491497342 to N.K. and grant 530157297 to S.P.); the British Heart Foundation (grants FS/ICRF/24/26111 and RE/18/3/342140 to A.J.M.L.), and the NIHR Oxford Biomedical Research Centre (A.J.M.L.). M.N. is a Mercator Fellow of the Deutsche Forschungsgemeinschaft (SFB 1525, project number 453989101). J.G. was funded by the DFG (grants SFB-1470 A04, SFB-1425 B19, and GR 5261/1-1), Corona-Stiftung Grant S199/10086/2022, the German Society for Cardiology, Deutsche Herzstiftung, and the German Center for Cardiovascular Research. The imaging core was supported by Center for the Study of Inflammatory Bowel Disease grant DK043351 and a Boston Area Diabetes and Endocrinology Research Center award DK135043. The AXR confocal imaging system was supported by NIH grant S10 OD032211. **Author contributions:** N.K. conceived the study; designed, performed, and analyzed the experiments; interpreted data; made the figures; and wrote the manuscript. J.G., N.M., L.S., S.P., Y.I., K.I.M., Y.Z., F.E.P., A.P., H.S., C.G.M., A.J.M.L., P.D., J.M., and K.K.Y.T. designed, performed, and analyzed the experiments. A.K. and V.K. collected and processed human samples. V.K.N., S.H., I.-H.L., and J.O.W. analyzed the data. F.K.S., K.N., M.A.M., D.C.P., L.V.H., D.B., R.K., K.R.K., N.R., and M.H. discussed results and strategy. M.N. conceived and directed the study. N.K. and M.N. wrote the manuscript with input from all authors. **Competing interests:** M.N. has received funds or material research support from Alnylam, Biotronik, CSL Behring, GlycoMimetics, GSK, Medtronic, Novartis, and Pfizer and has received consulting fees from Biogen, Gimv, IFM Therapeutics, Molecular Imaging, Sigilon, Verseau Therapeutics, and Bitterroot. J.M. and J.O.W. are employees of the company Abberior Instruments America, which commercializes the MINFLUX technology. A.J.M.L. is on the advisory board of Abbott, AstraZeneca, and Novartis. S.P. is employed by the Novartis Institute of Biomedical Research. S.H. is a cofounder and shareholder of Sequantrix GmbH and has received research funding from Novo Nordisk and AskBio. The remaining authors declare no competing interests. **Data and materials availability:** All data are available in the main manuscript or the supplementary materials.

SUPPLEMENTARY MATERIALS

science.org/doi/10.1126/science.adp7361
Materials and Methods; Figs. S1 to S13; References (*54*–*67*)

Submitted 9 April 2024; resubmitted 28 May 2025; accepted 3 July 2025

10.1126/science.adp7361

EVOLUTION

Evolution of thumbnails across Rodentia

Rafaela V. Missagia[1,2]*, Anderson Feijó[2,3]*, Lauren Johnson[4], Maximilian L. Allen[5], Bruce D. Patterson[2], Paulina D. Jenkins[6]*, Gordon M. G. Shepherd[7]*

The unguis (hoof, claw, or nail) of the first digit (D1, also known as the thumb or pollex) of the tetrapod hand exhibits numerous functional adaptations, but its macroevolutionary association with ecological diversity is unknown. Across Rodentia, we find that most extant genera and ancestral lineages bear D1 nails. Exceptions follow structure-function associations that arose independently multiple times, specifically, the gain of D1 claws with subterranean habits and the loss of D1 ungues with oral-only feeding behavior. We hypothesize that early acquisition of D1 nails and manually dexterous food handling was crucial for rodents to adaptively leverage cranial specializations for efficient gnawing and thereby exploit hard seeds and nuts, a niche that they dominated after the extinction of multituberculates. Our study recasts ideas about rodent evolution and uncovers a previously unrecognized contributor to their successful radiation.

The tetrapod hand is a key structure for functional interactions with the habitat. Hand morphology relates to locomotion, foraging, handling, and more, with the digits displaying diverse specializations. The ungues, keratinized structures at the tips of the terminal phalanges, are often conspicuously adapted and essential for behavior. For example, in mammals, claws are associated with carnivory and fossoriality, hoofs with cursoriality, and nails with arboreality (*1*–*3*).

The first digit (D1, also known as the thumb or pollex) can also be markedly specialized in form and function. The D1 is the last digit to appear developmentally and the first to become vestigial or lost evolutionarily ("Morse's law") (*4*–*6*). It has played a key role in the evolution of certain groups such as primates to enable better maneuvering (e.g., climbing and grasping) (*7*, *8*). Rarely considered, however, is the D1 unguis (*9*). For some mammals, the general rule appears to be that the D1, if present, has the same unguis type as the other digits of the hand, suggesting similar function across digits. For others, such as bats, the D1 and its unguis are morphologically and functionally highly distinct from the other digits (*10*).

Rodents, the most speciose group of mammals, display many habitat and lifestyle adaptations (*11*). The D1s of various rodents have long been known to bear either nails or claws or to lack an unguis altogether (*12*–*15*), but the macroevolutionary patterns and functionality of these unguis types are unknown. Prior studies of structure-function relationships of the manual ungues have focused on the longer digits (D2 to D5) (e.g., *16*, *17*). The D1 and its unguis are often simply omitted from species descriptions or are described as "vestigial," "nonfunctional," or "rudimentary" because of their diminutive size and unclear function (*12*, *15*).

A few reports suggest instead that the rodent D1 and its unguis may be highly functional. A high degree of bimanual dexterity has been noted for some rodents bearing a nail on their D1, such as heteromyids (*18*, *19*) and sciurids (*20*, *21*), including holding of food items between the two thumbs (*22*). Recent studies using high-speed video of laboratory mice show that for these murids, the nail-bearing D1s are indeed the principal digits for oromanual (mouth-hand) food handling (*23*, *24*). However, bimanual food handling has also been noted both for rodents such as bathyergids that bear a claw on D1 (*25*, *26*) and for others such as *Dinomys* that lack an external D1 and unguis (*27*).

The paucity of information and absence of systematic analysis leaves a fragmented and confusing picture of the prevalence and evolution of different D1 unguis types across Rodentia and their possible relationships to hand-related behaviors. Here, we explored the diversity of the D1 unguis across rodent genera and its evolution and relationships to different life modes and food-handling behaviors.

Results

D1 unguis diversity and evolution in rodents

We used a classification system centered on distinguishing the two basic D1 unguis types: claw and nail (Fig. 1A and fig. S1). We also included one additional category, "intermediate," for the possibility of hybrid morphology between claw and nail and another, "none," for cases with no visible unguis. The unguis morphology dataset (data S1 and S2 and fig. S2) included most genera (83%, 433 of 522 total) across all 35 extant families and all major taxonomic divisions of Rodentia. To explore the evolutionary history of the D1 unguis, we built ancestral state reconstruction models and found the equal rates model with two rate regimes to be the best supported [weighted Akaike information criterion (AICw) = 0.67; table S1], indicating heterogeneous rates between major clades, with Eumuroidea (a large clade within the supramyomorphs) showing generally lower transition rates between ungual states than the clade comprising hystricomorphs and sciuromorphs. Mapping the D1 unguis states across the rodent phylogenetic tree reveals nails as the most common (86% of analyzed genera) and likely ancestral state, both overall and within each of the three infraordinal clades (Fig. 1, B to D, and fig. S3). Claws arose independently multiple times and are the main or only D1 unguis type in many taxa, including families Pedetidae, Castoridae, Geomyidae, Spalacidae, Bathyergidae, and Ctenomyidae, as well as some genera in Sciuridae, Dipodidae, Cricetidae, and Echimyidae. Groups lacking a D1 unguis are less common and include Zenkerellidae, Ctenodactylidae, Erethizontidae, Dinomyidae, and Caviidae and additional genera in Gliridae, Sciuridae, Anomaluridae, Chinchillidae, and Abrocomidae. D1 ungues with intermediate morphology were rare, found only in four genera: *Ellobius*, *Heterocephalus*, *Lophuromys*, and *Parahydromys*.

Food handling and D1-unguis association

To explore possible structure-function relationships underlying D1 unguis diversity, we first considered food handling, a behavior that particularly involves the thumb. We distinguished two basic types: oromanual, which involves use of the hands to hold and manipulate the food at the mouth, and oral, which does not (Fig. 1A). A category for both oromanual and oral was also included for potential cases of hybrid behavior. The food-handling behavior dataset (data S1 and S2 and fig. S4) included many rodent genera (55%, 287/522) across all extant families and major clades.

The ancestral state reconstruction reveals two best-fitted models with similar AIC weights for food-handling behavior: the equal rates model [corrected AIC (AICc) = 67.82, AICw = 0.33] and the

[1]Department of Zoology, University of São Paulo, São Paulo, Brazil. [2]Negaunee Integrative Research Center, Field Museum of Natural History, Chicago, IL, USA. [3]Key Laboratory of Zoological Systematics and Evolution, Institute of Zoology, Chinese Academy of Sciences, Beijing, China. [4]Gantz Family Collections Center, Field Museum of Natural History, Chicago, IL, USA. [5]Illinois Natural History Survey, Prairie Research Institute, University of Illinois, Champaign, IL, USA. [6]Natural History Museum, London, UK. [7]Department of Neuroscience, Northwestern University, Chicago, IL, USA. ***Corresponding author. Email: rmissagia@usp.br (R.V.M.); afeijo@fieldmuseum.org (A.F.); p.jenkins@nhm.ac.uk (P.D.J.); g-shepherd@northwestern.edu (G.M.G.S.)**

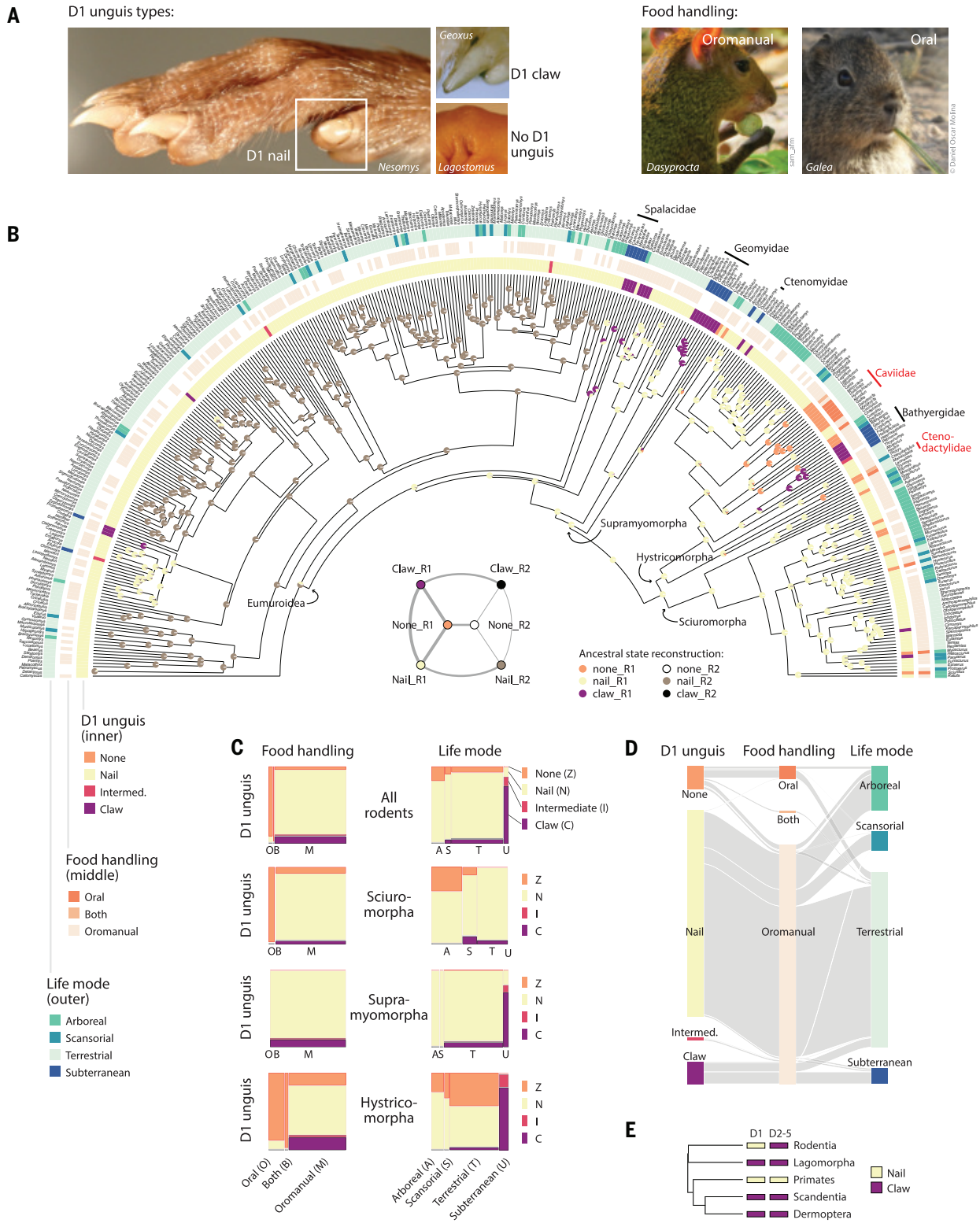

Fig. 1. Evolutionary diversity and structure-function relationships of the D1 unguis in Rodentia. (**A**) Types of rodent D1 ungues (left) and food-handling behavior (right). (**B**) Genus-level rodent phylogenetic tree. Traits are shown at the tips (see legends). Pie charts show the relative probabilities of the different ungual types at each ancestral node. Network plot (inset, at base of tree) shows the magnitude of transition rates (line thickness) among D1 ungual types following the equal rates with two rate regimes (rates R1 and R2) for ancestral state reconstruction. (**C**) Mosaic plots, for all rodents and each top-level clade. In these two-dimensional percentage stacked bar graphs, the *y* axes represent the percentages of rodents with each type of D1 unguis and the *x* axes represent the percentages of rodents with each type of food-handling behavior (left column of plots) and life mode (right column). Tiles are colored by D1 unguis type. Tile areas reflect the total number of observations for each combination of traits. (**D**) Alluvial plot for all rodents. Horizontal gray lines indicate the relative proportion of genera that share specific combinations of characters, showing patterns of association between unguis types and hand-related behaviors. (**E**) D1 and D2 to D5 unguis types mapped onto the Euarchontoglires tree.

all-rates-different model (AICc = 67.71, AICw = 0.35), both with one rate regime (table S1). Based on the simpler model criterion (*28*), we chose the former to estimate node state probabilities for this character. In this model, transitions between food-handling categories are assumed to be consistent across the phylogeny, indicating uniform evolutionary rates for this trait among rodent lineages. Mapping the food-handling characters on the tree (Fig. 1B and figs. S3, S5, and S6) shows that oromanual feeding is the most common and the ancestral form, both overall and within the three rodent infraorders (Fig. 1, B to D). Oral-only feeding, though uncommon, arose multiple times as a derived condition. It is found mostly in hystricomorph groups but also in some miniature squirrels. Only two genera, *Ctenodactylus* and *Lagostomus*, appeared to have hybrid ("both") behavior in which the food-handling mode appears to be flexible: frequently oral but also at times oromanual.

Exploring the association between D1 unguis types and food handling, we found that most taxa that feed orally (i.e., without using their hands) lack a D1 unguis (Fig. 1, B to D, and figs. S3 and S6); exceptions include Erethizontidae and Dinomyidae, which feed oromanually and yet lack a D1 unguis. Conversely, unguis-bearing oral feeders were rare (*Cuniculus*). Oromanual behavior is present in groups bearing a nail or claw on the D1.

Life mode and D1-unguis association

Another hand-dependent behavior potentially associated with D1 unguis type is life mode, which relates to both locomotion and microhabitat. We used a comprehensive (99%, 516/522 genera) dataset (*29*) that classifies the life modes of extant rodents as arboreal, scansorial, terrestrial, or subterranean (data S1). These life-mode data were mapped using the same tree (Fig. 1B and figs. S3, S5, and S6).

The best-fitting model of character evolution for the life-mode dataset was an all-rates-different model with one rate regime (AICw = 0.85; table S1). Terrestrial life mode is the most common and likely the ancestral mode in rodents, both overall and within the infraordinal clades (Fig. 1, B to D). This finding is consistent with recent fossil evidence for terrestriality in many early rodents, including *Paramys* (*30*, *31*). In contrast to feeding behavior, the life modes were highly diverse, with arboreal, scansorial, and subterranean modes occurring within and across groups and arising multiple times as derived states (figs. S5 and S6). Particular life modes were in some cases clustered in larger clades and in other cases scattered across the phylogeny. For example, subterranean behavior occurred in multiple families (e.g., Geomyidae, Spalacidae, Bathyergidae, and Ctenomyidae), as well as in some genera within heterogeneous families (e.g., *Ellobius* and *Spalacopus*). Arboreality appeared in two large tribes, Sciurini and Echimyini, as well as in Anomaluridae and diverse scattered groups (e.g., within Cricetidae and Muridae). Scansorial taxa occurred scattered across the tree, often mixed with arboreal taxa (e.g., Gliridae and Protoxerini). These findings are consistent with prior reports of this well-studied aspect of rodent diversity (*32*–*34*).

Overall, rodent genera with a subterranean life mode tend to have a claw for a D1 unguis, whereas arboreal and scansorial rodents typically bear a nail (Fig. 1, B to D, and figs. S3 and S6). Terrestrial life mode includes representatives of all D1 unguis types.

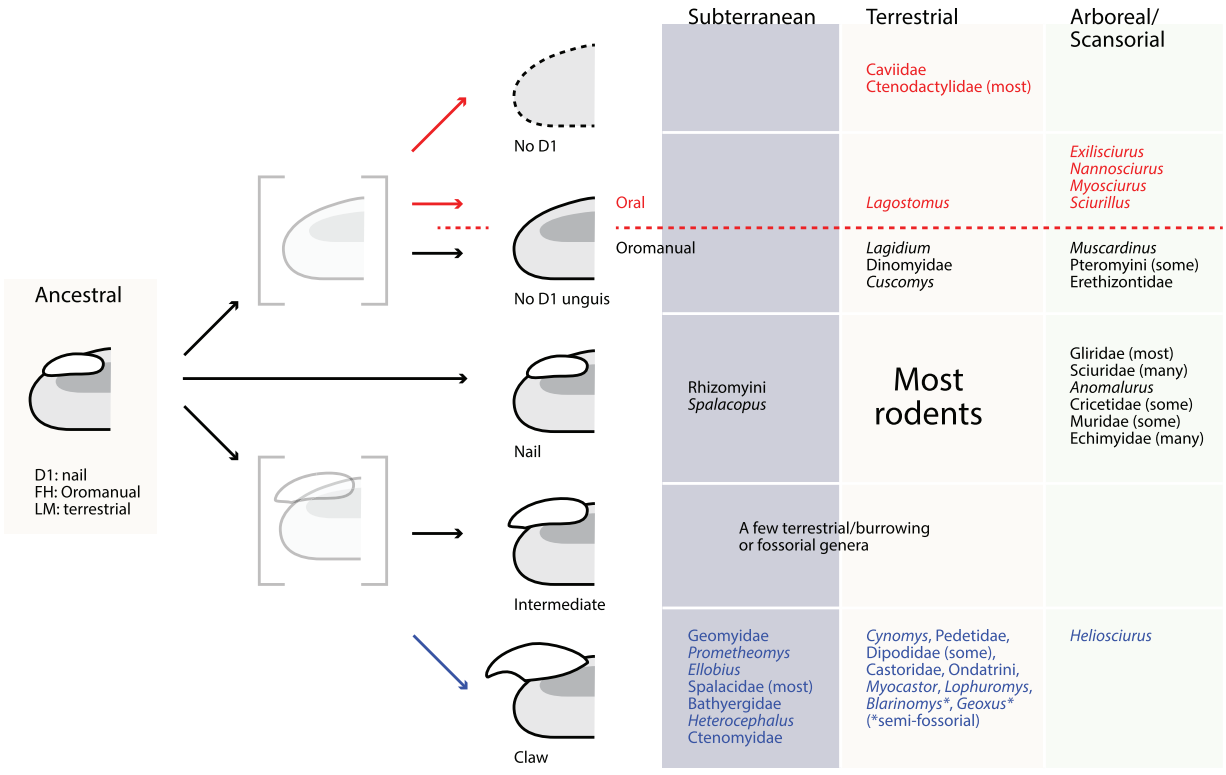

Fig. 2. Schematic summary and conceptual model for function-related morphological evolution of the D1 unguis in rodents. The proposed scheme depicts evolutionary diversification of the D1 unguis from the ancestral state to modern rodents, most of which retain the ancestral characters (D1 nail, oromanual food handling, and terrestriality). Claws on D1 (bottom of center column) emerged in association with fossoriality (subterranean genera and burrowing terrestrial genera), transitioning through an intermediate stage also seen in some modern genera. The loss of the unguis (top of center column) emerged in association with the loss of oromanual (i.e., switch to oral) feeding (above the red dashed line), particularly in lineages with complete loss of the underlying D1 bones ("No D1"), transitioning through an intermediate stage (with the bones present but the unguis lost) also seen in some modern genera, with variable association with oral versus oromanual food handling.

Correlation analyses of the structure-function relationships

To further explore the patterns described above, we used Pagel's correlation test to evaluate the dependency, or lack thereof, of unguis morphology and hand-related behaviors while considering phylogenetic relationships (*35*). To assess the correlation of D1 unguis types and life mode, we compared nail/claw and terrestrial/subterranean categories, and for D1 unguis and food-handling types, we compared unguis/no unguis and oromanual/oral behaviors. Other traits were either merged or excluded in alternative configurations yielding similar results. Models incorporating unguis morphology and hand-related behaviors as dependent traits received stronger support compared with independent models (AICw ≈ 1; table S2), indicating their interdependence.

Discussion

The rodent D1 unguis would seem to be an unlikely structure to yield fresh insight into the evolution of this exceptionally diverse mammalian order. However, mammalogists have long pointed to the underexplored potential of postcranial morphological features and their role in mammalian evolution (*36*, *37*). By broadly surveying D1 unguis morphology across Rodentia, we determined that the D1 nail is the most common and the likely ancestral state, with D1 claws and the loss of an unguis occurring as derived conditions in disparate clades and families. Food-handling and life-mode behaviors show structure-function relationships underlying the evolutionary diversity of D1 unguis types, suggesting new ways of conceptualizing rodent diversity.

The broadest generalization about the D1 unguis is that most rodents have them, and most have a nail rather than a claw, an apparently predominant trait throughout rodent evolutionary history. This is consistent with the available fossil evidence indicating that rodents had a nail-bearing D1 at least by the early Oligocene (~30 million years ago), based on our interpretations of descriptions of a short D1 with wide ungual phalanx for *Pseudoltinomys* (*38*), and likely by the Eocene (~55 million years ago), based on descriptions of a short, stout, and overall highly sciurid-like D1 in *Paramys*, one of the earliest known rodent genera (*39*). Across all digits of the manus, the Rodentia combination of a nail on D1 and claws on all other digits (D2 to D5) is unique among Euarchontoglires, contrasting with the all-claws pattern in Lagomorpha, Scandentia, and Dermoptera, as well as with the all-nails pattern in most primates (*10*, *32*, *33*), and thus constitutes a new postcranial autapomorphy for the group (Fig. 1E).

The D1 claw, which is over-represented among subterranean rodents, represents a derived trait, as does the subterranean life mode. The lack of an unguis is another derived condition and is over-represented among rodents with a derived lack of oromanual food-handling behavior. Behavioral traits may be more evolutionarily labile than morphological traits (*40*, *41*), with morphological responses lagging behavioral changes on geological time scales (*42*). In sharp contrast, however, oromanual food-handling behavior was widely distributed and relatively stable phylogenetically, suggesting that this hand-related behavior appears more generally conserved than the structural apparatus associated with it because oromanual behavior was conserved among rodents with any of the D1 unguis types. We further detected a clear association connecting D1 ungues, food handling, and life modes. Rodents with an unguis on D1 are generally oromanual feeders, whereas those without it are predominantly oral feeders with terrestrial, scansorial, or arboreal, but not subterranean, lifestyles. Oromanual feeders lacking a D1 unguis are found mainly in arboreal and scansorial groups (e.g., Erethizontidae, some flying squirrels, and *Anomalurus*; the terrestrial *Dinomys* is an exception). Species with D1 claws are strongly associated with subterranean habits but can also be found among terrestrial burrowing groups (e.g., Pedetidae and *Cynomys*), suggesting shared functionality of the D1 claw. Rodents with a nail on D1 span the spectrum of life modes but are predominantly oromanual feeders.

Our findings suggest a simple framework for the evolutionary diversification of the D1 unguis and hand-related behaviors (Fig. 2). In this hypothetical scheme, the starting point is the set of ancestral states (D1 nail, oromanual food handling, and terrestrial life mode). In one evolutionary direction, a claw on D1 emerged in association with fossorial and semifossorial behavior (subterranean genera and burrowing terrestrial genera), maybe transitioning through an intermediate stage also seen in some burrowing genera (e.g., *Heterocephalus* and *Ellobius*). In another evolutionary direction, loss of the D1 unguis occurred in association with the loss of oromanual feeding, particularly in lineages with complete loss of the underlying D1 bones, maybe transitioning through an intermediate stage (with the bones present but the unguis lost) also seen in some modern genera, with variable association with oral versus oromanual food handling. The combination of a D1 lacking an unguis and oral-only food handling appears in two markedly distinct forms: (i) in clustered groups of medium-to-large terrestrial grass-eating herbivores (all Caviidae and most ctenodactylids), with loss of D1 bones, and (ii) in scattered genera of miniature arboreal exudate-feeders ("bark-gleaners"; *Sciurillus*, *Myosciurus*, *Nannosciurus*, *Exilisciurus*, and likely also *Idiurus*), which retain the D1 bones in a reduced form despite the loss of the unguis (*43*–*45*). Most extant rodents, however, retain the ancestral states (D1 nail, oromanual food handling, and terrestrial life mode).

Such close association between the D1 unguis and food handling in Rodentia may reflect the group's early acquisition of diprotodonty (having a pair of massive incisors) and associated specializations for forceful gnawing (*37*). These include a cranial morphology featuring a long diastema separating the gnawing incisors from the chewing cheekteeth, a specialized arrangement of masticatory muscles that enhances their efficiency, and ever-growing incisors that are both actively and passively sharpened (*46*–*49*). Rodents have two distinct feeding modes, biting with the incisors and chewing with molars, that are mutually exclusive because the mandible is shorter than the maxilla, preventing the incisors and cheekteeth from occluding simultaneously (*50*). Incisive biting is specifically and intricately coordinated with hand movements during oromanual dexterity (*24*, *49*). Stabilization and manipulation of hard food items such as nuts, particularly using the D1 and its typically nail-type unguis, would require an early acquisition of dexterous manipulation to facilitate high-force biting with the incisors and thus conferred an advantage in exploiting this energy-rich food source—chiseling open a nut is much easier with a good grip. This provides strong evidence that gnawing incisors and the D1 nail arose in intimate coordination rather than independently. This idea aligns with prior evidence and speculation relating the rise of rodents to the rise of plants bearing hard seeds and nuts (*51*, *52*). The ability to handle and consume such foods represents an evolutionary specialization that is widespread among modern rodents across all major clades, and most of these genera bear a nail on the D1. How structural features of the D1 and its unguis may relate to the diverse dietary spectrum of rodents (variable in size, shape, hardness, and trophic range) can be studied building on the data and approach developed here.

Might similar structure-function relationships apply to multituberculates? This highly successful clade of extinct mammals had many rodent-like features, likely including the ability to gnaw hard foods (*53*–*60*), so perhaps they too benefited from handling food oromanually. There is an extreme paucity of D1 ungual phalanges of multituberculates in the fossil record, with one case suggesting more claw- than nail-like morphology (*61*). However, as we have shown, claws and nails on D1 are both compatible with oromanual food handling. Fossil evidence will be needed to clarify how D1 ungues and food handling evolved in multituberculates and other rodent-like mammalian ancestors.

In summary, the longstanding view is that the D1 nail borne by most rodents has evolved as it has because it is "vestigial" (or "nonfunctional," "rudimentary," and so forth). Our findings, which suggest the evolutionary persistence of this morphological feature across most extant rodents and by implication across much of their Cenozoic diversification, argue the opposite. We propose a different concept that the form of the D1 and its unguis have evolved to enable dual functionality of the hands. The D1 and its nail constitute morphological adaptations (with the exceptions described above) associated with dexterous oromanual food handling. That specialization allows other digits on the same hand to be differentially specialized for substrate interactions (e.g., clinging, burrowing, gripping, and more). This dimensionality contributed to the adaptive range of Rodentia. These outcomes highlight the intersection of evolutionary biology, functional morphology, and ethology, providing new insights into the adaptive significance and evolutionary persistence of the D1 nail in rodents. Our findings, including evidence for the coupled evolution of the D1 unguis and hand-related behaviors, point to a possible connection in rodents of diprotodonty and the form and function of the D1 unguis, and thus are a new way of conceptualizing rodent evolution.

REFERENCES AND NOTES

1. A. Huxley, *Nature* **333**, 592 (1988).
2. A. L. Gough-Palmer, J. Maclachlan, A. Routh, *Radiographics* **28**, 501–510 (2008).
3. T. J. Thomson, R. Motani, *J. Morphol.* **282**, 449–471 (2021).
4. E. S. Morse, *Ann. Lyceum Nat. Hist. N. Y.* **10**, 141–158 (1874).
5. P. Senter, J. G. Moch, *PeerJ* **3**, e1439 (2015).
6. A. C. Machado Cruvinel *et al.*, *Anat. Histol. Embryol.* **48**, 256–263 (2019).
7. D. Sustaita *et al.*, *Biol. Rev. Camb. Philos. Soc.* **88**, 380–405 (2013).
8. E. Pouydebat, D. Fragaszy, T. L. Kivell, *Bull. Mem. Soc. Anthropol. Paris* **26**, 129–133 (2014).
9. Y. F. Lin, N. Konow, E. R. Dumont, *Biol. Lett.* **15**, 20190503 (2019).
10. D. A. Kelt, J. L. Patton, *A Manual of the Mammalia: An Homage to Lawlor's "Handbook to the Orders and Families of Living Mammals"* (Univ. of Chicago Press, 2020).
11. E. H. Kay, H. E. Hoekstra, *Curr. Biol.* **18**, R406–R410 (2008).
12. S. F. Baird, *Reports of Explorations and Surveys, to Ascertain the Most Practicable and Economical Route for a Railroad from the Mississippi River to the Pacific Ocean. V.8. Part I. General Report Upon the Zoology of the Several Pacific Railroad Routes* (AOP Nicholson Printer, 1857), vol. 8.
13. G. S. Miller, *Genera and Subgenera of Voles and Lemmings* (US Government Printing Office, 1896), vol. 12.
14. R. I. Pocock, *Proc. Zool. Soc. Lond.* **1922**, 1171–1212 (1922).
15. C. A. Long, J. Captain, *Z. Säugetierkd.* **39**, 98–102 (1974).
16. W. H. Lehmann, *J. Morphol.* **113**, 59–76 (1963).
17. M. J. Tulli, L. V. Carrizo, J. X. Samuels, *J. Mamm. Evol.* **23**, 81–91 (2016).
18. G. J. Kenagy, *Science* **178**, 1094–1096 (1972).
19. J. C. Nikolai, D. M. Bramble, *Gt. Basin Nat. Mem.* **1**, 44–64 (1983).
20. R. F. Ewer, *Z. Tierpsychol.* **23**, 190–216 (1966).
21. T. L. Best, N. J. Granai, *Mamm. Species* **476**, 1–9 (1994).
22. I. Q. Whishaw, J. R. Sarna, S. M. Pellis, *Behav. Brain Res.* **96**, 79–91 (1998).
23. J. M. Barrett, M. E. Martin, G. M. G. Shepherd, *Curr. Biol.* **32**, 4842–4853.e6 (2022).
24. J. M. Barrett, M. G. Raineri Tapies, G. M. G. Shepherd, *PLOS ONE* **15**, e0226774 (2020).
25. T. A. Vaughan, *J. Mammal.* **47**, 132–133 (1966).
26. N. C. Bennett, *J. Zool.* **220**, 225–247 (1990).
27. E. Goeldi, *Proc. Zool. Soc. Lond.* **74**, 158–162 (1904).
28. L. J. Revell, L. J. Harmon, *Phylogenetic Comparative Methods in R* (Princeton Univ. Press, 2022).
29. B. H. Alhajeri, Y. Fourcade, N. S. Upham, H. Alhaddad, *Glob. Ecol. Biogeogr.* **29**, 2248–2260 (2020).
30. O. C. Bertrand, M. A. Schillaci, M. T. Silcox, *J. Vertebr. Paleontol.* **36**, e1014905 (2016).
31. K. A. Prufrock, C. B. Ruff, K. D. Rose, *J. Mamm. Evol.* **28**, 435–456 (2021).
32. D. E. Wilson, T. E. Lacher, R. A. Mittermeier, *Handbook of the Mammals of the World. Vol. 6. Lagomorphs and Rodents I* (Lynx Edicions, 2016).
33. D. E. Wilson, T. E. Lacher, R. A. Mittermeier, *Handbook of the Mammals of the World. Vol. 7. Rodents II* (Lynx Edicions, 2017).
34. B. P. Hedrick, B. V. Dickson, E. R. Dumont, S. E. Pierce, *Sci. Rep.* **10**, 717 (2020).
35. M. Pagel, *Proc. Biol. Sci.* **255**, 37–45 (1994).
36. J.-L. Hartenberger, in *Evolutionary Relationships Among Rodents: A Multidisciplinary Analysis*, W. P. Luckett, J.-L. Hartenberger, Eds. (Plenum Press, 1985), pp. 1–33.
37. L. Hautier, P. G. Cox, in *Evolution of the Rodents: Advances in Phylogeny, Functional Morphology and Development*, P. G. Cox, L. Hautier, Eds. (Cambridge Univ. Press, 2015), pp. 1–18.
38. M. Vianey-Liaud, L. Hautier, L. Marivaux, in *Evolution of the rodents: Advances in Phylogeny, Functional Morphology and Development*, P. G. Cox, L. Hautier, Eds. (Cambridge Univ. Press, 2015), pp. 539–588.
39. W. D. Matthew, *Bull. Am. Mus. Nat. Hist.* **28**, 43–72 (1910).
40. S. P. Blomberg, T. Garland Jr., A. R. Ives, *Evolution* **57**, 717–745 (2003).
41. J. M. Kamilar, N. Cooper, *Philos. Trans. R. Soc. Lond. B Biol. Sci.* **368**, 20120341 (2013).
42. A. M. Lister, *Nature* **500**, 331–334 (2013).
43. L. H. Emmons, *J. Mammal.* **60**, 431–432 (1979).
44. R. W. Thorington Jr., K. Darrow, A. D. Betts, *J. Morphol.* **234**, 155–182 (1997).
45. R. W. Thorington, J. L. Koprowski, M. A. Steele, J. F. Whatton, *Squirrels of the World* (Johns Hopkins Univ. Press, 2012).
46. S. O. Landry Jr., *Q. Rev. Biol.* **45**, 351–372 (1970).
47. W. D. Turnbull, *Fieldiana Geol.* **18**, 147–356 (1970).
48. R. Druzinsky, in *Evolution of the Rodents: Advances in Phylogeny, Functional Morphology and Development*, P. G. Cox, L. Hautier, Eds. (Cambridge Univ. Press, 2015), pp. 323–349.
49. J. M. Barrett *et al.*, *J. Neurosci.* **44**, e0856242024 (2024).
50. P. G. Cox *et al.*, *PLOS ONE* **7**, e36299 (2012).
51. M. E. Collinson, J. J. Hooker, *Palaeogeogr. Palaeoclimatol. Palaeoecol.* **157**, 127–149 (2000).
52. B. H. Tiffney, *Annu. Rev. Ecol. Evol. Syst.* **35**, 1–29 (2004).
53. D. W. Krause, *Rocky Mountain Geol.* **24**, 95–117 (1986).
54. N. F. Adams, E. J. Rayfield, P. G. Cox, S. N. Cobb, I. J. Corfe, *R. Soc. Open Sci.* **6**, 181536 (2019).
55. D. W. Krause, *Paleobiology* **8**, 265–281 (1982).
56. P. Del Tredici, *Biosystems* **22**, 327–339 (1989).
57. N. R. Longrich, M. J. Ryan, *Palaeontology* **53**, 703–709 (2010).
58. L. N. Weaver, G. P. Wilson, *J. Mammal.* **102**, 967–985 (2021).
59. G. P. Wilson *et al.*, *Nature* **483**, 457–460 (2012).
60. A. R. Biknevicius, *Am. J. Phys. Anthropol.* **71**, 157–171 (1986).
61. D. W. Krause, F. A. Jenkins, *Bull. Mus. Comp. Zool.* **150**, 199–246 (1983).
62. R. V. Missagia, A. Feijó, G. M. G. Shepherd, Observation data for: Evolution of thumbnails across Rodentia, Figshare (2025); https://doi.org/10.6084/m6089.figshare.26858230.
63. R. V. Missagia, A. Feijó, G. M. G. Shepherd, R code and input files for: Evolution of thumbnails across Rodentia, version v2, Zenodo (2025); https://doi.org/10.5281/zenodo.15438832.

ACKNOWLEDGMENTS

We thank J. Barrett, A. Ferguson, S. Goodman, L. Heaney, and J. Kerbis for valuable suggestions and discussions; O. Bertrand, L. Weaver, and an anonymous reviewer for comments and critiques on the manuscript; L. Revell for helpful insights and technical advice on the *phytools* package; D. Lunde and T. Hsu at NMNH and M. Surovy, E. Hoeger, and L. Caspers at AMNH for assistance with museum collections; K. Swagel and A. Shinya at FMNH for advice and assistance with radiography; A. Matsukawa, K. Rogovin, and G. Shenbrot for expert advice and sharing of unpublished observations; R. de Vries, D. Drukker, S. Musila, J. Philbois, T. Salah, K. Sarre, and M. Vedder for comments and discussions about iNaturalist observations; and D. Casali, G. Garbino, and C. Dias for valuable insights into discrete character evolution models. **Funding:** This work was supported by the Conselho Nacional de Desenvolvimento Científico e Tecnológico (CNPq grant 200897/2022-5 to R.V.M.); the National Institutes of Health (grants R37NS061963 and R34DA059723 to G.M.G.S.); and the National Natural Science Foundation of China (grant 3231101307 to A.F.). **Author contributions:** Conceptualization: R.V.M., A.F., B.D.P., P.D.J., G.M.G.S.; Data curation: R.V.M., A.F., L.J., M.L.A., B.D.P., P.D.J., G.M.G.S.; Formal analysis: R.V.M., A.F., G.M.G.S.; Funding acquisition: R.V.M., A.F., G.M.G.S.; Investigation: R.V.M., A.F., L.J., M.L.A., B.D.P., P.D.J., G.M.G.S.; Methodology: R.V.M., A.F., P.D.J., G.M.G.S.; Resources: A.F., L.J., M.L.A., B.D.P., P.D.J.; Writing – original draft: R.V.M., A.F., B.D.P., G.M.G.S.; Writing – review & editing: R.V.M., A.F., L.J., M.L.A., B.D.P., P.D.J., G.M.G.S. **Competing interests:** The authors declare no competing interests. **Data and materials availability:** The data are provided in the main manuscript and supplementary materials. Supplementary dataset 2 is also available at Figshare (*62*). The code used for analysis is available at Zenodo (*63*).

SUPPLEMENTARY MATERIALS

science.org/doi/10.1126/science.ads7926
Materials and Methods; Figs. S1 to S7; Tables S1 to S4; References (*64*–*92*); MDAR Reproducibility Checklist; Data S1 and S2

Submitted 5 September 2024; accepted 30 June 2025

10.1126/science.ads7926

LAYERED MATERIALS

Order-to-disorder transition due to entropy in layered and 2D carbides

Brian C. Wyatt[1], Yinan Yang[2], Paweł P. Michałowski[3]*, Tetiana Parker[4], Yamilée Morency[5], Francesca Urban[4], Givi Kadagishvili[6], Manushree Tanwar[6], Sixbert P. Muhoza[7], Srinivasa Kartik Nemani[8]†, Annabelle Bedford[1], Hui Fang[6], Zachary D. Hood[7], Junwoo Jang[8], Krutarth Kamath[1], Bethany G. Wright[8], Rebecca Disko[8], Anupma Thakur[1], Sanguk Han[5], Neil Ghosh[8], Xianfan Xu[8], Zahra Fakhraai[6]*, Yury Gogotsi[4]*, Aleksandra Vojvodic[5]*, De-en Jiang[2]*, Babak Anasori[1,8]*

In compositionally complex materials, there is controversy on the effect of enthalpy versus entropy on the structure and short-range ordering in so-called high-entropy materials. To help address this controversy, we synthesized and probed 40 M_4AlC_3 layered carbide phases containing two to nine metals and found that short-range ordering from enthalpy was present until the entropy increased enough to achieve complete disordering of the transition metals in their atomic planes. We transformed all of these layered carbide phases into two-dimensional (2D) sheets and showed the effects of the order versus disorder on their surface properties and electronic behavior. This study suggests the key effect that the competition between enthalpy and entropy has on short-range order in multicompositional materials.

Alloys containing stoichiometric mixtures of metallic elements in high-entropy alloys were systematically explored in the early 2000s (*1*, *2*). These studies demonstrated increased mechanical properties (*3*) and decreased thermal conductivity (*4*) beyond normal expectations of the "rule of mixture" approximations (*3*–*7*). In one of the early studies (*1*), it was proposed that increasing the total number of metallic elements in a single-phase material could result in entropy stabilization of enthalpically unfavorable mixtures of elements, which gained this class of metals the descriptor "high-entropy" alloys. Since this early report, high-entropy materials have been reported in other metallic alloys (*8*), as well as carbides (*9*), oxides (*10*), diborides (*11*), and other ceramics (*12*). However, since the "high-entropy" descriptor became popular, there has been push-back to using it as a general label (*13*) because it may not fully represent the major effect that enthalpy still has on the stability of a single-phase system. For example, short-range ordering in some high-entropy systems (*14*–*17*) suggests that enthalpic effects must still be present, even in entropy-stabilized materials (*18*). Therefore, there is a basic need to evaluate the true role of entropy versus enthalpy in the achieved configurations in single-phase "high-entropy" materials.

[1]School of Materials Engineering, Purdue University, West Lafayette, IN, USA. [2]Department of Chemical and Biomolecular Engineering, Vanderbilt University, Nashville, TN, USA. [3]Łukasiewicz Research Network - Institute of Microelectronics and Photonics, Warsaw, Poland. [4]A.J. Drexel Nanomaterials Institute and Department of Materials Science and Engineering, Drexel University, Philadelphia, PA, USA. [5]Department of Chemical and Biomolecular Engineering, University of Pennsylvania, Philadelphia, PA, USA. [6]Department of Chemistry, University of Pennsylvania, Philadelphia, PA, USA. [7]Applied Materials Division, Argonne National Laboratory, Lemont, IL, USA. [8]School of Mechanical Engineering, Purdue University, West Lafayette, IN, USA. ***Corresponding author. Email: banasori@purdue.edu (B.A.); de-en.jiang@vanderbilt.edu (D.J.), alevoj@seas.upenn.edu (A.V.); gogotsi@drexel.edu (Y.G.); fakhraai@sas.upenn.edu (Z.F.); pawel.michalowski@imif.lukasiewicz.gov.pl (P.P.M.)** †Present address: Department of Mechanical and Materials Engineering, University of Alabama Birmingham, Birmingham, AL, USA.

MAX phases are chemically denoted by their formula $M_{n+1}AX_n$, where M refers to n+1 layers of one or more early transition metals that are interleaved by X, which represents n layers of carbon or nitrogen (*19*). Between these $M_{n+1}X_n$ slabs, there are monoatomic layers of one or more A elements (commonly from groups 13 to 16 of the periodic table) (*20*). M is ionically or covalently bonded to X (*21*), similar to a transition metal carbide (*22*), whereas the surface M of each $M_{n+1}X_n$ slab is metallically bonded to the A element (*21*), which is structurally similar to a stacking fault in layered ceramics (*23*, *24*). As a result of this different structure and bonding at the $M_{n+1}X_n$-A-$M_{n+1}X_n$ interface, there can be a preference for the ordering of two or more transition metals in separate transition metal planes (*25*). When $n > 1$ in $M_{n+1}AX_n$, some transition metals prefer M sites bonded to both X and to A (M′ layers) or M sites only bonded to X (M″ layers), which is referred to as o-MAX (see Fig. 1A for M = 2) (*26*–*28*).

Although these o-MAX phases were reported a decade ago in two transition metal systems (*29*), the preference for an M' versus an M″ site in MAX phases is still not fully understood. Computationally, it has been shown that group 6 transition metals such as Cr, Mo, and W prefer M′ sites, whereas group 4 transition metals such as Ti, Zr, and Hf prefer M″ sites (*30*, *31*). Similarly, the earliest reported (in 2021) "high-entropy" 2D MXenes, $(TiVCrMo)_4C_3$ and $(TiVNbMo)_4C_3$ (*32*), were still predicted to have Cr and Mo in M' sites and Ti and Nb in M″ sites (*33*). Because MXenes are derived from their precursor MAX phases (*34*), this suggests that even in entropy-stabilized MAX phases (*32*), the enthalpic preference of M′ or M″ site occupancy is likely present.

We report the synthesis of 40 compositionally complex MAX phases containing two to nine transition metals. We demonstrate that MAX and MXenes let us evaluate the short-range ordering in multielemental materials and demonstrate the effects of enthalpy versus entropy on the order-to-disorder transition at the smallest scale (i.e., a few layers of atoms).

Theoretical studies of the order-to-disorder transition

To gain insight into the competition between enthalpy and entropy toward the order-disorder transition in high-entropy MAX phases (Fig. 1A), we first used density functional theory (DFT). To understand the M′ versus M″ preference for different transition metals in the M_4AlC_3 MAX phase, we built a symmetric model considering a pair of transition metals (M_1 and M_2) in either M' or M″ layers (M_1-C-M_2-C-M_2-C-M_1) for all possible combinations (from two to nine elements) (fig. S1). Figure S2 shows the formation energy (E_f) of these configurations; the calculation details are reported in the supporting information (see the materials and methods and tables S1 to S3).

After calculating these formation energies, we next used the difference in the formation energy (ΔE_f) between these structures with two given transition metals in either M′ or M″ sites to observe the enthalpic preference of the transition metals for different layers in the M_4C_3 structure (Fig. 1B). We focused on identifying the preference for out-of-plane ordering for M (i.e., to occupy separate transition metal planes), which we found to have a higher effect on the formation energy than any in-plane order (figs. S3 to S5). Trendwise, we observed that the M′ preference was Cr > Mo > W > V > Nb > Ta > Ti > Zr > Hf (inverse for M″ preference). This trend agrees with previous studies on both binary and high-entropy MAX phase (and carbide) literature showing that group 6 transition metals are usually less stable in the M_6C octahedra and, in MAX, tend to segregate toward M sites closest to the A layer (*9*, *30*). Overall, we show here that this preference is still present in M_4AlC_3 structures with more than two transition metals.

We used our model for short-range order to evaluate this hypothesis given the clear preference for transition metal arrangement in the M_4AlC_3 MAX phase structure. We first analyzed three M_4AlC_3 MAX phase structures with four transition metals: $(TiVNbTa)_4AlC_3$, $(TiVNbW)_4AlC_3$, and $(TiCrMoW)_4AlC_3$. Broadly, we found that when the same preference for order as found in double transition metal

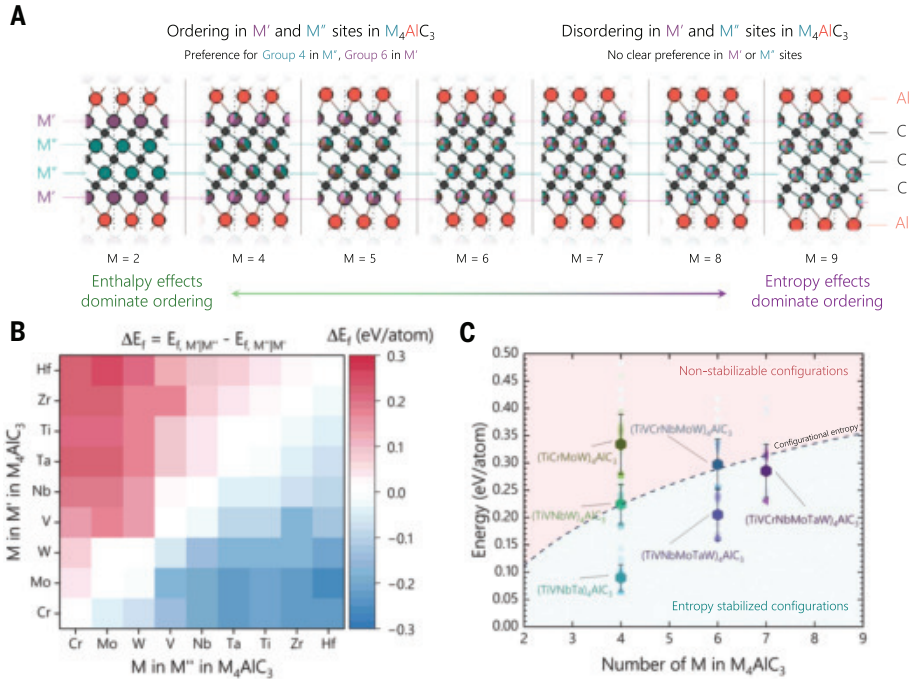

Fig. 1. Enthalpy versus entropy competition toward order-disorder in M_4AlC_3 MAX phases. (**A**) Schematic showing the hypothesis of increasing disorder with increasing entropy in M_4AlC_3 MAX phases. (**B**) Difference in formation energies for different pairs of transition metals in either M′ or M″ sites in M_4AlC_3 MAX. (**C**) Formation energy above the hull (ΔE_{hull}) versus configurational entropy in M_4AlC_3 MAX phases with the formation energy versus entropy-crossover around seven transition metals. Error bars represent SD.

o-MAX (labeled "ordered") was matched (figs. S4 to S6), the lowest formation energies were achieved. For example, when V and W occupied only M′ (outer) sites and Ti and Nb occupied only M″ (inner) sites in $(TiVNbW)_4AlC_3$, the formation energy was −0.544 ± 0.001 eV/atom. By contrast, if Ti and Nb occupied only M′ sites and V and W occupied only M″ sites, the opposite of the previous reports of o-MAX phases (labeled "inverse ordered"), then the formation energy was −0.430 ± 0.001 eV/atom. Similarly, solid-solution occupancies of Ti and Nb in M′ and M″ sites had a higher formation energy of −0.485 ± 0.006 eV/atom for $(TiVNbW)_4AlC_3$ than the ordered configuration.

Additionally, we found that group 6 elements always increased the distribution of the energy penalty because it is energetically preferred for group 6 elements to be in the M′ over the M″ sites (fig. S6). Broadly, this suggests two things: (i) MAX phases containing group 6 elements are generally less energetically favored and (ii) group 6 elements, if present, will most likely be in the M′ site. However, we found that the formation energy of MAX phases containing group 6 elements decreased with the increasing number of transition metals, which provides an avenue to their inclusion in MAX and potential MXenes (fig. S6). Therefore, after analyzing the contributions of enthalpy and entropy across several compositions (figs. S5 and S6), we predict that the transition from order to disorder likely occurs when a seventh element is introduced. However, because of the extensive computational demand, it was not feasible in the present study to simulate all possible compositions. A summary of this analysis of formation energy versus configurational entropy for the MAX phases containing four, six, and seven transition metals is shown in Fig. 1C, where the configurations below the dotted line are stabilizable by entropy and the configurations above the dotted line are not.

Experimental observation of the order-to-disorder transition due to entropy

With the gained knowledge from the energetic perspective, we next experimentally synthesized M_4AlC_3 MAX phases containing combinations of two and four to nine elements of group 4, 5, and 6 transition metals (Fig. 2, A and B). Synthesis and other details for these phases are provided in the supporting information. To determine whether we could experimentally observe ordering in M_4AlC_3 MAX phases, we first analyzed the x-ray diffraction (XRD) patterns (figs. S7 and S8). All of the 40 phases reported in this work can be found in table S4. All MAX phase characterization and analysis for each phase reported can be found in figs. S9 to S44. Figure 2C shows the scanning electron microscopy (SEM) image of $(TiVCrZrNbMoHfTaW)_4AlC_3$ with a layered grain structure; the energy-dispersive x-ray spectroscopy (EDS) shows that the grain contains all nine transition metals as well as Al (Fig. 2D). The XRD data (figs. S9 to S44) show the presence of impurity phases, including intermetallics and non-MAX carbides, which suggests that subsequent studies are required to improve the phase purity of these MAX phases. Although the XRD data provide some insight into the ordering, it is difficult to accurately compare transition metals with very similar x-ray scattering features (i.e., Ti versus V or Cr, Zr versus Nb or Mo, or Hf versus Ta or W) even when using Rietveld refinement. Therefore, we used an atomic-layer resolved dynamic secondary ion mass spectrometry (SIMS) method because this technique is better suited to differentiating the transition metals by elemental mass and charge (*35*–*37*).

To calculate the preference for site occupancy using SIMS, we determined atomic composition from the signal intensity (*37*) and calculated the average and SD of the occupancy of each element in either the M′ or M″ site. We then calculated a unitless comparative parameter, labeled α, for each transition metal from these values using Eq. 1 (*33*). As a result, when α is positive, it represents that a given transition metal prefers the M′ site. The inverse is also true. All SDs from the atomic composition were then propagated to this α using the root mean square method.

$$\alpha = \frac{M' - M''}{M' + M''} \quad (1)$$

SIMS indicates that Mo always occupies the M′ site and Ti, V, and Nb always occupy the M″ site for M_4AlC_3 MAX phases with two transition metals (fig. S45). This agrees with Fig. 1B, which states that group 6 transition metals most likely occupy M′ sites, whereas group 4 or 5 occupy M″ sites. Further, to calculate this site preference for M_4AlC_3 MAX phases with four or more transition metals, the difference in the atomic composition of each element in the M′ and M″ sites was evaluated by the α parameter (Eq. 1). Using this parameter, we noted that when four transition metals were placed into the M_4AlC_3 MAX phase, the trend in preference of a transition metal for an M′ or M″ site was the same as established for M_4AlC_3 MAX with two transition metals (Cr > Mo > W > V > Nb > Ta > Ti > Zr > Hf in M′ site) (Fig. 2E). This agrees with Fig. 1, B and C, suggesting that an enthalpic preference for M′ or M″ site ordering of the transition metals is still present even for these entropy-stabilized M_4AlC_3 MAX phases (*32*).

We observed that increasing the number of transition metals to five or six resulted in a diminished |α| for each transition metal (Fig. 2F). Together with Fig. 1C, this suggests that configurations with less preference for order are more likely to be stabilized by the increasing configurational entropy. For the SIMS data, this would result in a lower

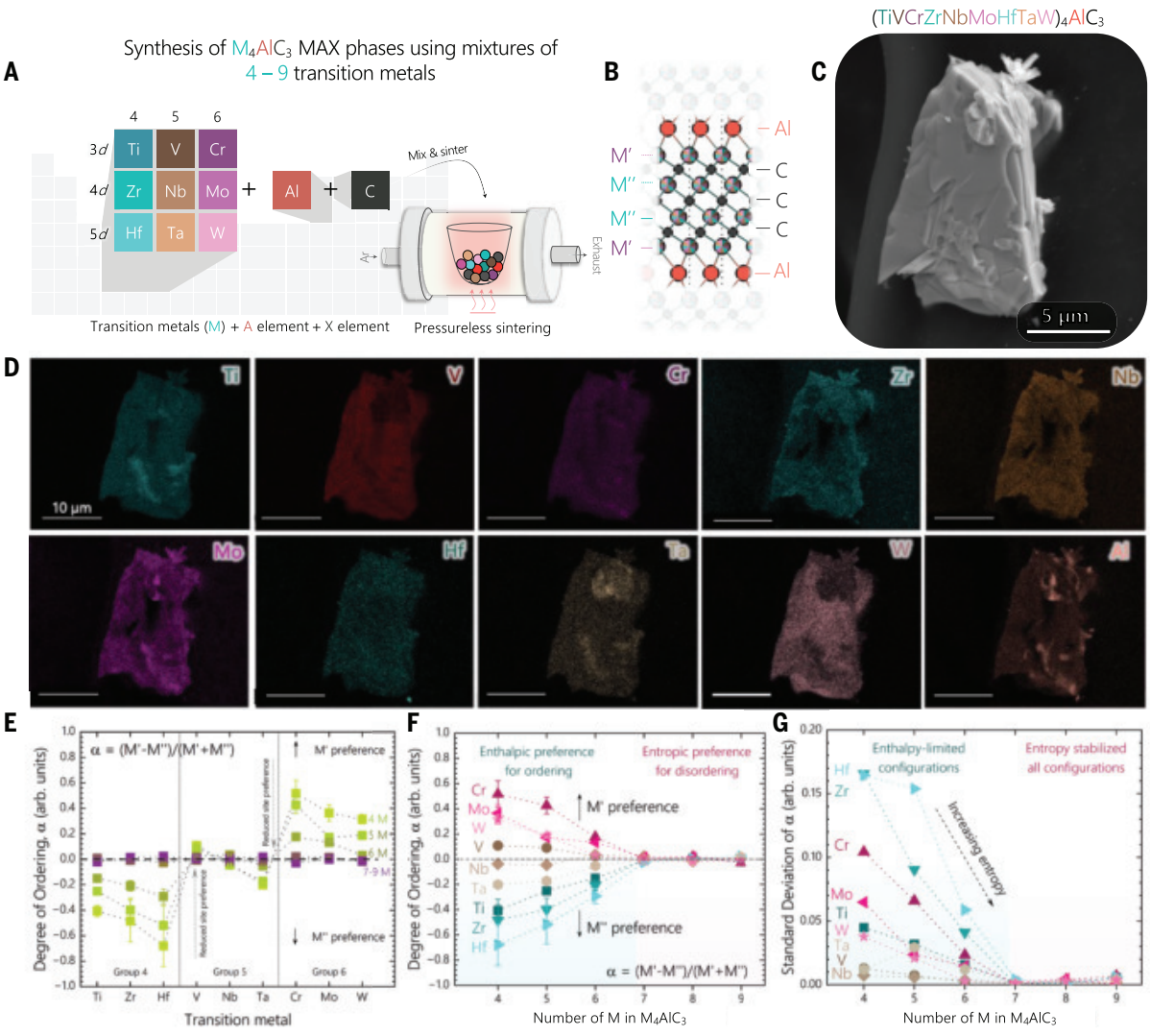

Fig. 2. Synthesis and analysis of $(TiVCrZrNbMoHfTaW)_4AlC_3$ and other M_4AlC_3 phases containing two to nine transition metals. (**A**) Schematic highlighting the mixed elements and synthesis approach. (**B**) Crystal structure of the targeted M_4AlC_3 MAX phase. (**C**) Electron microscopy image of a grain of $(TiVCrZrNbMoHfTaW)_4AlC_3$ MAX. (**D**) Elemental mapping of a grain of $(TiVCrZrNbMoHfTaW)_4AlC_3$ MAX showing the presence of all nine transition metals and aluminum. (**E**) SIMS measurements showing the preference for sites based on the transition metal and the total number of transition metals in M_4AlC_3 MAX. (**F**) SIMS showing the decreasing preference for different sites in M_4AlC_3 MAX plotted against the increasing numbers of transition metals. (**G**) Decrease in SD in the ordering term α as calculated by SIMS plotted against the increasing numbers of transition metals. Error bars represent SD.

|α| for each transition metal, because ordered (Fig. 1B) and disordered configurations of the transition metals would become observable in each transition metal layer. Probabilistically, however, we would not expect |α| to converge on zero yet in these low-to-medium–entropy systems because inverse-ordered configurations would not yet become stabilizable through entropy.

Conversely, beyond seven transition metals, we observed that the |α| converged on 0 for all transition metals (Fig. 2F). The convergence of |α| to zero suggests that ordered, solid-solution, and inverse-ordered configurations are stabilized. This would likely result in equal probabilistic chances to observe any configuration through SIMS measurements. We observed further support for this hypothesis by plotting the SD of |α| for all transition metals against the total number of transition metals (Fig. 2F), which further suggested that all configurations become stabilized at seven transition metals. Overall, our computational and experimental results indicate that the loss of short-range ordering in high-entropy MAX phases is only achievable once entropy can overcome the enthalpic penalties for all configurations. Broadly, these data demonstrate that (i) entropy-stabilized systems can display a preference for short-range ordering but (ii) systems only truly become "high-entropy" materials once entropy overcomes any remaining enthalpic preferences for the short-range order. However, high-throughput methods should be implemented to screen the effects of electronegativity, atomic size, electronic structure, oxygen substitution in the X sublattice, and other key features of the ordering and order-to-disorder transition to fully understand this transition. Further, subsequent studies must consider the impact of intermediate phases on the final phase formation and ordering. Although computational studies have shown that out-of-plane ordering trends are similar between $M_{n+1}AX_n$ phases with $n > 2$, subsequent studies should evaluate whether order-to-disorder transitions would be observed in other multitransition metal MAX phases.

Effect of order versus disorder on MXene surface chemistry

After confirming the synthesis and ordering behavior of the M_4C_3 structure in the M_4AlC_3 MAX phases, we evaluated the effect of order versus disorder and composition on the individual M_4C_3 lamellas. To do so, we synthesized the $M_4C_3T_x$ MXenes from their M_4AlC_3 MAX

phases using wet chemical synthesis (Fig. 3A) (*28*, *31*, *32*, *34*), which causes the MXene surface to be terminated with T groups, commonly –O, –OH, and –F (*34*). Some XRD patterns of MAX to MXene synthesis are shown in fig. S46. Further, we confirmed that our MXenes contained the same transition metals as the MAX, as shown for $(TiVCrZrNbMoHfTaW)_4C_3T_x$ in figs. S47 and S48. In addition, we used SIMS to confirm that the ordering of the transition metals remained similar in the MXenes as it was in the MAX for some select compositions (figs. S49 to S52). We were also able to successfully synthesize MXene films for a total number of transition metals between four and nine, as shown through XRD in fig. S53. Although we used a similar etching procedure for all MAX phases to obtain MXenes, subsequent studies are necessary to understand the exfoliation energy of each MAX to MXenes to best tune the synthesis process for any individual composition (*38*). All 2D MXenes produced in this study were dispersible in water (fig. S54). However, using x-ray photoelectron spectroscopy (XPS), we observed that the overall composition of T_x in the $M_4C_3T_x$ MXenes containing four to nine transition metals increased for –O (~33 at % to ~53 at %) and decreased for –OH (~37 at % to ~26 at %) and –F (~30 at % to 21 at %) (figs. S55 to S63 and table S5).

The ordering or disordering observed in the MAX phases is present in the MXenes (*36*) (figs. S49 to S52) and is a likely source of the changes in the T_x group composition in the respective $M_4C_3T_x$ MXenes. To gain insight into this trend, we used DFT to calculate the formation energy of –O and –F terminations on MXenes with different pairs of transition metals in either M′ or M″ sites (Fig. 3B). We observed that pairs of group 4 elements preferred F terminations, and pairs of group 6 elements preferred O terminations. We also observed that group 6 in M″ sites caused an increased preference for group 4 in M′ for O terminations, and group 4 in M″ sites caused an increased preference for group 6 in M′ for F terminations. As shown in the supporting information (fig. S64), the solid-solution combinations were typically between the two ordered configurations. The calculated values of O versus F preference for both ordered and solid-solution configurations of the paired transition metals are shown in fig. S65.

Because we cannot know the exact subsurface M″ metal atom for any given M′ metal atom bonded to T_x in our MXenes, we chose to plot the surface chemistry for M in M′ sites (bonded to T_x) against the valence electron concentration (VEC) in the M″ sites (Fig. 3, C and D), which was derived from SIMS using formal charges of the transition metals (Ti has four, V has five, Cr has six, etc.). In addition, in this plot, we consider both –OH and –F terminations together and –O terminations separately because –OH and –F would prefer a T^- oxidation state, whereas –O would prefer a T^{2-} oxidation state. In addition, we chose to add –OH and –F together because our use of tetramethylammonium hydroxide as a delamination agent could replace –F groups with –OH groups, and the two share a formal charge. As shown in Fig. 3, C and D, increasing the VEC in the M″ sites can increase the concentration of O terminations on Ti and –OH/F on V and Mo, which is broadly in agreement with the trends shown in Fig. 3B. A plot for easier comparison can be found in fig. S66. We observed agreement with the general increase of O as a T_x group on $M_4C_3T_x$ MXenes containing four to nine transition metals (see Fourier transform infrared spectra in fig. S67). In addition, through ultraviolet–visible–near infrared and Raman spectroscopy, we gained some insight into the effect of disorder in $M_4C_3T_x$ MXenes by increasing the total number of transition metals (figs. S68 to S71). Overall, this suggested that surface versus subsurface transition metals affect the chemical behavior and preference for surface terminations of the MXenes (*39*).

Effect of order versus disorder on MXene electrical conductivity

We evaluated the effect of multiple transition metals and order versus disorder on the electrical properties of thin films of these $M_4C_3T_x$ MXenes. When we investigated the $M_4C_3T_x$ MXenes containing two to nine transition metals, we found that the MXenes retained their metallic conductivity, as shown by both their linear *I* versus *V* behavior and their consistency with the Drude model of metallic electrical conductivity (figs. S72 to S78) (*40*). In addition, we noted that MXenes that contained Cr were up to an order of magnitude higher in electrical resistivity (fig. S79), which has been reported for high-entropy alloys

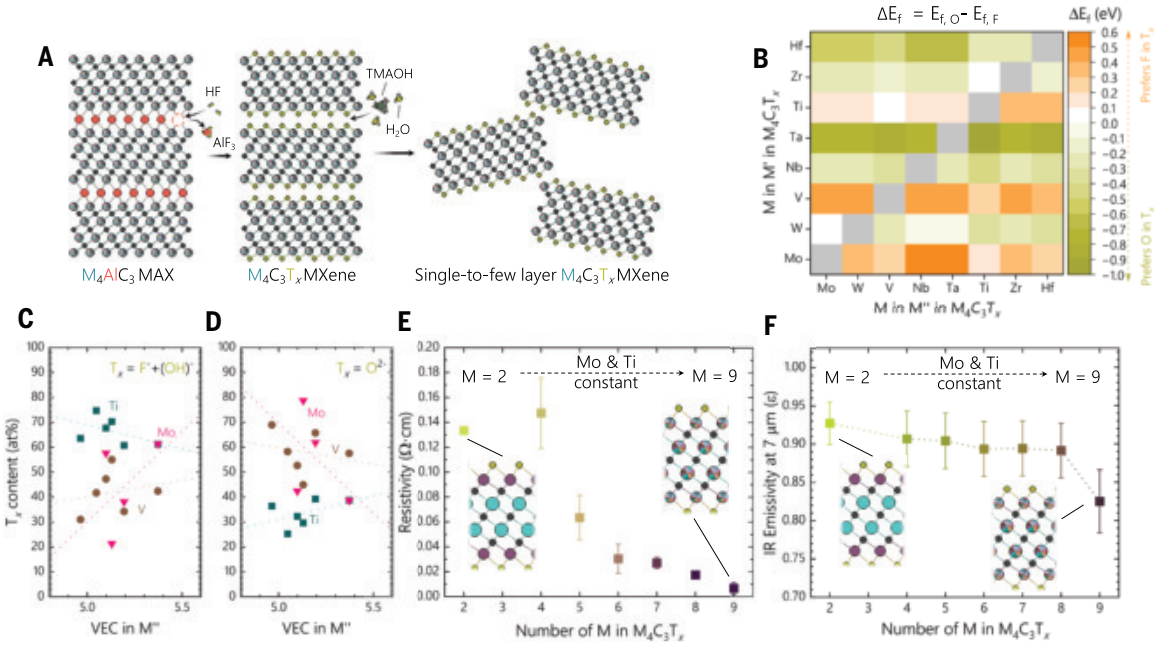

Fig. 3. Synthesis, surface chemistry, and properties of $M_4C_3T_x$ MXenes containing two to nine transition metals. (**A**) Schematic of the synthesis process of $M_4C_3T_x$ MXenes from M_4AlC_3 MAX. (**B**) Differences in formation energy of pairs of transition metals in $M_4C_3T_x$ with O versus F in termination sites (T). The gray boxes represent values for single-metal MXenes, which were not calculated in this study. (**C** and **D**) Content of O and F terminations, respectively, on Ti, V, and Mo atoms in $M_4C_3T_x$ MXenes versus the VEC in the M″ layers. The dotted lines are guides for the eye. (**E**) Electrical resistivity behavior of $M_4C_3T_x$ MXenes containing two to nine transition metals. (**F**) IR emissivity at 7-μm wavelength plotted against the total number of transition metals in the $M_4C_3T_x$ MXenes. Error bars represent experimental uncertainty.

with Cr (*41*). The flake sizes are shown using dynamic light scattering measurements in fig. S80. In figs. S81 to S89, atomic force microscopy images, height, and surface roughness analysis of some of the $M_4C_3T_x$ flakes containing two to nine transition metals are shown (table S6 summarizes the height and surface roughness results).

Decreasing electrical resistivity has been reported for high-entropy alloys with increasing numbers of transition metals (*42*), but the cause for this is not yet fully understood. In M_2C-type MXenes, computational work has shown that group 5 transition metals in MXenes should lower the electrical resistivity (*43*), whereas group 6 transition metals in MXenes have a higher electrical resistivity (*44*). Overall, in our high-entropy $M_4C_3T_x$ MXenes, we expected an increasing number of transition metals to cause disorder of group 5 and 6 transition metals throughout the $M_4C_3T_x$ structure. Therefore, we first plotted the electrical resistivity of our $M_4C_3T_x$ MXenes against the total number of transition metals, as shown in Fig. 3E. In Fig. 3E, we chose to keep Ti and Mo as consistent transition metals and systematically add one transition metal at a time to maintain comparability between samples. For example, at M = 2, we showed the fully ordered $Mo_2Ti_2C_3T_x$, and at M = 4, we showed the low entropy $(TiVNbMo)_4C_3T_x$ and then added W, Ta, Cr, Zr, and Hf for M = 5, 6, 7, 8, and 9, respectively.

In Fig. 3E, it can be seen that the resistivity of $Mo_2Ti_2C_3T_x$ at 0.13 Ω×cm initially increased for $(TiVNbMo)_4C_3T_x$ to 0.15 ± 0.03 Ω×cm and then decreased to 0.01 ± 0.01 Ω×cm $(TiVCrZrNbMoHfTaW)_4C_3T_x$. In addition, we observed a similar behavior in the infrared (IR) emissivity of these MXenes (Fig. 3F). This agrees with the changes in electrical resistivity shown in Fig. 3E, because decreasing electrical resistivity typically will result in a proportional decrease in IR emissivity (*45*). Broadly, we hypothesize that this decrease in resistivity could be attributed to two things (fig. S90): (i) the decrease in ordering results in fewer neighbors of group 6 to group 6 transition metals and (ii) the decrease in order creates structures with smaller differences in the total number of valence electrons (averaging to five) between neighbors in both M′ and M″ layers, both of which could improve the electron mobility in and between the M′ and M″ layers. However, subsequent studies are necessary to better understand the electron mobility and other properties in high-entropy MXenes and other high-entropy materials (*46*), such as approaches that focus on single-flake measurements or optical conductivity (fig. S91).

In summary, this work demonstrates a broad advancement in our understanding of the relation of enthalpy and entropy on short-range ordering in high-entropy materials. Specifically, by using M_4AlC_3 MAX phases with two to nine transition metals and analyzing their structural ordering using SIMS, we were able to evaluate the trend in the short-range ordering of transition metals in either outer (M′) or inner (M″) metal sites against the total number of transition metals. Doing so, we have shown that (i) in low- and medium-entropy combinations (i.e., up to six metals), the transition metals enthalpically prefer order in M′ or M″ sites; (ii) at seven metals or above, the structures become fully disordered (i.e., no clear preference for M′ or M″); and (iii) that this order-disorder transition is driven by an increasing contribution of configurational entropy. Finally, we showed that these MAX phases can be used to synthesize their respective MXenes, which allowed us to observe some effects of entropically driven disorder in these phases on the electrical and IR emissivity properties of these derived MXenes.

REFERENCES AND NOTES

1. J. W. Yeh *et al.*, *Adv. Eng. Mater.* **6**, 299–303 (2004).
2. B. Cantor, I. Chang, P. Knight, A. Vincent, *Mater. Sci. Eng. A* **375-377**, 213–218 (2004).
3. D. Utt *et al.*, *Nat. Commun.* **13**, 4777 (2022).
4. H.-P. Chou, Y.-S. Chang, S.-K. Chen, J.-W. Yeh, *Mater. Sci. Eng. B* **163**, 184–189 (2009).
5. L. Han *et al.*, *Nat. Rev. Mater.* **9**, 846–865 (2024).
6. S. Schweidler *et al.*, *Nat. Rev. Mater.* **9**, 266–281 (2024).
7. Y. Zhang, T. Zuo, Y. Cheng, P. K. Liaw, *Sci. Rep.* **3**, 1455 (2013).
8. F. Otto, Y. Yang, H. Bei, E. P. George, *Acta Mater.* **61**, 2628–2638 (2013).
9. P. Sarker *et al.*, *Nat. Commun.* **9**, 4980 (2018).
10. C. M. Rost *et al.*, *Nat. Commun.* **6**, 8485 (2015).
11. J. Gild *et al.*, *Sci. Rep.* **6**, 37946 (2016).
12. C. Oses, C. Toher, S. Curtarolo, *Nat. Rev. Mater.* **5**, 295–309 (2020).
13. M. Brahlek *et al.*, *APL Mater.* **10**, 110902 (2022).
14. S. Chen *et al.*, *Nat. Commun.* **12**, 4953 (2021).
15. P. Singh, A. V. Smirnov, D. D. Johnson, *Phys. Rev. B* **91**, 224204 (2015).
16. A. J. Wright, J. Luo, *J. Mater. Sci.* **55**, 9812–9827 (2020).
17. B. Jiang *et al.*, *J. Am. Chem. Soc.* **143**, 4193–4204 (2021).
18. S. Divilov *et al.*, *Nature* **625**, 66–73 (2024).
19. M. Dahlqvist, M. W. Barsoum, J. Rosen, *Mater. Today* **72**, 1–24 (2024).
20. M. Sokol, V. Natu, S. Kota, M. W. Barsoum, *Trends Chem.* **1**, 210–223 (2019).
21. M. Magnuson, M. Mattesini, *Thin Solid Films* **621**, 108–130 (2017).
22. B. C. Wyatt, S. K. Nemani, G. E. Hilmas, E. J. Opila, B. Anasori, *Nat. Rev. Mater.* **9**, 773–789 (2024).
23. A. Gusev, A. Kurlov, V. Lipatnikov, *J. Solid State Chem.* **180**, 3234–3246 (2007).
24. C. R. Weinberger, G. B. Thompson, *J. Am. Ceram. Soc.* **101**, 4401–4424 (2018).
25. M. Dahlqvist, J. Rosen, *Nanoscale* **14**, 10958–10971 (2022).
26. W. Hong, B. C. Wyatt, S. K. Nemani, B. Anasori, *MRS Bull.* **45**, 850–861 (2020).
27. B. Anasori *et al.*, *J. Appl. Phys.* **118**, 094304 (2015).
28. B. C. Wyatt *et al.*, *Nano Lett.* **23**, 931–938 (2023).
29. Z. Liu *et al.*, *J. Am. Ceram. Soc.* **97**, 67–69 (2014).
30. M. Dahlqvist, J. Rosen, *Nanoscale* **12**, 785–794 (2020).
31. B. Anasori *et al.*, *ACS Nano* **9**, 9507–9516 (2015).
32. S. K. Nemani *et al.*, *ACS Nano* **15**, 12815–12825 (2021).
33. Z. Leong *et al.*, *Chem. Mater.* **34**, 9062–9071 (2022).
34. K. R. G. Lim *et al.*, *Nat. Synth.* **1**, 601–614 (2022).
35. P. P. Michałowski *et al.*, *Nat. Nanotechnol.* **17**, 1192–1197 (2022).
36. B. C. Wyatt *et al.*, *Nat. Commun.* **15**, 6353 (2024).
37. P. P. Michałowski, *Nanoscale Horiz.* **9**, 1493–1497 (2024).
38. R. Khalediali dusti, M. Khazaei, S. Khazaei, K. Ohno, *Nanoscale* **13**, 7294–7307 (2021).
39. Y. Yang *et al.*, *2D Materials* **7**, 025015 (2020).
40. M. Han *et al.*, *ACS Nano* **14**, 5008–5016 (2020).
41. K. Jin *et al.*, *Sci. Rep.* **6**, 20159 (2016).
42. S. K. Dewangan, C. Nagarjuna, V. Kumar, in *High Entropy Materials*, A. Kumar, R. K. Gupta, Eds. (CRC Press, 2024), pp. 91–106.
43. M. Han *et al.*, *J. Am. Chem. Soc.* **142**, 19110–19118 (2020).
44. M. Khazaei, M. Arai, T. Sasaki, M. Estili, Y. Sakka, *Phys. Chem. Chem. Phys.* **16**, 7841–7849 (2014).
45. M. Han *et al.*, *Mater. Today* **64**, 31–39 (2023).
46. J.-W. Yeh, *Eur. J. Control* **31**, 633–648 (2006).

ACKNOWLEDGMENTS

G.K. and Z.F. thank T. E. Mallouk of the University of Pennsylvania for giving us access to the UV-Vis-NIR spectrometer and the Harrick Plasma Cleaner and R. Stephens for providing valuable ideas. **Funding:** This work was supported by the National Science Foundation (Center for Chemical Innovation M-STAR program grant CHE-2318105 to B.C.W., Y.Y., T.P., Y.M., F.U., G.K., M.T., S.K.N., A.B., H.F., K.K., B.G.W., R.D., A.T., S.H., Z.F., Y.G., A.V., D.J., and B.A.; Solid State & Materials Chemistry program grant DMR-2419026 to B.C.W., S.K.N., A.B., K.K., B.G.W., R.D., A.T., and B.A.; grant CBET-2051525 to J.J., N.G., and X.X.); National Science Centre, Poland (SONATA BIS 14 2024/54/E/ST11/00171 to P.P.M.); National Centre for Research and Development, Poland (LIDER XII LIDER/8/0055/L-12/20/NCBR/2021 to P.P.M.); Laboratory Directed Research and Development (LDRD) of Argonne National Laboratory, Office of Science, US Department of Energy (contract DE-AC02-06CH11357 to S.P.M. and Z.D.H.); the Vagelos Institute for Energy Science and Technology, University of Pennsylvania (graduate fellowship to Y.M.); the National Energy Research Scientific Computing Center, a DOE Office of Science User Facility (supported by the Office of Science of the US Department of Energy contract DE-AC02-05CH11231 using NERSC award BES-ERCAP0023161 to Y.M. and A.V.); and the Ministry of Trade, Industry, and Energy (MOTIE) Korea (Global Industrial Technology Cooperation Center program grant P0028332 supervised by the Korea Institute for Advancement of Technology to B.C.W., Y.G., and B.A.). **Author contributions:** Conceptualization: B.C.W., B.A. Investigation: B.C.W., Y.Y., P.P.M., T.P., Y.M., F.U., G.K., M.T., S.P.M., S.K.N., A.B., H.F., J.J., K.K., B.G.W., R.D., A.T., S.H., N.G., X.X. Methodology: B.C.W., P.P.M., S.K.N., Y.G., A.V., D.J., B.A. Project administration: B.C.W., Z.F., Y.G., A.V., D.J., B.A. Supervision: X.X., Z.F., Y.G., A.V., D.J., B.A. Writing – original draft: B.C.W., Y.Y., T.P., G.K., S.K.N., J.J., K.K. Writing – review & editing: All authors. **Competing interests:** B.C.W. and B.A. declare that a provisional patent on the synthesis of high-entropy MAX phases has been filed under patent number 70880-01. Y.G. declares his role as a board member of MXene Inc. and is also affiliated with Sumy State University, Ukraine. The remaining authors declare no competing interests. **Data availability:** All data are available in the main manuscript or the supplementary materials.

SUPPLEMENTARY MATERIALS

science.org/doi/10.1126/science.adv4415
Materials and Methods; Supplementary Text; Figs. S1 to S91; Tables S1 to S6; References (*47*–*68*)

Submitted 19 December 2024; accepted 1 July 2025

10.1126/science.adv4415

QUALITY CONTENT FOR THE GLOBAL SCIENTIFIC COMMUNITY

Multiple ways to stay informed on issues related to your research

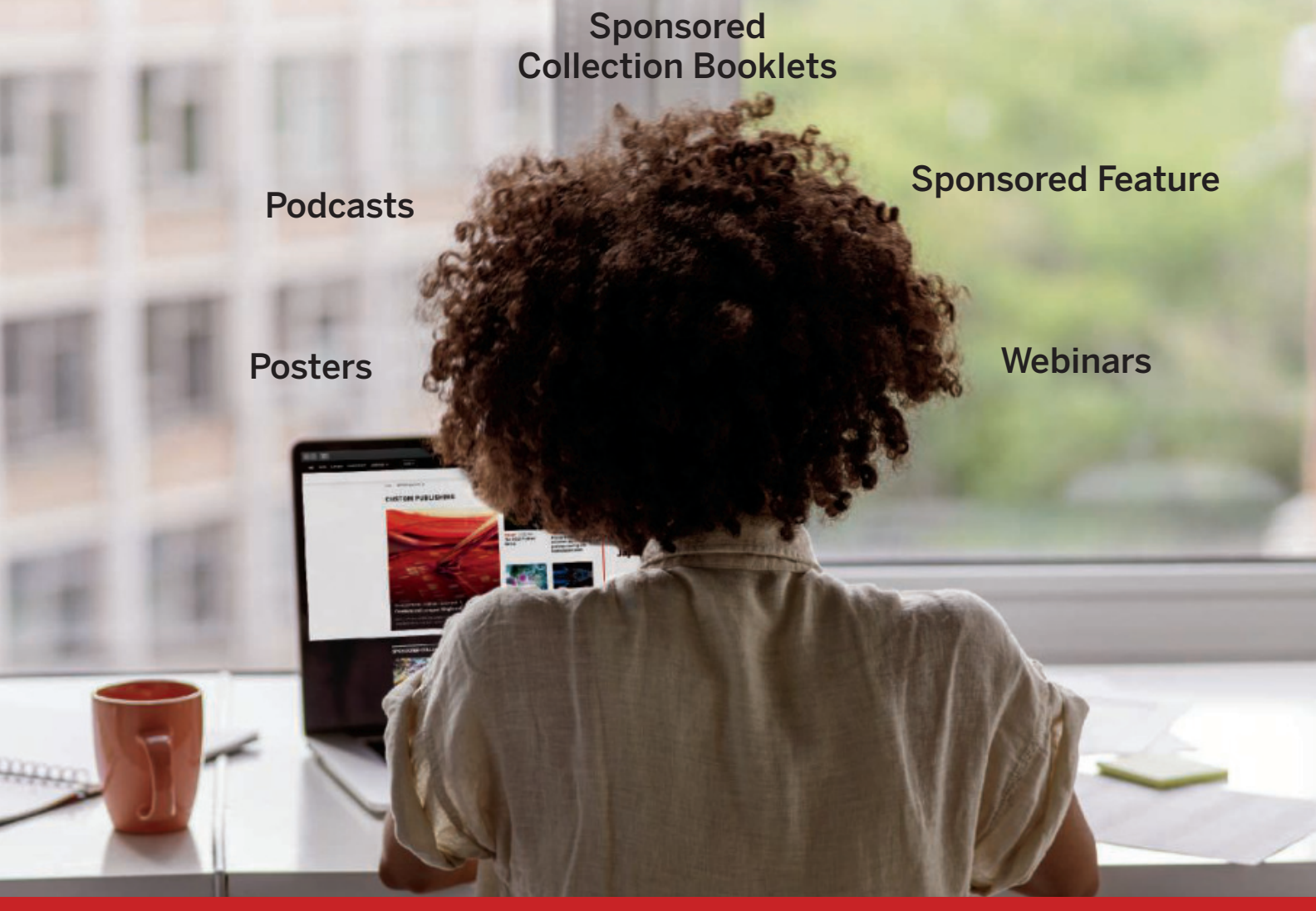

Science
AAAS

Scan the code and start exploring the latest advances in science and technology innovation!

Science.org/custom-publishing

Brought to you by the *Science*/AAAS Custom Publishing Office.

Posters | **Podcasts** | **Sponsored Collection Booklets** | **Sponsored Feature** | **Webinars**

Automated serial dilution

In a new independent research report by SuperMicrobiologistes, technicians and lab managers share their experiences using the Inlabtec Serial Diluter. To help microbiology labs solve long-standing problems with repetitive manual serial dilution techniques that strain technicians and limit efficiency, Inlabtec developed their automated Serial Diluter UC system. To secure feedback that truly represents why microbiology labs are adopting automated serial dilution, SuperMicrobiologistes interviewed users at both high-throughput contract labs (90,000 to 800,000 dilutions per year) and internal labs handling more moderate volumes (10,000 to 20,000 dilutions per year). Microbiology labs reported significantly less strain on hands and shoulders when using the Inlabtec Serial Diluter, thanks to its ergonomic design and the elimination of repetitive cap handling. Further reported benefits of the automated Serial Diluter UC include reduced training time—especially valuable in high-turnover environments—and more consistent results due to standardized dilution and mixing processes. Most notably, every lab interviewed said it would not go back to using traditional glass tube serial dilution techniques. This move from manual to automated serial dilution techniques is not only about comfort, but also about adopting smarter lab operations. Running the automated system with 300 bags consumes roughly the same amount of energy as a single dishwasher cycle. Combined with the device's low cost and the affordability of consumables, the solution is both economically and environmentally sustainable.

Inlabtec AG
For info: +41 71 222 48 65
www.inlabtec.com

IDS i20

The IDS i20 platform offers fully automated processing of specialty assays in endocrinology, allergy, autoimmune, and infectious diseases, Alzheimer's disease, and therapeutic drug monitoring. Revvity, Inc. (NYSE: RVTY) recently announced the launch of its new IDS i20™ analytical random-access platform from EUROIMMUN, enabling full automation of chemiluminescence immunoassays (ChLIA). The IDS i20 platform is a CE-marked and FDA-listed device that allows laboratories to consolidate multiple specialty tests on a unique single instrument with greater reagent capacity and higher test throughput compared to existing offerings. The highly versatile IDS i20 instrument allows users to simultaneously run 20 analytes from six diagnostic specialties on a single device. While specialty assays in these diagnostic areas tend to be processed manually or with semi-automated, low-throughput analyzers, the IDS i20 platform offers labs a new means of more flexible, fully automated ChLIA processing. With the ability to process up to 140 tests per hour (assay dependent), the IDS i20 instrument is the latest addition to the well-established IDS i-device series, built on more than 50 years of experience in medical device design and innovation. The IDS i20 platform features state-of-the-art software offering a high degree of adaptability and scalability, along with a superior graphical user interface that meets the latest standards in ergonomics, usability, and cybersecurity. Continuous loading of samples and reagents as well as the integrated cooling of ready-to-use reagent cartridges allow for nonstop operation of the system, maximizing efficiency and minimizing hands-on time.

Revvity
For info: 781-462-5126
www.revvity.com

Embedded AI in image sensors

SI Sensors reports progress on designing a next-generation image sensor that enables high-speed artificial intelligence (AI) processing within the sensor unit, on top of image processing. Traditionally, image sensor design has focused on capturing high-quality images and transmitting raw data to central processing units for analysis. However, the advent of embedded AI on image sensors offers a transformative way of capturing and processing visual data. By incorporating AI directly into the sensor, these devices can now perform complex data processing tasks on chip, reducing both latency and power consumption while enhancing performance. In high-speed imaging applications, embedded AI can be used to process data and significantly reduce the output from image sensors. This has been shown to alleviate the transmission bottleneck and enable higher frame rate and dynamic range. By processing most data locally, the necessity to transmit sensitive information externally is minimized. This is especially valuable in fields like health and security, where data protection is paramount. SI Sensors is a division of Specialised Imaging, focused on innovative CMOS image sensor design and development. The company's aim is to use its extensive in-house IP and design experience, together with the latest software tools, to design novel image sensors using the most appropriate foundry technologies globally.

SI Sensors
For info: +44-1442-827728
www.si-sensors.com

Automated plate seal remover

The Automated Plate Seal Remover from Azenta Life Sciences is a compact system for removing seals from a wide range of microplates with one touch of a button, without damaging the plate or seal. Hands-on removal of a seal from a microplate is a routine, seemingly undemanding laboratory task. However, removing and/or replacing tens or hundreds of seals at a time on a repetitive basis can be challenging, particularly in high-throughput and high-content screening laboratories. Designed for unattended operation, the Automated Plate Seal Remover is an ideal solution for life science labs that routinely remove microplate seals. It streamlines workflows by eliminating manual bottlenecks, helping to protect sample integrity and minimize degradation by reducing time spent on the benchtop. With its unique design, the Automated Plate Seal Remover eliminates the need for mechanical removal mechanisms, which can be prone to failure. Each plate is passed under a freshly exposed section of the patented de-sealing tape, which gently lifts and peels away the seal as it adheres to the tape. The device is engineered to hold plates securely in place, ensuring consistent removal—even for the most stubborn seals.

AZENTA Life Sciences
For info: +44 -161-777-2098
www.azenta.com

Electronically submit your new product description or product literature information! Go to www.science.org/about/new-products-section for more information.

Newly offered instrumentation, apparatus, and laboratory materials of interest to researchers in all disciplines in academic, industrial, and governmental organizations are featured in this space. Emphasis is given to purpose, chief characteristics, and availability of products and materials. Endorsement by *Science* or AAAS of any products or materials mentioned is not implied. Additional information may be obtained from the manufacturer or supplier.

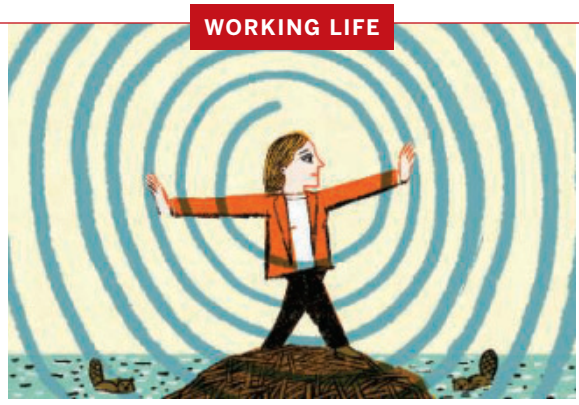

Unsteady ground

Cherie Westbrook

I look at the beaver dam with trepidation. As an ecohydrologist who studies the engineering abilities of beavers, I've crossed hundreds of these structures with little hesitation. But now each step feels like braving a precipice. I move slowly, scanning the logs underfoot for stable ground, my students carrying the equipment I once shouldered. I'm conscious that at any moment the world can suddenly spin, leaving me reaching for the nearest willow branch just to stay upright. Vertigo has rewired how I move through wetlands, lecture halls, and life in general, making me hyperaware of balance—both physical and professional.

My vertigo roller coaster began with a strange incident 4 years ago. On my first day back on campus after the pandemic lockdowns, three masked men burst into my office as I met with a student on Zoom. It was straight out of a movie. The student kept talking, unaware of what was unfolding. After what seemed like an eternity, the man closest to me muttered "wrong person" and walked out. They didn't physically hurt me, or—thankfully—the faculty member whom I later learned they intended to harm. But the intrusion unsettled me in ways I couldn't shake.

I booked a massage to calm my frayed nerves. Instead, as my neck was being massaged, the room began to violently spin. As I later learned, the pressure dislodged tiny crystals in my inner ear that are crucial to balance. In a single moment, the ground shifted beneath me. And I didn't know when—or whether—it would stop.

Afterward, days blurred into weeks as I stayed in bed, propped up to sleep upright, afraid to move my head lest I vomit uncontrollably. I abandoned all my duties except teaching, which I did on Zoom with my camera off, my mother-in-law advancing the slides and whispering occasional prompts as I spoke from memory. It was a dark time: harder than the pandemic, harder even than raising children. As the main income provider, I worried constantly about my family's future if I didn't recover.

Physiotherapy eventually helped stabilize my inner ear. Gradually the room steadied. But my journey wasn't over. A year later, the vertigo returned, and then slowly faded over 10 months. Now, I live with the anxiety that at any moment, the floor might begin to shift again.

More than once, I've felt the spins come on midlecture, forcing me to grab the edge of the nearest table to steady myself. I've learned that vertigo demands constant mental energy just to keep upright. It's work no one sees. And that's part of what makes it hard to talk about.

I haven't had any mishaps when I've been out in the field with my students studying beavers. But the fear is always there. So, too, is the shift in how I see myself as a scientist. Despite my love of fieldwork, I have had to accept that some seasons, I will do less of it. I've learned to build more flexibility into research plans, delegate in ways that help students grow, and focus on aspects of ecohydrology for which a steady gait isn't crucial, like data analysis, writing, mentoring, and service.

My own vertigo has made me alert to signs of it in others. I notice the colleague who sits through standing ovations. The one who avoids certain terrain. The one who always takes the elevator. I see now that many of us are navigating invisible limitations while still showing up fully for our work.

These days I move with a kind of cautious attention I never needed before. But a slower pace has also opened up space for quiet gratitude. For months I couldn't walk without assistance. I couldn't look at a computer without vomiting. Now, I can be back in the field. I can travel. I can still do the work that makes me feel alive. My steps are slower, and the fear is still there—but so is the joy of taking them. □

Cherie Westbrook is a professor at the University of Saskatchewan.
Do you have an interesting career story to share? Send it to SciCareerEditor@aaas.org.

ILLUSTRATION: ROBERT NEUBECKER

Apply for the BII and Science Translational Medicine **Prize for Innovations in Women's Health**

BII Science Translational Medicine — Prize for Innovations in Women's Health

The prize seeks to recognize researchers who have developed innovative advances with translational potential to impact women's health.

BioInnovation Institute (BII) and Science Translational Medicine introduce a new annual prize to celebrate scientists whose research has advanced translation and innovation to address high unmet medical needs in the underserved fields of women's health.

The winner will have their essay published in Science Translational Medicine, will receive a cash reward of $25,000, and be invited to BII headquarters in Copenhagen, Denmark, for the grand award ceremony.

Contributions within any area of women's health will be considered. These include:

- Female specific conditions;
- Reproductive health;
- Conditions that affect females and males differently.

Deadline
November 1, 2025
bii.dk/community/prizes

BII BioInnovation Institute

Science Translational Medicine